

University of Nottingham
UK | CHINA | MALAYSIA

A study on the use of three-dimensional dielectric crossed compound parabolic concentrator for daylighting control application

by

Meng TIAN, BEng

Student ID: 4225898

Supervisors: Dr. Yuehong Su, Prof. Saffa Riffat

Thesis Submitted in Partial Fulfilment of the Requirements for the Degree of

Doctor of Philosophy

in the Department of Architecture and Built Environment

Faculty of Engineering

University of Nottingham

I hereby certify that this is entirely my own work unless otherwise stated, and I have all necessary rights and consents to publicly distribute this dissertation via the University of Nottingham's eTheses archive.

08 November 2017

Abstract

As a low concentration concentrator with a larger acceptance angle and without a tracking requirement, compound parabolic concentrator is regarded as an attractive solution to improve the system performance and reduce the cost of photovoltaic (PV) system, solar thermal system, daylighting and lighting systems, etc. As a typical type of three-dimensional compound parabolic concentrator (CPC), dielectric crossed compound parabolic concentrator (dCCPC) has drawn a significant research attention in these years to explore its angular characteristics in solar collection for concentrating photovoltaics and daylighting control in buildings.

This thesis provides a comprehensive study on dCCPC in aspect of daylighting control. The work starts from a general review that provides a detailed introduction of the background of CPC applications in solar energy. Then the fundamental property of dCCPC when it is utilized as skylights for daylighting control is investigated, and the performance of dCCPC is also compared to other types of CPC. With the consideration of actual application, the dCCPC panel should be designed as small as possible to reduce its weight and maintain the optical characters simultaneously. Several criteria relating to the dimension of dCCPC panel are proposed and investigated about their effects on the optical performance of dCCPC, followed by the experiments that are taken for validation.

As ray-tracing simulation is the most common way to determine the optical performance of dCCPC which provides accurate result but requires long time to run, the multiple nonlinear regression model and artificial neural network model are put forward in the beginning of the second half of this thesis. The coefficients of determination of these models could reach 0.99 which imply the high accuracy of them. The optical performance of dCCPC can be calculated rapidly by knowing the sun position and sky condition. Afterwards, because the performance of dCCPC can be calculated easily for any time and any location with the mathematical model, a case study was taken to investigate the dCCPC effects on building energy consumption, indoor visual environment and economic benefits.

This research proves the potential of dCCPC in terms of daylighting control. As a stationary skylight, the transmittance of it is adjusted automatically depending the sky condition and sun position. It also provides outstanding performance in indoor

illuminance distribution. The dCCPC is suggested to be used in the locations with long hot seasons for the purpose of energy saving, and it is suggested for all locations with a view to glare control. For further work, more related criteria are encouraged to be added into the prediction models. The method of manufacturing dCCPC is suggested to be improved. Finally, the asymmetric dCCPC is expected to have high potential in daylighting control as vertical building facade, which is worth to be investigated.

Publications

Tian, M. and Y. Su, Multiple nonlinear regression model for predicting the optical performances of dielectric Crossed Compound Parabolic Concentrator (dCCPC). Solar Energy, 2018. 159: p. 212-225.

Tian, M., et al., A review on the recent research progress in the compound parabolic concentrator (CPC) for solar energy applications. Renewable and Sustainable Energy Reviews, 2018. 82(Part 1): p. 1272-1296.

Tian, M., et al., A study on incorporation of transpired solar collector in a novel multifunctional PV/Thermal/Daylighting (PV/T/D) panel. Solar Energy, 2018.

Ma, X., H. Zheng, and M. Tian, Optimize the shape of curved-Fresnel lens to maximize its transmittance. Solar Energy, 2016. 127: p. 285-293.

Tian, M. and Y. Su, An Improvement to Calculation of Lighting Energy Requirement in the European Standard EN 15193:2007. Journal of daylighting, 2014. 1: p. 16-28.

Tian, M. and Y. Su, Three dimensional dielectric compound parabolic concentrator (3D dCPC) for daylighting control in roofing, in 11th Conference on Advanced Building Skins. 2016: Bern, Switzerland.

Su, Y., et al., The effect of non-uniform irradiation on PV cell performance in a lens-walled CPC Bulgarian Chemical Communications, 2016. 48(E): p. 173-117.

Tian, M. and Y. Su, A study on use of three-dimensional miniature dielectric compound parabolic concentrator (3D dCPC) for daylighting control application, in 14th International Conference on Sustainable Energy Technologies -SET 2015. 2015: Nottingham, UK.

Zhang, L., et al., A case study of energy efficiency retrofit and renewable technology utilisation in a UK schools group, in 14th International Conference on Sustainable Energy Technologies -SET 2015. 2015: Nottingham, UK.

Tian, M., L. Zhang, and Y. Su, Two novel prediction models for the transmittance of dielectric crossed compound parabolic concentrator (dCCPC) under various sky conditions. Renewable Energy, 2018. (In press)

Tian, M., L. Zhang, and Y. Su, Energy and visual performance of building with dielectric crossed compound parabolic concentrator (dCCPC) panel as skylights. Energy and Buildings, 2018. (In press)

Acknowledgements

First and foremost I would like to express my sincere gratitude to my supervisor Dr. Yuehong Su. I appreciate all his contributions of time, ideas and continuous supports of my study. It has been an honour and fortunate to be one of his Ph.D. students. I have had a joyful, meaningful and memorable research time in the past three years.

I would also like to thank the head of the architecture, energy & environment research group, Prof. Saffa Riffat, who introduced me a lot of frontier technologies and aroused my interests of my research area.

My sincere thanks also goes to two personal tutors in university when I was in undergraduate, Derek Armstrong and Dr. Robin Wilson. Their encouragements have been with me from undergraduate to Ph.D. and helped me conquer many difficulties in my study.

I am grateful to my colleague Dr. Xu Yu. Without his outstanding previous-work on compound parabolic concentrator, my research could not go as well as it is now. My thanks also goes to my colleague Dr. Hang Zhou who helped me a lot in my experiment.

A special thanks to my parents for all their love and encouragement. They raised me with so many loves and supported me in all my pursuits. Words cannot express my appreciations to them.

A very special gratitude goes to my boyfriend Shuiting Su for accompanying me across eight time zones in the past five years when I studied abroad. This work cannot be finished successfully without his love, trust, patience, support and encouragement.

My time in University of Nottingham was enjoyable owing to my dear friends: Li Zhang, Yiyi Chen, Wendy Cook, Dafei Li, Bing Chen, Fang Tang, Zhengcheng Zhou, Kongying Zhou, Yuwei Wang, Wu Wen. I am really grateful for the moments we spent together.

Lastly, I would like to thank myself for always living up to my own expectations.

Content

Abstract II
Publications IV
Acknowledgements VI
Content VII
List of Tables XII
List of Figures XIV
Chapter 1 1
Introduction 1
1.1. Background 2
1.2. Thesis objectives and structure 3
Chapter 2 7
A review on the recent research progress about the compound 7
parabolic concentrator 7
(CPC) 7
2.1. Introduction 8
2.2. Fundamentals and considerations in CPC design 9
2.2.1. Design principles of CPC 9
2.2.2. Design considerations in structure 11
2.2.3. Design considerations in material 17
2.2.4. Solar geometry and tracking system 18
2.3. CPC studies in literature 20
2.3.1. CPC in photovoltaic system 21
2.3.2. CPC in solar thermal 32
2.3.3. CPC in daylighting 40
2.3.4. CPC in photocatalytic water degradation and purification 47
2.4. Simulation tools 48
2.5. Observations and outlook 55
2.5.1. Summary and observations on CPC studies in literature 55
2.5.2. Prospects and outlook 58
2.6. Summary 61
Chapter 3 77

Fundamental research of the property for three-dimensional dielectric crossed compound parabolic concentrator (3D dCCPC) 77
3.1. Introduction 78
3.1.1. Summary of a previous work on 2D dCPC 78
3.1.2. Introduction of Photopia 79
3.1.3. Improvement of dCPC in current research and objectives 80
3.2. Comparison of 2D and 3D dCPCs 83
3.2.1. Relationship between incident angle and transmittance of different CPC structures 83
3.2.2. Transmittance of 2D and 3D dCPCs under clear sky 85
3.2.3. Transmittance of 2D and 3D dCCPC under overcast sky 88
3.2.4. Discussion 91
3.3. Effect of tilt angle on 3D dCCPCs 93
3.3.1. Effect of tilt angle on 3D dCCPC under sunny sky 94
3.3.2. Effect of tilt angle on 3D dCCPC under overcast sky 102
3.3.3. Discussion 107
3.4. Effects of horizontal rotation angle on 3D dCCPC and r-dCPC 110
3.4.1. Effects of horizontal rotation angle of 3D dCPCs under sunny sky 110
3.4.2. Effects of horizontal rotation angle of 3D dCPCs under overcast sky 116
3.4.3. Discussion 122
3.5. Summary 124
Chapter 4 127
Manufacture and experiment design of 127
dielectric crossed compound parabolic 127
concentrator (dCCPC) panel 127
4.1. Introduction of 3D dCCPC panel properties 128
4.2. Effects of design criteria on CPC panel performance 129
4.2.1. Conjunction cover 129
4.2.2. Truncation 130
4.2.3. Gaps between CPC elements 134
4.3. Discussion 136
4.3.1. Conjunction cover 136
4.3.2 Truncation 137
4.3.3. Gap 139

4.3.4 Relationship between three criteria....141
4.4 Further modifications....143
4.4.1 Design requirements....143
4.4.2 Prediction of truncation effects....144
4.4.3 Validations of truncation predictions....145
4.4.3. Scaling....147
4.5 Experiment methodology....148
4.5.1 Design of dCCPC panel....148
4.5.3 Test PV output to estimate transmittance....149
4.6 Results and discussion....152
4.7 Summary....155
Chapter 5....157
Multiple nonlinear regression model for predicting the optical performances of dielectric Crossed Compound Parabolic Concentrator (dCCPC)....157
5.1. Introduction....158
5.2. Methodology....160
5.2.1. Models of dCCPC....160
5.2.2. Software settings....160
5.2.3. Multiple nonlinear regression....162
5.2.4. Independent variables....164
5.2.5. Dependent variables....165
5.3. Results and regression....166
5.3.1. Transmittance prediction model for non-coated dCCPC....166
5.3.2. Transmittance prediction model for base-coated dCCPC....174
5.3.3. Optical efficiency prediction model for base-coated dCCPC....177
5.4. Discussion....181
5.4.1. Verification of prediction models....181
5.4.2. Model limitations....182
5.4.3. Significance of prediction models....183
5.5. Summary....184
Chapter 6....185
Comparison between multiple nonlinear regression and artificial neural network for predicting the transmittance of dCCPC under standard sky conditions....185
6.1. Introduction....186

6.2. Methodology 188
6.2.1. Model description 188
6.2.2. Multiple Nonlinear Regression (MNLR) 190
6.2.3. Artificial Neural Network (ANN) 190
6.2.4. Evaluation criteria 192
6.3. Modification of Multiple Nonlinear Regression (MNLR) model 193
6.4. Development of Artificial Neural Network (ANN) model 196
6.5. Advantages and limitations 199
6.5.1. Comparison between ANN and MNLR 199
6.5.2. Significance and limitation of prediction models 201
6.6. Summary 202
Chapter 7 204
Energy and visual performance of building with dCCPC panel 204
as skylights 204
7.1. Introduction 205
7.2. Calculation of equivalent altitude angle and equivalent azimuth angle for dCCPC in any south-facing tilt angle 206
7.2.1. Calculation of equivalent altitude angle 208
7.2.2. Calculation of equivalent azimuth angle 209
7.2.3. Example of calculating transmittance of dCCPC for random location, time and sky condition 210
7.3. Comparison of indoor illuminance distribution of dCCPC and other diffuse panels 211
7.3.1. Comparison between dCCPC, prismatic and hemispheric panels 212
7.3.2. Comparison between tilted roof and flat roof 215
7.3.3. Summary of indoor illuminance distribution of different skylights 217
7.4. Introduction of software for energy simulation 219
7.4.1. Software overview 219
7.4.2. Selection of skylight material used in Grasshopper 221
7.5. Methodology 224
7.5.1. Model description 224
7.5.2. Location 226
7.5.3. Glare analysis 228
7.6. Results and discussion 229

7.6.1. An example of variations of hourly energy consumption.....229
7.6.2. Monthly and annual cooling and heating loads 231
7.6.3. Energy consumption of artificial lighting.....237
7.6.4. Visual environment and glare analysis 239
7.7. Economic analysis.....242
7.7.1. Methodology and hypothesis.....242
7.7.2. Calculation of discounted payback period.....244
7.8. Summary 245
Chapter 8 247
Conclusion 247
8.1. Conclusion of main achievements.....248
8.2. Recommendations for further work 250
Reference.....252
Appendix A. MNLR model for predicting the optical efficiency of base-coated dCCPC under all sky conditions 275
Appendix B. Supplementary figures and tables.....278
Appendix C. Calculation of inner perpendicular projection angle 280
Appendix D. Predictions of the optical efficiency by inner perpendicular projection angle for dCCPC 283
D.1. Inner perpendicular projection angle and optical efficiency 283
D.2. Inner perpendicular projection angle and transmittance.....285
D.3. Investigations of the correlations among inner perpendicular projection angle, sky clearness factor and other dependent variables.....287

List of Tables

Table 2.3.2.1: Solar energy collectors [116] 32

Table 2.4.1. Summary of the software used in CPC simulation 62

Table 2.5.1.1. Comparison of CPC studies covered in manuscript (NA: Not available; the test prototype without additional comments are indoor experiment) .. 65

Table 3.3.3.1. Transmittance of 3D dCCPCs with different tilt angles 108

Table 4.2.3.1. Relationship between truncated thickness and gap width 134

Table 4.4.1.1. Summary and suggestions of three design criteria of CPC panel 143

Table 4.4.2.1. Values of constants for fitting equations 4.4.2.1 144

Table 5.2.2.1. Comparisons of sunlight lumen ratio, horizontal sunlight illuminance ratio and sky clearness factor and corresponding sky conditions 162

Table 5.3.1.1. Regressing equations attempted for the correlations of altitude, azimuth and sky clearness factor to the transmittance of non-coated dCCPC 170

Table 5.3.1.2. Goodness of regressions (Eq. 5.3.1.1-1 – Eq. 5.3.1.1-12) for non-coated dCCPC 171

Table 5.3.1.3. Parameter values of Eq. 5.3.1.1-12 for predicting the transmittance of non-coated dCCPC 172

Table 5.3.2.1. Parameter values of Eq. 5.3.1.1-12 for predicting the transmittance of base-coated dCCPC 177

Table 5.3.3.1. Parameter values of Eq. 5.3.1.1-13 for predicting the optical efficiency of base-coated dCCPC 180

Table 5.4.1.1. Verification of predicted optical performance to simulation results for dCCPC on various dates and times 181

Table 5.4.3.1. Summary of multiple nonlinear regression models 183

Table 6.3.1. Parameter values of Eq. 6.3.1a-6.3.1b for non-coated and base-coated dCCPC 194

Table 6.4.1. Correlation coefficients of trained ANN models 198

Table 6.5.1.1. Comparison between the correlations of regression formula and ANN model 200

Table 7.3.3.1. Summary of the performances for different skylights 218

Table 7.4.2.1. Simulated illuminance distribution on work plane under different sky conditions 223

Table 7.5.1.1. Properties of skylight materials (DB, dCCPC-DB and dCCPC-lowE) 226

Table 7.5.2.1. Locations and climates of simulated cities 227

Table 7.7.1.1. Summary of the costs and economic benefits for using dCCPC 243

Table A-1. Table 5.3.2.1. Parameter values of Eq. A-1 for predicting the optical efficiency of base-coated dCCPC 276

Table A-2. Comparison between the correlations of regression formula and ANN model.....277

Table B-1. Parameter values of Eq. 5.3.1.1-1 - Eq. 5.3.1.1-11 for simulated non-coated dCCPC 279

Table D.3-1. Correlation coefficients of trained ANN models 2 (Independent variables: $\theta n'$, ε; dependent variables: T or $T + Rref$).....288

List of Figures

Fig. 2.2.1.1. Construction of the CPC profile from the edge-ray principle [31].....10

Fig. 2.2.2.1. Example of 2D and 3D CPCs a) 2D trough CPC with a glass on top and PV on bottom [68] b) 3D CPCs with polygonal apertures of 4, 5, 6, 8, 12 sides and revolved CPC (n = ∞) [67].....11

Fig. 2.2.2.2. Plot of the transmittance as a function of concentration ratio (factor) for square, hexagonal, and circular 3D CPCs with reflectance of 95% of surface. [66].12

Fig. 2.2.2.3. (a) A dielectric-filled CPC with $\theta' c$ of 18 °and a refractive index of 1.5; (b) The maximum internal and external acceptance angles for a dielectric-filled CPC with total internal reflection, as functions of the refractive index [70].....13

Fig. 2.2.2.4. Asymmetric ideal CPC (*L*, *R*: parabolas; F_l: focus of *L*; F_r: focus of *R*; acceptance angle: $2\theta_c$; ϕ_r, ϕ_l: subtended angle of parabola axes) [72].....14

Fig. 2.2.2.5. Section view of a stationary "Sea shell" collector with the maximum output in summer [72].....15

Fig. 2.2.2.6. Section view of an ideal cylindrical concentrator with arbitrary absorber shape, a) concentrator with pipe-shaped absorber; b) concentrator with flat absorber [72].....16

Fig. 2.2.2.7. Section view of lens-walled CPC, a) conventional lens-walled CPC b) lens-walled CPC with air gap [76, 78].....17

Fig. 2.2.4.1. A fixed aperture with its orientation defined by the tilt angle (β) and the aperture azimuth angle (γ). N is the aperture normal; vector S is a ray of the direct solar radiation; α is the angle of solar radiation to the earth's surface; A is the solar azimuth; θi is the angle of incidence, which is the angle between the ray and the aperture normal; the direction cosines of N along the z, e and n axes respectively as N_z, N_e and N_n [93].....19

Fig. 2.3.1. Flow chart of Section 2.3.....21

Fig. 2.3.1.1. Hierarchy of CPVT system.....22

Fig. 2.3.1.2. Cross section view of the hybrid 2D CPC PV/T system [80].....23

Fig. 2.3.1.3. Schematic diagram of 2D trough CPC a) 3D model of glazed PV-CPC system b) cross section of glazed PV-CPC system with/without cooling pipes [81] 23

Fig. 2.3.1.4. Section view of CPC coupled with prism as secondary concentrator [100] 24

Fig. 2.3.1.5. Cross section of Chen's high concentration system [103] 25

Fig. 2.3.1.6. Schematic diagram of lens-walled CPC with air gap [77] 26

Fig. 2.3.1.7. Schematic diagram of lens-walled CPC with air gap integrating with PV/T system (1) Front glazing (2) Lens-walled CPC with air gap (3) UV Glue (4) TPT (tedlar-polyester-tedlar) (5) EVA (ethylene-vinylacetate) layers (6) PV cell (7) Copper pipe (8) Thermal insulation [78] 26

Fig. 2.3.1.8. Reflective film and encapsulant on CPV [92] 28

Fig. 2.3.1.9. Schematic diagram of CCPC integrating with non-imaging dish concentrator (NIDC) [110] 29

Fig. 2.3.1.10. dCPC integrating with UC-SC, a) UC-SC with a regular two-dimension array of integrated dCPC; b) Schematic and optical setup [88] 30

Fig. 2.3.1.11. Section view of CPC coupled with convex lens as secondary concentrator [112] 30

Fig. 2.3.1.12. Schematic diagram of VFP, a) Circular focus spot on solar cell; b_1) Square focus spot on solar cell; b_2) Cross section of VFP with square focus spot [113] 31

Fig. 2.3.1.13. Structure of RACPC, a) schematic diagram of producing RACPC by angular rotating 2D cross section; b) 3D model of RACPC c) prototype of RACPC [114, 115] 32

Fig. 2.3.2.1. Diagram of DPT and FBT, a_1) DPT is formed by rotating two parabola inwards by 15°; a_2) DPT with horizontal disposition of flat plate absorber; b_1) FBT is formed by rotating the two parabola inwards until the base is flat; b_2) FBT with vertical disposition of flat plate absorber [121] 34

Fig. 2.3.2.2. Four CPC solar thermal collectors with different absorber [123] 35

Fig. 2.3.2.3. TCPC solar collector (a) The schematic view of TCPC collectors (b) photo of TCPC collectors [127] 36

Fig. 2.3.2.4. Design concept for the hybrid CPC-PV/T system with wavelength selective film [128] 36

Fig. 2.3.2.5. Section view of concentration system consisting of CPC absorber and Fresnel reflector [129].....37

Fig. 2.3.2.6. Section view of inverted absorber ICSSWH [133].....38

Fig. 2.3.2.7. a) Schematic of CPC collector b) Representation of an evacuated tube collector with U-pipe [134].....39

Fig. 2.3.2.9. Schematic diagram of water steam generation and distillation system with CPC3.2.3 CPC for soil heating with optical fibres [138].....40

Fig. 2.3.3.1. Two types of smart windows with 2D CPC array a) Replication of CPC array generated by interference lithography in PMMA, with reflective coatings on base b) CPC array with reflective coatings on side wall [85].....41

Fig. 2.3.3.2. Schematic diagram of hybrid solar window a) Design concept for hybrid solar window b) Typical cross-section view of hybrid solar window and dimensions [142].....42

Fig. 2.3.3.3. Schematic diagram of PRIDE systems a) First generation with symmetric CPC and asymmetric CPC b) Second generation 3) Third generation with reflective film on edge [82, 84, 87, 143-145].....44

Fig. 2.3.3.4. Section of 5 anidolic collector systems (type 1-5) and two test collectors (type 6 and 7); abutting funnels are outlined in dashed lines (all sizes are in meter) [147].....46

Fig. 2.3.3.5. Structure and optical path of the novel sunlight concentrator unit [148].....47

Fig. 2.3.3.6. Conceptual schematic diagram of the daylighting systems a) Parabolic trough type b) Linear Fresnel lens type [149].....47

Fig. 2.3.4.1. Schematic diagram of a photocatalytic water purification system with CPC reactor [150].....48

Figure 2.4.1.1 flow chart of 3D ray tracing steps code for CCPC in MATLAB [105].....50

Fig. 2.5.1.1. CPC studies according to publication year and CPC type.....56

Fig. 2.5.1.2. CPC studies according to application area and concentration ratio.....57

Fig. 2.5.1.3. CPC studies according to countries of research institutes.....58

Figure 3.1.1.1. Schematic diagram of dCPC structure in previous research [15].....78

Figure 3.1.3.1. Dimension of 3D dCPC and right square pyramid structure.....81

Figure 3.1.3.2. Installation position of dCPC under real sky.....82

Figure 3.1.3.3. Structure of 3D revolved dCPC (3D r-dCPC).....82

Figure 3.1.3.4. Flow chart of methodology.....83

Figure 3.2.1.1. Schematic diagram of five different dCPC structures and incident angle.....84

Figure 3.2.1.2. Relationship between incident angle and transmittance for five different structures.....84

Figure 3.2.2.1. Transmittance of 2D and 3D dCPCs under sunny sky (Nottingham, south-facing, 37 °tilted).....86

Figure 3.2.2.2. Transmitted daylight illuminance of 2D and 3D dCPCs under sunny sky (Nottingham, south-facing, 37 °tilted).....87

Figure 3.2.3.1. Transmittance of 2D and 3D dCPCs under overcast sky (Nottingham, south-facing, 37 °tilted).....89

Figure 3.2.3.2. Transmitted daylight illuminance of 2D and 3D dCPCs in Spring Equinox, Summer Solstice and Winter Solstice under overcast sky (Nottingham, south-facing, 37 °tilted).....91

Figure 3.2.4.1. 2D and 3D dCPCs under representative sun paths during the whole year.....92

Figure 3.3.1. Schematic diagram of 3d dCCPC tilt angle.....94

Figure 3.3.1.1. Transmittance of 3D base-coated dCCPC in different tilt angles in spring equinox, summer solstice and winter solstice (Nottingham, south facing).....96

Figure 3.3.1.2. Transmittance of 3D non-coated dCCPC in spring equinox, summer solstice and winter solstice (Nottingham, south facing).....98

Figure 3.3.1.3. Transmitted daylight illuminance of 3D base-coated and non-coated dCCPCs with different tilt angles in spring equinox, summer solstice and winter solstice (Nottingham, south facing, 29 °tilted).....99

Figure 3.3.1.4. Transmitted daylight illuminance of 3D base-coated and non-coated dCCPCs in spring equinox, summer solstice and winter solstice (Nottingham, south facing, 37 °tilted).....100

Figure 3.3.1.5. Transmitted daylight illuminance of 3D base-coated and non-coated dCCPCs in spring equinox, summer solstice and winter solstice (Nottingham, south facing, 45 °tilted).....101

Figure 3.3.1.6. Transmitted daylight illuminance of 3D base-coated and non-coated dCCPCs in spring equinox, summer solstice and winter solstice (Nottingham, south facing, 53 °tilted).....101

Figure 3.3.2.1. Transmittances of 3D base-coated dCCPC with different tilt angles in spring equinox, summer solstice and winter solstice (Nottingham, south facing)...103

Figure 3.3.2.2. Transmittances of 3D non-coated dCCPC with different tilt angles in spring equinox, summer solstice and winter solstice (Nottingham, south facing)...104

Figure 3.3.2.3. Transmitted daylight illuminance of 3D base-coated dCCPC with different tilt angles in spring equinox, summer solstice and winter solstice (Nottingham, south facing) 106

Figure 3.3.2.4. Transmitted daylight illuminance of 3D non-coated dCCPC with different tilt angles in spring equinox, summer solstice and winter solstice (Nottingham, south facing) 107

Figure 3.3.3.1. Summary of the transmitted daylight illuminance for selected 3D dCCPCs.....109

Figure 3.4.1. Top view of 3D dCCPC with different horizontal rotation angle 110

Figure 3.4.1.1. Transmittance of 3d base-coated dCCPC with 0 °, 15 °, 30 °and 45 ° horizontal rotation angle and 3D base-coated r-dCPC under sunny sky (Nottingham, south facing, 37 °tilted).....112

Figure 3.4.1.2. Transmitted daylight illuminance of 3d base-coated dCCPC with 0 °, 15 °, 30 °and 45 °horizontal rotation angle and 3D base-coated r-dCPC under sunny sky (Nottingham, south facing, 37 °tilted).....113

Figure 3.4.1.3. Transmittance of 3D non-coated dCCPC with 0 °, 15 °, 30 °, 45 ° horizontal rotation angle and 3D non-coated r-dCPC under sunny sky (Nottingham, south facing, 37 °tilted).....115

Figure 3.4.1.4. Transmitted daylight illuminance of 3d non-coated dCCPC with 0 °, 15 °, 30 °, 45 °horizontal rotation angle and 3D non-coated r-dCPC under sunny sky (Nottingham, south facing, 37 °tilted) 116

Figure 3.4.2.1. Transmittance of 3d base-coated dCCPC with 0 °, 15 °, 30 °and 45 ° horizontal rotation angle and 3D base-coated r-dCPC under overcast sky (Nottingham, south facing, 37 °tilted) 117

Figure 3.4.2.2. Transmitted daylight illuminance of 3d base-coated dCCPC with 0 °, 15 °, 30 °and 45 °horizontal rotation angle and 3D base-coated r-dCPC under overcast sky (Nottingham, south facing, tilted 37 °).....119

Figure 3.4.2.3. Transmittance of 3D non-coated dCCPC with 0 °, 15 °, 30 °, 45 ° horizontal rotation angle and 3D non-coated r-dCPC under overcast sky (Nottingham, south facing, 37 °tilted) 120

Figure 3.4.2.4. Transmitted daylight illuminance of 3d non-coated dCCPC with 0 °, 15 °, 30 °, 45 °horizontal rotation angle and 3D non-coated r-dCPC under overcast sky (Nottingham, south facing, 37 °tilted).....121

Figure 3.4.2.5. Outdoor illuminance and transmitted daylight illuminance of 3D base-coated and non-coated r-dCPC in spring equinox, summer solstice and winter solstice under sunny/overcast sky (Nottingham, south facing, tilted 37 °).....123

Figure 3.4.2.6. Outdoor illuminance and transmitted daylight illuminance of 3D non-coated r-dCPC in spring equinox, summer solstice and winter solstice under sunny/overcast sky (Nottingham, south facing, tilted 45 °).....124

Figure 4.1.1 Schematic diagram of designed CPC panel with four CPC components 128

Figure 4.1.2 Flow chart of CPC panel design process (In section view).....129

Figure 4.2.1.1. Transmittance of CPC panels with 1-8mm thick covers (BC-C/NC-C *mm: Base-coated/non-coated) CPC panel with *mm thick cover; BC/NC original: base-coated/non-coated CPC panel without cover) 130

Figure 4.2.1.2. Transmittance variations to incident angle of CPC panels with 1-8mm thick covers compared to CPC panels without covers (BC-C/NC-C *mm: Base-coated/non-coated CPC panel with *mm-thick cover) 130

Figure 4.2.2.1. Transmittance of CPC panels which were truncated by 1-8mm (BC-T /NC-T *mm: Base-coated CPC panel truncated by *mm; BC/NC original: the base-coated/non-coated CPC panel without truncation) 131

Figure 4.2.2.2. Transmittance variations to incident angle of CPC panels which were truncated by 1-8mm (BC-T/NC-T *mm: Base-coated/non-coated CPC panel truncated by *mm) 132

Figure 4.2.2.3. Transmittance of CPC panels which were truncated by 1-8mm and with corresponding 1-8mm covers (BC-TC/NC-TC *mm: Base-coated/Non-coated CPC panel which was truncated by *mm and with *mm-thick cover; BC/NC original: the base-coated/non-coated CPC panel without truncation and cover).....133

Figure 4.2.2.4. Transmittance variations to incident angle of CPC panels which were truncated by 1-8mm and with corresponding 1-8mm thick covers (BC-T/NC-T *mm: Base-coated/non-coated CPC panel that was truncated by *mm and with *mm-thick cover).....133

Figure 4.2.3.1. Transmittance of CPC panels which were truncated by 1-8mm, with corresponding 1-8mm covers and gaps between CPC components (BC-TC-G/NC-TC-G *mm: Base-coated/Non-coated CPC panel which was truncated by *mm, with the cover of *mm thick and gap between CPC components corresponding to the truncated thickness *mm; BC/NC original: the base-coated/non-coated CPC panel without truncation and cover) 135

Figure 4.2.3.2. Transmittance variations to incident angle of CPC panels which were truncated by 1-8mm, with corresponding 1-8mm covers and gaps between CPC components (BC-TC-G/NC-TC-G *mm: Base-coated/Non-coated CPC panel which was truncated by *mm, with the cover of *mm thick and gap between CPC components corresponding to the truncated thickness *mm) 135

Figure 4.3.1.1. Transmittance variations to cover thickness for base-coated CPC panels with 1-8mm cover at different incident angles comparing with original base-coated CPC panel 137

Figure 4.3.1.2. Transmittance variations to cover thickness for non-coated CPC panels with 1-8mm cover at different incident angles comparing with original non-coated CPC panel 137

Figure 4.3.2.1 Transmittance variations to truncated thickness for base-coated CPC panels truncated by 1-8mm at different incident angles comparing with original base-coated CPC panel 138

Figure 4.3.2.2. Transmittance variations to truncated thickness for non-coated CPC panels truncated by 1-8mm at different incident angles comparing with original non-coated CPC panel 139

Figure 4.3.3.1. Transmittance variations to cover thickness (or truncated thickness) at different incident angles for base-coated CPC panels truncated by 1-8mm, cooperating with 1-8mm covers and corresponding gaps, at different incident angles comparing with original base-coated CPC panel 140

Figure 4.3.3.2. Transmittance variation to cover thickness (or truncated thickness) at different incident angles for non-coated CPC panels truncated by 1-8mm, cooperating with 1-8mm covers and corresponding gaps, at different incident angles comparing with original non-coated CPC panel 140

Figure 4.3.4.1. Deviations between the transmittance of truncated-covered CPC panels and the sum of transmittance of truncated CPC panels and covered CPC panels (BC*/NC*: base-coated/non-coated CPC panels truncated by *mm and with *mm cover) 141

Figure 4.3.4.2. Transmittance variations affected by gaps only on CPC panels with 1-8mm covers, 1-8mm truncations and corresponding gaps, compared to original CPC panel (BC-TC-G/NC-TC-G *mm: base-coated/non-coated CPC panel that was truncated by *mm, with *mm cover and with gap between CPC components, and the gap width corresponds to the truncated thickness) 142

Figure 4.4.2.1. Predicted transmittance of base-coated CPC panels truncated by 1-14mm (BC-T *mm: base-coated CPC panels truncated by *mm)..... 145

Figure 4.4.2.2. Predicted transmittance of non-coated CPC panels truncated by 1-14mm (NC-T *mm: non-coated CPC panels truncated by *mm)..... 145

Figure 4.4.3.1. Validations of predicted and simulated transmittance for CPC panels truncated by 10mm..... 146

Figure 4.4.3.2. Validations of predicted and simulated transmittance for CPC panels truncated by 12mm..... 146

Figure 4.4.3.3. Validations of predicted and simulated transmittance for CPC panels truncated by 14mm.....147

Figure 4.4.3.1. Transmittance comparisons of scaling CPC panels (NC-B/BC-B: non-coated/base-coated CPC panel before scaling; NC-S/BC-S: non-coated/base-coated CPC panel that is scaled down by 0.5) 148

Figure 4.5.1.1. Dimensions of designed CPC panel for experiment.....149

Figure 4.5.1.2. Photos of the dCCPC panel used in experiment (left: general view; right: detail view).....149

Figure 4.5.3.1. Configurations of CPC experiment by using PV.....150

Figure 4.5.3.2. Experiment rigs for PV-I testing 151

Figure 4.5.3.3. Relative spectral sensitivity of light sensor and spectral response of PV [177, 178].....152

Fig. 4.6.1. Tested transmittance of dCCPC with the horizontal rotation angle of 0 ° and 45 °by experiments.....153

Fig. 4.6.2. Comparisons between the transmittances obtained from experiment and simulation of the dCCPC without PV attached on base.....154

Fig. 4.6.3. Comparisons between the transmittances obtained from experiment and simulation of the dCCPC with PV attached on base.....154

Figure 5.2.4.1. Schematic of azimuth, altitude and selected sun positions for simulation.....165

Figure 5.3.1. Independent and dependent variables used in data regression and prediction.....166

Figure 5.3.1.1. 3D contour plots of transmittance versus solar altitude and azimuth under clear sky with different sunlight lumen ratios in sky model ($\varphi lumen$): a) only direct sunlight; b) $\varphi lumen = 1:1$ ($\varepsilon \geq 6.6$) ; c) $\varphi lumen = 1:4$ ($\varepsilon \approx 3.6{\sim}6.6$) ; d) $\varphi lumen = 1:9$ ($\varepsilon \approx 3{\sim}3.6$) (2D contour plot is shown in Appendix Figure B-1)167

Figure 5.3.1.2. Transmittance of non-coated CCPC under clear sky with different sunlight lumen ratios in sky model (Altitude of sun ranges from 10 °-90 °; Azimuth of sun ranges from 0 °-45 °).....169

Figure 5.3.1.3. Comparisons between predicted and simulated transmittance of non-coated dCCPC (Regression: Eq. 5.3.1.1-12) 173

Figure 5.3.1.4. Absolute values of the residuals of predicted and simulated transmittance for non-coated dCCPC (Regression: Eq. 5.3.1.1-12) 174

Figure 5.3.2.1. Transmittance of base-coated dCCPC under clear sky with different sunlight lumen ratios in sky model (Altitude of sun ranges from 10°-90°; Azimuth of sun ranges from 0°-45°) 175

Figure 5.3.2.2. Comparisons between predicted and simulated transmittance of base-coated dCCPC (Regression: Eq. 5.3.1.1-12) 176

Figure 5.3.2.3. Comparisons between predicted and simulated transmittance of base-coated dCCPC (Regression: Eq. 5.3.1.1-12, separate parameter values for $\theta h \geqslant 70^\circ$ and $\theta h < 70^\circ$) 177

Figure 5.3.3.1. Optical efficiency of base-coated dCCPC under clear sky with different sunlight lumen ratio in sky model (Altitude of sun ranges from 10°-90°; Azimuth of sun ranges from 0°-45°) 178

Figure 5.3.3.2. Comparisons between predicted and simulated optical efficiency of base-coated dCCPC (Regression: Eq. 5.3.1.1-13) 179

Figure 5.3.3.3. Comparisons between predicted and simulated optical efficiency of base-coated dCCPC (Regression: Eq. 5.3.1.1-12, separate parameter values for $\theta h \geqslant 70^\circ$ and $\theta h < 70^\circ$) 180

Fig. 6.2.1.1. Schematic and dimensions of dCCPC 189

Fig. 6.2.3.1. Feedforward ANN architecture with one hidden layer 192

Fig. 6.3.1. Comparison between simulated and predicted transmittance of non-coated dCCPC under clear and intermediate skies (MNLR, Eq. 6.3.1a) 195

Fig. 6.3.2. Comparison between simulated and predicted transmittance of base-coated dCCPC (MNLR, Eq. 6.3.1a) 196

Fig. 6.4.2. Comparison of predicted and simulated transmittance of non-coated dCCPC (ANN) 199

Fig. 6.4.3. Comparison of predicted and simulated transmittance of base-coated dCCPC (ANN) 199

Fig. 6.5.1.1. Summary of pros and cons for MNLR and ANN models 201

Fig. 7.2.1. Coordinate system of an optical path through a south-facing tilted dCCPC. S: sun position; SO: incident ray; $OS1$: refracted ray; ABCD: top surface of tilted dCCPC; β: tilt angle; NON': normal of the plane ABCD; E: projection of point S onto the plane ABCD; S': projection of point S onto the horizontal plane; OM: equivalent north direction of the plane ABCD; θh: solar altitude; γ: solar azimuth angle; $\theta h'$: equivalent solar altitude; γ': equivalent solar azimuth angle.....208

Fig. 7.3.1.1. Dimensions of the test room and different skylight diffusers.....213

Fig. 7.3.1.2. Illuminance distribution on work plane of example room (Sky type: Clear sky; Solar altitude: 60 °; Solar azimuth: 180 °; Outdoor average illuminance: 91,922lux) 214

Fig. 7.3.1.3. Illuminance distribution on work plane of example room (Sky type: Overcast sky; Solar altitude: 10 °; Solar azimuth: N/A; Outdoor average illuminance: 3,692lux) 215

Fig. 7.3.2.1. Dimensions of test room with slanted roof and flat roof 216

Fig. 7.3.2.2. Illuminance distribution on work plane of example room (Sky type: Clear sky (Altitude: 60 °; Azimuth: 180 °; Outdoor average illuminance: 91,922lux)/Overcast sky (altitude: 10 °; azimuth: N/A; Outdoor average illuminance: 3,692lux); Roof pitch of slanted roof: 37 °; Tilt angle of dCCPC: 37 °).....217

Fig. 7.4.1.1. Relations among Rhinoceros, Grasshopper, Ladybug and Honeybee in building simulations.....220

Fig. 7.4.1.2. Workflow diagram of running daylighting and energy simulation for target building in Grasshopper.....221

Fig. 7.4.2.1. Dimension of the test room for simulating illuminance distribution of work plane.....222

Fig. 7.5.1.1. Test building and sun path of Birmingham on 21st June from 4am to 8pm in Rhino 3D.....225

Fig. 7.5.1.2. Hourly transmittance of dCCPC for a whole year in Birmingham.....226

Fig. 7.5.2.1. Percentages of daytime sky conditions during the whole year for selected locations 228

Fig. 7.6.1.1. Hourly solar gain from skylights and transmittance of skylights on 22nd Jun in Birmingham, UK (52.45 °N, 1.73 °W).....230

Fig. 7.6.1.2. Hourly total thermal load and sky clearness factor on 22nd Jun in Birmingham, UK (52.45 °N, 1.73 °W) 231

Fig. 7.6.2.1. Monthly cooling and heating loads for the office building in 14 cities with the skylights of dCCPC-DB, DB and dCCPC-lowE 233

Fig. 7.6.2.2. Annual cooling load of example building with the skylights of dCCPC-DB, DB and dCCPC-lowE.....234

Fig. 7.6.2.3. Annual heating load of example building with the skylights of dCCPC-DB, DB and dCCPC-lowE.....235

Fig. 7.6.2.4. Total annual thermal load of example building with the skylights of dCCPC-DB, DB and dCCPC-lowE 236

Fig. 7.6.3.1. Total Energy consumption of artificial lighting of example building with the skylights of dCCPC-DB, DB and dCCPC-lowE 238

Fig. 7.6.3.2. Sum of annual cooling, heating and lighting consumptions of example building with the skylights of dCCPC-DB, DB and dCCPC-lowE 239

Fig. 7.6.4.1. Comparisons of HDR images of target building under different sky conditions.....241

Fig. 7.6.4.2. Comparisons of indoor luminance by false colour HDR images of target building under different sky conditions 242

Figure 7.7.2.1. Cumulative discounted cash flow of dCCPC (Hong Kong).....244

Figure 7.7.2.2. Discounted payback period for selected locations 245

Figure A.1 Comparison between simulated and predicted optical efficiency of non-coated dCCPC under clear and intermediate skies (MNLR) 275

Figure A.2. Comparison between simulated and predicted optical efficiency of non-coated dCCPC (ANN).....276

Figure B-1. 2D contour plots of transmittance versus solar altitude and azimuth under clear sky with different sunlight lumen ratios in sky model ($\varphi lumen$): a) only direct sunlight; b) $\varphi lumen = 1:1$ ($\varepsilon \geq 6.6$) ; c) $\varphi lumen = 1:4$ ($\varepsilon \approx 3.6{\sim}6.6$) ; d) $\varphi lumen = 1:9$ ($\varepsilon \approx 3{\sim}3.6$).....278

Fig. C-1. Coordinate system of an optical path through a south-facing tilted dCCPC. S: sun position; SO: incident ray; $OS1$: refracted ray; ABCD: top surface of tilted dCCPC; β: tilt angle; NON': normal of the plane ABCD; E: projection of point S onto the plane ABCD; S': projection of point S onto the horizontal plane; OM: equivalent north direction of the plane ABCD; $OS1'$ is the extension of the line $S1O$; θh: solar altitude; γ: solar azimuth angle; $\Delta\theta i$: difference between incident angle and refraction angle. 280

Figure D.1-1. The correlation between inner south projection angle and optical efficiency for various solar azimuths of base-coated 2D dCPC [94] 284

Figure D.1-2. The correlation between inner perpendicular projection angle (projected plane: north-south plane) and optical efficiency for various solar azimuths of base-coated dCCPC (direct sunlight only) 284

Figure D.2-1. The correlation between inner south projection angle and the sum of transmittance and surface reflection for various solar azimuth of base-coated 2D CPC [94] 286

Figure D.2-2. The correlation between inner perpendicular projection angle and the sum of transmittance and surface reflection for various solar azimuth of base-coated CCPC (direct sunlight only) 287

Figure D.3-1. Comparison between predicted and simulation results for ANN models when the independent variables are $\theta n'$ and ε 288

Chapter 1

Introduction

1.1. Background

The utilization of daylighting has been developed through human history, which was used as dominant source and became to be dependent on artificial lighting. In recent years, daylight is proposed again to be used on energy saving in a natural way as the issue of energy shortage arise. The dependence on artificial lighting leads to many problems in respects of environmental pollution, light quality and human health. For non-residential buildings, lighting systems occupy 20%-60% of annual energy consumption which is around on-third of electricity budget [1, 2]. For the residential sector which takes percentage of about 30 of Europe energy demand, energy consumption of lighting takes around 15-20% of total electricity bill [3]. The artificial lighting is still increasing by around 6% annually [4] in worldwide. Artificial lighting systems becomes the major contributors to CO2 emissions and global warming at the same time. Different type of light also affects human psychology and physiology. In 1994, Liberman [5] has already mentioned the light plays a part in maintaining health. A report [6] pointed out that the light is used by human body for metabolic processes which is same to water and food in 1997. The constant variations of pattern, intensity and color composition afforded by daylight is more pleasant to be accepted by human being comparing with other light [7, 8]. A survey conducted by Hourani et al. [9] in 2012 shows 80% of the working staffs express that they are willing to sit by windows, and the similar results are obtained in students and patients groups. In the analysis about the effect of correlated color temperatures of light on human performed by Ashok Sivaji et al. [10], it is found that the daylight is preferred by workers and leads to higher productivity.

As the significance of daylight was recognized, it is begun to be integrated in lighting technologies and building design. In terms of building design, passive design is an important way to lead daylight into building to provide sufficient indoor illuminance level to reduce the use of artificial lighting. This do make achievements in the past decades. Another way is to integrate daylight with new technologies, such as artificial daylight, fiber optics and hybrid lighting systems. As the changing of outdoor illuminance during the whole day, a stable and sufficient indoor illuminance level with visual comfort is the goal of all daylight or lighting devices design.

Dielectric compound parabolic concentrator (dCPC) is a new material used to control daylight to the building. Because the high concentration efficiency of dCPC, it was

applied to the photovoltaic generation of electricity initially put forward by Schertz et al. in 1977 [11]. It is an improvement of the well know solar collecting concentrator - compound parabolic concentrator (CPC), the curved reflective surfaces of which allow the capture of diffuse UV sunlight without solar tracking and produce a illumination over base surface. The dielectric concentrator array is made of acrylic plastic and the absorbers are photovoltaic arrays. A series of research are conducted to develop its efficiency on collecting solar energy. During this period, the potential of integrating with building design of dCPC is discovered. Sarmah et al. [12] proposed a dCPC design for building facades integration in northern latitudes. Li et al. [13] investigated the integration of novel-air-lens-walled compound parabolic concentrator with photovoltaic/thermal system. Another application of dCPC for receiving daylight was also put forward. Cooper et al. [14] discussed the performance on receiving daylight of compound parabolic concentrators with different polygonal apertures. It was found that the dCPCs with polygonal apertures having different number of sides perform different efficiencies and flux distributions. In the study conducted by Yu et al. [15], the performances of dCPC under different sky conditions are evaluated, which provides an idea on daylight control of dCPC except for solar energy collection.

1.2. Thesis objectives and structure

Dielectric crossed compound parabolic concentrator (dCCPC) has been widely used in concentrating solar radiation for generating electricity and thermal energy in the past decades, but none of the study explored its application in daylighting. This study aims to investigate the optical performance of dCCPC in a comprehensive way from fundamental property to practical daylighting application. This is a totally novel research which explored and discussed the feasibility of utilizing dCCPC for daylighting control. The flow chart in Fig. 1.1 illustrates a simplified summary of how the works were taken to accomplish the proposed research objectives.

This thesis consists of nine chapters in total. The first one is introduction, which provides an overview of the whole research. The second chapter presents a detailed literature review focusing on summarizing the studies about utilizing CPC in solar energy applications since 2000. It introduces the works related to CPC in PV, solar thermal, water degradation, and the most important, daylighting that is intended to be discussed in this thesis in the following chapters. The review is taken as

comprehensive as possible to contribute to the ongoing efforts to understand, design, build and demonstrate CPC.

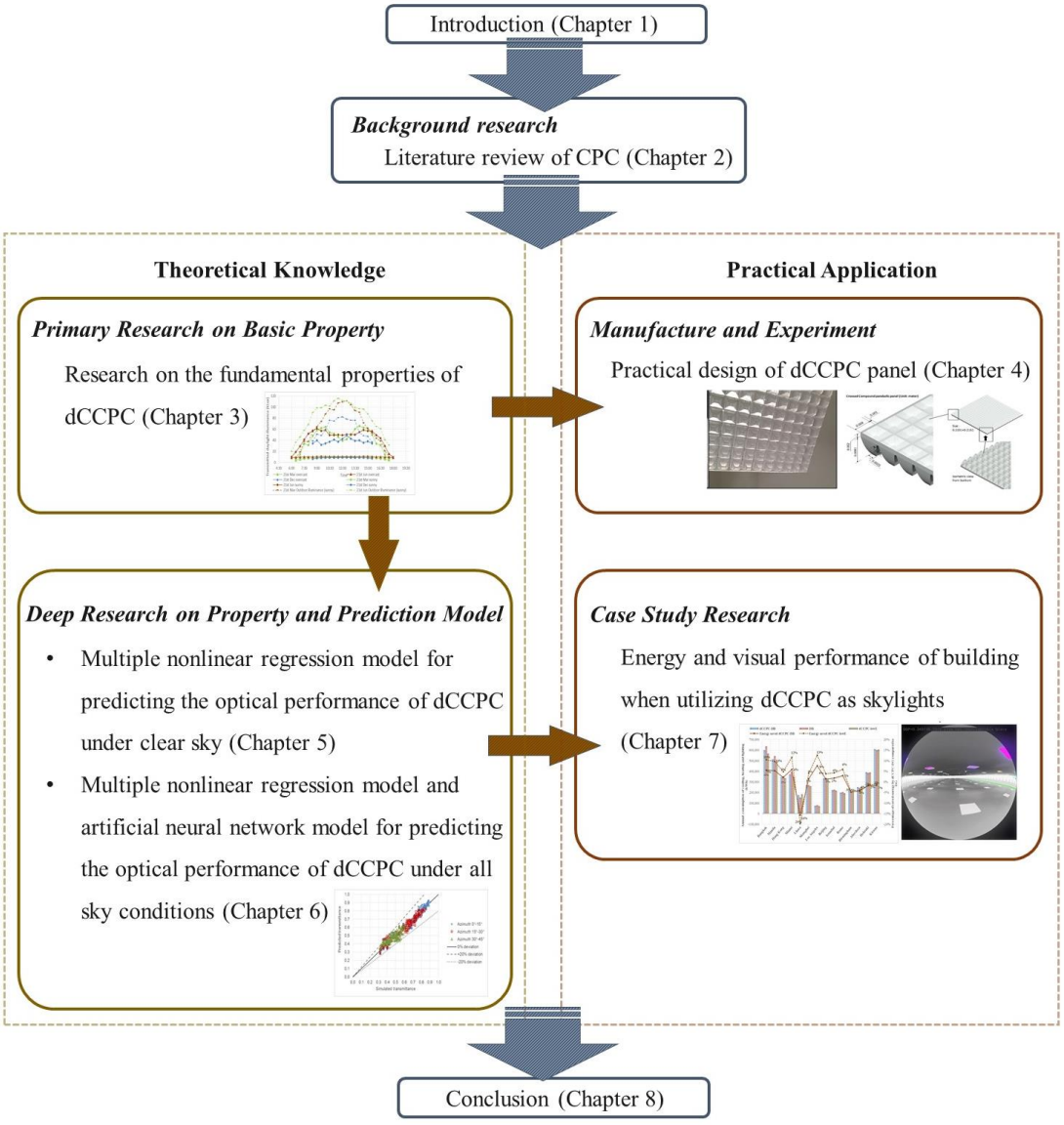


Fig. 1.1. Overview of the research

After the review, a fundamental research about dCCPC was taken, which is demonstrated in Chapter Three. As a further research on two dimensional dielectric compound parabolic concentrator, two different types of 3D dCCPC, which are non-coated dCCPC and base-coated dCCPC. Non-coated dCCPC is the common CCPC made by dielectric material, and base-coated dCCPC is the dCCPC with a black material (e.g. PV panel) attached to its base that is used to absorb the incident solar radiation. The transmittance and transmitted daylight illuminance of these two dCCPCs are compared in three specific days (spring equinox, summer solstice, and

winter solstice) of the year. Then the influences by tilt angle and horizontal rotation angle on the optical performance of dCCPC are discussed. The works in this chapter aims to figure out the feasibility of using dCCPC as skylights in daylighting control and find the best way to put dCCPC in practice in order to achieve the best performance.

In Chapter Four, the practicability of dCCPC is investigated. As dCCPC is designed to be used as skylights, the thickness and weight are expected to be reduced as much as possible. Considering the limitations of manufacture and material, four factors related to the dimension of dCCPC are proposed which are the scale ratio, thickness of truncation, thickness of conjunction cover and the width of gap between dCCPC components. This chapter discussed their effects on the optical performance of dCCPC. In addition, experiments are taken to validate the simulation results.

For all of the research about dCCPC, simulation is the most common and accurate way to determine the optical performance of dCCPC currently but a lot of time is required for finishing a simulation. None of the simple and fast model has been put forward yet to predict the performance of dCCPC. Chapter Five proposes several mathematical models for predicting optical performance of dCCPC under clear sky condition, which are derived through multiple nonlinear regression based on a mass of simulation results. The optical performance of dCCPC is expected to be obtained through these models with the given azimuth angle, altitude angle and sky clearness factor.

Chapter Six is the further work of Chapter Five, which improve the mathematical models so that the models are available to predict the optical performance, especially the transmittance, of dCCPC under all sky conditions including overcast, intermediate and clear sky. In addition, another powerful forecasting tool called artificial neural network (ANN) is attempted to be used for predicting the performance of dCCPC. New ANN models are built and compared with the multiple nonlinear regression models. The advantages and drawbacks for the two kinds of models are discussed by comparing the results of prediction.

With the accurate mathematical model proposed in previous chapters, the transmittance of dCCPC can be obtained easily for any random location and time. Taking the advantage of this, Chapter Seven analyzes the energy and visual performance of an example building when utilizing dCCPC as skylights. Different

locations all over the world are applied to find the most appropriate place for using dCCPC. The indoor illuminance distribution and glare probability after using dCCPC are investigated and compared with double glazing and low-E double glazing. The illuminance distribution of dCCPC is also compared with other types of diffuse panels. The economic analysis is also provided in this chapter in order to figure out the economic benefits and payback period of installing dCCPC.

Finally, the thesis is concluded in Chapter Eight with the summary of current works and outlook for the further study.

Chapter 2

A review on the recent research progress about the compound parabolic concentrator (CPC)

2.1. Introduction

Imaging and nonimaging are two broad categories of solar concentrators. In the study of nonimaging optics, the original nonimaging concentrator is a straight cone concentrator which is one of the first 3D concentrator systems [16]. The compound parabolic concentrator (CPC) comes from the development and optimization of cone concentrator during which the theoretical concentration ratio was desired to be the maximum.

The compound parabolic concentrator (CPC) belonging to nonimaging optics is regarded as a highly potential and appealing option for solar energy concentration and illumination since mid-1960s [17-24]. It is well known that the principle and geometry of two-dimensional (2D) CPC was firstly described by Winston [25] in 1974. Afterwards, Winston and Hinterberger [26], and Rabl and Winston [27] put forward further explanations in detail. Since then, the term "CPC" has become generic for the whole family of similar devices. In the early stage of CPC design, the applications of three-dimensional (3D) CPC were discussed in terms of infrared collection [28] and retinal structure [29-31].

With the development of CPC in the past fifty years, it has been mainly and widely applied in solar energy like photovoltaic (PV) and solar thermal system as a significant component. The basic of CPC is still as the same as it was designed at the beginning, but researchers have spared no effort to investigate its optic performance and applications in much more disciplines in these years. The rest of applications are in quite various areas, such as gas sensing system [32], wireless communication system [33], infrared temperature sensor system [34], solar thermal water splitting system [35], sky radiator [36], photodiode [37], lasers [38, 39], LED projector[40-42], terahertz technology [43, 44] and overmoded waveguide [45]; CPC does not play critical roles in these applications usually. In the aspect of solar energy, there are a lot of review articles on CPV/CPVT technology [46-50] and solar thermal technology [50-55] that refer to CPC as one of the practical solution in those areas. However, it's still hard to find a review that is solely dedicated to discussing the basics and advances of the CPC studies appearing in recent years.

This chapter aims to summarize the CPC studies focusing on solar energy applications since 2000, and to review CPC as comprehensive as possible to contribute to the

ongoing efforts to fundamentally understand, design, build, and demonstrate CPC. The review will begin from the concept, design principles and considerations of CPC in Section 2.2. In Section 2.3, an exhaustive coverage of all CPC studies in the literature will be demonstrated according to four main application areas. Then the software applied for simulating CPC performance will be compared and discussed in Section 2.4. Finally, the future outlook and research directions for CPC studies from early works up till state-of-the-art advances will be presented in Section 2.5.

It is also important to mention that this thesis proposed the findings about dCPC in daylighting control that is part of solar energy application. Because CPC is a relatively new technology comparing with other solar energy technologies such as PV and solar thermal, providing a comprehensive introduction about CPC in solar energy application is significant for having an overview about how it has developed and worked in different fields and how they has cooperated with each other over the past decades. It is also meaningful for designing multi-function technologies relating to CPC in the future.

2.2. Fundamentals and considerations in CPC design

2.2.1. Design principles of CPC

According to Snell's law, Fermat's principle and ray tracing method, the design process of CPC can be described as follows with the reference to Fig. 2.2.1.1, which is called 'edge-ray principle' or the 'string' method [56-58]: In the meridian section of a 3D CPC, assuming all of the rays entering at the extreme collecting angle θ_c shall emerge through the rim point P' of the exit aperture, the parabolic curve with its axis parallel to the direction θ_c and its focus at P' will be derived as one branch of the reflector shape; The complete CPC concentrator in 3D geometry is then obtained by rotating the parabola about the concentrator axis (not the axis of the parabola). If the diameter of the exit aperture is $2a'$ and the maximum allowable incidence angle is θ_c, and the overall length L is:

$$L = (a + a') \cot \theta_c \qquad \text{(Eq. 2.2.1.1)}$$

The diameter of the entry aperture is

$$a = a'/\sin \theta_c \qquad \text{(Eq. 2.2.1.2)}$$

The geometrical concentration ratio is a critical parameter in the design of nonimaging optics which is defined as the ratio of the aperture area relative to the receiver's area. The theoretical concentration ratio of CPC in 2D geometry is shown in Eq. 2.2.1.3 [59, 60], which implies that CPC becomes close to being an ideal concentrator [59]. 'Ideal' means all of the rays inside the maximum collection angle will not be reflected back and emerge from the exit aperture. In addition, the meridian section of CPC in 2D space is actually ideal and has the maximum theoretical concentration ratio. The principles of designing 2D CPC are also provided in several U.S. patents [61-63].

$$C = a/a' = 1/\sin\theta_c \qquad \text{(Eq. 2.2.1.3)}$$

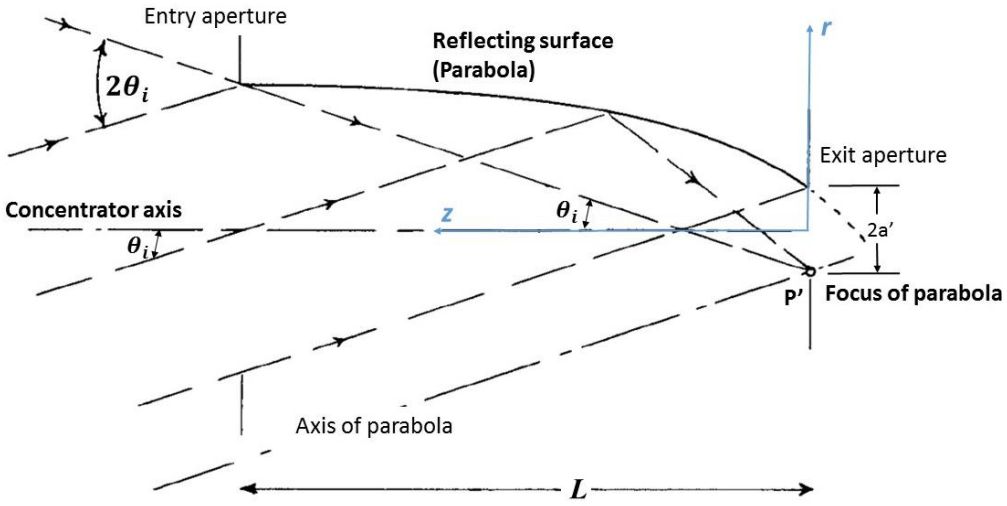


Fig. 2.2.1.1. Construction of the CPC profile from the edge-ray principle [31]

If taking the centre of the exit aperture as an origin for Cartesian coordinates and taking z-axis along the concentrator axis as shown in Fig. 2.2.1.1, the equation of the meridian section of a CPC can be expressed as Eq. 2.2.1.4 [59] where the diameter of exit aperture is $2a'$ and the acceptance angle (maximum allowable incidence angle) is θ_c. As the CPC surface is obtained by revolving a parabolic curve about the z-axis, this surface can be described by Eq. (4) with $r^2 = x^2 + y^2$. Winston [59] also presented the surface equations derived from the polar equation of the parabola and azimuthal angle. Another study [64] provides a novel method to calculate the maximum concentration of CPCs in direction cosine space on a polar plane.

$$(r\cos\theta_c + z\sin\theta_c)^2 + 2a'(1+\sin\theta_c)^2 r - 2a'\cos\theta_c\,(2+\sin\theta_c)^2 z - a'^2(1+\sin\theta_c)(3+\sin\theta_c) = 0 \qquad \text{(Eq. 2.2.1.4)}$$

2.2.2. Design considerations in structure

2.2.2.1. 2D and 3D CPC

Generally, CPC can be roughly classified into two categories which are two-dimensional (2D) and three-dimensional (3D). The 2D CPC refers to the CPC that has a longitudinal axis as shown in Fig. 2.2.2.1 a). It can also be called linear CPC or trough-like CPC for some special cases. 3D CPC (Fig. 2.2.2.1 b)) represents the CPC whose geometry is obtained by rotating a 2D meridian section of CPC at an angular interval. CPCs can be symmetric or asymmetric. The one with four parabolic surfaces and square apertures are called crossed CPC (CCPC) or orthogonal CPC. With the consideration of different geometrical translations, the optical performance of various 3D CPCs were investigated by many researchers. For example, Timinger et al. [65] investigated the optimization of faceted CPCs with discretization of the curvature in both the circumferential and axial directions; van dijk, et al. [66] simulated the relationship between transmittance and concentration ratio (C) of circular, square and hexagonal concentrators with reflectance (R) of 95% as shown in Fig. 2.2.2.2, which illustrates that the more sides of CPCs apertures has, the closer of optical performance approaches to ideal transmittance; The study by Cooper et al. [67] also implies similar results, in which the optical properties of CPCs with polygonal apertures having 3, 4, 5, 6, 8, 12 sides and circular aperture were compared.

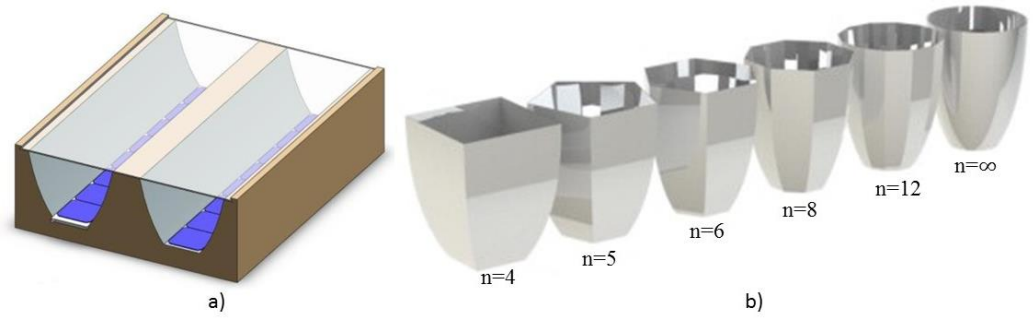


Fig. 2.2.2.1. Example of 2D and 3D CPCs a) 2D trough CPC with a glass on top and PV on bottom [68] b) 3D CPCs with polygonal apertures of 4, 5, 6, 8, 12 sides and revolved CPC (n = ∞) [67]

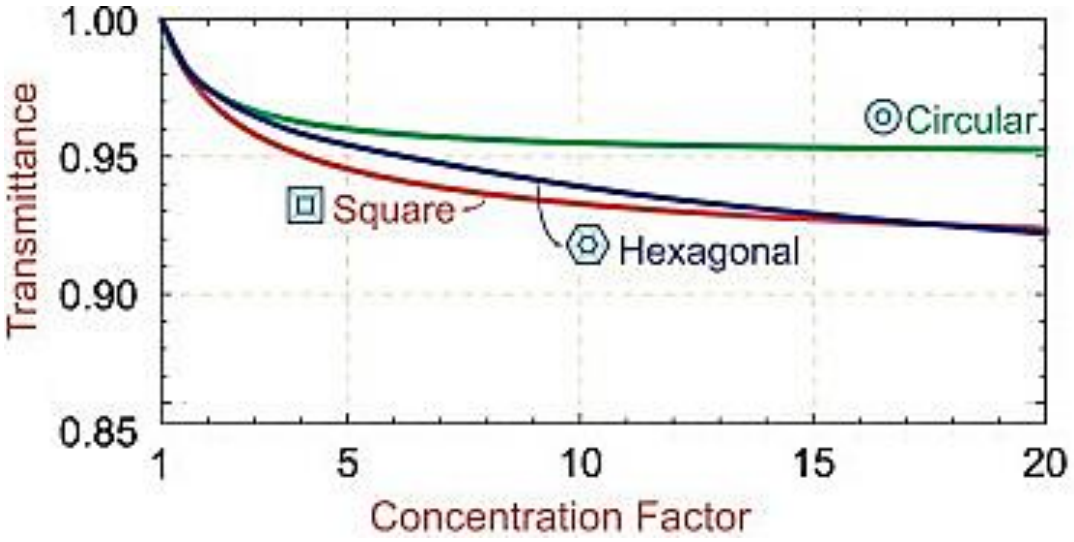


Fig. 2.2.2.2. Plot of the transmittance as a function of concentration ratio (factor) for square, hexagonal, and circular 3D CPCs with reflectance of 95% of surface. [66]

2.2.2.2. Dielectric filled CPC (dCPC)

The dielectric CPC is filled with a dielectric material, which is used to enlarge the acceptance angle of a CPC for the same geometry. The dielectric filled 2D and 3D CPCs with total internal reflection were put forward by Winston [69]. The acceptance angle θ'_c inside the dielectric and the acceptance angle θ_c of dCPC are shown in Fig. 2.2.2.3 (a). According to the law of refraction, if the refractive index of the dielectric is n, the maximum values of both internal and external acceptance angles that can be designed under total internal reflection conditions at certain refractive indices are shown in Fig. 2.2.2.3 (b). In addition, there will be a small enhancement on the angular acceptance of the dielectric-filled 2D CPC for nonmeridional rays [59].

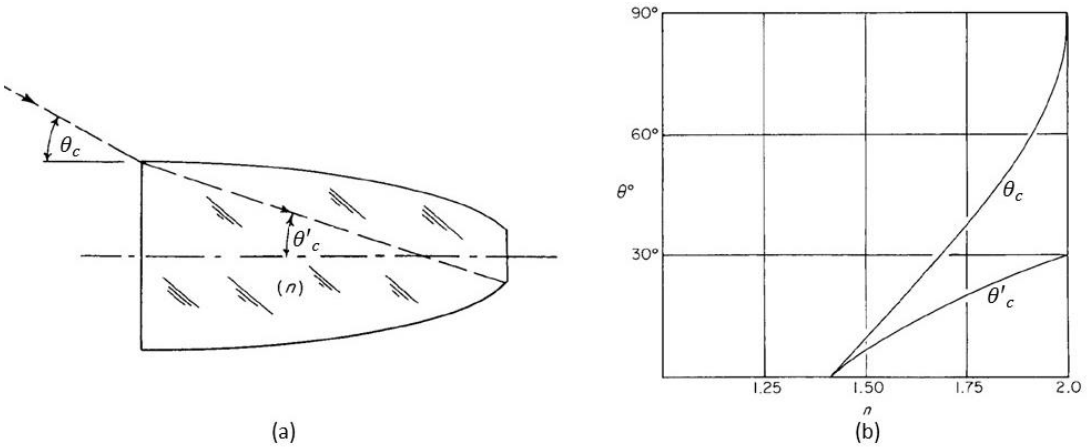


Fig. 2.2.2.3. (a) A dielectric-filled CPC with θ'_c of 18 °and a refractive index of 1.5; (b) The maximum internal and external acceptance angles for a dielectric-filled CPC with total internal reflection, as functions of the refractive index [70]

Therefore, the maximum theoretical concentration ratio of dCPCs can be expressed as Eq. 2.2.2.1 where θ_c is the acceptance angle inside the dielectric and the refractive index of air is assumed as 1. It is clearly to see that the concentration ratio increases by the factor n or n^2 comparing with reflective CPC.

$$C = n/sin\theta_c \ (for\ trough\ CPC) \quad or \quad C = n^2/sin^2\theta_c \ (for\ 3D\ CPC) \quad (2.2.2.1)$$

According to Snell's law (Eq. 2.2.2.2), for the rays whose incidences are larger than the acceptance angle of dCPC, whether they exiting dCPC from parabolic surfaces depends on that whether their incident angles on the dielectric-air interface in dielectric are larger or smaller than the critical angle. In addition, for the rays that have smaller incidences, it is possible for them to get turned back due to total internal reflection.

$$\theta_{crit} = \sin^{-1}(n_2/n_1) \quad (2.2.2.2)$$

where θ_{crit} is the critical angle, n_1 is the higher refractive index and n_2 is the lower refractive index.

2.2.2.3. Truncation of CPC

As a concentrator that is close to the ideal design, the geometry of CPC is very practical in real application, but the only weakness is that it is very long comparing with its diameter of the collecting aperture which should be considered in large-scale application for the purpose of economic and light weight. Because the parts close to

the entrance aperture of the CPC are nearly parallel the optical axis which does not affect the size of entrance aperture too much, CPC can be 'truncated' well short of full development. The effects of truncated length on the sizes of apertures of 2D and 3D CPCs were investigated by Winston and Hinterberger [26], Rabl [71], and Welford and Winston [70] in detail. As a rule of thumb, truncating half of the fully CPC height leads to a good tradeoff between concentration and mirror area [56].

2.2.2.4. CPC in special shape

2.2.2.4.1. Asymmetric CPC

The 2D and 3D CPCs are symmetric in the original design with two equal half acceptance angles around the symmetry. However, the evolution in the design of a CPC has led to asymmetric CPC for some special purposes. The asymmetric CPC was introduced by Rabl [72] who also pointed out that the ordinary CPC is a special limiting case of the asymmetric CPC. Fig. 2.2.2.4 demonstrates an example of asymmetric ideal concentrator with the acceptance angle of $2\theta_c = \varphi_l + \varphi_r$ and the geometric concentration ratio of $C = 1/\sin\theta_c$. The effective concentration ratio changes with the incident angle [72]. The axis of the left (right) parabola subtends an angle φ_l (φ_r) with the normal of absorber and F_l (F_r) is the focus of the left (right) parabola. In practical application, asymmetric CPC is mostly utilized in vertical facade which will be introduced in the following section in detail.

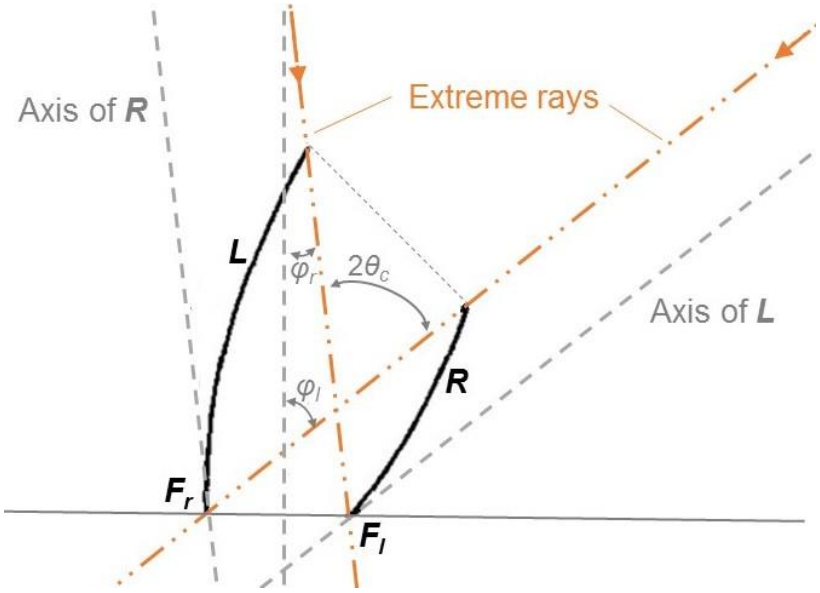


Fig. 2.2.2.4. Asymmetric ideal CPC (*L*, *R*: parabolas; F_l: focus of *L*; F_r: focus of *R*; acceptance angle: $2\theta_c$; ϕ_r, ϕ_l: subtended angle of parabola axes) [72]

2.2.2.4.2. Sea shell

The "Sea shell" is another special case of a general asymmetric CPC as shown in Fig. 2.2.2.5. It constitutes a single parabola CD whose axis is parallel to one of the extreme rays. The focus of the parabola is at the edge A of the absorber. It is used to concentrate all incident rays through the aperture AD with the incident angle $|\theta| < \theta_c$ (apart from the usual $cos\theta$ factor for non-normal incidence).

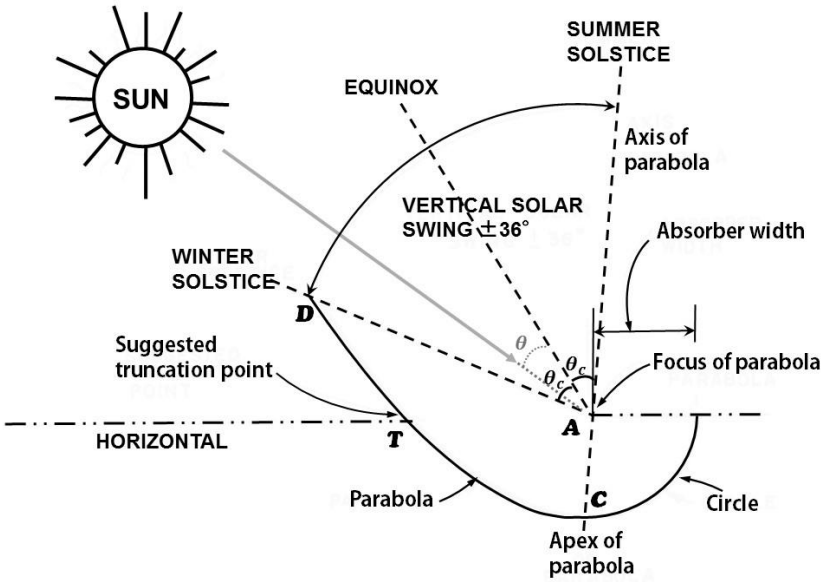


Fig. 2.2.2.5. Section view of a stationary "Sea shell" collector with the maximum output in summer [72]

2.2.2.4.3. CPC with convex absorber

Winston and Hinterberger [26] proposed that the absorber of ideal concentrator can be not only flat and parallel to the aperture, but also convex. When the absorber is straight, the concentrator includes parabolic and circular sections. Fig. 7 demonstrates two examples of ideal cylindrical concentrators for different absorbers. The shape of reflectors depends on the shape of absorber. For example, in Fig. 2.2.2.6 (a), AD and AF are convolutes of sections AC and AB of absorber; in Fig. 2.2.2.6 (b), sections DD' and D'E belongs to different parabolas. Study [73] provides the calculations of determining the shape of reflector. This kind of design is popular in solar thermal application because it use absorber material more efficiently and there are no losses through the back [72].

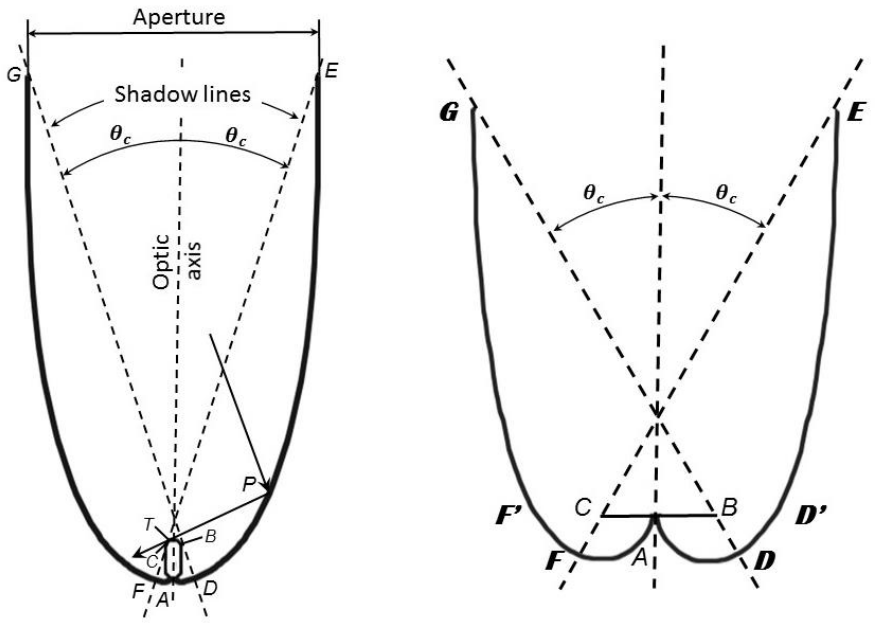


Fig. 2.2.2.6. Section view of an ideal cylindrical concentrator with arbitrary absorber shape, a) concentrator with pipe-shaped absorber; b) concentrator with flat absorber [72]

2.2.2.4.4. Lens-walled CPC

Lens-walled CPC can be considered as a combination of reflective CPC with a thin CPC-shape lens, or particular dielectric CPC. As shown in Fig. 2.2.2.7 a), the conventional lens-walled CPC [74-76] is designed by rotating the parabola of symmetric CPC around the end point C (D) of aperture toward the inside by a certain degree. The formed cavity is filled with dielectric to form the CPC-shape lens. The outside surface of the lens is layered with a reflective coating. Fig. 2.2.2.7 b) demonstrates an improved lens—walled CPC proposed by Li et al. [77-79] which adding a thin air gap between the CPC-shape lens and the CPC reflector to improve the optical performance. Lens-walled CPC can be utilized in PV or PV/T system with the advantages of light weight and more uniform illumination.

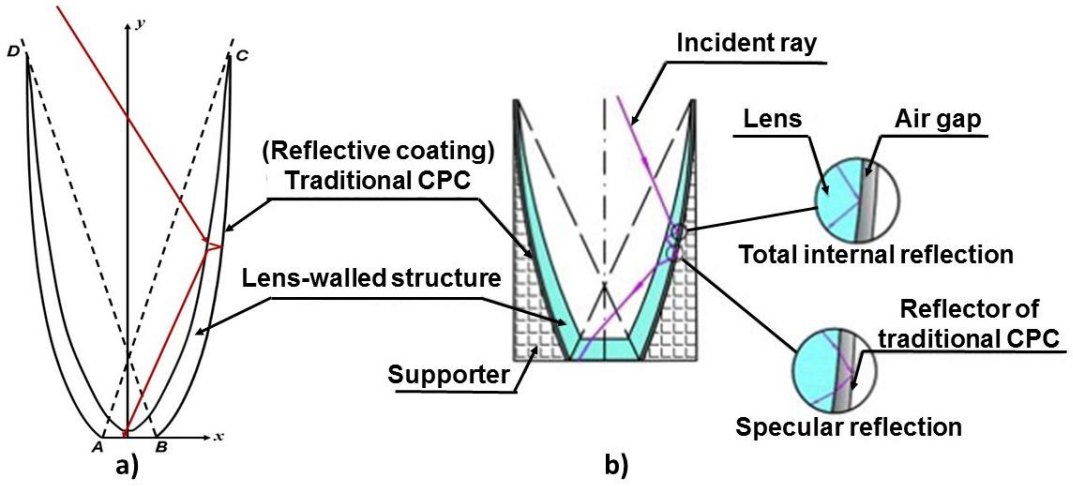


Fig. 2.2.2.7. Section view of lens-walled CPC, a) conventional lens-walled CPC b) lens-walled CPC with air gap [76, 78]

2.2.3. Design considerations in material

In accordance of the CPC structure, it can be divided into side wall material and dielectric filled material generally. Considering the application of CPC for concentrating and illumination, the side wall of CPC is made by reflective material or the material with reflective coating. The metal with high reflectivity, such as stainless steel [80-82], aluminum [82], aluminum plating [82, 83] and Nickel-Gold plating [37]. Except metal, dielectric material is also another choice for side wall with metallic coating on it [37, 84, 85]. For dielectric filled CPC, the common optical materials in useful visible and infrared regions can be utilized as the dielectrics depending on the requirements of refractive index, for instance, clear polyurethane [86, 87], PMMA (poly methyl methacrylate) also called acrylic [85], and borosilicate glass [88], etc.

The selection of material depends on both the properties and the manufacture requirements of it. Most of CPCs are formed by the Computer Numerical Control (CNC) technology which can produce a one-off as effectively as repeated identical production. It is an automatic and precise system. However, when producing small or complex CPC components, the accuracy of CNC should also be taken into account. Van Dijk et. al. [66] manufactured several CPCs in different shapes by 3D-printing in high fabrication accuracy successfully. They obtained the 13% improvements on short circuit current of CPV system with 3D printed CPCs. Molding is another way to fabricate precise CPCs, especially dielectric CPCs, with high accuracy molds. It can also be applied to creating the CPCs in more complicated shape. The optical properties,

such as color, clarity, transparency, and so forth should be noticed during the molding for dielectric materials. For instance, inclusions, voids and all crystallinity should be prevented when the transparency is required because the change of refractive index would interfere with the passage of light [89]. For some particular designs, like microstructure CPC array proposed in the study by Walze et al. [85], the PMMA is manufactured by interference lithography. The metallic coating can be finished by sand blast technique [37].

When CPC incorporates with PV cell, the encapsulant between them is also need to be taken into account. A silicone elastomer (Sylgard-184) is a common encapsulant in CPV systems which has excellent transmission properties within the UV-visible spectral range with refractive index 1.5 [87, 90, 91]. Baig et al. [92] found that when the thickness of encapsulant interface becomes thicker, the optical and energy performance of Crossed CPC (CCPC) system will decrease.

2.2.4. Solar geometry and tracking system

2.2.4.1. Solar geometry

For trough CPC, its long axis is positioned along east-west direction, the normal to the apertures is tilted downward from the zenith which is called tilt angle of CPC, and the position of 3D CPC follows the same principles. Based on the sun movement, the annual solar collection is expected to be maximum when the tilt angle equals the local latitude. According to Fig. 9, the cosine of the angle of the incident ray is [93]:

$$\cos\theta_i = \sin\alpha\cos\beta + \cos\alpha\sin\beta\cos(\gamma - A) \quad (2.2.4.1)$$

If assuming the direction solar radiation is I_{direct}, the solar radiation at the normal direction I_{r} onto the surface of CPC entry aperture is [93]:

$$I_r = I_{direct}\sin\alpha\cos\beta + I_{direct}\cos\alpha\sin\beta\cos(\gamma - A) \quad (2.2.4.2)$$

The annual collection of CPC can be roughly predicted by the Eqs. 2.2.4.1 and 2.2.4.2 and optical efficiency based on the direct and diffuse solar irradiation in weather data. Yu and Su [94] introduced a concept of inner south projection angle that considering solar altitude, solar azimuth, CPC tilt angle and refractive index of dielectric, which provides a novel approach for indicating solar radiation through dielectric-filled CPC.

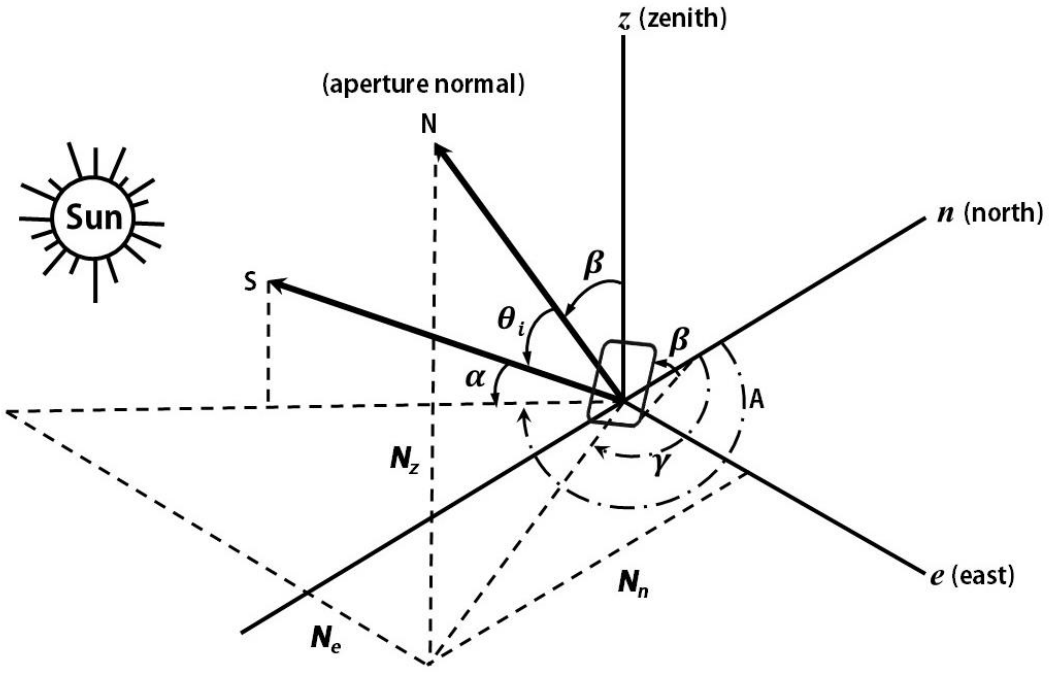


Fig. 2.2.4.1. A fixed aperture with its orientation defined by the tilt angle (β) and the aperture azimuth angle (γ). N is the aperture normal; vector S is a ray of the direct solar radiation; α is the angle of solar radiation to the earth's surface; A is the solar azimuth; θ_i is the angle of incidence, which is the angle between the ray and the aperture normal; the direction cosines of N along the z, e and n axes respectively as N_z, N_e and N_n [93].

2.2.4.2. Consideration of tracking system

In accordance to CPC geometry, it can be seen that the larger the concentration ratio is, the smaller the acceptance angle will be. The CPC, or most nonimaging optics are designed to have good concentration without tracking because they can achieve the widest possible angular field of view for a given geometric concentration. Thus the geometrical design of CPC is the most important factor to determine whether the stationary or passive tracking mechanism would be utilized [95]. The stationary concentrator, which is fixed throughout the whole year, can provide the concentrations from low to moderate (1.1 × ~2 ×; in special cases, up to 4 ×). For example, A design of stationary concentrator with larger acceptance angle $\theta_c = 55°$ and lower concentration ratio $C_{geom} \cong 1.1 \times \sim 1.2 \times$ can receive the sunlight up to 7.3 h per day throughout the year when it is positioned along either horizontal (east-west) position or polar (north-south) position. The most common stationary CPC is with the half acceptance angle $\theta_c = 35°$ and concentration ratio $C_{geom} \cong 1.3 \times \sim 1.6 \times$ [56].

However, in some applications such as concentrating photovoltaic and concentrating solar thermal requires higher concentration for more irradiation or higher temperature. The concentrators with slightly higher concentrations ($\sim 3\times \sim 10\times$) or higher concentrations ($> 10\times \sim 40{,}000\times$) are needed. The former usually with seasonal adjustment to collect more diffuse insolation. The concentrators with higher concentrations ($> 10\times \sim 40{,}000\times$) would be incorporated with tracker. The concentrator in this level collects more "circumsolar" radiation rather than diffuse insolation. Nonimaging optics, especially CPC, can provide lager optical tolerances so that the requirements of tracker accuracy are not that high. However, utilizing tracker is still not always practical: the precise solar trackers are sufficient expensive; utilizing trackers bring installation difficulty; the moving mechanical parts may reduce the reliability of whole system; the trackers consume electricity as well; not all applications are appropriate for installing trackers [64]. Therefore, when high concentration is not significant, the non-tracking system has high priority to be considered.

2.3. CPC studies in literature

In this section, a series of experimental and theoretical studies about CPC are presented. The literatures will be categorized according to their applications. In the first part, several PV systems employing CPCs as concentrators are introduced, which are classified based on CPC geometry. In second part, CPC working on solar thermal is discussed. Section 2.3.3 demonstrated that how CPC cooperates with daylighting in either control or collection. The last part talks about some typical areas that CPC is involved to. Fig. 2.3.1 illustrates a flow chart of this section. It is important to mention that the CPC studies presented are expected to be comprehensive to cover all of its applications but there might be some missed published but its knowledge contribution is still appreciated.

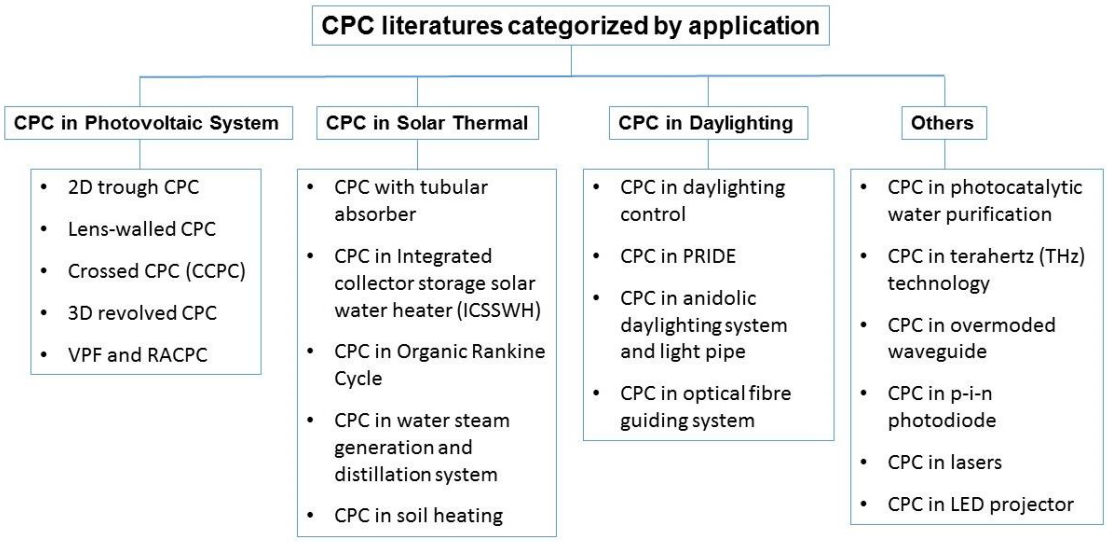


Fig. 2.3.1. Flow chart of Section 2.3

2.3.1. CPC in photovoltaic system

According to recent data by SolarPower Europe (the new European Photovoltaic Industry Association EPIA) [96], the cumulative capacity of global solar photovoltaic (PV) achieved 178 GW in 2014, and it is predicted that there will be 540 GW market of PV in the next five years. On the other hand, the massive cost reduction (75% reduction on PV price in less than 10 years) also speeds up the popularization of PV technology. Concentrating photovoltaic (CPV) is a part of PV technology which focuses on capturing more light to generate energy by minimising the usage of PV. Therefore the optical devices are employed. Although CPV only offers 357.9MW in the total installed capacity in 2014, this will reach 1GW in 2020 [97]. As shown in the hierarchy of CPVT (Fig. 2.3.1.1), CPC is one of the key optical devices utilized in CPVT and lots of studies have been conducted in this area [98]. It concentrates solar radiation onto PV with intermittent tracking or without tracking in view of its wide acceptance angle. The concentration ratio determines the enhancement of relative radiation on PV. The flux distribution and temperature of PV are two main factors to improve PV efficiencies. Most researches about CPC with PV focus on the amount of collected light and radiation distribution on PV cell. In addition, with the consideration of cell temperature, PV is usually coupled with thermal system to remove heat or generate thermal energy simultaneously. Therefore, PV/T system is also a common type when designing the PV system with CPC. The CPVs will be introduced and classified in different shapes in this section.

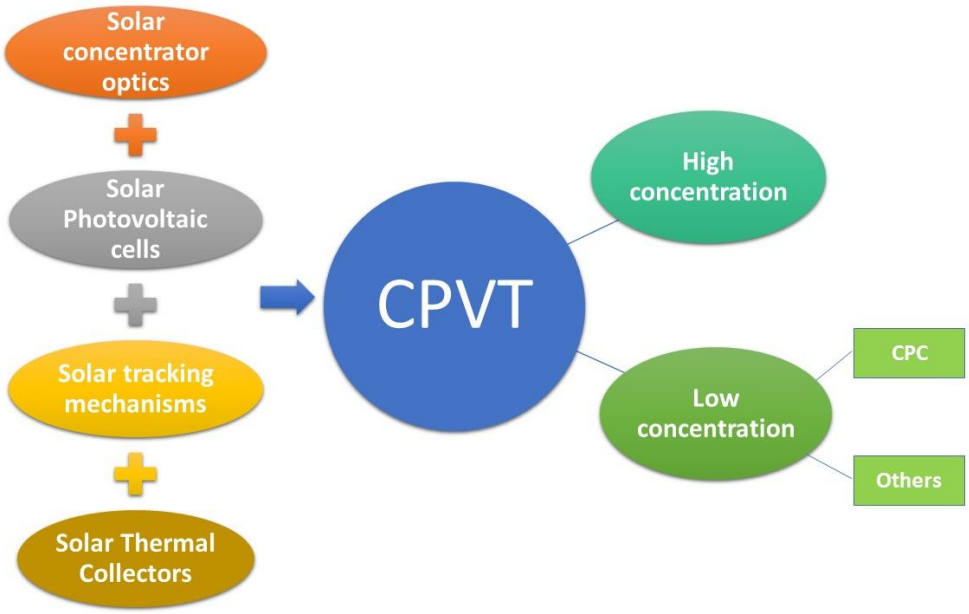


Fig. 2.3.1.1. Hierarchy of CPVT system

2.3.1.1. 2D trough CPC

2D trough CPC is the most popular type for PV application in practice. A 2D CPC integrated with single-pass photovoltaic/thermal (PV/T) solar system was designed and tested by Sun and Shi [80]. The trough CPC was made by a mirrored stainless steel material. The hybrid system had solar cells on base of CPC and fins attaching to the back side of PV panel to speed up the heat transfer to the air in chamber, as shown in Fig. 2.3.1.2. Experiments were taken outdoor to investigate the electrical and thermal performance under real weather conditions. Results implied that the air cooled down the solar cell effectively when the velocity was increased. The maximum short circuit current was higher than twice of the current of standard PV panel. On the test taken on 20th of Aug, the maximum temperature rising was 13°C and the thermal efficiency increased from 60% to 70% at the same time. Karathanassis et al. [99] designed a similar CPVT system consisting plate-fin cooling channels under the PV cells attached on the CPC base, which provides 6% electrical efficiencies and 44% thermal efficiencies at the same time.

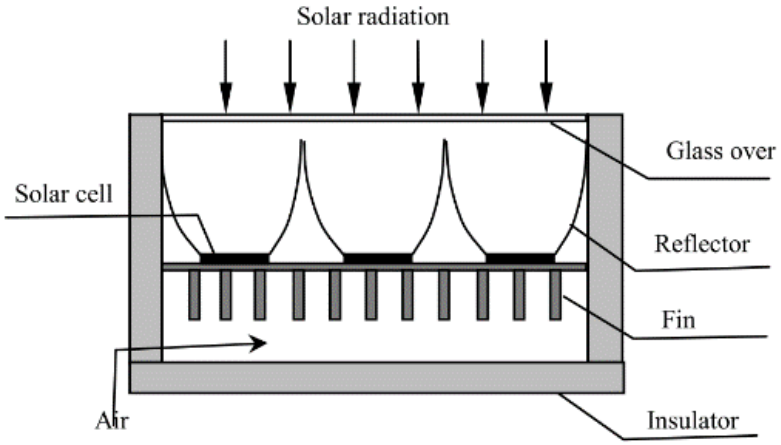


Fig. 2.3.1.2. Cross section view of the hybrid 2D CPC PV/T system [80]

In another CPC PV/T system (Fig. 2.3.1.3) with cooling pipes [68], effects of glazing cover and cooling pipes were investigated according to the optical, thermal and electrical performance. The intermittent tracking is required for this system. It was found that the 2D unglazed CPC improved the electricity generation by 49.4% of solar cells. The glazing cover was not suggested owing to the reduction of electric output and increase of heat gain, but the compensation and dust should be paid attention on uncovered solar cells. The cooling pipe could increase the electricity generation considerably and thermal gain of PV/T system. Following the previous work, Bahaidarah et al. [81] did a comparative experiment for the 2D unglazed trough CPC with cooling pipes. The other three test prototypes for comparisons were the flat PV with cooling, flat PV without cooling and unglazed CPC without cooling. The experiments results demonstrated that the PV with CPC and cooling generated the electricity most, which was twice as much as the PV-CPC without cooling generated and 61.9% higher than the flat PV strings with cooling generated.

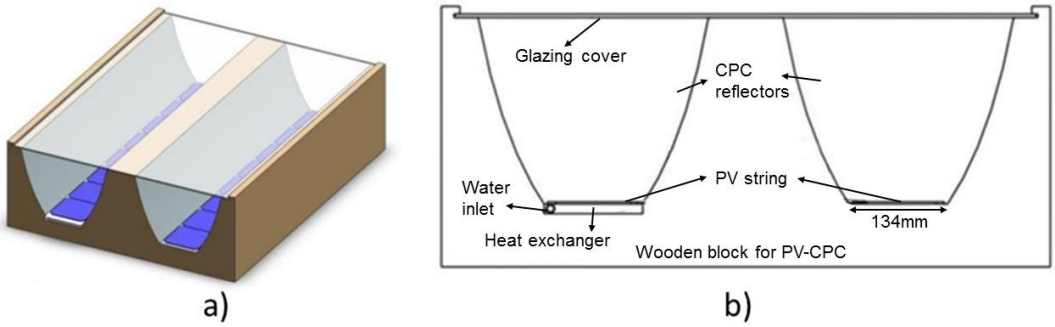


Fig. 2.3.1.3. Schematic diagram of 2D trough CPC a) 3D model of glazed PV-CPC system b) cross section of glazed PV-CPC system with/without cooling pipes [81]

Except for individual CPC, some lenses with special shapes are integrated to CPC to enhance its concentration. Grasso et al. [100] proposed a trough CPC integrated with a prism for PV application. As shown in Fig. 2.3.1.4, CPC is reflective as primary concentrator and prism is dielectric with high refractive index. PV cell is attached on base of CPC. According to the ray tracing and prototype test, the geometrical concentration ratio of it was $5\times$ and the effective optical performance ratio was up to 81%.

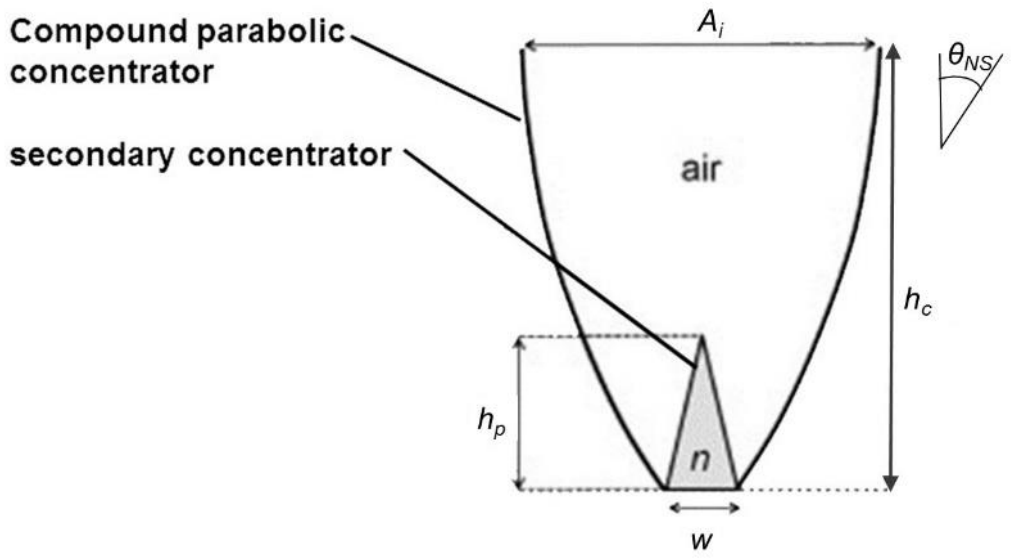


Fig. 2.3.1.4. Section view of CPC coupled with prism as secondary concentrator [100]

Another example of several concentrators in PV system is incorporating CPC and Fresnel lens. Chen [101, 102] patented a kind of high concentration system, which consists three or four optical concentrations as shown in Fig. 2.3.1.5. One or two layers of Fresnel lens are located above a trough CPC, and a third or fourth concentrator which is glass lens with reflective coating is attached then with PV cell. Therefore the whole system can enhance the solar intensity 300- 1000 times within a six-inch distance. This kind of design is applied to PV power generation mostly.

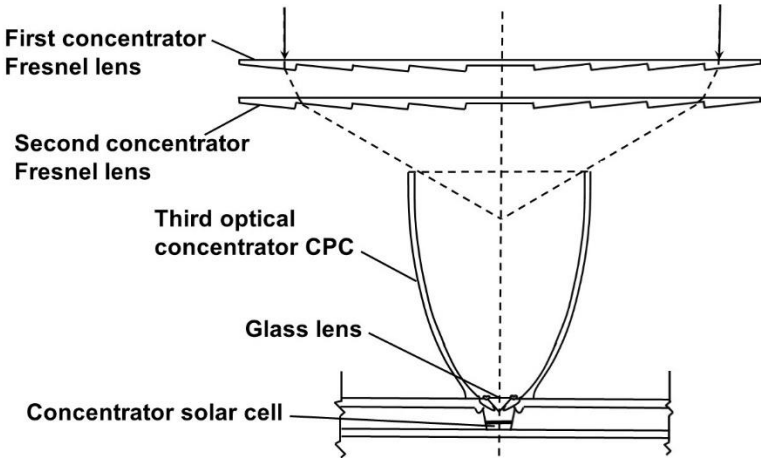


Fig. 2.3.1.5. Cross section of Chen's high concentration system [103]

2.3.1.2. Lens-walled CPC

Except conventional 2D CPC, lens-walled CPC may play an important role in PV concentration as well. Su et al [74] investigated the optical performance of lens-walled CPC with the comparison of conventional 2D reflective CPC and dielectric filled CPC. Under the incident light with different angles, results showed that the lens-walled CPC has great advantages on acceptance angle and flux distribution on base. It had higher optical efficiency than reflective CPC but slightly lower than dielectric filled CPC. In terms of annual solar energy collection, six cities which were Birmingham, Paris, Rome, Beijing, Hefei and Shanghai were selected as examples [75]. The monthly accumulative solar energy collection demonstrated similar results. The collected solar energy by lens-walled CPC was 20% less than dielectric filled CPC and 20-30% more than reflective CPC. However, lens-walled CPC has outstanding feature of its light weight compared to solid CPC and almost same cost on manufacture. Li et al. [76] evaluated the flux distribution and PV performance of test prototype for lens-walled CP and compared to the reflective CPC. Experiment results demonstrated that the lens-walled CPC had more uniform flux distribution on PV according to the change of fill-factor, which caused higher efficiency and output of PV cell.

Based on the previous researches, an improvement of lens-walled CPC was put forward by adding an air gap between the lens structure and reflector [77], as shown in Fig. 2.3.1.6. A test prototype of a lens-walled CPC with air gap was made for experiment to compare with reflective CPC and traditional lens-walled CPC. It was found that the lens-walled CPC with air gap can reduce more optical losses compared

to other two CPCs. For irradiance distribution on PV, the two lens-walled CPCs have similar performance but both of them were better than reflective CPC.

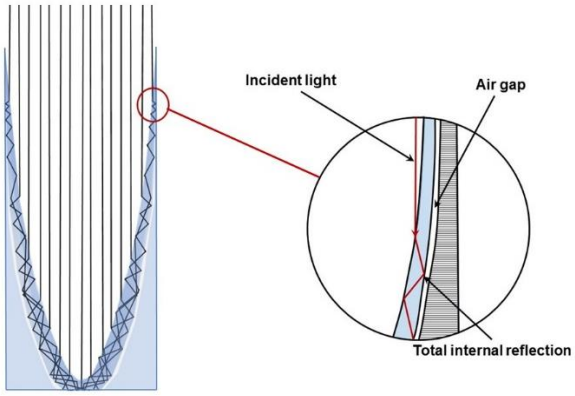


Fig. 2.3.1.6. Schematic diagram of lens-walled CPC with air gap [77]

The lens-walled CPC integrating with PV/T system was also explored [13, 78, 104]. Fig. 2.3.1.7 illustrates the structure of the whole system: the solar cell is in the middle of encapsulated materials; CPC is fixed on a square tube with insulation. Comparing with the PV/T system without concentrator, it showed the great advantages of lens-walled CPC on concentration: the average optical efficiency was up to 83% when the incident lights were within the half acceptance angle. The experiment under real sky showed that the overall optical efficiencies of a daytime were 62% and 67.9% for 31th of March and 13th of May [78].

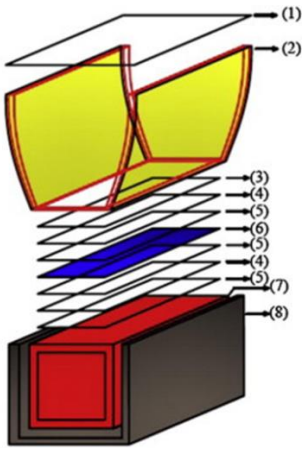


Fig. 2.3.1.7. Schematic diagram of lens-walled CPC with air gap integrating with PV/T system (1) Front glazing (2) Lens-walled CPC with air gap (3) UV Glue (4) TPT (tedlar-polyester-tedlar) (5) EVA (ethylene-vinylacetate) layers (6) PV cell (7) Copper pipe (8) Thermal insulation [78]

2.3.1.3. Crossed CPC (CCPC)

Because CCPC is created by combining two 2D CPC, CCPC performs well in PV generation. Sellami and Mallick [105] compared the optical efficiency and the flux distribution between 3D CCPC and 3D revolved CPC to investigate their potential when cooperating with PV. The CCPC with concentration ratio 3.6× and half acceptance angle 30 ºwas found to be an ideal concentrator. Similar to revolved CPC, the maximum optical efficiency of CCPC reached to 95%, but CCPC with square entry and exit aperture of CCPC could reduce the losses more [106]. They also made a test prototype of CCPC, which had reflective film covering on inner surfaces and PV cells on base. Both simulation and experiment results demonstrated that the optical flux distribution was not uniform at the exit aperture. Some of the hot spots could as 50 times higher than incident light that would decrease the efficiency of solar cells.

With the consideration of temperature influence on PV, the air flow and temperature distribution of an isolated CCPC with solar cell was investigated [107]. The side walls made by dielectric materials were covered with reflective film of CCPC prototype. It was found that a vortex-loop changes with the incident sunlight in the filled chamber. The high temperature core on solar cell was supposed to decrease the efficiency of solar cell.

Apart from reflective CCPC, the potential of dielectric filled CCPC has been explored. Baig et al. [86] simulated and tested the optical and energy performance of a 3D dielectric filled CCPC with 1cm ×1cm solar cells on base. The dielectric filled material was clear polyurethane. It was found that the maximum optical efficiency reached 73.4% and the maximum power ratio was 2.67. The experiment results demonstrated the non-uniformity of flux distribution results in the decrease of power output for solar cells. The operating temperature also applied parasitic effects which is up to 14.6% decrease on the power generation of PV cells as well.

Taking into account the escaping light from edges of CPC, the dielectric filled CCPC with reflective film on edges has been put forward. In the study [92], the influence of reflective film on edges and encapsulant interface on trapping the light escaping were mainly discussed as shown in Fig. 2.3.1.8. Results demonstrate that the optical efficiency increased from 55.6% to 84.5% when the thickness of encapsulant spillage decreased from 3mm to 0.1mm. The reflective film along the edges reduced the optical

losses effectively. The positive effect of reflective film also reflected on the energy output of solar cells. The maximum increase 8.5% of short circuit current was and 6.6% of maximum power ratio. Another study [108] investigated and proved that the partial reflective coating of edges also works on 2D dielectric filled CPC, which could improve the optical efficiency by 13.5%. Lamnatou et al. [109] also proposed that the reflective film on edges of 2D dielectric filled CPC could provide 11% reduction in energy payback time and 12% reduction in greenhouse-gas payback time for a CPV system.

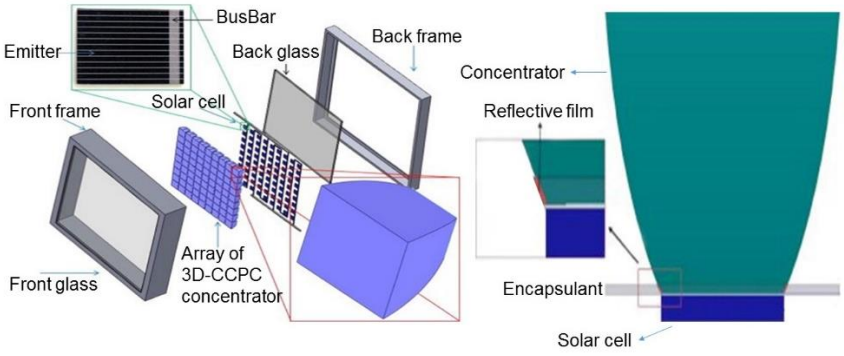


Fig. 2.3.1.8. Reflective film and encapsulant on CPV [92]

CCPC can also be integrated with non-imaging dish concentrator (NIDC). According to Fig. 2.3.1.9, the NIDC is primary concentrator with the rim angle of θ and the dielectric-filled CCPC is secondary concentrator. It is a sun-tracking and dense-array CPV system. The larger entrance aperture of CCPC components provide more space for flexibility of inter-connection among PV cells; the square exit aperture of CCPC suits the commercial PV cell very well. This system [110] was compared to normal dense-array CPV (DACPV) module for different pointing errors. Results showed that the NIDC+CCPC module used 77% less CPV cells than DACPV module but performed better electricity output. Chong et al. [111] put forward another concentrator photovoltaic system using NIDC as the primary concentrator and CPC as the secondary concentrator. The two concentrators were positioned face to face and the NIDC was designed to produce uniform solar flux distribution onto the top of CPC with PV attached on base. The on-site measurement in Malaysia showed that the system efficiency of this CPV system was 17% and the maximum output power was 639W as the direct normal irradiance was normalized to 1000W/m^2.

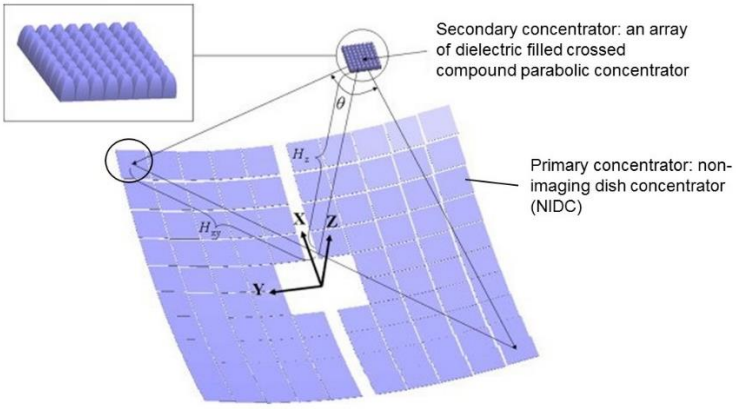


Fig. 2.3.1.9. Schematic diagram of CCPC integrating with non-imaging dish concentrator (NIDC) [110]

2.3.1.4. 3D revolved CPC

As indicated in previous sections, CCPC performs less optical losses than 3D CPC. However, 3D CPC is also worth to be explored in PV application. Arnaoutakis et al. [88] integrated dielectric compound parabolic concentrators (dCPCs) with a planar bifacial silicon solar cell (SC) and a 25% Er3+ doped hexagonal sodium yttrium fluoride (β-NaYF4:Er) up-conversion (UC) phosphor as shown in Fig. 2.3.1.10. The functions of dCPCs are concentrating, transmitting broadband of the excitation and coupling the isotropic emission. The dielectric filled material was B270 borosilicate glass. The critical findings were the efficiency increased 32% under sub-band-gap illuminance and the external quantum efficiency (EQE) was increased from 1.33% to 1.80%, which implied the capability of dCPC cooperating with UC-SC due to enhancing the concentration in forward direction and in the same time maintaining high collection efficiency of UC emission in the reverse direction. The design also provides a way to optimize the solar concentration on UC phosphor independently for the solar cell as required.

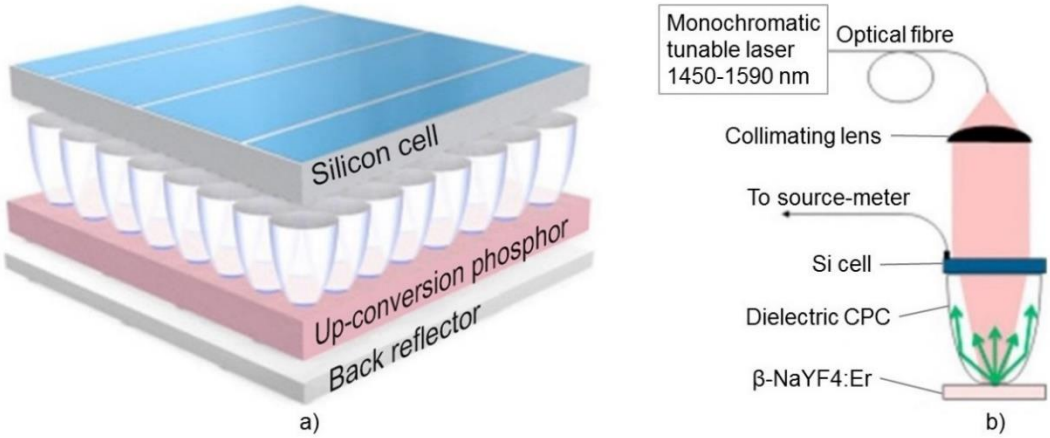


Fig. 2.3.1.10. dCPC integrating with UC-SC, a) UC-SC with a regular two-dimension array of integrated dCPC; b) Schematic and optical setup [88]

Similar to 2D CPC, 3D CPC can also integrate other lenses to enhance its concentration. Andreev et al. [112] proposed a reflective 3D CPC with a convex lens as secondary concentrator for electricity generation as shown in Fig. 2.3.1.11. The PV cell is AlGaAs-GaAs heterostructure attached on base of CPCs. The convex lens on CPC base could increase the concentration ratio of CPC from 21× to 30×. The optical efficiency of the whole system could reach 90%.

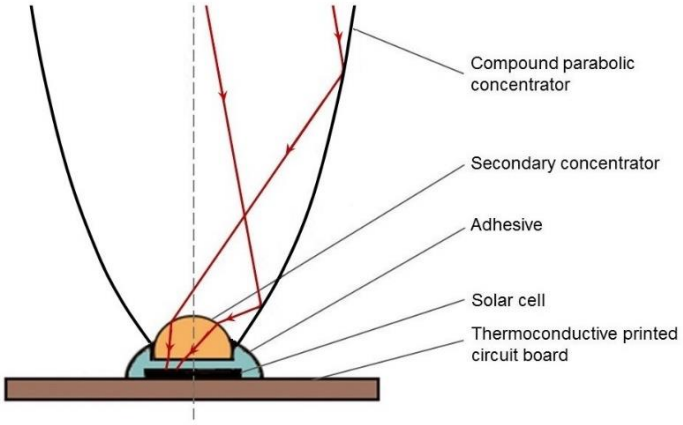


Fig. 2.3.1.11. Section view of CPC coupled with convex lens as secondary concentrator [112]

2.3.1.5. Variable-focus-parabolic (VPF) and rotationally asymmetrical compound parabolic concentrator (RACPC)

In order to solve the problem of non-uniform flux distribution, a novel parabolic concentrator called variable-focus-parabolic (VFP) reflector was proposed by Tsai [113]. It has a square solar cell on base, and the focal length varies as a function of the

horizontal displacement of the incident point relative to the vertical centerline of the solar cell on base. Two types of VFP reflectors with circular focus spot and square focus spot were designed and compared. Fig. .3.1.12 shows a cross section of the VFP reflector with square spot and two different focus spots. In this research, the performance of VFP reflector were compared with the conventional standard parabolic concentrator by exact analytical model and skew-ray tracing approach. The geometry of VFP reflector was optimized in order to maximize the uniformity of flux distribution on solar cells. Results illustrated that the four-step VFP reflector that guided up to 89.8% incoming rays onto the solar cell and improved uniformity of flux distribution by 92%, which provided great advantages to conventional standard parabolic concentrator.

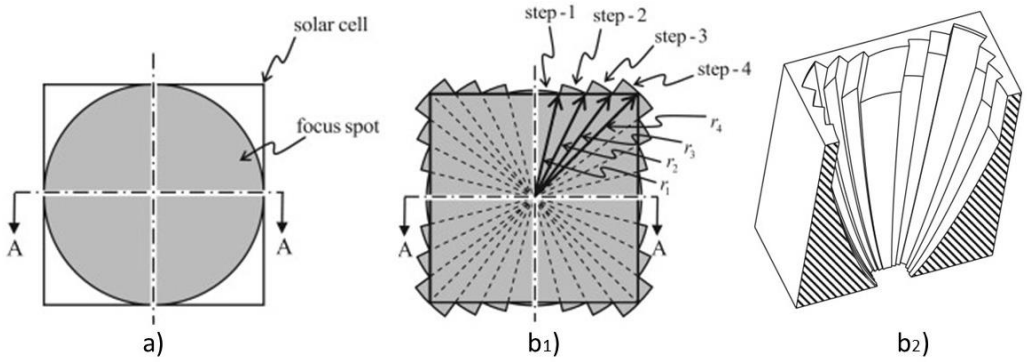


Fig. 2.3.1.12. Schematic diagram of VFP, a) Circular focus spot on solar cell; b_1) Square focus spot on solar cell; b_2) Cross section of VFP with square focus spot [113]

Abu-Bakar et al. [114] designed a novel rotationally asymmetrical compound parabolic concentrator (RACPC) and did a series of research [115] on it. The RACPC shown in Fig. 2.3.1.13 has the planar entry aperture with four axis of symmetry and square exit aperture. The test prototype of RACPC was integrated with a 1cm by 1cm monocrystalline laser grooved buried contact silicon solar cell. Both of simulation and experiment results demonstrated that the RACPC provided good concentration gains within its designed acceptance angle. Comparing with a bare solar cell, the short circuit current was increased by 3.01 times and the maximum power was increased by 3.33 times.

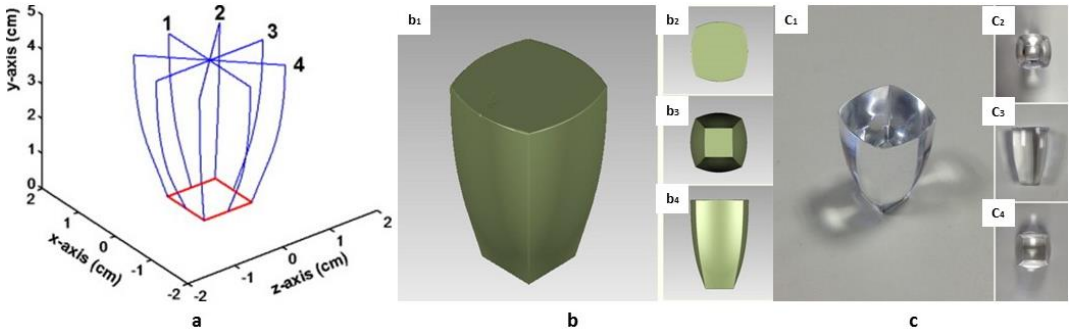


Fig. 2.3.1.13. Structure of RACPC, a) schematic diagram of producing RACPC by angular rotating 2D cross section; b) 3D model of RACPC c) prototype of RACPC [114, 115]

2.3.2. CPC in solar thermal

The CPCs utilized in solar thermal systems will be introduced in this section. The working principle is quite same as CPV system, which is concentrating more light onto an absorber near the base. A CPC can be designed into different shapes to meet the requirements of a variety of absorbers. Different from CPV, the concentration ratio of CPC in collector can reach 10 without diurnal tracking. Vacuum technology will be applied for evacuated tubular absorber to surround the surface of absorber that is often a selectively coated pipe with a double-walled evacuated glass tube [51]. Researches in this section are about the design of CPC and tubular absorber to improve the thermal efficiency of collectors. Table 2.3.2.1 summarizes the properties of typical solar energy collectors.

Table 2.3.2.1: Solar energy collectors [116]

Motion	Collector type	Absorber type	Concentration ratio	Indicative temperature range (°C)
Stationary	Flat plate collector (FPC)	Flat	1	30–80
	Evacuated tube collector (ETC)	Flat	1	50–200
	Compound parabolic collector (CPC)	Tubular	1–5	60–240
Single-axis tracking			5–15	60–300
	Linear Fresnel reflector (LFR)	Tubular	10–40	60–250
	Parabolic trough collector (PTC)	Tubular	15–45	60–300
	Cylindrical trough collector (CTC)	Tubular	10–50	60–300

Two-axes tracking	Parabolic dish reflector (PDR)	Point	100–1000	100–500
	Heliostat field collector (HFC)	Point	100–1500	150–2000

2.3.2.1. Traditional CPC solar collector

The CPC with tubular absorber is a common solar thermal collector, especially in domestic hot water heating system. The researches on it have lasted several years, and were mainly based on numerical model and experiment prototype. The numerical model is an important and accuracy tool to design system, validate experiment results, and optimize the system performance [117].

Ortiz-Rivera and Feliciano-Cruz [118] evaluated thermal performance of a solar thermal power plants with CPC as solar collector in Puerto Rico. The local weather data were considered. Results showed that under sunny sky conditions, more solar radiation was collected, but the power output decreased under cloudy sky conditions depending on the solar transients: system could return to stable energy output with short appearance (5-10 min) of cloudy sky; the power generation would reduce greatly even to zero when the sun is missing for a long time.

Because of concentrating solar radiation onto base surface, CPC is also attempted to be integrated with flat absorber. Al-Ghasem et al. [119] tested a prototype performance of 2D trough CPC with a flat absorber on base under Jordan, Irbid climate from March to May in 2013. The flat absorber was designed to be a heat source for the applications in low temperature range (below 90°C). Results showed that comparing with stationary CPC, the tracking one increased the highest temperature of absorber by 27.7%, 16.7% and 8.3% for March, April and May respectively, but the cost of tracking system which occupied 38.6% of the whole test system should be taken into account. Mishra et al. [120] optimized the U-shaped evacuated tubular collector (ETC) by integrating with compound parabolic concentrator in accordance with the analysis of energy matrices.

Ratismith et al. [121] proposed the performance of two novel CPCs for solar thermal collection, as shown in Fig. 2.3.2.1, one is double-parabolic trough (DPT) and the other is flat-base trough (FBT). Both of them have a double sided absorber plate in middle. The ray tracing results demonstrated that the FBT with vertical alignment of double sided absorber plate was more efficient than the DPT with horizontal alignment

of absorber. The prototype of FBT was tested under real sky condition in Bangkok with the comparison of 512 SUNDA-Seido standard flat-bed collector [122]. Because FBT applied wet metal-to-water contact so that provided effective heat transfer comparing with commercial collector with dry metal-to-metal contact. It generated almost same energy compared with common commercial collectors but with 50% less evacuated tubes, which led to 30% less cost in manufacture. In addition, the high temperatures (>100℃) provided made it to be capable in either domestic or industrial use.

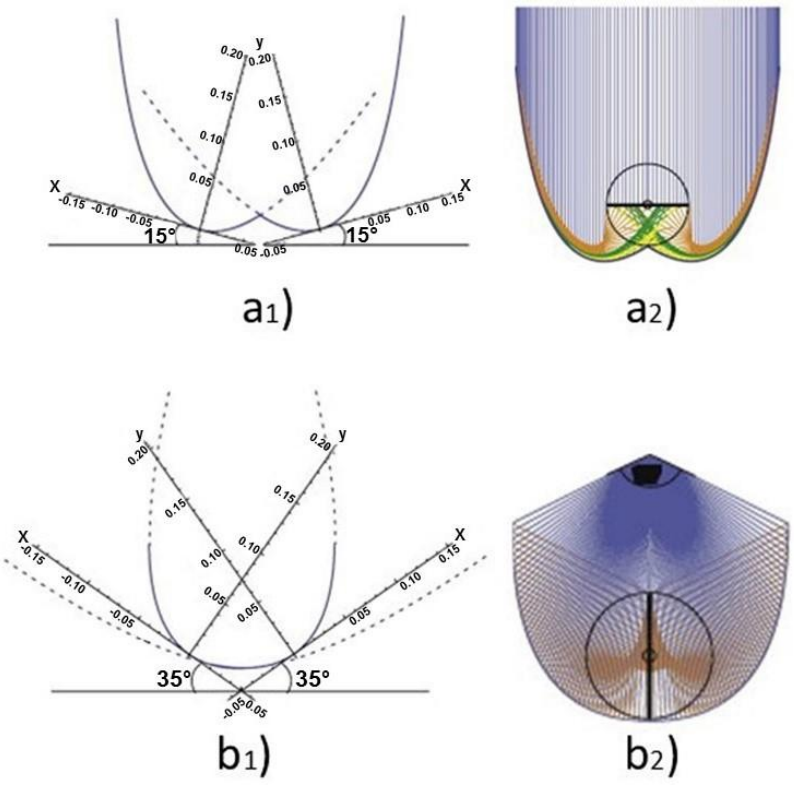


Fig. 2.3.2.1. Diagram of DPT and FBT, a_1) DPT is formed by rotating two parabola inwards by 15 °; a_2) DPT with horizontal disposition of flat plate absorber; b_1) FBT is formed by rotating the two parabola inwards until the base is flat; b_2) FBT with vertical disposition of flat plate absorber [121]

Expect the effect of parabolic wall of CPC collector, the tubular absorber also plays an important role in energy receiving. Abdullahi et al. [123, 124] compared the performance of four CPC collectors with different absorbers (Fig. 2.3.2.2). Comparing with conventional collector with one tubular receiver, the one with two receiver aligned horizontally and with elliptically shaped receiver increased the daily optical efficiency by 15% and 17% respectively. Locating two receiver in vertical could not

improve the optical efficiency. In addition, the heat transferred to the cooling water by the collector with double tube receivers outperformed the collector with single receiver by 21%, 19.8% and 18.3% for acceptance angles of 30°, 40°and 60° respectively. These results are significant to improve the solar thermal collector by changing the tubular absorber. Gang et al. [125] proposed another novel CPC solar water heater with a U-pipe inside the tubular absorber. The experiment results show that the overall thermal efficiency of this system is still high, above 49%, when the hot water in is at higher temperature (55–95 ℃). In addition, the exegetic efficiency is above 4.62% at the same time. This design provides a new idea to solve the problem of low efficiency under higher water temperature of common solar water heater.

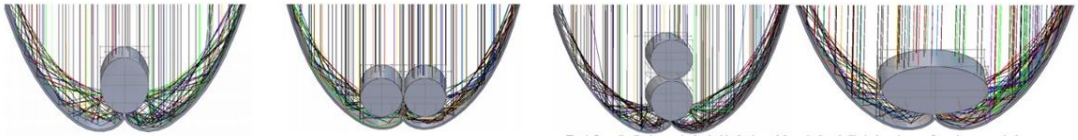


Fig. 2.3.2.2. Four CPC solar thermal collectors with different absorber [123]

Xu et al. [126] proposed to replace the tubular absorber in traditional CPC collector by a closed-end pulsating heat pipe. The concentration ratio of CPC was 3.4 and the diameter of heat pipe is 4mm for the experiment prototype. HFE7100 was used as the working fluid at a filling ratio of 40%. The thermal efficiency of prototype was as high as 50% when the normal radiation is 800W/m^2.

In order to obtain more solar energy, some CPC solar collector cooperates with tracking system. Wang et al. [127] investigated the effects of tracking mode on a tracking compound parabolic concentrating (TCPC) solar collector. The schematic view and photo of TCPC collectors are shown in Fig. 2.3.2.3. The main parts are reflective trough CPCs, evacuated tubular collectors and tracking mechanism. The CPC is with the concentration ratio of 2.3. The tracking mechanism has three different modes, which are fixed mode (FM), intermittent tracking mode (ITM) and continuous tracking mode (CTM). It was found that the average optical efficiency of ITM was the highest which reaches 63.6% among the three modes. It also provided highest output energy based on daily operation data.

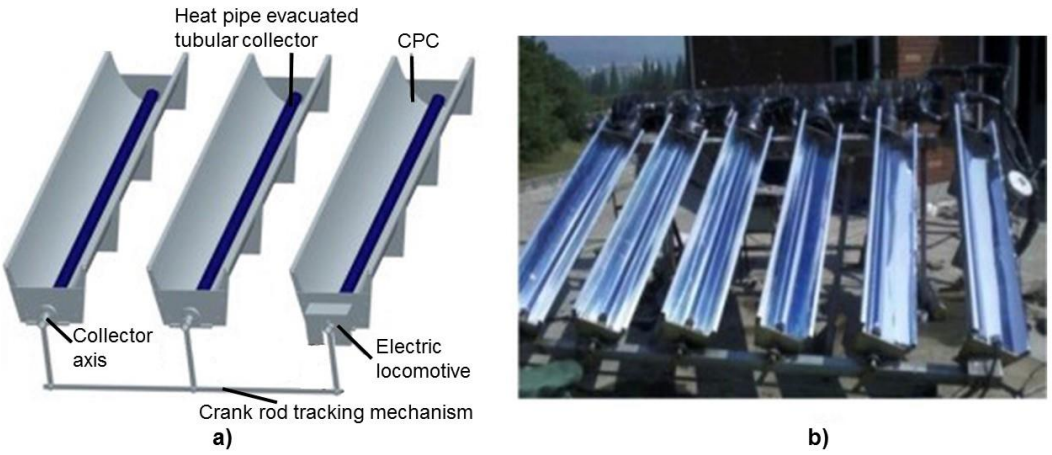


Fig. 2.3.2.3. TCPC solar collector (a) The schematic view of TCPC collectors (b) photo of TCPC collectors [127]

2.3.2.2. Hybrid solar collector with CPC

Ulavi et al. [128] designed a hybrid CPC-PV/T system with wavelength selective film as shown in Fig. 2.3.2.4. The film is integrated with CPC to reflect the solar radiation in infrared portion onto tubular absorber and transmit the visible spectrum to the thin PV film on base. Results showed that the total energy conversion efficiency of CPC-PV/T system was 20% higher than the independent PV and solar modules, while the individual efficiencies of electricity and thermal were decreased. This hybrid system still has potential if the energy requirement of per unit installed area is high.

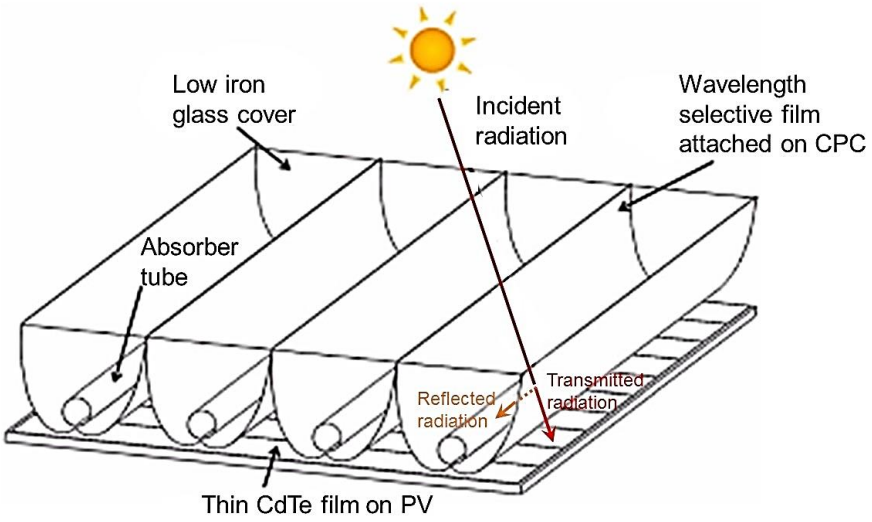


Fig. 2.3.2.4. Design concept for the hybrid CPC-PV/T system with wavelength selective film [128]

In respect of solar thermal, there is also an application in which CPC is worked with Fresnel reflector together. Yanhua et al. [129] investigated the thermal performance of this kind of concentration system shown in Fig. 2.3.2.5, which constitutes a linear Fresnel reflector concentrator (LFRC) with mirrors on bottom and reflect solar radiation into the top CPC absorber. The thermal analysis determined that the temperature of absorber increased with the length of receiver tube significantly, but the total heat loss would increase as well. Reducing the heat loss through the glass pane was an efficient way to solve this problem. The optical parameters of concentrator were the key to thermal performance, and the improvements could be made on transmittance of glass pane and reflectivity of CPC. Prasad et al. [130] tested the similar system in Vallipuram (12 °N, 79 °E), India and it was found that the optical efficiency was 76.4% and the coefficient of flux variation was 0.13. Baljit et al. [131] utilized Fresnel lens as glazing cover and primary concentrator onto the conventional PVT-CPC system. The maximum efficiency was up to 90% when this system was incorporate with dual fluid. Ma et al. [132] proposed a novel compound cylindrical solar concentrator (CCSC) which comprised of cylindrical Fresnel lenses, parabolic reflectors, secondary reflector, evacuated tube receiver and single-axis tracking. The optical efficiency of this system was as high as 84.1% which means it utilized the solar radiation efficiently. It could provide heat at 200 ℃ easily and the highest temperature was about 250 ℃ under the solar radiation of 1050W/m^2.

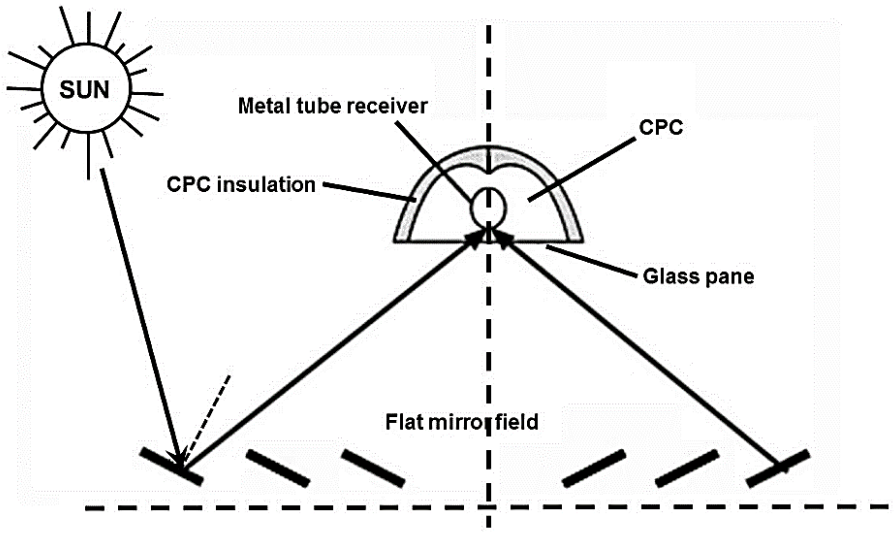


Fig. 2.3.2.5. Section view of concentration system consisting of CPC absorber and Fresnel reflector [129]

2.3.2.3. CPC in ICSSWH system

2D trough CPC with tubular absorber for solar thermal collection were introduced in previous sections. There is another innovative 'integrated collector storage solar water heaters' (ICSSWH) [133], of which un-truncated CPC was applied as primary reflector. The structure of ICSSWH is shown in Fig. 2.3.2.6: the CPC is connected with a 120 ℃everse circular reflector, a tertiary cavity and the storage vessel. The collection efficiency of this system was around 53%, and the water in vessel could be heated reaching to a temperature rise of 32℃.

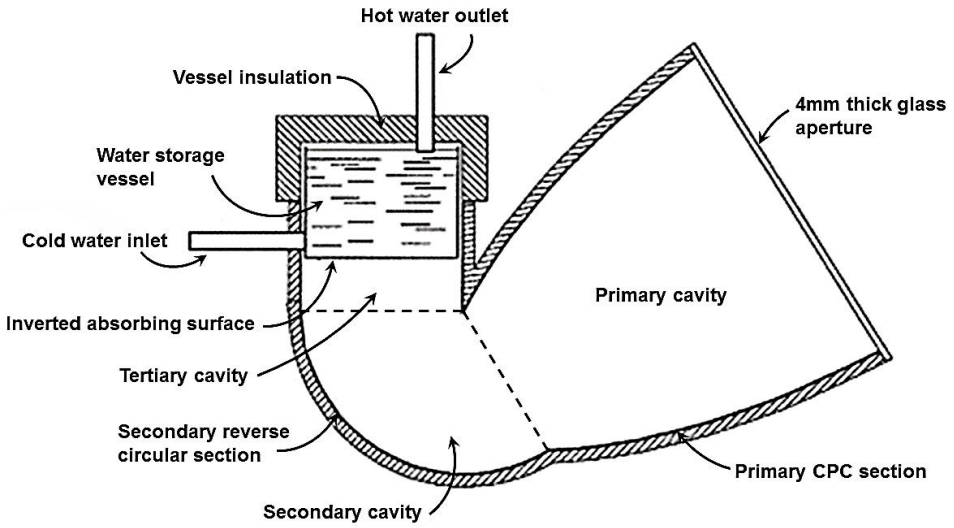


Fig. 2.3.2.6. Section view of inverted absorber ICSSWH [133]

2.3.2.4. CPC in Organic Rankine Cycle (ORC)

Antonelli et al. [134] proposed a small scale Organic Rankine Cycle (ORC) plant utilizing CPCs as heat source and a volumetric machine as an expansion device. The CPC collector is a traditional trough CPC reflector with a tubular absorber at bottom (Fig. 2.3.2.7 a)). The tubular absorbers are commercial U-pipe evacuated tubes as shown in Fig. 2.3.2.8 b). Results showed that the best performance of the solar collector part was to ensure at least 3000 operating hours per year. The energy production was maximized when concentration was between 1.1 and 1.4 and the tilt angle was smaller than 20-25 °. In addition, they also put forward that a proper choice of concentration ratio and tilt angle could reduce the initial investment cost of the components. Tiwari et al. [135] integrated a novel glazed reverse absorber conventional compound parabolic concentrator (GRACCPC) in a recuperated organic Rankin cycle which utilized low global warming potential and zero ozone depletion

potential working fluid mixture of cyclohexane/R245fa. The temperature at outlet of the test prototype could reach 398K at noon.

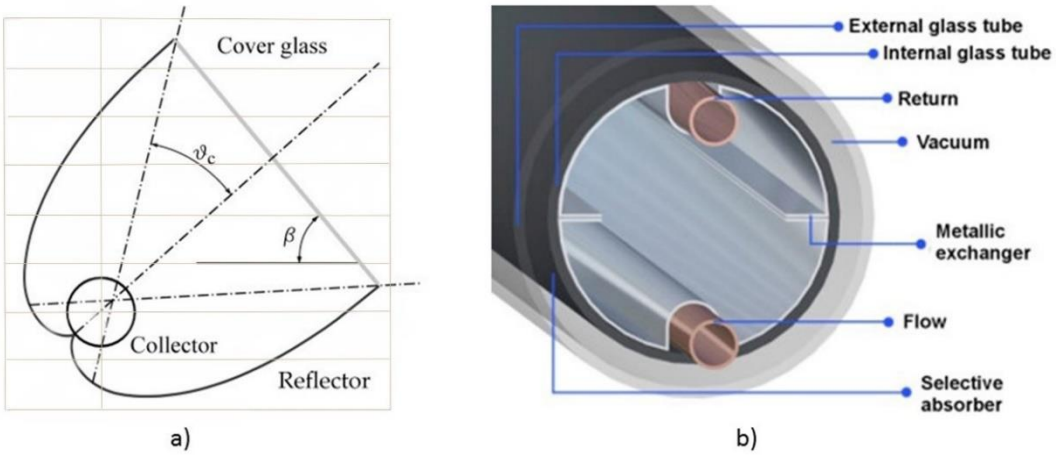


Fig. 2.3.2.7. a) Schematic of CPC collector b) Representation of an evacuated tube collector with U-pipe [134]

2.3.2.5. CPC in water steam generation and distillation system

The principle of CPC being used in water steam generation and distillation system is quite similar to that in solar thermal heating, which is concentrating light onto an absorber. Singh and Tiwari [136, 137] utilized a PVT-CPC active solar distillation system in their study of investigating the effect of water depth of distillation system. Nishi and Sema [138] tested a prototype of this kind of system with a 3D reflective CPC as concentrator, as shown in Fig. 2.3.2.9. It was found that the maximum exergy efficiency of this system could reach 12% when the flow rate was maximum. Elashmawy [139] investigated the performance of tubular solar still incorporating with CPC and manual tracking system in Hail city (27.5 ℃N, 41.7 ℃E), Saudi Arabia. Results showed that the new distillation system provided lower cost and its productivity was about six times higher than traditional tubular solar still.

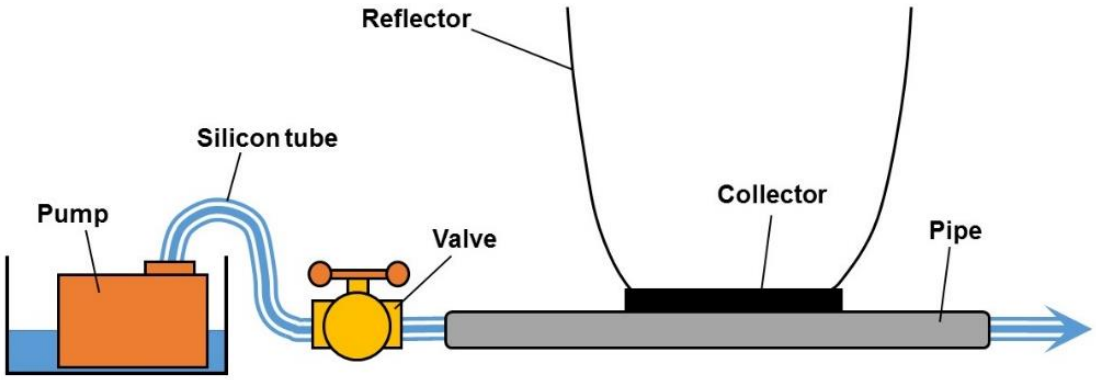


Fig. 2.3.2.9. Schematic diagram of water steam generation and distillation system with CPC3.2.3 CPC for soil heating with optical fibres [138]

2.3.2.6. CPC in soil heating

Noyes [140] referred to a special application of CPC which is heating soil. The working process is quite similar to the CPC concentrating daylighting into optical fibres. Because the sun is a low intensity source for soil heating, CPC is utilized to catch sky light and direct sunlight and integrated to optical fibres which can transmit solar radiation in long distance and still maintain high efficiency. Although heat loss will occur during transmission, the heat can be still radiated to the collecting surfaces in view of the relatively low temperature.

2.3.3. CPC in daylighting

The benefits of daylighting on visual comfort, human health and energy saving have been discussed for decades. With the rising of energy problems, daylighting becomes a significant part in new building design for the purpose of sustainability. CPC has been used for concentration application in the past, however its potential in daylighting was discovered in recent years. CPC can be mainly utilized in two different ways when it works with daylighting: the one is to control sunlight in different incident angle, as it is used on window and skylight; the other is to collect and guide more sunlight to interior, in the application of light pipe or funnel. In this section several researches investigated the possibility of CPC in daylighting application will be introduced.

2.3.3.1. CPC in daylighting control

Walze et al. [85] put forward two smart windows with the microstructure of 2D CPC array on surface. It can reduce the unneeded solar radiation by refraction or diffraction and improve the light-guiding abilities with the control of switchable coatings. For the

first type, the microstructure on surface is 2D CPCs with the period of 9.1μm and a switchable metallic-mirrored coating on base, as shown in Fig. 2.3.3.1 a). The replication of CPC array is manufactured by interference lithography in PMMA [85]. Solar radiation will be selectively transmitted according to its incident angle. This smart window can reduce the CPC in mirror state when the light is within the acceptance angle, and more light can be prevented by switch on the mirrored coating. Another smart window has same working principle but the reflective coatings are on one side wall of CPCs as shown in Fig. 2.3.3.1 b). It causes opposite effects on sunlight which is accepting the light with smaller incident angles and preventing those with larger incident angles.

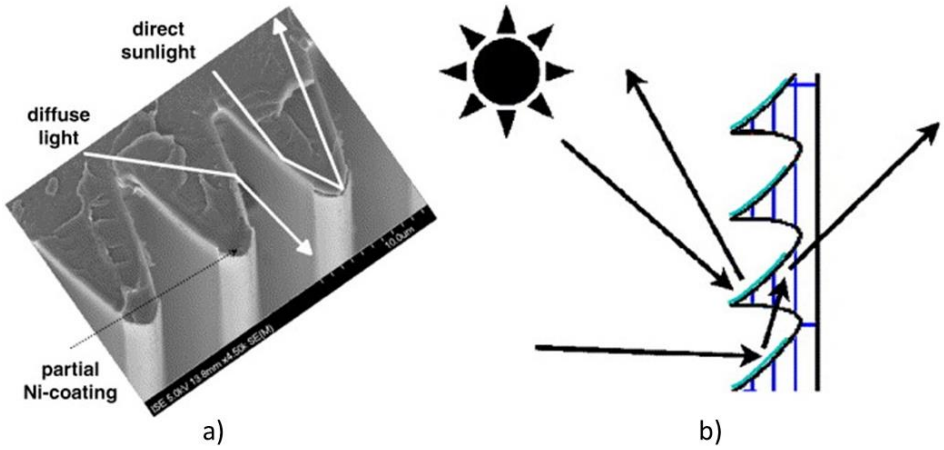


Fig. 2.3.3.1. Two types of smart windows with 2D CPC array a) Replication of CPC array generated by interference lithography in PMMA, with reflective coatings on base b) CPC array with reflective coatings on side wall [85]

In macro view, CPC controls sunlight in similar way. Yu et al. [15] explored the feasibility of 2D dielectric filled CPC (dCPC) in daylighting control when it is used as skylights for atrium. Results showed that when it was east-west orientated, the transmittance it provided would be lower at noon and larger in the morning and afternoon under sunny sky conditions in summer time, which is significant to control the indoor heat gain. In cloudy day, transmittance of it would stay at a relatively high level due to the diffuse skylight. They also tried to integrate the 2D dCPC with PV cells on base, and it achieved that generating electricity and control daylight at the same time. But the transmittance of the dCPC with PV was lower than the one without PV panel.

Another hybrid solar window focusing on solar thermal collection was introduced by Ulavi et al. [141, 142], which consists of 2D CPCs and a tubular absorber as shown in Fig. 2.3.3.2. The CPC is coated with a wavelength selective film for two functions: reflecting or concentrating the solar radiation in infrared portion onto absorber; transmitting the solar spectrum in visible portion into room. Single glazing and double glazing are attached with CPC to present the window glazing options. Simulations were considered when it was used as vertical window and horizontal skylights. Comparing with existing glazing technology in terms of visible transmittance, solar heat gain, U-factor and spectral selectivity, the hybrid solar window with double glazing had almost equivalent performance with low-e double glazing. According to the climate in Minneapolis, the annual thermal efficiency of double glazed type ranged from 21% to 26% when it was used for skylight and 15-24% for south or east facing windows with the adjustment of CPC geometries. In addition, this hybrid window could be switched to non-concentrating mode if the solar heat gain is too high.

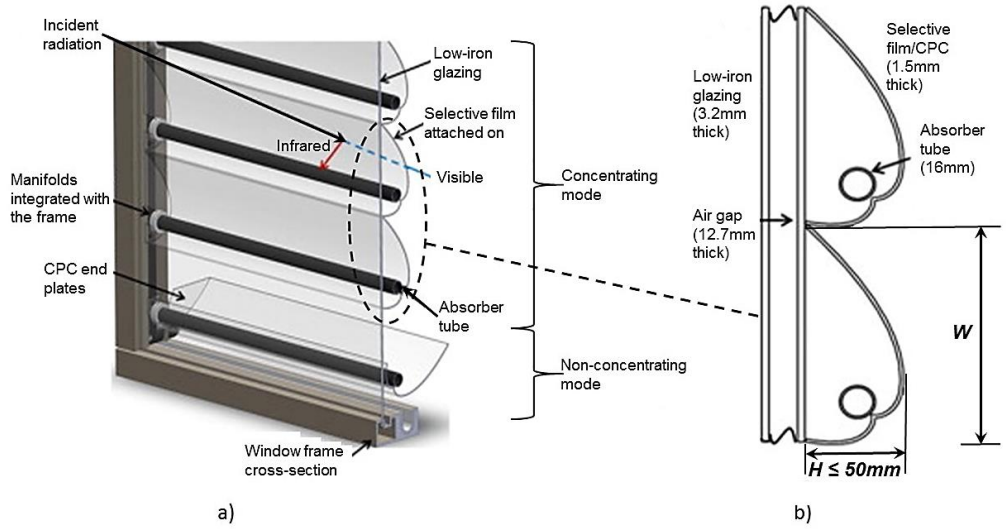


Fig. 2.3.3.2. Schematic diagram of hybrid solar window a) Design concept for hybrid solar window b) Typical cross-section view of hybrid solar window and dimensions [142]

2.3.3.2. PRIDE

The full name of PRIDE is 'Photovoltaic Facades of Reduced Costs Incorporating Devices with Optically Concentrating Elements', which is applied on building facade as double glazing and integrated photovoltaic system by concentrating technology. The first generation of PRDIEs was proposed by Zacharopoulos et al. [143]. Two designs (Fig. 2.3.3.3 a)) are introduced: the one consists of 2D symmetric CPC and an

extra silvered dielectric circular reflector; the other is 2D asymmetric CPC with two parabolas in different acceptances. CPCs are stationary and dielectric-filled. For both designs, the optical efficiencies were higher than 90%. Compared to the PV with flat covers, the solar radiation collected by asymmetric and symmetric CPCs were 2.3 and 2.7 times higher respectively under the weather data of Grete, Greece. However the asymmetric CPC maintains optical efficiencies more than 40% when the incident angles excessed the two-dimensional angular acceptance angle.

Mallick et al. [82, 144] tested a prototype of first generation PRIDE with the line-axis half acceptance angles of 0 °and 50 °(ACPPVC-50) by the outdoor experiment in Northern Ireland (54 °36′ N, 5 °37′ W). The CPC reflector was made by stainless steel with reflective coating and attached PV cells on base. Results illustrated that the maximum power ratio of ACPPVC-50 was 1.62 which was 62% higher than the PV panel without concentration. The average temperature of solar cell for ACPPVC-50 was 12℃ higher than that of PV panel, and it resulted in the lower efficiency of ACPPVC-50.

In view of the excellent power output of the first generation for PRIDE which incorporated 3 and 9mm wide single crystal silicon PV cells, Mallick and Eames [84] made an improvement of the first generation PRIDE concentrator with the selected 'Saturn' solar cells which was 6mm wide, as illustrated in Fig. 2.3.3.3 b). The line-axis half acceptance angles of this 2D asymmetric reflective CPC are 0 °and 37 °. The fabrication process of it was investigated in this research followed with cost analysis. Outdoor experiment demonstrated that the maximum power ratio was 2.01 comparing to the PV cell without concentration and electrical conversion efficiency of PV panel was 10.2%. The cost of manufacturing process could be reduced by 42% after improvements. Sarmah and Mallick [145] modeled the secondary generation of PRIDE to optimize the cell metallization and analyze the temperature effects on the whole system performance, as well as the non-uniformity effects. It was found that both high temperature and un-uniform flux distribution on cell result in decrease of solar cell output.

Based on the previous works, Baig et al. [87] put forward the third generation of PRIDE concentrating system which was dielectric filled and with reflective film along the edges, called DiACPC (Dielectric asymmetric compound parabolic concentrator),

as shown in Fig. 2.3.3.3 c). The line-axis half acceptance angles of this 2D asymmetric reflective CPC are 0 °and 55 °. The reflective film was designed to catch the escaping light from the corner of CPC in order to reduce the optical loss. Experiment results showed that there was 15.9% increase of average power output by comparing the DiACPC with and without reflective film while the temperature was keeping at 25℃, and the improvement of performance was 6% if the thermal effects was taken in to consideration. In addition, the reflective films changed the hotpots position and peak illumination intensity. The maximum power decreased by 0.5% in view of the thermal effects for the DiACPC with reflective film and it was smaller than the 0.94% drop for the DiACPC with reflective film.

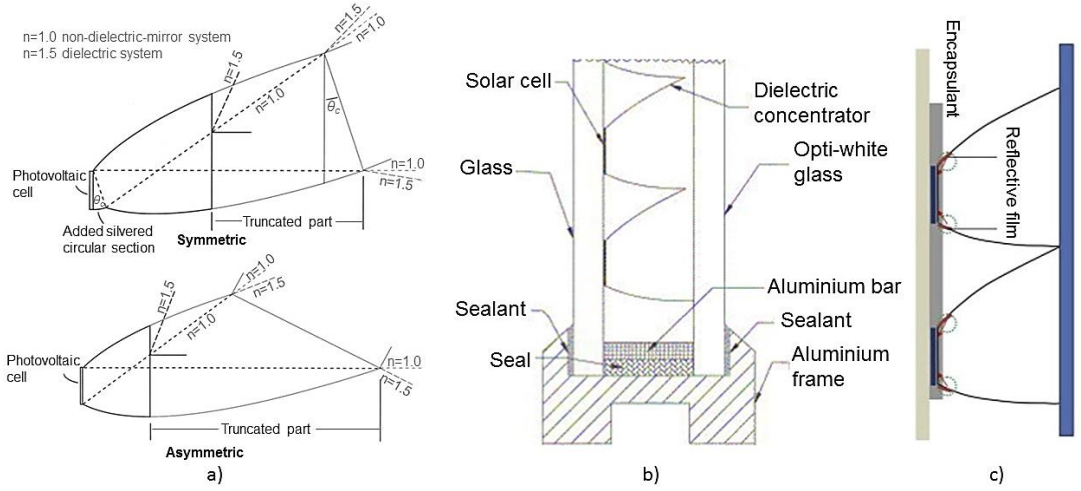


Fig. 2.3.3.3. Schematic diagram of PRIDE systems a) First generation with symmetric CPC and asymmetric CPC b) Second generation 3) Third generation with reflective film on edge [82, 84, 87, 143-145]

Sarmah et al. [90] investigated the performance of a 2D asymmetric dielectric-filled CPC with PV on base that is similar to the third generation PRIDE in northern latitudes (>55 °). The line-axis half acceptance angles of this DiACPC are 0 °and 55 °. The CPC with and without reflective film along the edge were compared. Similar to the previous researches, the DiACPC with reflecting film performed less optical loss, and its maximum power ratio reached 2.27 compared to the 1.97 of DiACPC without film. The electrical conversion efficiency was 9.43% in average within the range of acceptance angle. Based on the current market scenario, the DiACPC system could reduce up to 20% per unit power output comparing with the conventional PV module. Continuing to the previous research [90], Sarmah and Mallick [145] tested the

performance of the same DiACPC with reflective film along the edge in Edinburgh, UK under different weather conditions. Results showed that the maximum power output of DiACPC was 2.27 times higher, and the average short circuit current was 2.22 times higher than those of conventional flat PV panel on sunny interval day. On rainy day, the average diurnal power of DiACPC was 2.17 times higher than the flat PV panel. The excellent performance of DiACPC in different weather also corresponded to the indoor test results.

2.3.3.3. CPC in anidolic daylighting system and light pipe

Light funnel and light pipe are the new daylighting control strategies in recent years. CPC is also involved in the researches in these areas. Taengchum et al. [146] proposed a roof mounted light pipe with anidolic CPC to concentrate direct and diffuse sunshine into tubular light pipe. Due to the properties of CPC, it was found that CPC would reject the light with large incident angle which may not be suitable for collecting light as more as possible in light pipe application.

CPC is less optimistic as well in application of horizontal funnel. Wittkopf et al. [147] investigated the CPC feasibility when it was integrated with horizontal funnels for illuminating deep buildings. The innovative method called luminous intensity distribution curves (LIDC) derived from ray tracing was applied to compare the performance of different collectors shown in Fig. 2.3.3.4. New criteria such as 2D flux, percentage of 2D flux within a selected angle, horizontal offset angle and angular spread were proposed to quantify the optical performance of anabolic collectors based on LIDC. Type 4 and 5 are the CPC with an extra de-concentrator, and attach to two simple flat reference collector. However CPC collector is not optimal for the light funnels. The one with simple baffle and parabolic reflectors can capture more light owing to its larger entry aperture.

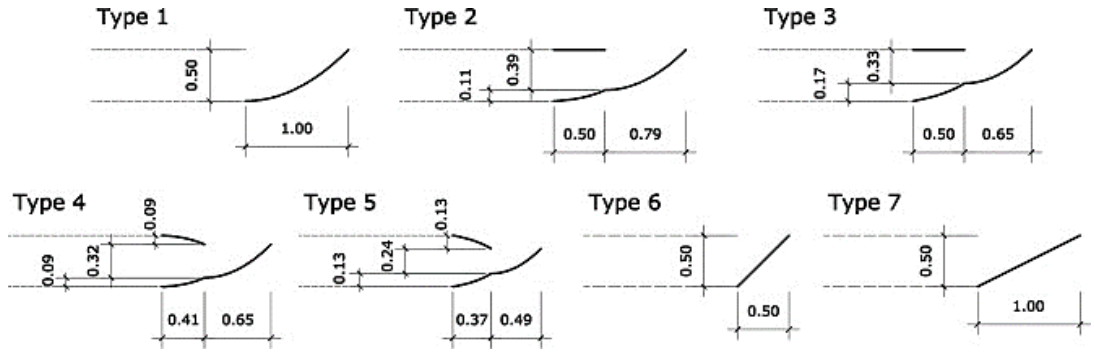


Fig. 2.3.3.4. Section of 5 anidolic collector systems (type 1-5) and two test collectors (type 6 and 7); abutting funnels are outlined in dashed lines (all sizes are in meter) [147]

2.3.3.4. CPC in optical fibre guiding system

Optical fibre has outstanding performance in transmitting light. Therefore CPC becomes an important component for light collection in application of optical fibre. Arashi et al. [83] tested a solar concentration system consisting of a parabolic dish concentrator, CPC and an optical fibre bundle. Because the collected solar radiation will reduce at the end of optical fibre, CPC was utilized to re-concentrate the light exiting from the end of optical fibre bundle, which improved the solar energy output by up to 3.5 times based on experiment.

On the contrary, CPC can also be used to concentrate light into optical fibre. Xue et al. [148] introduced a novel solar optical fibre tracking system consisting two CPCs as first and secondary concentrators and a cylindrical reflector in middle, as shown in Fig. 2.3.3.5. This system has the concentration ratio of 273 and can enhance the illuminance more than 10 times in view of several reflections and deflections in outdoor experiment; the transmittance ranges between 8% and 17.5% with the change of the length and diameter of optical fibre.

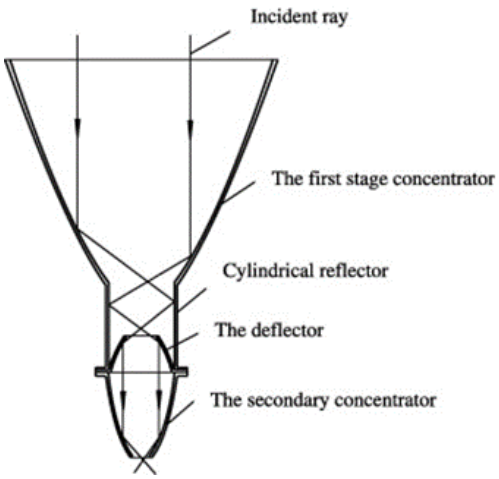


Fig. 2.3.3.5. Structure and optical path of the novel sunlight concentrator unit [148]

Two large-scale optical fibre daylighting system was put forward by Ullah and Shin [149] as shown in Fig. 2.3.3.6, the one uses parabolic trough and the other uses linear Fresnel lens to guide incident light to the trough CPC and then optical fibres for interior of multi-floor building. CPC is applied as a third concentrator to capture the concentrated light to light fibre. With cooperating with light-emitting diode (LED) light together, this system achieved better illumination quality and illuminance level than traditional lighting systems.

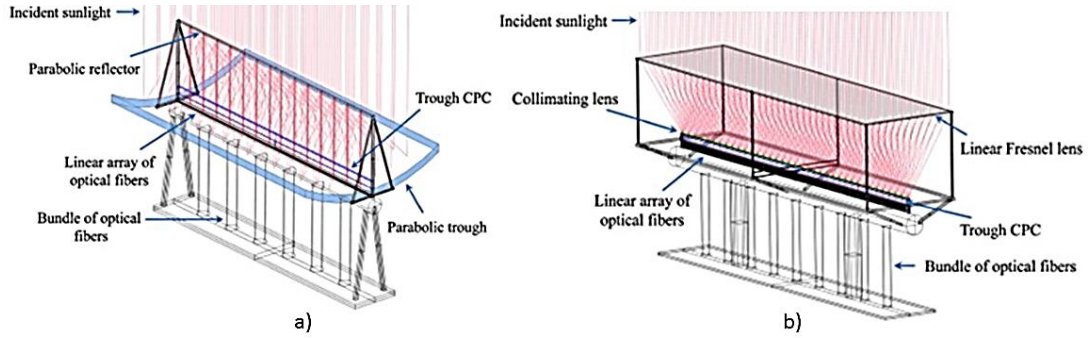


Fig. 2.3.3.6. Conceptual schematic diagram of the daylighting systems a) Parabolic trough type b) Linear Fresnel lens type [149]

2.3.4. CPC in photocatalytic water degradation and purification

Except the three main applications, PV, thermal and lighting, CPC also plays an important role as a reactor in photocatalytic water purification owing to its high commercial potential of simplicity, cost effectiveness, easy operation and low capital investment [150]. As the most advanced non-concentrator solar reactor, it has outstanding performance in photocatalytic degradation of refractory organic

compound and photocatalytic disinfection of water [151]. Fig. 2.3.4.1 demonstrates a typical CPC photocatalytic water purification system. The CPC has similar structure with solar thermal collection system which contains two parabolic curves and a tubular tube in middle. The reflective surfaces of CPC catch UV sunlight without tracking system, and provide a 360 ° illumination over the tubular reactor. The reflective surfaces are coated with Al and TiO2-SiO2 so that the usage efficiency of UV range of solar spectrum reached 95%. The water flowing through tubular reactor could reclaim 99% of TiO_2 from the slurry. Tanveer and Tezcanli Guyer [151] summarized five main design parameters of CPC that affect system performance, which are reflective surface, absorbing tube material, absorbing tube diameter, acceptance angle and radiation absorption; to make the degradation system work more effectively, photocatalytic type, catalyst loading, reaction pH, and light intensity are the important parameters of photocatalytic reactor should be considered.

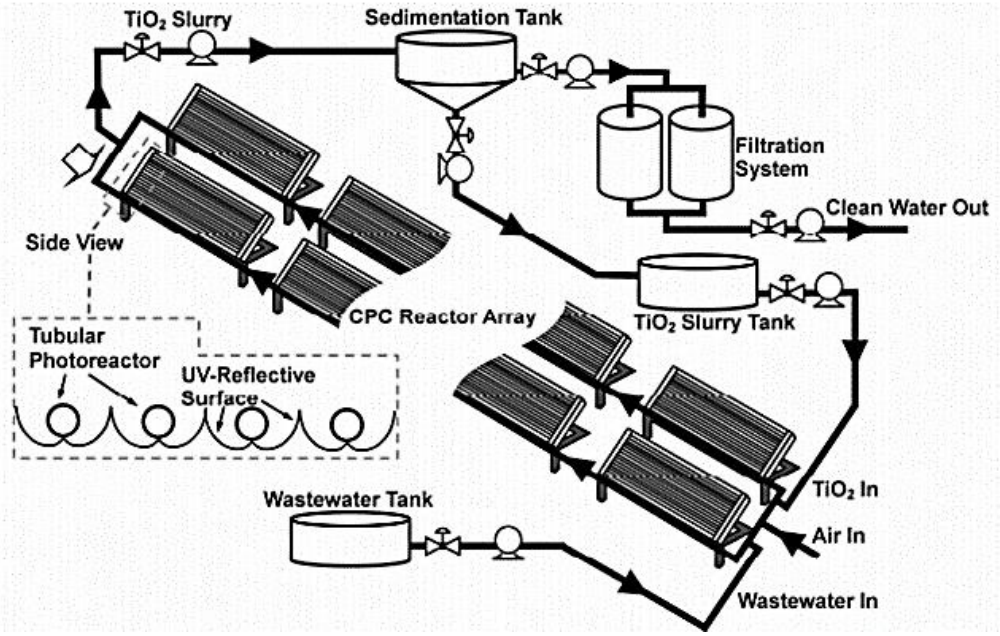


Fig. 2.3.4.1. Schematic diagram of a photocatalytic water purification system with CPC reactor [150]

2.4. Simulation tools

In this section, eleven simulation tools which are all useful in analyzing the systems with CPCs will be introduced. All of them were used by the CPC studies referred in Section 2.3. Table 2.4.1 provides a summary of them which labeled their key features and required operating platforms. Each one has specific characteristics that can satisfy

various requirements of different users. The software provide not only optical analysis of CPCs, but present thermal and electrical simulations if needed. In general, they can be divided into two types, one has graphical user interfaces between user and the software which benefits the users who have few knowledge of computer programming or of the mathematics and equations that govern building physics, such as LightTools, ZEMX, APEX, OptisWorks, Radiance and Photopia; the other is high-level language and interactive environment that requires specific code or module input for simulation, which is suitable for the users who are familiar with programming, mathematics, physics or require particular principles, equations or modules for simulation, like MATLAB, Energy Equation Solver (EES), COMSOL Multiphysics. In most software, Monte Carlo method, which provides numerical results by repeating random sampling, is a main technology in optical simulation. All of them are professional and widely used in either academic research or commercial development. In CPC simulations, users can select the most suitable one for themselves based on their requirements, such as operating system, interactive environment, results type, flexibility and simplicity, etc.

2.4.1. MATLAB

MATLAB (matrix laboratory) is a high-level language and interactive environment, which is for numerical computation, visualization and application development. It is widely used in various disciplines by researchers, practitioners and students, etc. all over the world [152]. For ray tracing simulation, new code can be written in MATLAB based on the law of reflection and refraction. Figure 2.4.1.1 demonstrates a flow chart of 3D ray tracing step code for reflective CCPC which is developed by Sellami and Mallick [105] specially. It is shown that when the incident rays reach a surface of CCPC, they will be determined either hit exit aperture without reflection or hit one of the side walls to be reflected. Then the following reflections are divided in three conditions, which are hitting exit aperture, exiting from entry aperture and reaching another side wall. All the incident rays are analyzed by repeating the steps until hitting the exit aperture or exiting the CCPC from entry aperture. The number and directions of incident rays are determined when a simulation is started. The number of rays concentrating on base, coordinates, number of reflections and drawing path of all incident rays will be demonstrated in the final results. Comparing with the experiment results, the deviation of $12 \pm 2\%$ to the simulation results by this ray tracing code was

obtained which proves the feasibility of writing 3D ray tracing code in MATLAB. Similarly, Taengchum et al. [146] coded the algorithms in MATLAB for tracing light rays from the sun and sources in the sky dome to the light pipe with anidolic CPC, the results of which match the experiment results well. On the other hand, MATLAB works very well in dealing with CPC geometry. Abu-bakar et.al [114] created the RACPC model by MATLAB. The geometry of RACPC is output in 3-D coordinate system when inputting the parameters of concentrator height, half-acceptance angle, length and width of PV cell, trial width of entrance aperture, refraction index of materials and number of extremes. Al-Ghasem et al. [119] utilized MATLAB to solve the optimization of the minimum CPC height within a range of required acceptance angle and a certain value of entrance aperture.

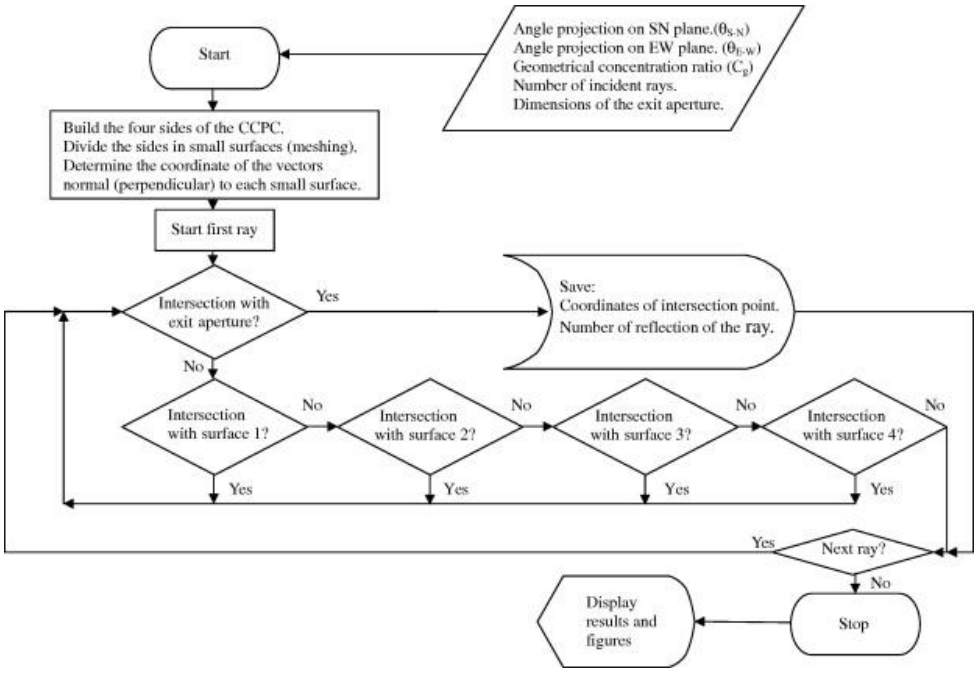


Figure 2.4.1.1 flow chart of 3D ray tracing steps code for CCPC in MATLAB [105]

2.4.2. Simulink

Simulink is an additional package of MATLAB which contains graphical multi-domain simulation and model-based design for dynamic and embedded systems. It is a block diagram environment. It can be applied to simulate the electricity generation of a CPV system [110], as well as the solar thermal collection regarding to different weather conditions [118].

2.4.3. LightTools

LightTools is a 3D optical engineering and design software that provides virtual prototyping, simulation, optimization and photorealistic renderings of illumination applications. It performs both rapid evaluation of optical behavior during design iterations with point-and-shoot ray tracing, and an accurate illumination analysis with rapid and robust Monte Carlo simulations [153]. It also provides accurate predictions of colorimetric performance. The LightTools functions can be incorporated into other COM-enabled applications like Microsoft Excel or MATLAB. It also works with CAD data and SOLIDWORKS models. Many studies [77, 110, 148] about different types of CPCs utilize LightTools to simulate the solar flux distribution. Studies [76, 149] link SOLIDWORKS models to LightTools to simulate the irradiance distribution on PV for lens-walled CPC and do the ray tracing analysis of a large-scale optical fiber daylighting system for a multi-floor building.

2.4.4. ZEMAX

ZEMAX is an optical and illumination design software that supports seamless transition between optical and illumination designs to create, model and optimize for prototyping, manufacturing and research [154]. It can be applied for both imaging and illumination system. ZEMAX can provide standard sequential ray tracing through optical elements, non-sequential ray tracing for analysis of stray light, as well as physical optics beam propagation. The tolerancing capability of it allows the analysis of the effect of manufacturing defects and assembly errors. In the research of RACPC by Abu-Bakar et al. [115], the deviations of optoelectronic gain between ZEMAX simulation and experiment results is around 11%. In the study of VFP reflector [113], the ZEMAX simulation results also perform good qualitative agreement with the analytical results. Owing to the versatile features, ZEMAX is also applied in the simulations of CPCs in some particular areas, such as diode pump [38], solar-pumped Nd:YAG laser [39] and THz technology [44].

2.4.5. APEX

APEX is an add-in to the industry-standard SolidWorks 3D-modeling environment and based on BRO's ASAP kernel technology, which operates in one environment through a true CAD interface [155]. It is designed to analyze optical and illumination system by an ease-of-use and easy-to-follow workflow. Fast and accurate optical

simulation via ASAP non-sequential ray tracing can be provided. In the research by Baig et al. [92], the optical performance of 3D dielectric CCPC to investigate the effects of reflective film and encapsulant interface on trapping escaping light by APEX.

2.4.6. TracePro

TracePro is an opto-mechanical software for designing and analyzing optical and illumination systems, which is known for its performance and accuracy [156]. It provides a comprehensive set of tools to view and analyze ray-tracing results such as irradiance maps, candela plots, and ray history tables, etc. It also provides a variety of commercially-available materials and coatings in database. The optical analysis are based on Monte Carlo simulations. TracePro can integrate with SOLIDWORKS and AutoCAD when creating models. Wang et al. [127] simulated the optical efficiency of a solar collector with CPC by TracePro.

2.4.7. COMSOL Multiphysics

COMSOL Multiphysics is a finite element analysis, solver and simulation software package for modelling and simulating coupled or multiphysics phenomena simultaneously [157]. It is an integrated user interface environment designed for cross disciplinary product development with a unified workflow for electrical, mechanical, fluid, and chemical applications. In addition, it allows for entering coupled systems of partial differential equations. It has different interfacings to numerous software, such as MATLAB, CAD, Inventor and Excel, etc. Baig et al. analysed the electricity output of a 2D dielectric filled asymmetric CPV system by finite element method in COMSOL Multiphysics [87, 91].

2.4.8. OptisWorks

OptisWorks is the only software to provide a complete light simulation solution based on a physical model inside a CAD/CAM software, which is for the scientific simulation of light and human vision within a Virtual Reality Environment by SPEOS technology [158]. Arnaoutakis et.al [88] applied Monte Carlo simulations for dCPC-UC-SC model by OptisWorks. It was also used to do the ray tracing for solar thermal collectors in the study [37, 123].

2.4.9. RADIANCE and The RADIANCE Photon map (Pmap) Extension

The RADIANCE rendering system is a versatile tool for lighting simulation and a physically based renders with available source code, which is a highly accurate ray-tracing software for UNIX computers [159]. The simulation utilize a light-backwards ray-tracing method with extensions to solve the rendering equation efficiently under most conditions [160]. The photon map is based on a (light) particle transport simulation. A Monte Carlo sampling method is applied to generate the reflected or transmitted directions of a photon if it survives [161]. The photon map algorithm consists of two steps, one is photon distribution and the other is photo gathering. The RADIANCE photon map is used to the computation of light source contributions for annual and climate-based daylight simulation. Su et al. [74] simulated the optical performance of lens-walled CPC in ray tracing, flux distribution and optical efficiency by Radiance/Pmap. The results are compared with the results by the commercial optical analysis software Photopia, and the average relative difference between them is within 5%.

2.4.10. Photopia

Photopia is a commercial photometric analysis program which is for producing comprehensive performance evaluations for non-imaging optical designs. The software provides virtual luminaires in a fraction of the time and for a fraction of the cost of physical prototypes. It includes a large selection of sun and sky dome models to analogue real sky conditions. In terms of material selection, numerous material data sorted by refractive, transmissive and refractive could be chosen in database. By the cooperation with CAD packages, the optical properties of designed dCPCs could be simulated. In simulation, Photopia use probabilistic method to obtain results [162]. For example, for each ray incident onto a transmissive material, a ray will be reflected or transmitted depending on the reflective and transmissive properties of the material at the particular incident angle. At the given angle, Photopia will probabilistically determines whether the ray should be reflected or transmitted by the material reflectance and transmittance values. For the model emanating rays, Photopia is also randomly distribute the emanation points into angular zones on the emanation sphere. Therefore, the simulated results may not be demonstrated in perfect and smooth curves. The source models provided in Photopia are based on the ISENA RP-21 daylight

equations which include variable luminance values across the hemisphere. In the research of anidolic ceiling produced by Wittkopf. S. K.[163], the difference between experimental values and simulated results from Photopia ranges from 1% to 2%, which shows the high accuracy of Photopia in optical efficiency simulation. Wittkopf et al. [147] did the ray tracing for horizontal light funnels with CPC by Photopia. In the studies by Yu and Su [15, 75, 94], the hourly solar energy collection for various CPCs are simulated by Photopia according to the hourly beam and diffuse solar irradiation values in EnergyPlus weather data.

2.4.11. ANSYS CFD, CFX

ANSYS CFD, CFX are high-performance computational fluid dynamics (CFD) software tools that enables product design and analysis in a virtual environment. It has revolutionized fluid dynamics by automating the solution even for problems that are numerically large[164]. The ANSYS CFX can analyze both optical and thermal performance of CPC. In the study by Li et al. [107], the optical and thermal behavior of CCPC is investigated by ANSYS CFX 15.0 where the sunlight is described by the Maxwell equation and refraction is followed by Snell's law. The reflection and refraction of sunlight in CFX is simulated by assuming the radiation is unplolarized and two-component subject to an equal intensity. ANSYS CFX, CFD can also be utilized to analyze the thermal performance like fluid flow and temperature distribution of CPCs especially for CPV [107] and CPC solar thermal systems [129]. The steady-state models are usually used in thermal simulation.

2.4.12. Engineering Equation Solver (EES)

Engineering Equation Solver (EES) is a commercial software package to solve thousands of coupled non-linear algebraic and differential equations numerically. The main feature of it is that it provides a high accuracy thermodynamic and transport property database that contains hundreds of substances [165]. It accepts user-written functions, procedures, modules and tabular data. The software supports numerous functions such as publication-quality plots, linear and nonlinear regression, consistency checking, and uncertainty analysis, etc. Bahaidarah et al. [68, 81] simulated the optical, thermal and electrical performance for 2D CPC-PV system with or without cooling pipes by different models in EES. For example, the Isotropic Model

is utilized for optical modelling. Eq. 2.4.12.1 below shows the absorbed radiation for CPC in the model.

$$S_{cpc} = G_{b,cpc}\tau_{cpc,b}(\tau\alpha)_b + G_{d,cpc}\tau_{cpc,d}(\tau\alpha)_d + G_{g,cpc}\tau_{cpc,g}(\tau\alpha)_g \quad \text{(Eq. 2.4.12.1)}$$

where $(\tau\alpha)$ is the transmittance-absorbance product of solar cell which is calculated separately for beam, diffuse and ground reflected radiation from Eq. 2.4.12.2.

$$\tau\alpha(\theta) = e^{-\left(\frac{KL}{\cos\theta_r}\right)}\left[1 - \frac{1}{2}\left(\frac{\sin^2(\theta_r - \theta)}{\sin^2(\theta_r + \theta)} + \frac{\tan^2(\theta_r - \theta)}{\tan^2(\theta_r + \theta)}\right)\right] \quad \text{(Eq. 2.4.12.2)}$$

where θ_r is the angle of refraction, *K* is the extinction coefficient and *L* is the thickness of glass.

The absorbed energy is further used to solve the energy balance equations on different no des of the system. Results show that the maximum difference of system power output between simulation and experiment results ranges from 5% to 11%.

2.4.13 Advanced modelling Environment for performing Simulation of engineering systems (AMESim)

The advanced modelling environment for performing simulation of engineering systems (AMESim) is a software based on an intuitive graphical interface to analyze multi-domain intelligent systems [166]. It is based on the Bond graph theory. Models are described by nonlinear time-dependent analytical equations that represent the behavior of systems. AMESim does not require a full 3D geometry representation of a system. Up to 40 libraries are offered by AMESim to solve various application problem such as Control, electric, and mechanics, etc. Antonelli [134] simulated the thermal performance, including thermal module power output and isentropic efficiency, of an organic ranking cycle that utilizing a CPC solar collector as heat source.

2.5. Observations and outlook

2.5.1. Summary and observations on CPC studies in literature

Table 2.5.1.1 summarizes and compares all CPC-focused studies referred in Section 2.3 and 2.4. Fig. 2.5.1.1 demonstrates the relationship between CPC types focused with respect to publication year of study. Although CPC has been proposed for decades, there are not many studies of it between 2000 and 2013. The investigation of

it began to increase in recent 3 years. It can be seen that the reflective CPC (both 2D and 3D) acted as the main type that was focused by researchers among all CPC types. However, from 2014, the dielectric filled CPC was paid attention to by researchers and it took a large proportion in 2015. Fig. 2.5.1.2 illustrates the CPC studies according to concentration ratio with respect to application area. The main area of CPC being utilized was PV as an attractive concentration facility without tracker. It was also popular in solar thermal and daylighting. As a low concentration optic, the concentration ratio of most CPCs in application ranged between 2× and 4×. Fig. 2.5.1.3 presents the countries that put forward CPC studies. CPC was proposed by Winston in USA, but most of the focused studies in recent years were done by UK which took 30%, and then China took 21%. USA and Japan occupied 6% and 5% respectively.

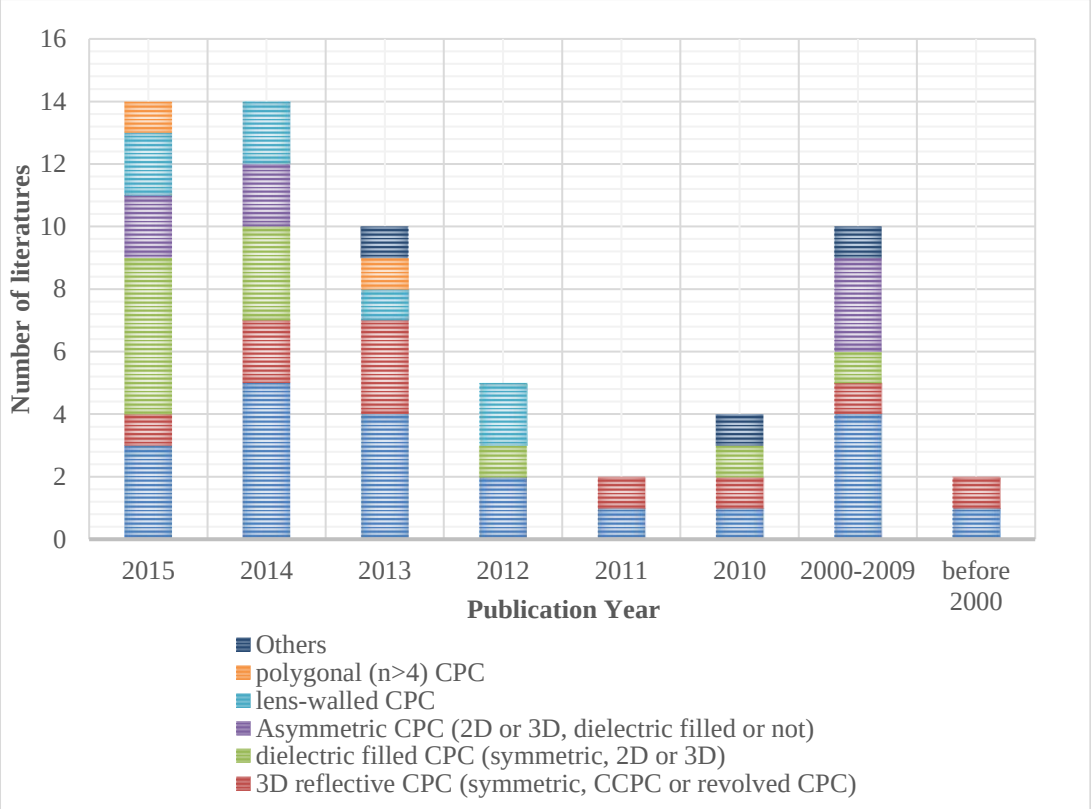


Fig. 2.5.1.1. CPC studies according to publication year and CPC type

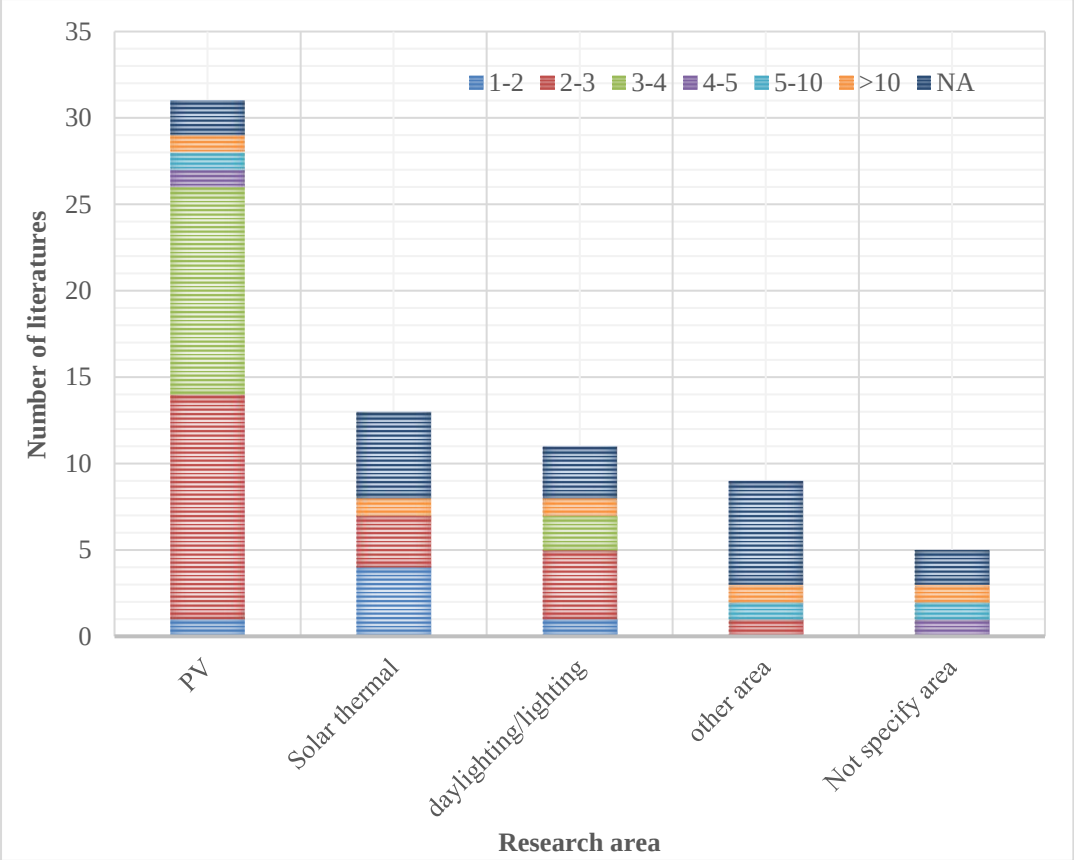


Fig. 2.5.1.2. CPC studies according to application area and concentration ratio

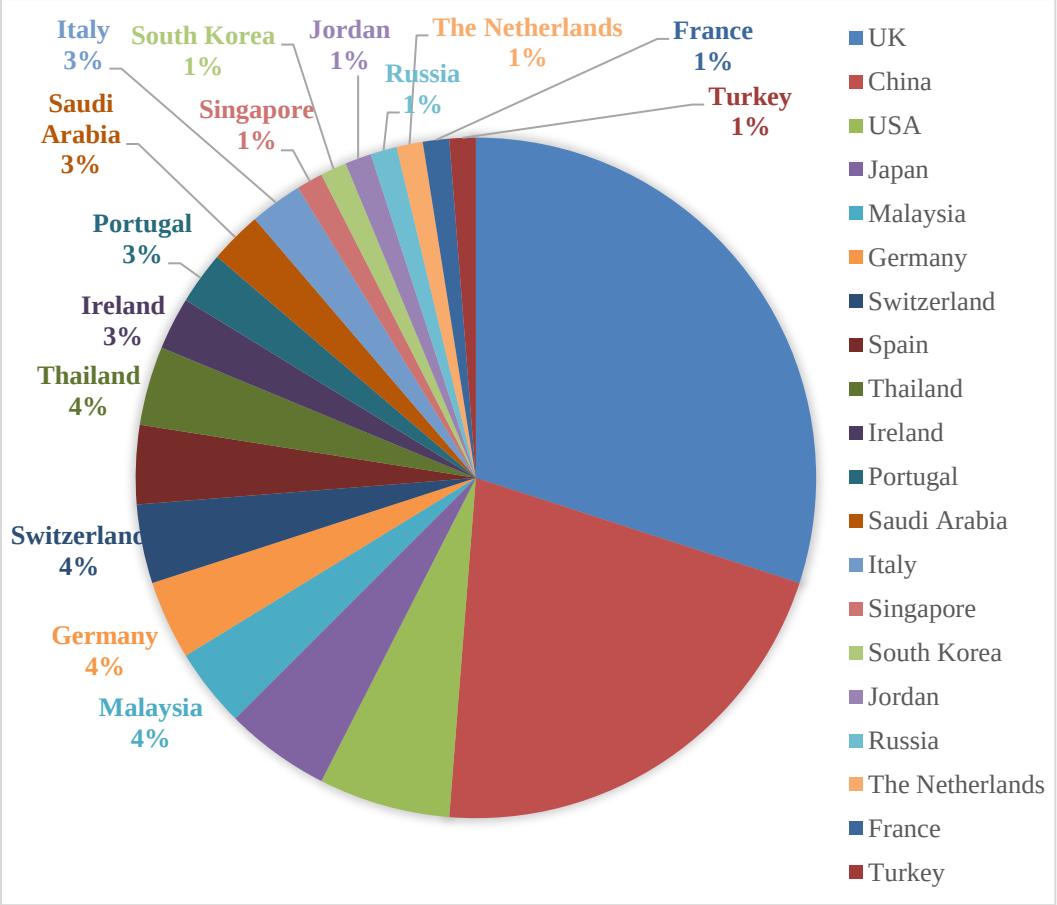


Fig. 2.5.1.3. CPC studies according to countries of research institutes

2.5.2. Prospects and outlook

Based on the literature review above, several recommendations can be put forward which may be improved in the future work on CPC.

1) CPCs geometry and edge effects

CPC can be designed in various shapes. However, the pros and cons of any new design should be considered first in practice. In terms of dielectric filled CPC, the weight of it is a disadvantage when it is applied as building facade and skylight. Truncation is one of the basic approaches to mitigate this. In addition, the lens-walled CPC can be proposed to solve this problem with maintaining the large acceptance angle.

Almost every research of CPC discussed the optical losses due to the light escaping from its edges, especially for dielectric filled CPC. In some PV applications, reflective films or partial coatings are utilized on the edges of CPC to weaken the edge effects [87, 92, 106-108]. The edge effects are also determined by the geometry of CPC. Several studies [105, 106, 114] demonstrate that comparing with polygonal CPC, the

revolved symmetric CPC leads to more losses on edge area which results in decrease of optical efficiency. However in some hybrid systems, the escaping light are applied for energy generation [128] or daylighting [15]. Hence, with the innovative design, the escaped light can be overcome or reused.

In addition, when CPC components are applied to build a CPC panel, the optical losses on connecting edges are significant. Comparing with revolved CPCs, some polygonal CPCs can be positioned next to each other without any extra junctions. In respect of manufacture, polygonal CPCs are easier and more economic to be fabricated under the current manufacture technology with the consideration of massive production.

2) Manufacture effects

Manufacture effect is an important factor that cause the deviations of experiment results [90]. It is based on the current fabrication technology. As discussed in Section 2, the excellent design, materials and manufacture process should be considered to improve its precision in massive production.

3) Tracking system

The requirements of tracking system should be considered when a CPC is designed. Generally CPC is non-tracking. But for some particular application in which CPC has higher concentration ratio, 2D CPC may need one-axis tracking and 3D CPC may need two-axis tracking. The accuracy, complexity, maintenance and lifetime of trackers need to be calculated. In addition, the cost on tracking system should be taken into account. For instance, a tracking system of a 2D trough CPC with flat absorber (for solar thermal collection) occupies about 39% of the total system cost, and percentage will decrease when the collector is utilized for certain application due to the costs on extra components [119]. With the advantages of large acceptance angle of CPCs, trackers are not suggested generally only if there is a good tradeoff between the energy collected and trackers.

4) Further improvements of irradiance distribution and temperature on CPC

Irradiance distribution and temperature are the two main factors to be taken into account when designing CPC for some typical applications. For example, when it is integrated with PV system, both of non-uniformity of flux distribution and high temperature result in reduction of electricity generation by PV, but for solar thermal

system, high temperature is always required. Improvements on CPCs are encouraged depending on different requirements. Some researchers use adding reflective film [87] or adjusting CPC shape [113] to improve the flux distribution. Many studies [68, 81] demonstrate that adding cooling on CPC-PV system (CPVT system) can increase its performance, and removed heat can also be utilized for other thermal applications.

5) Thermal performance and condensation problems of CPC

When CPC is utilized on building facade, its thermal performance should be taken into consideration. In the research by Mallick and Eames [84], CPC was attached single glazing and double glazing respectively to compare their general properties with common glazing in market, which provides a good example of whether it is practicable as building facade. Apart from thermal performance, the condensation is another problem that may affect the performance of the system with CPC, especially for PV. A glass cover is applied to overcome this problem in some researches [68, 81, 90].

6) Outdoor experiment

According to the summary of literatures, it can be seen that most of experiments were taken indoor by solar simulator. Indoor experiment is a fast and easy way to test CPC performance. However, outdoor experiments are recommended in view of different weather conditions. For some CPC applications, when it is influenced much by diffused sky light, the outdoor experiments may show different results with simulations and indoor test. For example, in a research [118] for solar thermal collector, the outdoor experiments presented that the different cloudy interval causes different performance of whole systems. Therefore, the outdoor experiment is important because it is difficult to analog real weather variations by solar simulator.

7) Deposition effects

Although there are few literatures that refer to the effects on CPC performance by dust and chemical deposition, this factor is still important to be considered in real application. Many studies [167-171] indicate the dust effects on the thermal and electric performance of PV. For example, Omer and Zala found 13.4% reduction of thermal efficiency and 4.57% reduction of electrical efficiency on PV when comparing the PV with and without dust on the front surfaces [167]. In general, the reduction of PV performance ranges from 2%-60% depending on the amount of deposition and local environment condition. In another study investigating the influences by dirt and

dust deposits on window indicates that the percentage loss in transmittance due to deposition is usually than 10%. As CPC is used as a window or cover to penetrate light, deposition effects is an important factor that is worth to be taken into account especially in practice for CPC.

2.6. Summary

A comprehensive review of the recent research progress on the compound parabolic concentrator (CPC) has been presented in this chapter. The concept and design principles of a CPC were introduced. The reviewed literatures mainly cover the period since 2000 and they have been classified according to the structures and applications. The simulation methods that suitable for CPC analysis were demonstrated. A couple of flow charts and tables have been used to give a holistic view of those literatures on CPC and make a clear summarization of those studies. Moreover, some thoughts and outlook have been put forward regarding the published work and future research on the CPC.

Table 2.4.1. Summary of the software used in CPC simulation

Software name	**Key features**	**Special features for CPC simulation**	**Operating platform**
MATLAB	-High-level language and interactive environment -For numerical computation, visualization and application development	-New codes are required to be written for ray tracing simulation -Optimize CPC geometry	Windows, Mac, Linux
Simulink	-An additional package of MATLAB -Block diagram environment for multidomain simulation and model based design	-Simulate electricity generation of CPV system -Simulate solar thermal collection of CPC system	Windows, Mac, Linux
LightTools	-3D optical engineering and design software -Supports virtual prototyping, simulation, optimization and photorealistic renderings of illumination application -Provide point-and-shoot ray tracing and Monte Carlo simulations -Incorporates with CAD, SOLIDWORKS and other COM-enabled applications, like Microsoft Excel or MATLAB	-Provides accurate predictions of colorimetric performance	Windows
ZEMAX	-An optical and illumination design software -Applied for both imaging and illumination system -Provides standard sequential ray tracing through optical elements, non-sequential ray tracing for analysis of stray light and physical optics beam propagation	-Its versatile features meet the requirements of CPC analysis under either normal or special conditions, such as simulate the optoelectronic gain of RACPC, the performance of diode pump with CPC, etc.	Windows

APEX	-An add-in of SOLIDWORKS for analyzing optical and illumination system -The core of APEX is time-proven ray tracing engine in BRO's ASAP	-Create, design and analyze in one program environment - Simulate optical and illumination system with an easy-to-follow workflow	Windows
TracePro	-A commercial, fast and accurate optical engineering software program -Incorporates with CAD products and the software using a Dynamic Data Exchange client/server interface -Has an add-in to SOLIDWORKS	- Provides Monte Carlo simulations for CPCs - Define custom properties or choose from database of commercially-available materials and coatings	Windows
COMSOL Multiphysics	-A finite element analysis, solver and simulation software package -Model and simulate coupled or multiphysics phenomena simultaneously -For cross disciplinary product development with a unified workflow	-Incorporates with various software like CAD and SOLIDWORKS -Simulate the electricity output of CPV system	Windows, Mac, Linux
OptisWorks	-The only software to provide a complete solution for optical simulation in CAD/CAM -Simulation is based on physical model and SPEOS technology -Simulations are for light and human vision within a Virtual Reality Environment	-Provides complete optical simulation solution in CAD/CAM -Provides Monte Carlo simulations for CPCs	Windows
Radiance and The RADIANCE Photon map (Pmap) Extension	-A versatile lighting simulation system -A physically based renders with available source code for UNIX computers -Use light-backwards ray-tracing method -Photon map is based on a light particle transport simulation by a Monte Carlo sampling method	-Can obtain not only accurate ray-tracing results, but photon map for analyzing the light source distributions in annual and climate-based daylight simulations	Windows, Mac, Linux

Photopia	-An fast and accurate photometric analysis program -For non-imaging optical designs -The results are obtained based on probabilistic method -The source model are based on the ISENA RP-21 daylight equations	-Provides a large selection of sun and sky dome models and numerous material data -Incorporates with Auto CAD and also available as an add-in for SOLIDWORKS	Windows
ANSYS CFX, CFD	-High-performance computational CFD tools -Designed for complete virtual prototypes of complex products and systems -Has revolutionized fluid dynamics by automating the solution	-Incorporates with other CAD tools -CFX can also be used to analyze the optical performance for CPC except thermal performance	Windows, Linux
Engineering Equation Solver (EES)	-A high accurate software to numerically solve thousands of coupled non-linear algebraic and differential equations -Provide a high accuracy thermal dynamic and transport property database -Accepts user-written functions, procedures, modules and tabular data	-Can deal with the optical, thermal and electrical performance for CPC and CPV systems -Specific models are required for typical simulations	Windows, Linux using Wine
Advanced modelling Environment for performing Simulation of engineering system (AMESim)	-A commercial simulation software for the modeling and analysis of multi-domain systems. -Models are described by nonlinear time-dependent analytical equations that represent the behavior of systems. -Doesn't require a full 3D geometry representation of system -Allow users focus on design and engineering issues rather than spending time in creating and validating models.	-Simulate thermal performance of CPC collectors.	Windows, UNIX, Linux

Table 2.5.1.1. Comparison of CPC studies covered in manuscript (NA: Not available; the test prototype without additional comments are indoor experiment)

Categories	Reference	Country	Publication year	CPC type	Extent of study	Research methodology /Software	Application area	Tracking	concentration ratio	Half acceptance angle
Design consideration	[66]	The Netherlands	2015	3D CPC, CCPC and hexagonal CPC made by 3D printing	Conceptual design/Test prototype	Test prototype	3D printing, multiple area	none	6, 15	NA
	[64]	USA	2010	2D reflective CPC, 2D and 3D dielectric filled CPC	Theoretical analysis	Design CPC geometry in direction cosine space on a polar plane	multiple area	none	NA	NA
	[94]	UK	2015	2D dielectric filled CPC	Theoretical analysis	PHOTOPIA	multiple area	none	4	22.02
	[67]	Switzerland	2013	3D CPC with Polygonal apertures	Theoretical analysis	Monte Carlo ray-tracing by in-house VeGaS code	multiple area	none	NA	NA
	[95]	USA	2017	2D and 3D CPC	Literature review	NA	Multiple area	NA	NA	NA
CPC in PV	[98]	Malaysia	2017	2D and 3D CPC	Literature review	NA	Multiple area	NA	NA	NA

	[99]	Greece	2017	2D reflective trough CPC	Conceptual design/test prototype (outdoor)	Ray-tracing simulation/ Test prototype	PV/T system	Two-axis tracking	14.2-113.4	NA
	[80]	China	2010	2D reflective trough CPC	Test prototype (outdoor)	test prototype	single-pass PV/T system	none	NA	30
	[68]	Saudi Arabia	2013	2D reflective trough CPC	Conceptual design	Engineering Equation Solver (EES) software	PV	one-axis	2.3	41.75
	[81]	Saudi Arabia	2014	2D reflective trough CPC	Conceptual design/test prototype (outdoor)	Engineering Equation Solver (EES) software	PV/T system	seasonal tilt adjustment	2.3	41.75
	[100]	Italy	2012	2D reflective CPC with prism	Conceptual design/Test prototype	ray tracing simulation	PV cell	none	5	24
	[74]	UK/China	2012	Lens-walled CPC with reflective coating outside	Conceptual design	Radiance/Pmap and PHOTOPIA	PV	none	4	The lens-forming angle is 3
	[75]	UK/China	2012	Lens-walled CPC with reflective coating outside	Conceptual design	PHOTOPIA	PV	none	2.5	The lens-forming angle is 3-5

	[76]	China/ UK	2013	Lens-walled CPC with reflective coating outside	Conceptual design/Test prototype	SolidWorks for model built, Light tools for ray tracing	PV	none	4	The lens-forming angle is 3
	[77]	China/ UK	2014	improved Lens-walled CPC with air gap	Conceptual design/Test prototype	LightTools	PV	none	4	The lens-forming angle is 3
	[78]	China/ UK	2014	Lens-walled CPC with air gap integrating with PV/T system	Conceptual design/Test prototype (outdoor)	LightTools	PV/T	none	2.4	The lens-forming angle is 5
	[13]	China/ UK	2015	Lens-walled CPC with air gap integrating with PV/T system	Conceptual design/Test prototype (outdoor)	Ray tracing simulation	PV/T	none	4	The lens-forming angle is 5
	[104]	China/ UK	2015	Lens-walled CPC with air gap integrating with PV/T system	Theoretical analysis/Test prototype (outdoor)	CFD/Test prototype	PV/T	none	4	The lens-forming angle is 5
	[105]	UK	2013	reflective CCPC	conceptual design/test prototype	Ray tracing by MATLAB	PV	none	3.6	30
	[107]	UK	2015	reflective, CCPC	conceptual design	multiphysics model and ANSYS CFX 15.0	PV	none	3.6	20

	[86]	UK/Spain	2014	dielectric filled CCPC	conceptual design/test prototype	OptisWorks	PV	none	3.6	48.5
	[92]	UK	2015	dielectric filled CCPC	conceptual design/test prototype	APEX	PV	none	3.6	48.5
	[108]	China/ UK	2012	2D dielectric filled trough CPC	Conceptual design/Test prototype	LightTools	PV	none	2.41	36.8
	[109]	Spain/ UK	2015	2D dielectric filled CPC	Conceptual design/Test prototype	Life cycle assessment	PV	none	2.8	55
	[111]	Malaysia	2017	CPC incorporates with dish concentrator	Literature review	NA	PV	NA	NA	NA
	[110]	Malaysia	2015	dielectric filled CCPC incorporates with dish concentrator	Conceptual design	LightTools for flux distribution, Simulink for electricity generation	PV	two-axis	6.0	24.1
	[88]	UK/Germany/ Switzerland	2015	dielectric filled, 3D revolved CPC	Conceptual design	Monte Carlo simulations by Optisworks	up-conversion solar cells	none	2.8	25 or 45

	[112]	Russia	1994	2D reflective CPC with convex lens	Conceptual design/Test prototype	ray tracing, didn't know software	PV cell (AlGaAs-GaAs heterostructure)	one-axis	21	NA
	[113]	Taiwan, China	2013	reflective, variable-focus-parabolic (VFP) reflector with circular and square focus spot	Conceptual design	Analytical model, skew-ray tracing by ZEMAX	PV	none	NA	NA
	[114]	UK/Malaysia	2014	reflective, rotationally asymmetrical CPC (RACPC)	Conceptual design	Matlab, ZEMAX	PV	none	3.7	42
	[115]	UK/Malaysia	2015	reflective, rotationally asymmetrical CPC (RACPC)	test prototype	test prototype	PV	none	3.7	42
CPC in solar thermal	[117]	Mexico	2017	2D Reflective CPC	Conceptual design/Test prototype (outdoor)	Numerical computation/ Test prototype	Solar thermal	none	1.8	15

or hybrid	[118]	USA	2009	2D reflective CPC with absorber	Conceptual design	Simulink, Matlab	solar thermal	none	NA	NA
	[119]	Jordan	2013	2D reflective trough CPC with flat absorber	Test prototype (outdoor)	MATLAB for optimizing the minimum CPC height	Solar thermal	one-axis	2.5	28
	[121]	Thailand/Germany	2014	2D reflective CPC with absorber	Conceptual design	Ray tracing simulation	solar thermal	none	NA	63.5, 40
	[122]	Thailand	2015	2D reflective CPC with absorber	Operational prototype (outdoor)	Operational prototype	solar thermal	none	NA	NA
	[120]	India	2017	2D reflective CPC integrated with U-shape ETC	Test prototype (outdoor)	Test prototype	solar thermal	none	NA	NA
	[123, 124]	UK	2014, 2015	2D reflective CPC with absorber	Conceptual design	Ray tracing by OptisWorks	solar thermal	none	NA	30, 40, 60
	[125]	China/UK	2012	2D reflective CPC with absorber	Test prototype	Test prototype	Solar thermal	none	NA	NA

	[126]	China/ UK	2017	2D reflective CPC with pulsating heat pipe	Test prototype (outdoor)	Test prototype	Solar thermal	none	3.4	NA
	[127]	China	2015	2D reflective CPC with absorber	Conceptual design/Test prototype (outdoor)	TracePro	Solar thermal	Two-axis tracking mechanism	2.3	23.5
	[128]	USA	2013	2D CPC with tubular, coupled with wavelength selective film	Conceptual design	Monte Carlo ray tracing	PV and solar thermal	none	1.2-2	45-87
	[129]	China	2011	2D reflective CPC with tubular, integrated with reflective Fresnel lens	Conceptual design	CFD	Solar thermal	none	25	NA
	[130]	India	2017	2D reflective CPC, integrated with Fresnel lens	Conceptual design/Test prototype (outdoor)	Advanced Systems Analysis Program	Solar thermal	none	58	NA

	[131]	Malaysia	2017	2D reflective CPC, integrated with Fresnel lens	Conceptual design	Numerical computation by MATLAB	Solar thermal	none	1.78	NA
	[132]	China	2017	2D CPC integrated with Fresnel lens	Conceptual design/Test prototype	Test prototype (outdoor)	Solar thermal	One-axis tracking	10	40.5
	[133]	UK/Ireland	2005	2D reflective CPC	Conceptual design/Test prototype	Test prototype	Solar thermal water heaters	none	1.84	30
	[134]	Italy	2015	2D reflective CPC with absorber	Conceptual design	AMESim	Solar thermal	none	1.1-1.4	NA
	[135]	India	2017	2D reflective CPC with absorber	Conceptual design	Numerical computation by MATLAB	Solar thermal	none	NA	NA
	[136, 137]	India	2017	2D reflective trough CPC	Conceptual design	Numerical computation by MATLAB	Solar distillation	none	NA	NA
	[138]	Japan	2013	3D reflective CPC	Conceptual design/Test prototype (outdoor)	ray tracing, didn't know software	water steam generating	none	NA	30

	[139]	Saudi Arabia/ Egypt	2017	2D reflective trough CPC	Test prototype (outdoor)	Test prototype	Solar distillation	Manually one-axis tracking	NA	NA
CPC in daylighting or hybrid	[85]	Germany	2005	Microstructure 2D trough CPC with facet-selective coating	Conceptual design/Test prototype (outdoor)	test prototype	microstructure, daylighting control	none	NA	NA
	[15]	UK/China	2014	2D dielectric filled CPC	Conceptual design/Test prototype (outdoor)	PHOTOPIA	PV /daylighting control	none	3.6	22.05
	[141, 142]	USA	2014	2D dielectric CPC with tubular absorber	Conceptual design	Monte Carlo ray tracing	Tubular absorber and daylighting	none	1.5-2.3	25-45
	[143]	UK	2000	2D dielectric filled symmetric CPC and asymmetric CPC	Conceptual design	Ray tracing based on the criterion of total internal reflection	PV/building facade	none	2.46, 2.96	37, 36.4
	[82, 144]	UK/Ireland	2006	2D reflective asymmetric CPC	Test prototype (outdoor)	test prototype	PV cell/building facade	none	2.0	50 and 0

	[84]	UK	2007	2D reflective asymmetric CPC	Test prototype (outdoor)	test prototype	PV cell/building facade	none	2.45	37 and 0
	[145]	UK	2015	2D dielectric filled asymmetric CPC	Test prototype (outdoor)	test prototype, outdoor experiment	PV cell/building facade	none	2.8	0 and 55
	[87]	UK/Spain	2014	2D dielectric filled trough CPC	Conceptual design/test prototype	COMSOL Multiphysics software	PV cell/building facade	none	2.8	55
	[90]	UK	2014	2D dielectric filled asymmetric CPC	Conceptual design/Test prototype	Ray tracing, indoor experiment	PV cell/building facade	none	2.8	0 and 55
	[146]	Thailand	2014	3D reflective CPC	Conceptual design/Test prototype (outdoor)	Matlab	roof mounted light pipe	none	2.42	40
	[147]	Singapore/Switzerland	2010	3D reflective CPC	Conceptual design	Ray tracing by PHOTOPIA	anidolic daylighting system	none	NA	NA
	[83]	Japan	1997	3D reflective CPC	Conceptual design/Test prototype (outdoor)	NA	concentrate light exiting from optical fibre	Two-axis	3.6-4.4	26

	[148]	China/ UK	2011	3D reflective CPC	Conceptual design/Test prototype (outdoor)	Ray tracing by LightTools	solar optical fibre system	two-axis tracking	278	3.4
	[149]	South Korea	2014	2D reflective trough CPC	Conceptual design	LightTools and SolidWorks, DIALux for interior lighting	optical fibre daylighting system	none	NA	NA
CPC in other areas	[151]	Turkey	2013	2D reflective trough CPC	Literature review	NA	Water degradation	none	NA	NA
	[44]	Japan	2013	3D CPC with an extra cavity	Conceptual design/ Test prototype	ZEMAX	Terahertz technology	none	100	5.5
	[45]	USA	2014	3D reflective CPC	Conceptual design/Test prototype	ray tracing, didn't know software	Overmoded waveguide	none	6.3 or 64	NA
	[37]	Japan	2002	3D reflective CPC	Conceptual design/Test prototype	OptiCAD	p-i-n photodiode	none	NA	Maximum emitting angle from GI-POF is 15.6
	[38]	Portugal	2007	2D reflective CPC with elliptical cavity or CPC cavity	Conceptual design	ZEMAX	Diode pumping	none	NA	56

	[39]	Portugal/France	2007	2D reflective CPC as pump cavity	Conceptual design	ZEMAX	solar-pumped laser	none	NA	NA
	[41]	China	2010	3D dielectric CCPC	Conceptual design/Test prototype	ray tracing simulation	LED projector	none	2.25	12
	[40]	HongKong	2007	3D dielectric CCPC	Conceptual design/Test prototype	ray tracing simulation	LED projector	none	NA	NA

Chapter 3

Fundamental research of the property for three-dimensional dielectric crossed compound parabolic concentrator (3D dCCPC)

3.1. Introduction

3.1.1. Summary of a previous work on 2D dCPC

This chapter continues the dCPC study put forward by Yu et al. [15] in which the daylighting control performance between two dCPC rods and two common prismatic elements were discussed. The structures of them are shown in Figure 3.1.1.1 below. The dCPC with two parabolic surfaces and symmetrically to its mid plane is named as two-dimensional dCPC (2D dCPC). All of them are made of acrylic with refraction index 1.5. The length of dCPCs rod are 96mm, and the two parabolic surfaces are symmetrically located about the mid-plane of a collector along the long edge. One of the dCPC rod is without coating on its bottom surface, which is considered for daylight application only. This dCPC is represented by non-coated dCPC. The base of another dCPC rod referred as base-coated dCPC is affixed with non-reflective material. Besides of dCPC, the section view of other two prismatic elements are equilateral triangle and isosceles right triangle. The lengths of this two elements are the same as dCPC which is 96mm.

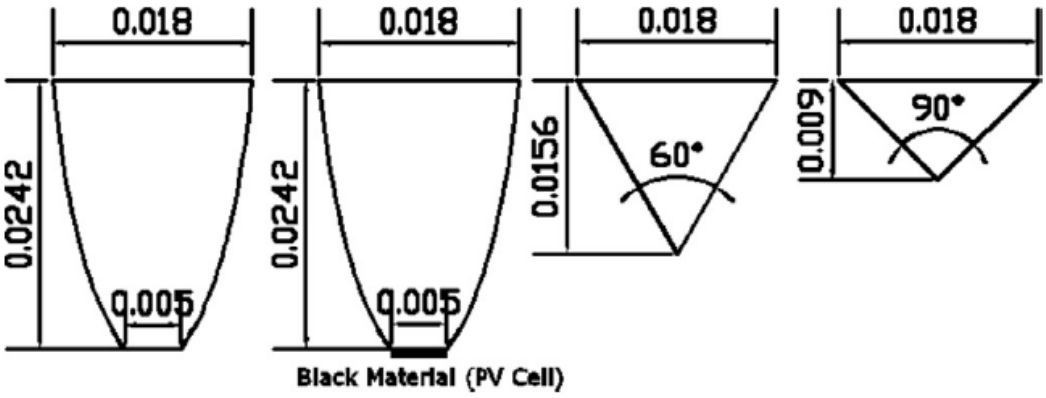


Figure 3.1.1.1. Schematic diagram of dCPC structure in previous research [15]

Because the outer half acceptance angle of dCPC is about 22.05 °, the simulation was processed when dCPC is tilted to 37 °and facing to south. According to the sun path in whole year, four specific day, which are spring equinox, summer solstice, autumn equinox and winter solstice are chosen to obtain the change of transmittance and transmitted daylight illuminance in each day. Nottingham, UK (53 °N, 1.2 °W) is selected as the simulation location. The results demonstrate the dCPC rod preforms adequate control of sunlight in daytime under sunny sky conditions in four specific day, especially in summer solstice, spring equinox and autumn equinox compared to

the two prism rods. This presents the great potential of daylight control of dCPC. However, the transmitted illuminance is expected to be higher in the morning and afternoon, and under overcast sky condition to guarantee the indoor illuminance level.

3.1.2. Introduction of Photopia

Photopia is a fast and accurate photometric analysis program which is for producing comprehensive performance evaluations for non-imaging optical designs. It provides a large selection of sun and sky dome models to analogue real sky conditions. In terms of material selection, numerous material data sorted by refractive, transmissive and refractive could be chosen in database. By the cooperation with AutoCAD software, the optical properties of designed dCPCs could be simulated. In simulation, Photopia use probabilistic method to obtain results [162]. For example, for each ray incident onto a transmissive material, a ray will be reflected or transmitted depending on the reflective and transmissive properties of the material at the particular incident angle. At the given angle, Photopia will probabilistically determines whether the ray should be reflected or transmitted by the material reflectance and transmittance values. For the model emanating rays, Photopia is also randomly distribute the emanation points into angular zones on the emanation sphere. Therefore, the simulated results may not be demonstrated in perfect and smooth curves. The source models provided in Photopia are based on the ISENA RP-21 daylight equations which include variable luminance values across the hemisphere. In the research produced by Wittkopf. S. K. [163], the difference between experimental values and simulated results from Photopia ranges from 1% to 2%, which shows the high accuracy of Photopia in optical efficiency simulation.

The dCPC used for simulation is made of acrylic. In material input data of Photopia, refraction index of outside material (air), refraction index of inside material (acrylic) and extinction coefficient are required. As it is known that the refraction index for air is 1.0 and 1.5 for standard acrylic. The extinction coefficient is a measurement of the extent by which the intensity of a beam of any transmitted light is reduced by passing through a distance x. It is defined from Bouguer's Law [172] as follows:

$$I = I_0 e^{-\sigma x} \qquad (Eq.\,3.1.2.1)$$

Where I is illuminance (luminous flux density) at a selected point in space

I_0 is source illuminance

x is the distance of point from source

σ is the extinction coefficient

Therefore $\frac{I}{I_0}$ is the transmissivity of the dCPC. For the acrylic-air interface boundaries, the Fresnel loss is expressed as [15]:

$$R = 100 \times \left(\frac{n_1 - n_2}{n_1 + n_2}\right)^2 \qquad \text{(Eq. 3.1.2.2)}$$

Where n_1 and n_2 are the refraction indexes for each medium respectively. Therefore, the Fresnel loss for acrylic-air interface is 4%. Therefore, the extinction coefficient of acrylic used on dCPC is 0.0641 $inch^{-1}$ [15].

3.1.3. Improvement of dCPC in current research and objectives

This chapter is a further research of two dimensional dielectric compound parabolic concentrator (2D dCPC). The objective is to improve the structure of dCPC to provide better control on daylight.

DCPC controls the light mainly by its curved surface. 2D dCPC performs huge differences on transmittance in summer solstice, spring equinox (autumn equinox) and winter solstice. This is caused by the different solar zenith angle at noon. However, it does not provide strong control in one day because there is no curved surfaces in east-west direction. In addition, coating the base of dCPC is difficult and costly on manufacturing, especially integrating with photovoltaics. An improvement on structure of 2D non-dCPC is expected to achieve better control of sunlight economically. Therefore, a three-dimensional dielectric crossed CPC (3D dCCPC) is proposed. It has polygonal apertures with 4 sides. The four curved surfaces whose dimensions are same as 2D dCPC on east-west and north-south direction, which can not only controls the sunlight from south, also acts on the east-west sunlight. The entry aperture of one 3D dCCPC element is a 0.018m*0.018m square, and the 2D dCPC rod could be assumed as a composition of small 2D dCPC elements as well. In order to do the ray-tracing simulation, an element with right square pyramid structure whose entry aperture is 0.018m*0.018m square is compared together. The dimensions of them are shown in Figure 3.1.3.1 below.

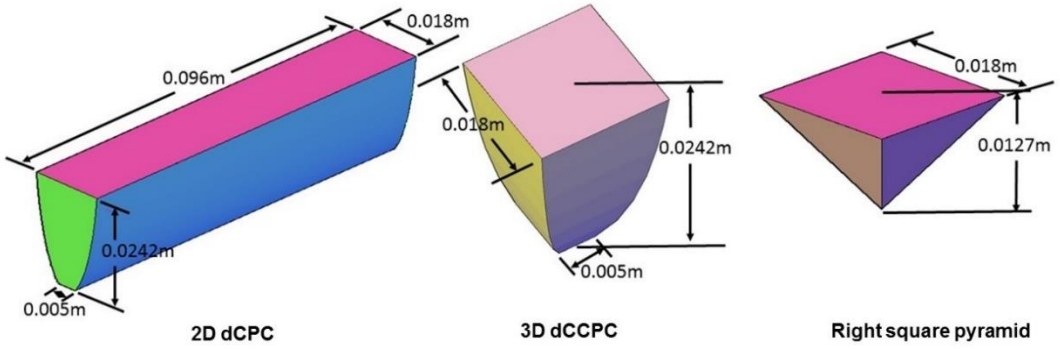


Figure 3.1.3.1. Dimension of 3D dCPC and right square pyramid structure

The discussion about the performances on controlling sunlight will be put forward in the following sections among 5 types of dCPC, which are 2D base-coated dCPC, 2D non-coated dCPC, 3D base-coated dCCPC, 3D non-coated dCCPC and right square pyramid structure element. Similar to 2D dCPC, the difference between 3D base-coated and non-coated dCCPC is whether the non-reflective material is affixed on the base. The ray tracing simulation will be put forward by Photopia first to investigate the influence of transmittance by different incident angle. With the purpose of verifying the optical properties of different structures, the incident light beam is parallel to the mid-plane of each elements. Then the performance of daylight control between 2D dCPC and 3D dCCPC will be explored under real sky conditions. The installation position of dCPC element is shown in Figure 3.1.3.2. It is oriented in an east-west direction and tilted towards the south at a tilt angle from the horizontal plane. During the whole year, the sun moves between Northern Tropic and Southern Tropic. Because the sun path are almost same in spring equinox and autumn equinox, this research will focus on three specific days, which are summer solstice, spring equinox and winter equinox. With adjusting sun position and applying different sky dome model in Photopia, the real sky condition could be imitated. The output data demonstrate the optical properties of dCPC for every 30mininutes at daytime. Two sky conditions, which are sunny sky and overcast sky, are applied to investigate the optical performances of dCPC under different sky conditions. The effect of tilt angle and tolerance of horizontal rotation angle is investigated as well.

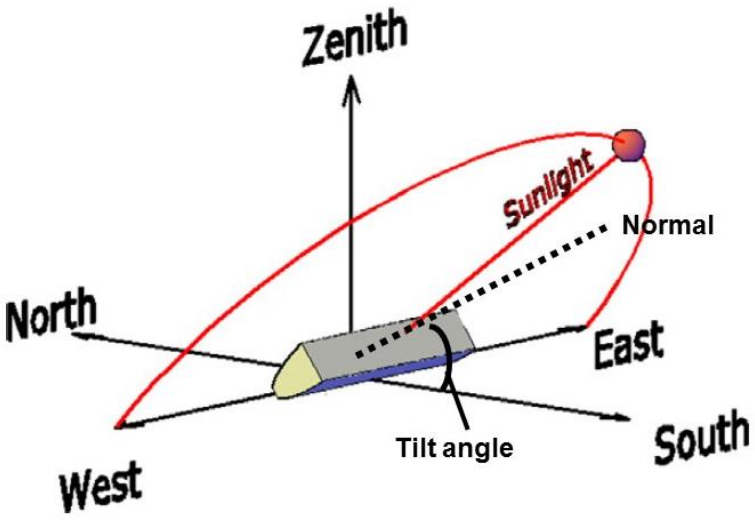


Figure 3.1.3.2. Installation position of dCPC under real sky

Another 3D compound parabolic concentrator is cylindrical symmetry whose reflecting surface is obtained by rotating the parabola about the concentrator axis (not about the axis of the parabola) shown in Figure 3.1.3.3. It is named as 3D r-dCPC. The input and output apertures of this dCPC are circular. A research put forward by Cooper et al. [14] demonstrates that the performance of this revolved CPC is slightly better than polygonal CPCs and revolved CPCs performs more uniform flux distribution. In order to distinguish it from the 3D dCCPC with four parabolic surfaces, it is named as 3D r-dCPC. The parabolas applied on the 2D dCPC, 3D r-dCPC and 3D dCCPC are the same. Comparing with 3D dCCPC, 3D r-dCPC does not concern the effects of horizontal angular deviations due to installation. The optical properties of 3D dCCPC will be explored under different sky conditions and compared with 3D r-dCPC.

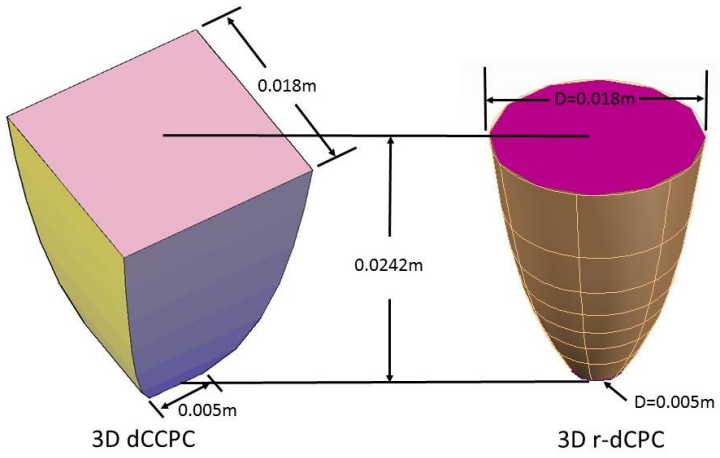


Figure 3.1.3.3. Structure of 3D revolved dCPC (3D r-dCPC)

For the purpose of investigating optical properties of dCPCs, transmitted daylight illuminance is another important aspect that illustrates the performance on daylight control of dCPCs intuitively. If the uneven distribution of light is ignored, it can be calculated by Eq. 3.1.3.1 below:

$$E = E_0 \cdot T \qquad \text{(Eq. 3.1.3.1)}$$

Where E is transmitted daylight illuminance

E_0 is the received illuminance on the surface of entry aperture

T is the transmittance of dCPC

The methodology of research in this report is summarized in Figure 3.1.3.4 below in flow chart.

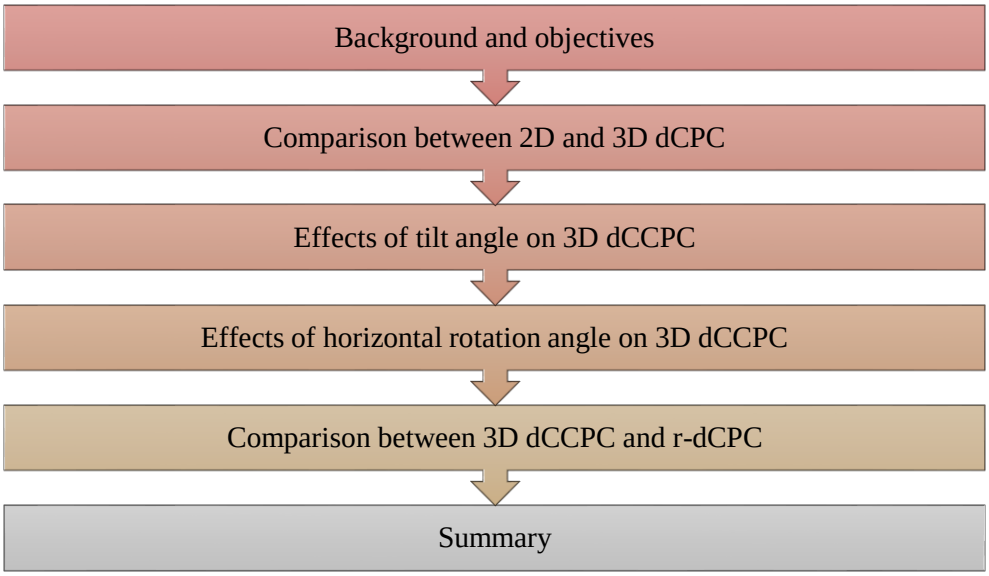


Figure 3.1.3.4. Flow chart of methodology

3.2. Comparison of 2D and 3D dCPCs

3.2.1. Relationship between incident angle and transmittance of different CPC structures

The effects of incident angle on transmittance will be firstly investigated for five different structures, which are 2D base-coated dCPC, 2D non-coated dCPC, 3D base-coated dCCPC, 3D non-coated dCCPC and right square pyramid. A light beam is shot on to the receiving surfaces, which are the top surfaces, of dCPCs in different angles from 0 °to 90 °. The light path and geometries of CPCs are shown in Figure 3.2.1.1.

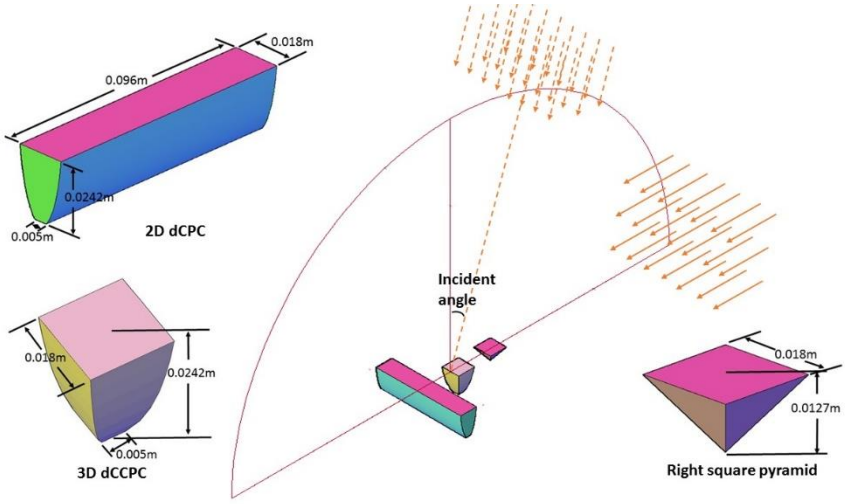


Figure 3.2.1.1. Schematic diagram of five different dCPC structures and incident angle

With the results simulated by PHOTOPIA shown in Figure 3.2.1.2, it can be observed that 3D dCCPC performs the similar optical properties comparing with 2D dCPC for base-coated type. For non-coated type, 3D dCCPC has better ability on controlling incident light, whose transmittance, ranging from 0.1 to 0.2, is smaller than the transmittance of 2D dCPC when incident angle is within 0 °- 35 °; when the incident angle increases from 35 ° to 90 °, the transmittances of CPCs are almost same. The structure of right square pyramid does not show good performance on controlling light with the change of incident angle. Therefore, only 2D and 3D dCPCs will be discussed in the following sections to explore their control ability of light further.

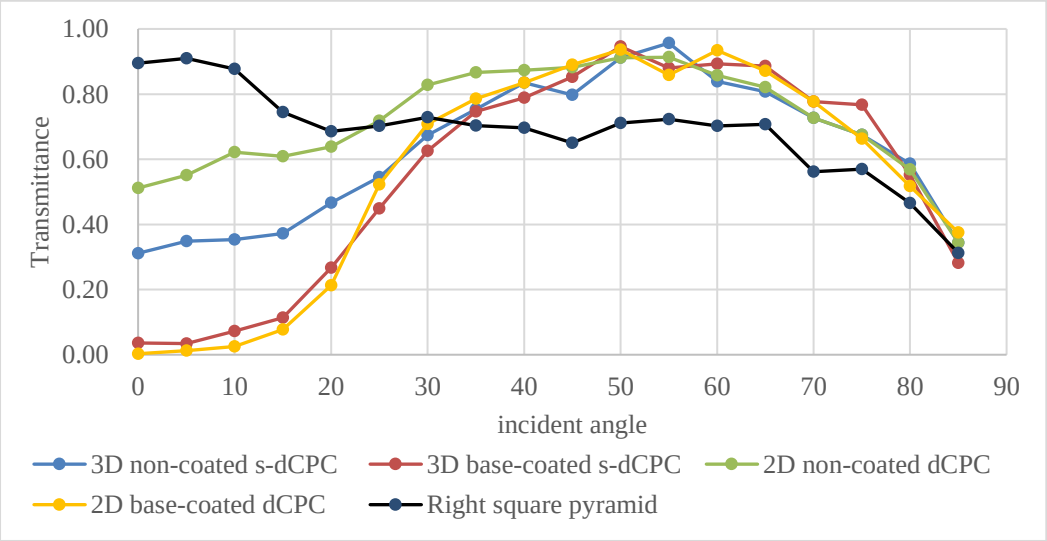
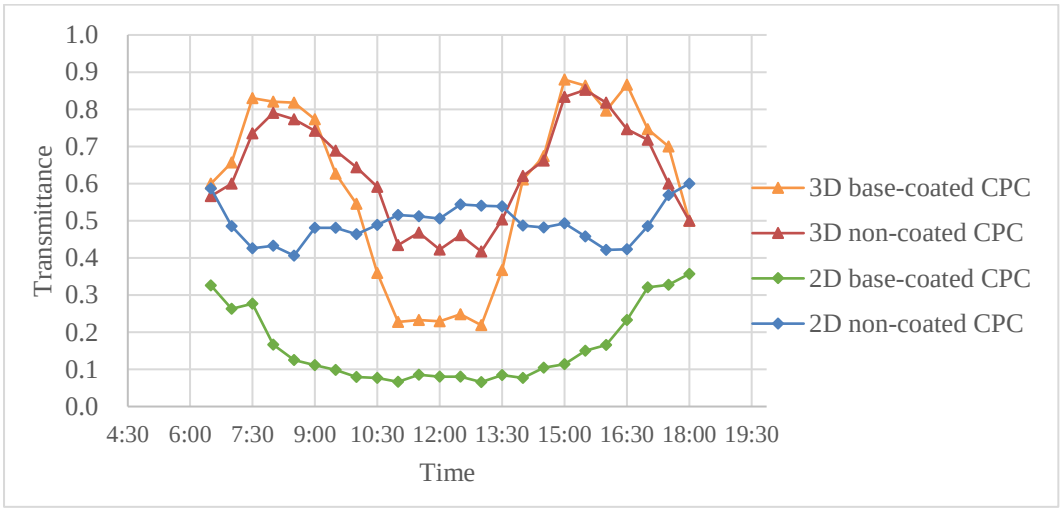


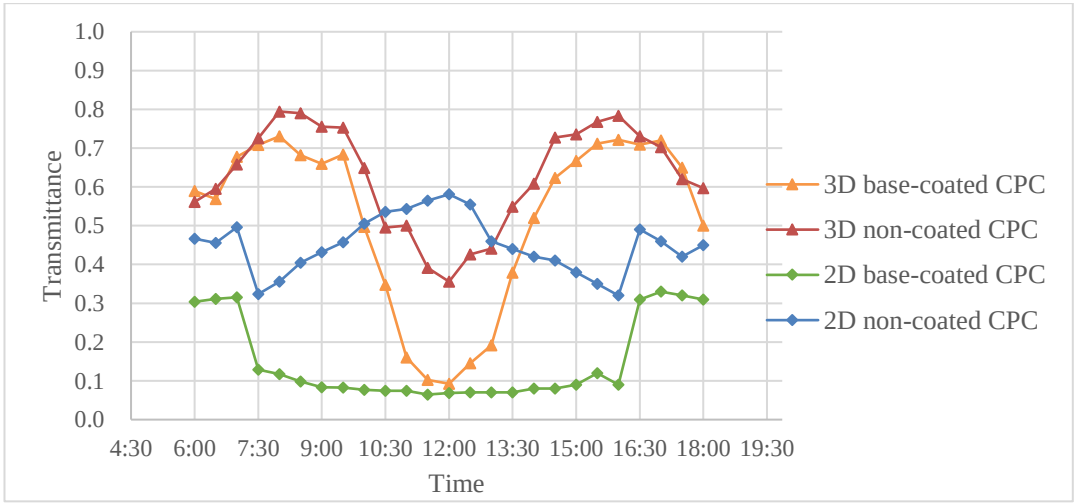
Figure 3.2.1.2. Relationship between incident angle and transmittance for five different structures

3.2.2. Transmittance of 2D and 3D dCPCs under clear sky

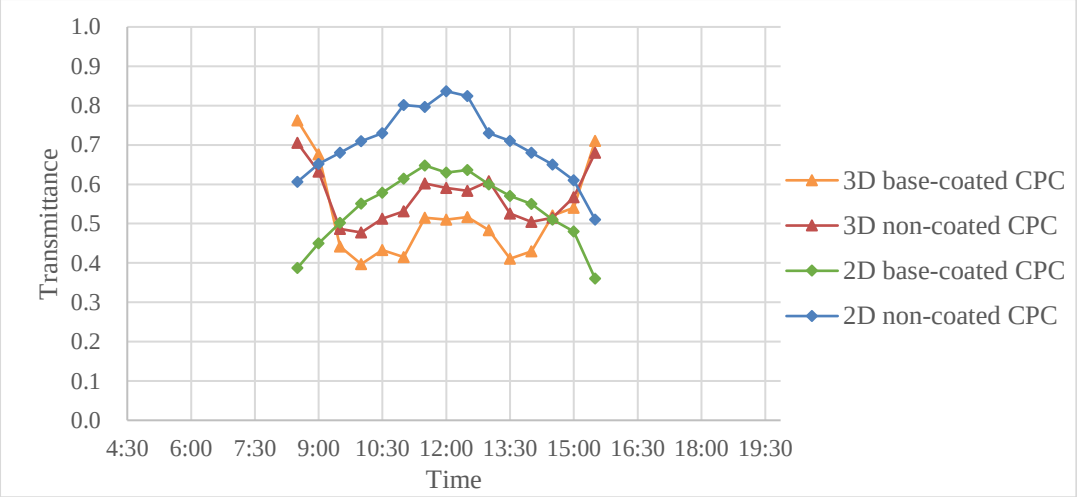
The solar zenith angle at noon various from 30 °to 54 °in Nottingham (53 °N, 1.2 °W) during March to September and outer half acceptance angle of the dCPC is about 22.05 °. According to the previous study by Yu et al. [15], the CPC tilt angle should be about 37 °to fit in the angular range required to achieve the shading effect. Therefore, the control abilities of 2D and 3D dCPCs are compared in 37 °tilt angle under clear sky conditions in three specific day (summer solstice, winter solstice and Spring Equinox). The 3D dCPC investigated in this and the following part of Chapter 3 is 3D dCCPC unless otherwise stated. The results of transmittances and transmitted daylight illuminance are shown in Figure 3.2.2.1 and Figure 3.2.2.2.



(a) Transmittance of 2D and 3D dCPCs in Spring Equinox



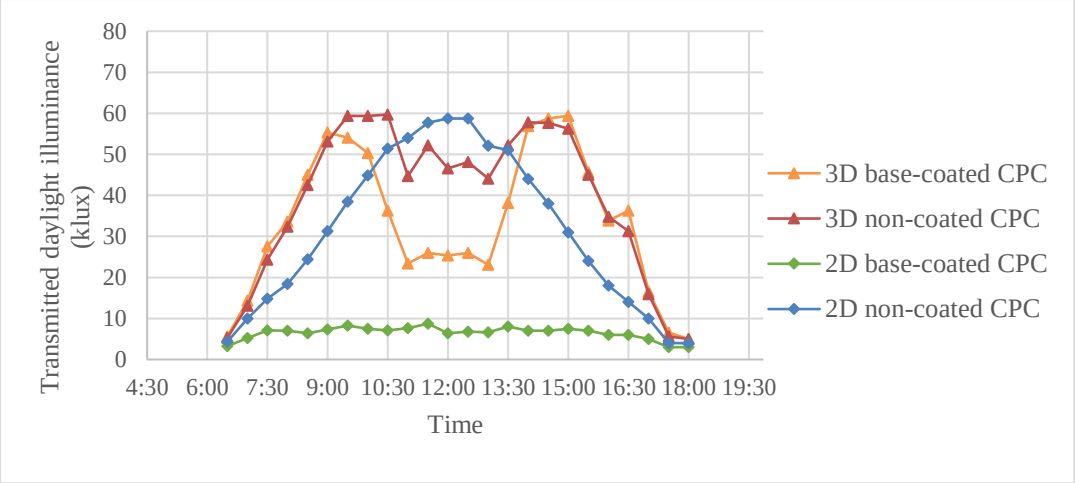
(b) Transmittance of 2D and 3D dCPCs in Summer Solstice



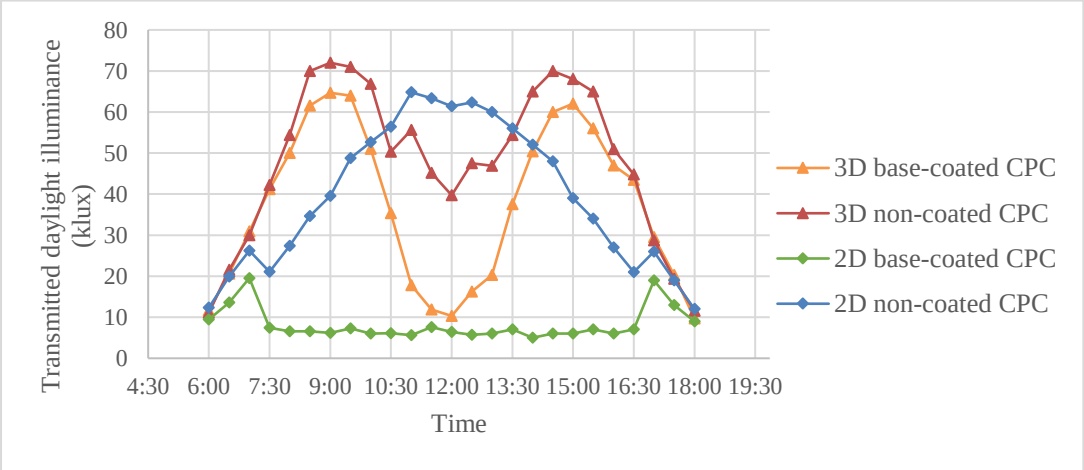
(c) Transmittance of 2D and 3D dCPCs in Winter Solstice

Figure 3.2.2.1. Transmittance of 2D and 3D dCPCs under sunny sky (Nottingham, south-facing, 37 °tilted)

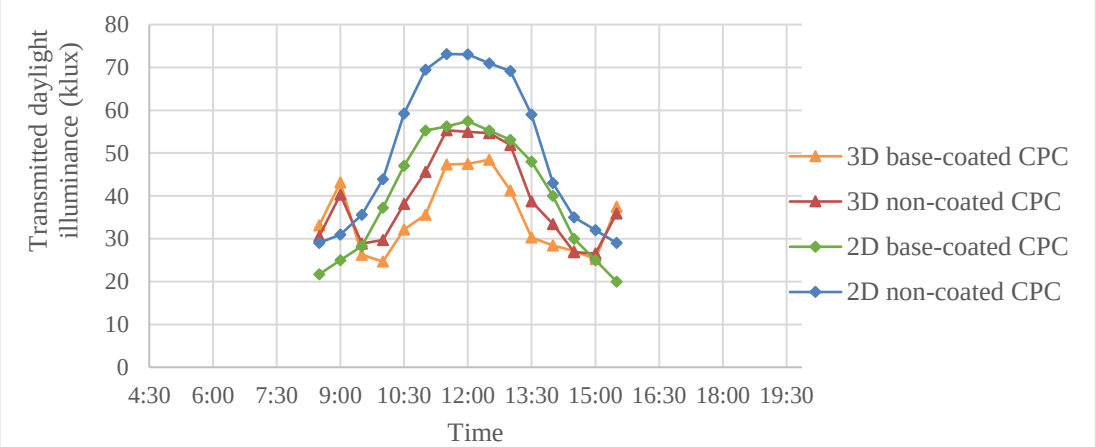
It is observed that 3D dCPC has great advantages than 2D dCPC in controlling sunlight in the three specific days. For 2D base-coated dCPC, sunlight is prevented from 8:00 to 16:00, during which its transmittance is lower than 0.2 in spring equinox, and it is similar to summer solstice. In winter solstice, 2D base-coated dCPC does not provide control on sunlight. Comparing with this, 3D base-coated dCPC provides remarkable control of sunlight in these three days. It lets light pass through before 10:00 and after 13:30, and prevents light during 10:00 to 13:30 in spring equinox and summer solstice. In winter solstice, it controls the light from 9:00 to 15:00, and the lowest transmittance is 0.4, which could provide adequate illuminance for indoor environment. Similarly, 3D non-coated dCCPC also has great advantages than 2D non-coated dCPC. It has same control strategy with 3D base-coated dCPC, while the lowest transmittance is 0.2 higher than 3D base-coated dCPC. 2D non-coated dCPC hardly provides control on sunlight.



(a) Transmitted illuminance of 2D and 3D dCPCs in Spring Equinox



(b) Transmitted illuminance of 2D and 3D dCPCs in Summer Solstice



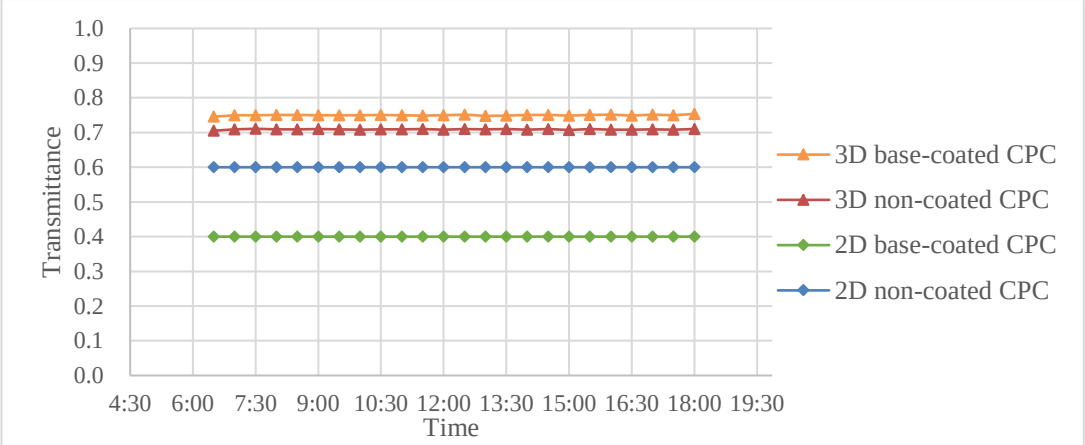
(c) Transmitted illuminance of 2D and 3D dCPCs in Winter Solstice

Figure 3.2.2.2. Transmitted daylight illuminance of 2D and 3D dCPCs under sunny sky (Nottingham, south-facing, 37 °tilted)

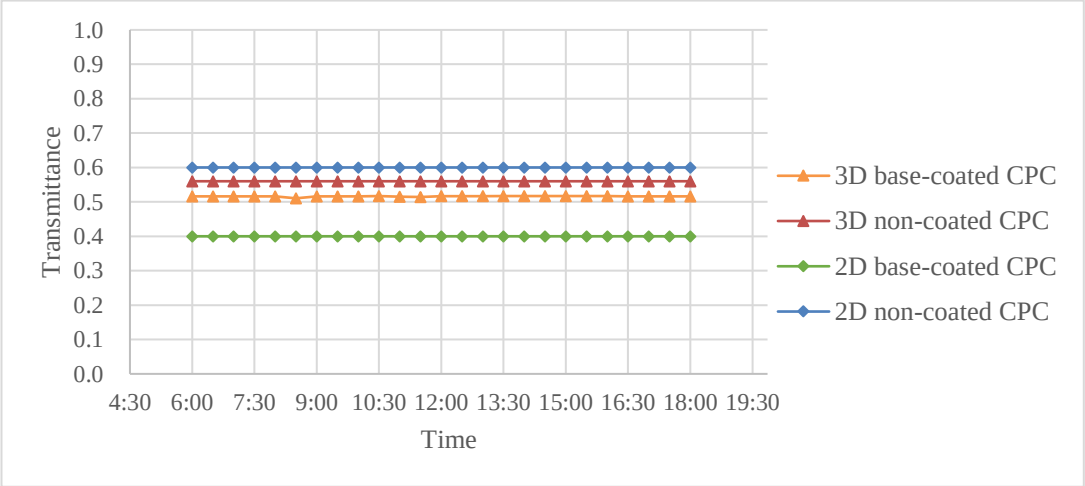
The effects on transmitted daylight illuminance performance by different structures are shown in Figure 3.2.2.2. For spring equinox and summer solstice, 2D base-coated dCPC provides strong control of sunlight, whose transmitted illuminance level is under 10klux during the whole day. The low transmittance will cause insufficient illuminance level under overcast sky, which is not appropriate for practical application. Comparing with 2D non-coated dCPC, both base-coated and non-coated 3D dCPC perform well in controlling sunlight during daytime in spring equinox and summer solstice: the transmitted illuminance is high in the morning and afternoon, while it is controlled in a lower level at noon. This properties could reduce solar gain at noon under sunny sky condition and guarantee enough indoor brightness. In winter solstice, 2D and 3D dCPCs don't provide effective control on daylight. Considering the cold weather and few sunny sky conditions, this performance can also help to reduce heating load in winter time.

3.2.3. Transmittance of 2D and 3D dCCPC under overcast sky

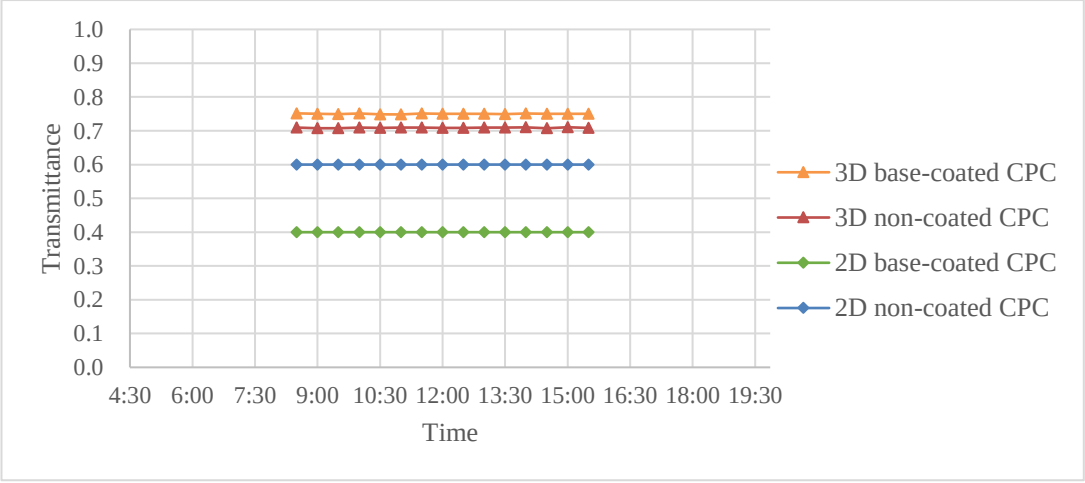
The control abilities on daylight of 2D and 3D dCCPC under overcast sky condition will be investigated in this section. Different from the transmittances under sunny sky, the transmittances of both 2D and 3D dCCPC stay stable in a day at different time, but the transmittances are slightly different in various seasons, which depend on the solar altitude. Because 3D dCCPC has smaller base area compared to the 2D dCPC, the effect of base-coating are reduced. According to Figure 3.2.3.1, the transmittance deviation of 3D base-coated and non-coated dCPC are around 0.05, while it is around 0.2 of 2D dCPCs. The incident light to dCPC are in variety of directions under overcast sky condition, 3D dCPC demonstrates worse control ability of daylight comparing with 2D dCPC in spring equinox and winter solstice, of which the transmittances are around 0.7. In summer solstice, the transmittances are located between the values of 2D dCPCs, which are around 0.5. For 2D base-coated dCPC, it could be seen that the transmittance is 0.4, and 0.6 for non-coated one in the three specific days. However, the higher transmittance of 3D dCPC could provide better indoor visual environment under overcast sky condition. In addition, more heat gain could reduce heating load in cold seasons.



a) Spring equinox



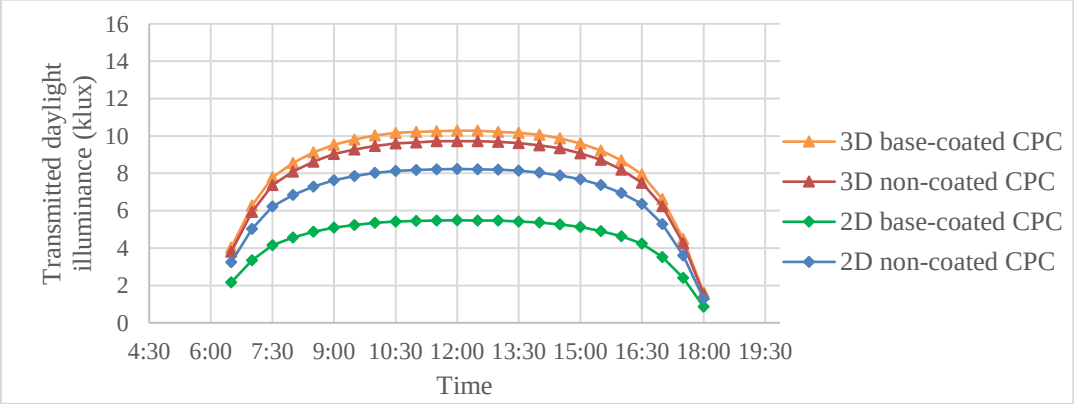
b) Summer solstice



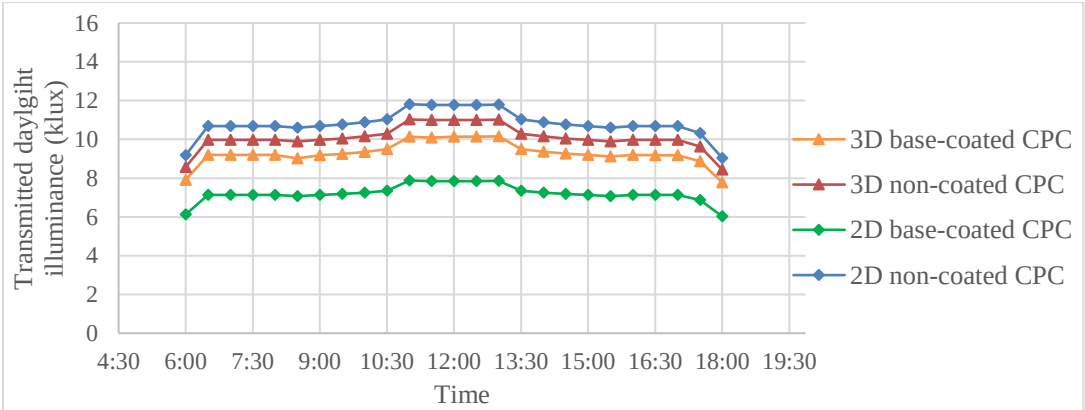
c) Winter solstice

Figure 3.2.3.1. Transmittance of 2D and 3D dCPCs under overcast sky (Nottingham, south-facing, 37 °tilted)

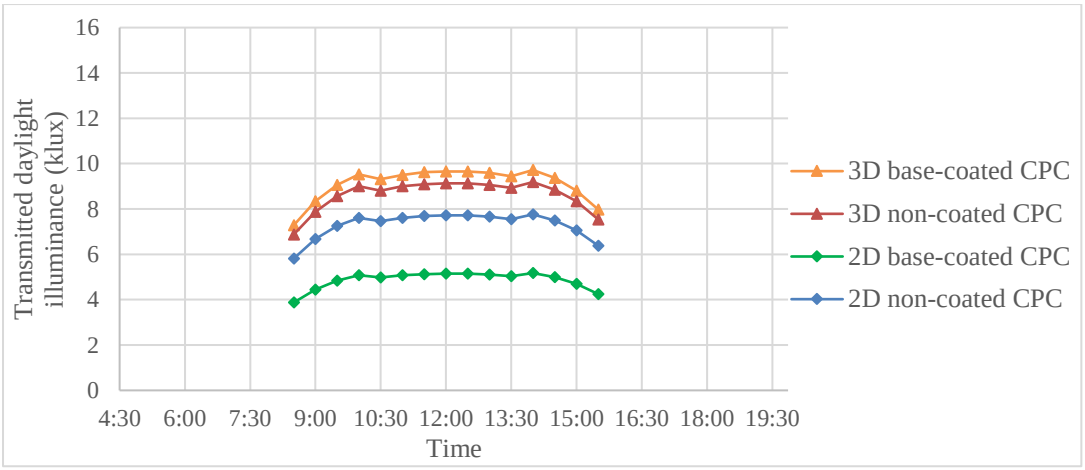
The transmitted daylight illuminance of 2D and 3D dCPCs are shown in Figure 3.2.3.2. Because of the low sun lumen under overcast sky, higher transmittances of dCPCs do not cause extreme high transmitted illuminance level. In spring equinox, the transmitted illuminance ranges from 4klux to 10klux for 3D base-coated and non-coated dCPCs. The illuminance for 2D base-coated dCPC is within 2-5klux, and 3-8klux for non-coated types. In winter solstice, the transmitted illuminance are similar to spring equinox, but the durations are shorter because of the shorter daytime. In summer solstice, the highest transmitted illuminance is produced by 2D non-coated dCPC, which is about 9klux to 12klux. 3D non-coated and base-coated dCPC perform lower transmitted illuminance ranges, which are 9-11klux and 8-10klux respectively. 2D base-coated dCPC provides lowest illuminance level which is within 6-8klux in summer solstice. The transmitted daylight illuminance reflect the transmittance of different types of dCPCs. It is illustrated that under overcast sky condition, 3D dCPCs performs better indoor visual environment than 2D dCPCs in various seasons also they do not provide stronger control abilities than 2D dCPCs.



a) Spring equinox



b) Summer solstice



c) Winter solstice

Figure 3.2.3.2. Transmitted daylight illuminance of 2D and 3D dCPCs in Spring Equinox, Summer Solstice and Winter Solstice under overcast sky (Nottingham, south-facing, 37 °tilted)

3.2.4. Discussion

In this section, the optical performances of 2D dCPC, 3D dCCPC and right square pyramid structure are compared, and both 2D dCPCs and 3D dCCPCs are separated into base-coated and non-coated types. The relationship between transmittances and incident angle of light are investigated first. With the incident angle changing from 0 °- 90 °, 3D base-coated dCCPC performs almost same optical properties comparing with 2D dCPC for base-coated type, which the transmittances are constrained from 0.5 to 0.05 as the incident angle is reduced from 25 ° to 0 °. For non-coated dCPCs, 3D dCCPC has better ability on controlling incident light than 2D dCPC but worse than the base-coated 2D and 3D dCPCs. The right square pyramid structure performs poor control on light with the change of incident angle. The results corresponds to the theoretical values of the dCPCs of which the outer half acceptance angle is about 22.05 °.

Then the control ability of 2D and 3D dCPCs are explored in respect of transmittance and transmitted daylight illuminance. Each of them are separated into base-coated and non-coated types, and all of them are simulated under sunny sky and overcast sky conditions respectively. The results demonstrate that 3D dCPCs have strong advantages compared to 2D dCPCs. In sunny days, 3D dCPCs perform higher transmittances in the morning and afternoon, and prevent daylight at noon in spring

equinox and summer solstice. 2D dCPCs also provides some control on daylight but do not varies a lot at different time in one day, and do not perform strong prevention at noon. The variations of transmittances result in the change of transmitted daylight illuminance by dCPCs. The similar optical performances occur in base-coated and non-coated dCPCs, while the lowest transmittance of 3D non-coated dCCPC is 0.2 higher than 3D base-coated dCCPC. 2D non-coated dCPC hardly provides control on sunlight.

The reason for quite different performances of 2D and 3D dCPCs is that dCPC controls the incident lights by reflecting them to the bottom surface or out of dCPC mainly by the curved surfaces. Figure 3.2.4.1 demonstrates three representative sun paths during the whole year for 2D and 3D dCPCs. The surfaces in blue refer to the parabolic surfaces. 2D dCPC has only two curved surface so that it can only control the sunlight with different solar zenith angle. Therefore the transmittances of 2D dCPC have large difference in different season during the whole year, but it is difficult to control the sunlight at different time in the same day. 3D dCPC has four curved surfaces facing four different directions which can control the sunlight not only for different seasons, but also for different times in one day.

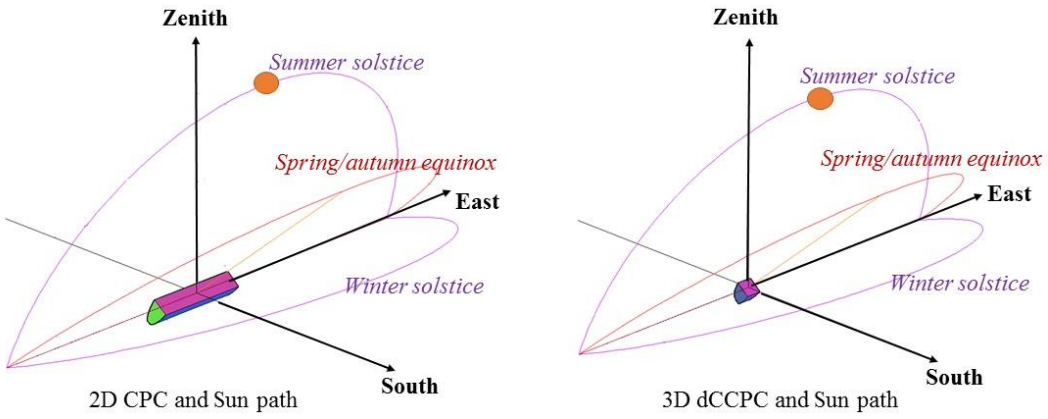


Figure 3.2.4.1. 2D and 3D dCPCs under representative sun paths during the whole year

The transmittances of different structures affect the variable illuminance when the light passing through dCPCs which relates to the significance in practical applications. For spring equinox and summer solstice, the low transmittance of 2D base-coated dCPC will cause insufficient illuminance level under overcast sky, which is not appropriate for practical application. In terms of transmitted illuminance, it is difficult

to see any control on daylight provided by 2D non-coated dCPC. However, the transmitted illuminance is high in the morning and afternoon, and in lower level at noon for both base-coated and non-coated 3D dCPC in spring equinox and summer solstice. The lower illuminance level at noon will reduce cooling load requirement, and higher illuminance level in the morning and afternoon rise the indoor brightness. In winter solstice, both of 2D and 3D dCPCs do not provides efficient control of daylight, which leads to more heat gain and decrease the heating load in cold season. Under overcast sky conditions, the transmittances of 2D and 3D dCPCs are constant in one day, but 3D dCPCs provides relatively higher transmittances in spring equinox and winter solstice, and lower in summer solstice, which could provide brighter indoor visual environment in cooler seasons and prevent heat gain in hot seasons.

It is obviously demonstrated that 3D dCCPCs have strong control not only in different seasons during whole year, but also at different time in one day. Therefore, 3D base-coated and non-coated dCPC provides better control on daylight than 2D dCPC. Therefore further investigations of 3D dCPCs will be put forward in different criteria in the following sections.

3.3. Effect of tilt angle on 3D dCCPCs

Tilt angle of dCPC is an important factor that influences dCPC performance, which affects how the acceptance angle works on controlling sunlight. Figure 3.3.1 is the schematic diagram of tilt angle for 3D dCCPC. Because the location of Nottingham is 53 °N, 1.2 °W, and the solar zenith angle at noon varies from 29 °to 53 °, four tilt angles, which are 29 °, 37 °, 45 °and 53 ° are chosen to explore their effects on dCPC performance. Two types of 3D dCCPC, which are base-coated and non-coated will be discussed separately under both sunny and overcast sky conditions.

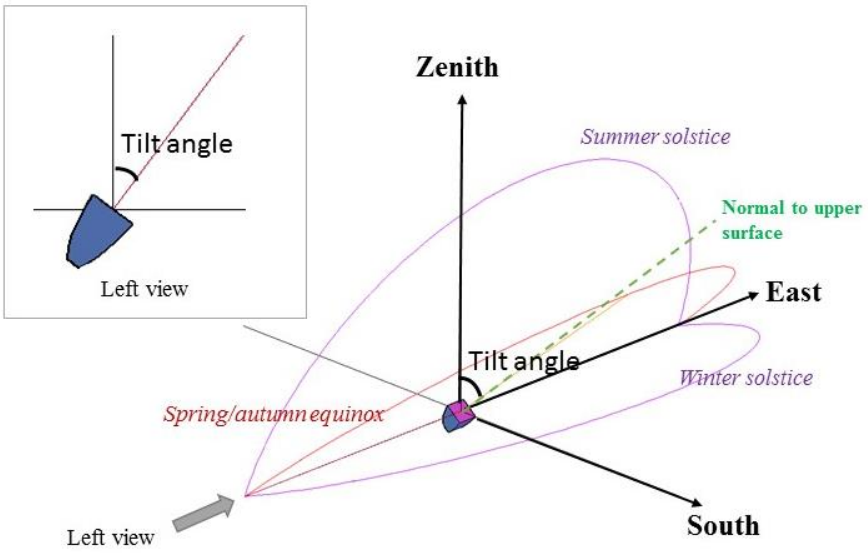


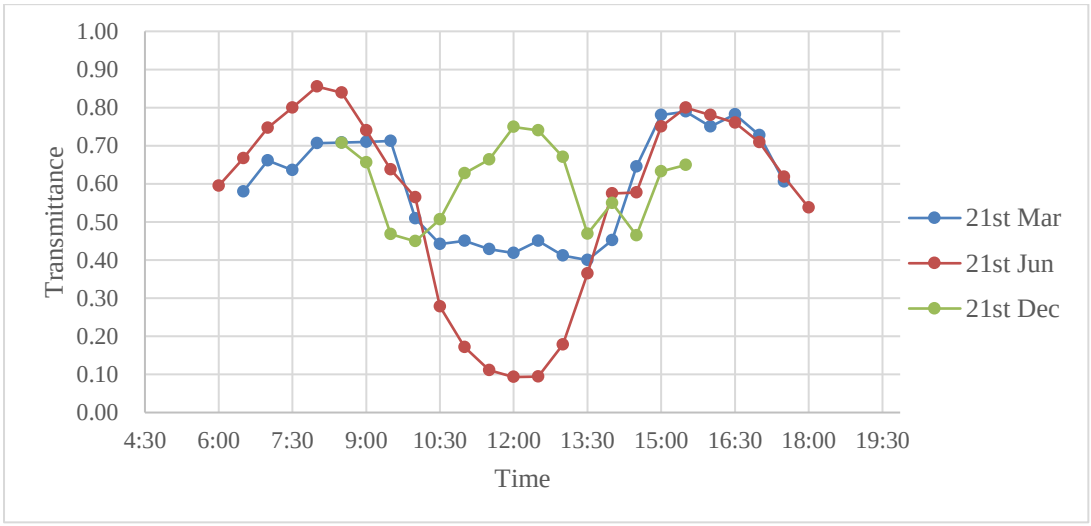
Figure 3.3.1. Schematic diagram of 3d dCCPC tilt angle

3.3.1. Effect of tilt angle on 3D dCCPC under sunny sky

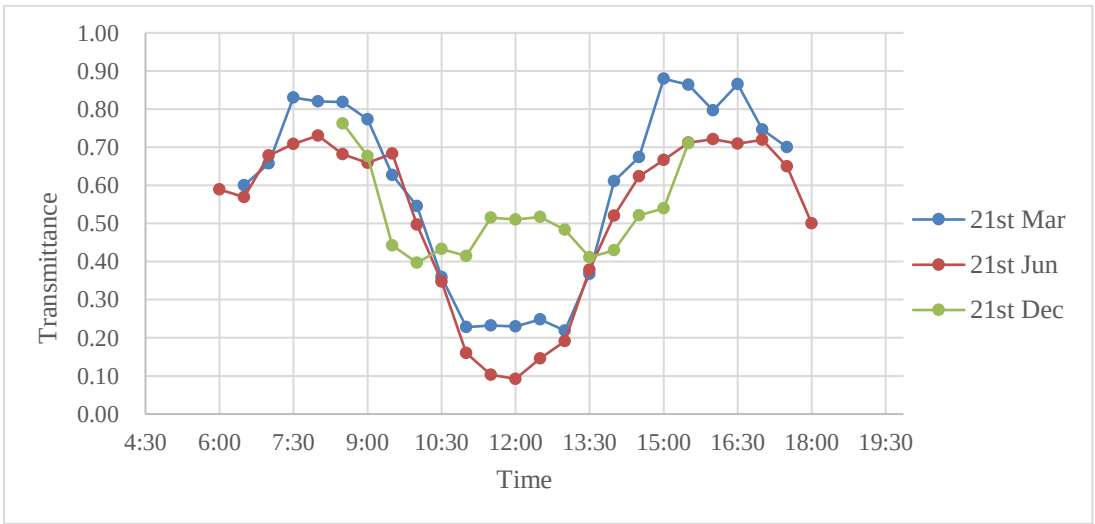
3.3.1.1. Transmittance

The transmittances of 3D base-coated dCCPC with different tilt angles are demonstrated in Figure 3.3.1.1 in three specific days. It can be seen that the tilt angle of dCPC mainly affects the transmittance from 10:30 to 13:30. Different tilt angles cause different transmittance distribution in three specific days. For 29 °tilt angle, the transmittance at noon in winter solstice ranges from 0.4-0.8; the transmittance is around 0.4 in spring equinox and ranges from 0.4 to 0.1 in summer solstice. For 37 ° tilt angle, the transmittance is within 0.4-0.6 at noon in winter solstice and it is around 0.2 or lower in both spring equinox and summer solstice. When the dCPC is tilted to 45 °, it performs strong control in all three days. The transmittances are lower than 0.4 at noon. The transmittance of dCPC with 53 °tilt angle continues this changing trend: it prevents sunlight at noon in winter solstice and spring equinox during which the transmittances are lower than 0.2 at noon, while the transmittances stay around 0.4 in summer solstice from 10:30 to 13:30. This changing trend also conforms the working principle of dCPC. The solar zenith angle at noon varies from 30 °to 54 °, which means the solar zenith angle is around 30 ° at noon in summer solstice and 54 ° at noon in winter solstice. The best performance of dCPC appears when incident angle is 0 °for incident light. When the tilt angle is 29 °, the top receive surface of dCPC is nearly normal to the incident light at noon in summer solstice whose incident angle is around 0 °to dCPC top surface. Similarly, the 35 °tilt angle corresponds to the 54 °solar zenith

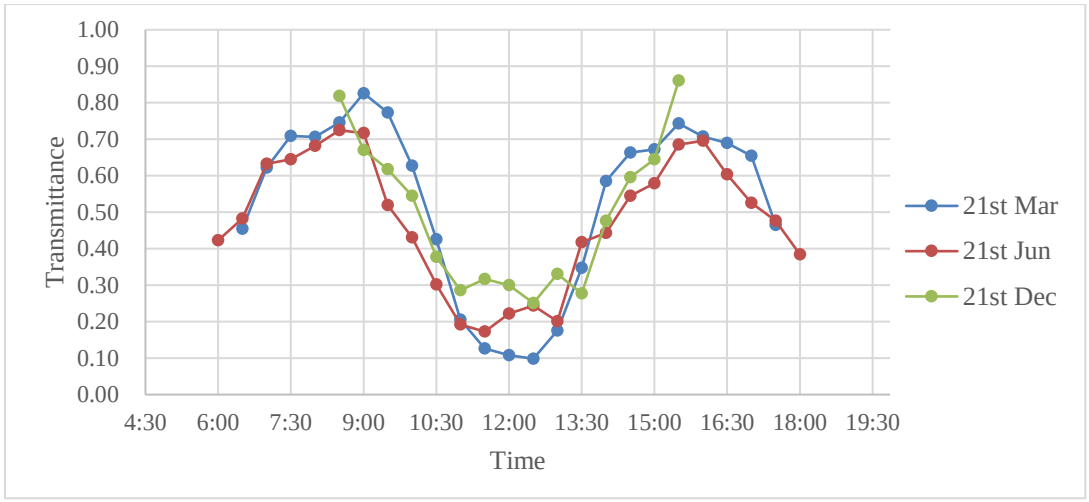
angle at noon in winter solstice. Hence dCPC provides strong control at that day. Because the outer half acceptance angle of the dCPC is about 22.05 °, dCPC could also performs control when solar zenith angle changes within 30 ° - 54 °. This relationship between transmittance and tilt angle is important to practical application. Taking actual weather and cooling/heating load into account, the prevention of sunlight in summer is helpful to reducing cooling load, and less control of daylight in winter could increase heat gain in order to decrease heating load. Therefore, both 29 ° and 37 ° tilt angle may be more suitable for Nottingham weather conditions.



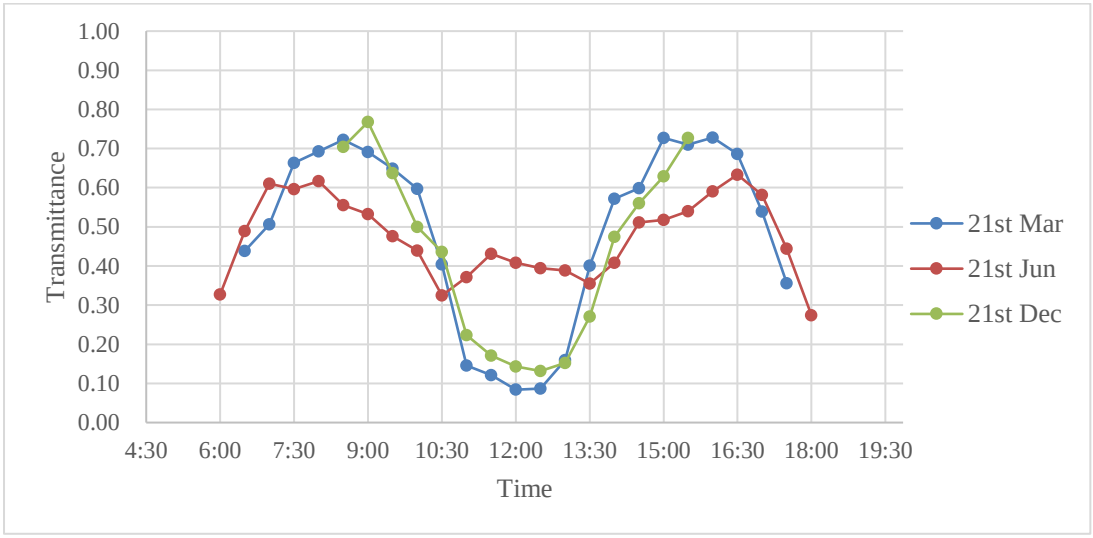
(a) 29 °tilt angle



(b) 37 ° tilt angle



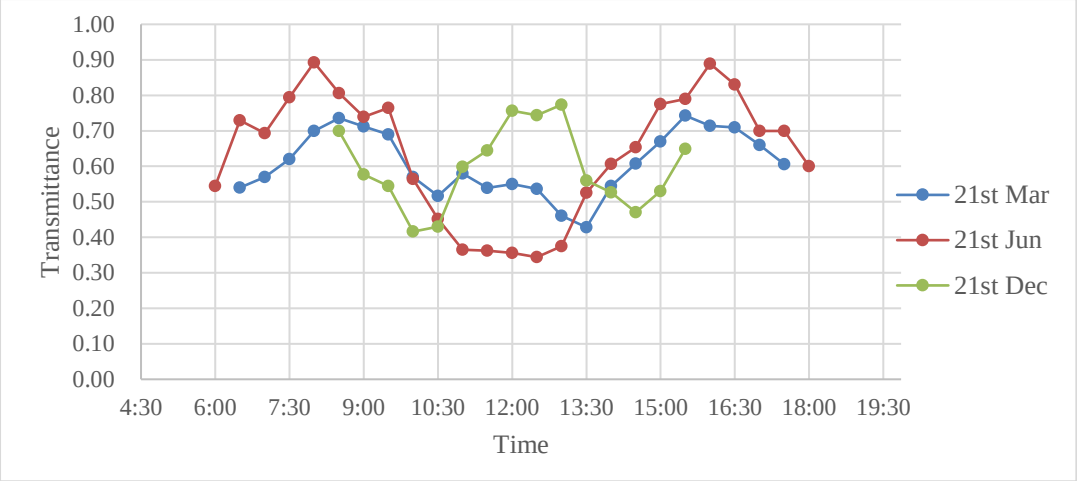
(c) 45 °tilt angle



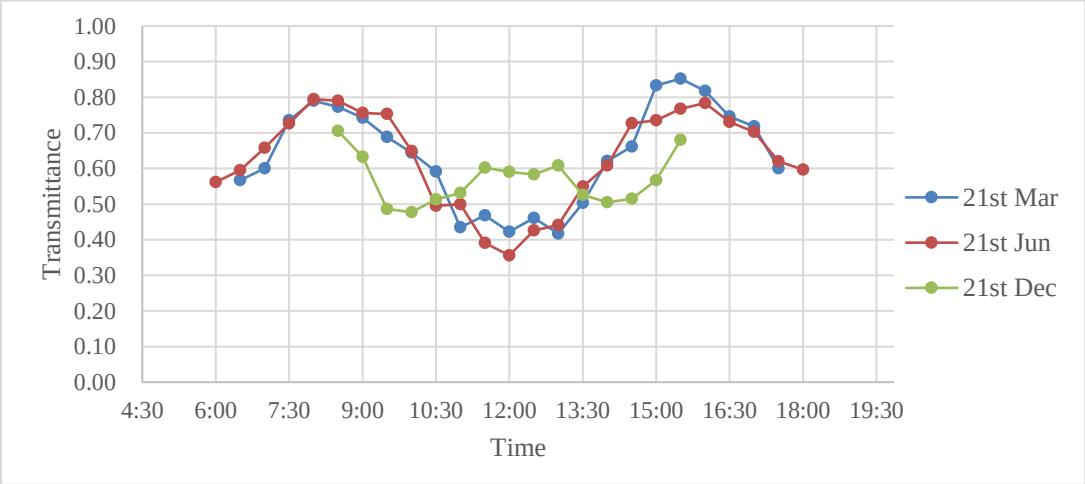
(d) 53 °tilt angle

Figure 3.3.1.1. Transmittance of 3D base-coated dCCPC in different tilt angles in spring equinox, summer solstice and winter solstice (Nottingham, south facing)

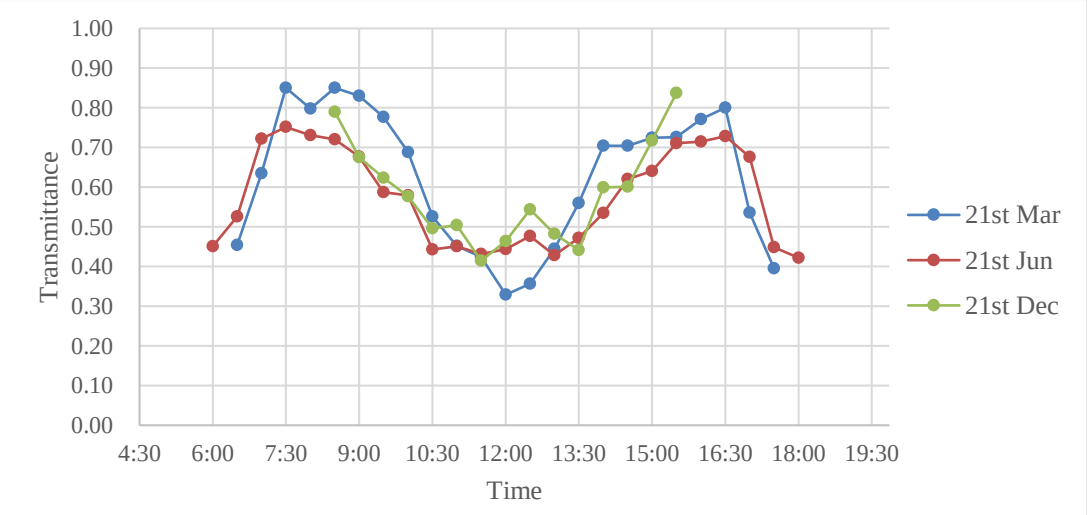
The influences on transmittances by tilt angle for 3D non-coated dCCPC are shown in Figure 3.3.1.2. Comparing with 3D base-coated dCPC, 3D non-coated dCPC also has similar changing trends of transmittance with the influence of tilt angle. However, it does not perform strong control of sunlight at noon because this dCPC cannot receive the lights which are refracted on to the bottom surface. The transmittances do not differ a lot in three specific days especially when the tilt angle is 45 °.



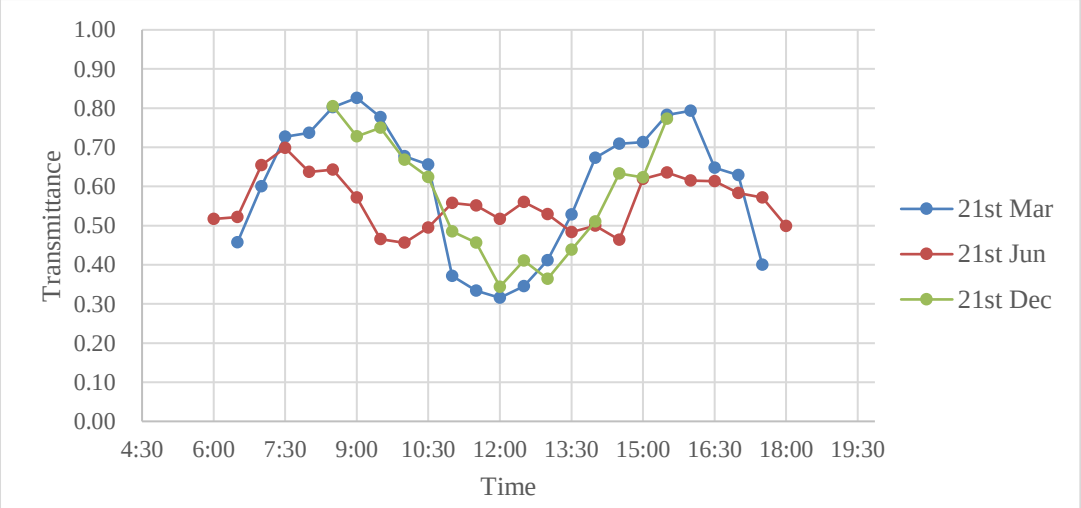
(a) 29 ℃tilt angle



(b) 37 °tilt angle



(c) 45 °tilt angle

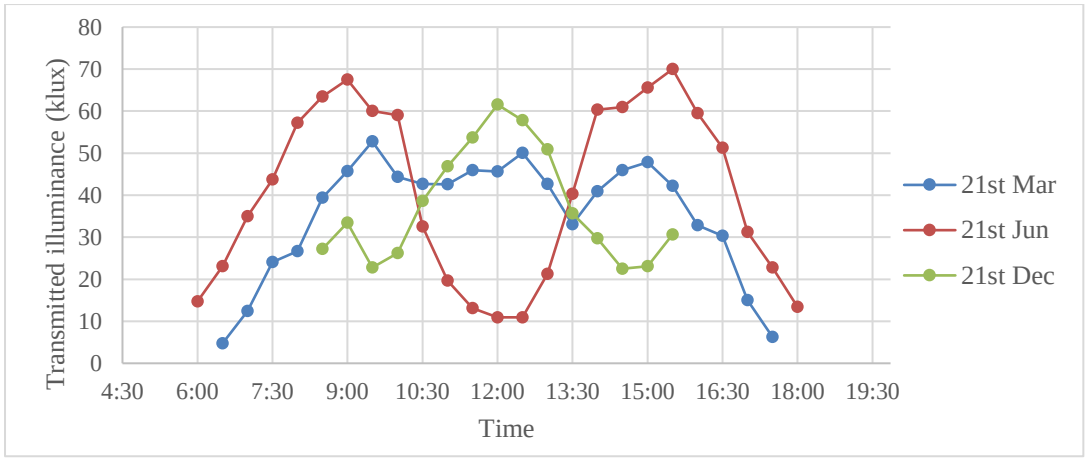


(d) 53 °tilt angle

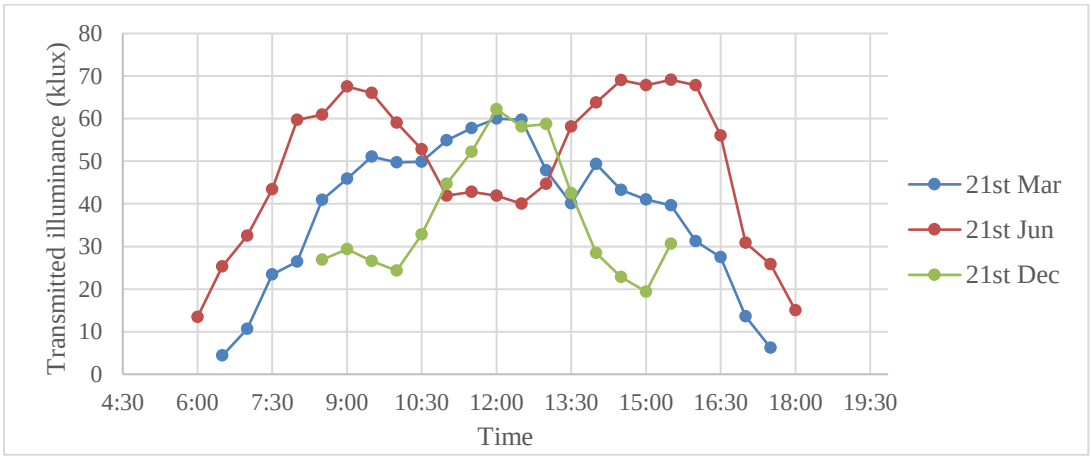
Figure 3.3.1.2. Transmittance of 3D non-coated dCCPC in spring equinox, summer solstice and winter solstice (Nottingham, south facing)

3.3.1.2. Transmitted daylight illuminance

The transmitted daylight illuminance for 3D base-coated and non-coated dCCPCs with different tilt angles are shown in Figure 3.3.1.3 – 3.3.1.6. The illuminance perform similar changing trends as results of transmittance. For base-coated dCCPC with 29 ° tilt angle, the low transmitted illuminance appears in summer solstice from 10:30 to 13:30. During same time, steady illuminance at around 45klux is given in spring equinox and higher illuminance level in winter solstice. Non-coated dCCPC performs almost same illuminance except in summer solstice, the transmitted illuminance is controlled at 40klux which is much higher than base-coated dCPC. The transmitted illuminance in spring equinox at noon is 20klux higher than base-coated dCPC as well. In terms of the dCCPC tilted to 37 °, the base-coated one provides strongest control at noon in summer solstice and less control in spring equinox, of which the corresponding daylight illuminance at noon is 10klux and 25klux respectively. For non-coated type, the transmitted illuminance is controlled to 50klux at noon in spring and summer. Less control is provided in winter solstice. The non-coated dCPC with 37 °performs lower illuminance at noon compared to the dCPC with 37 °tilt angle.

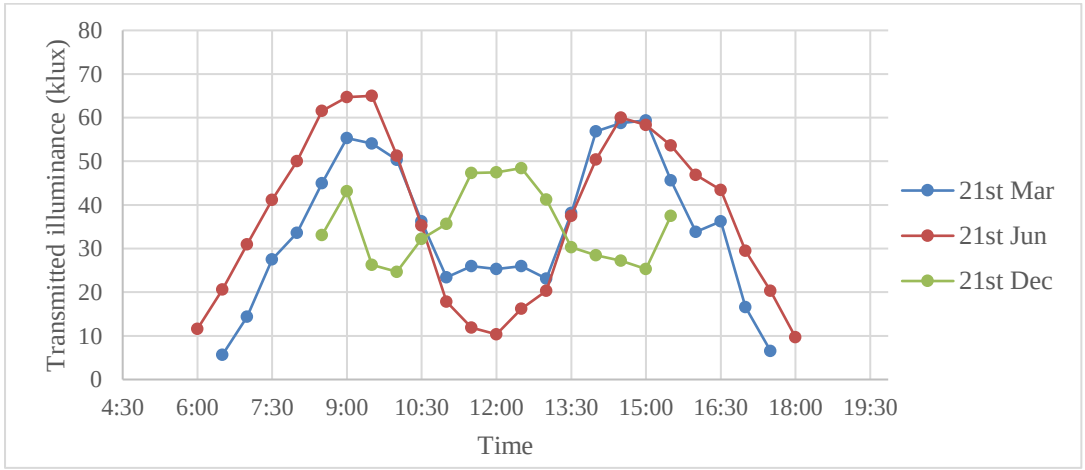


a) Base-coated

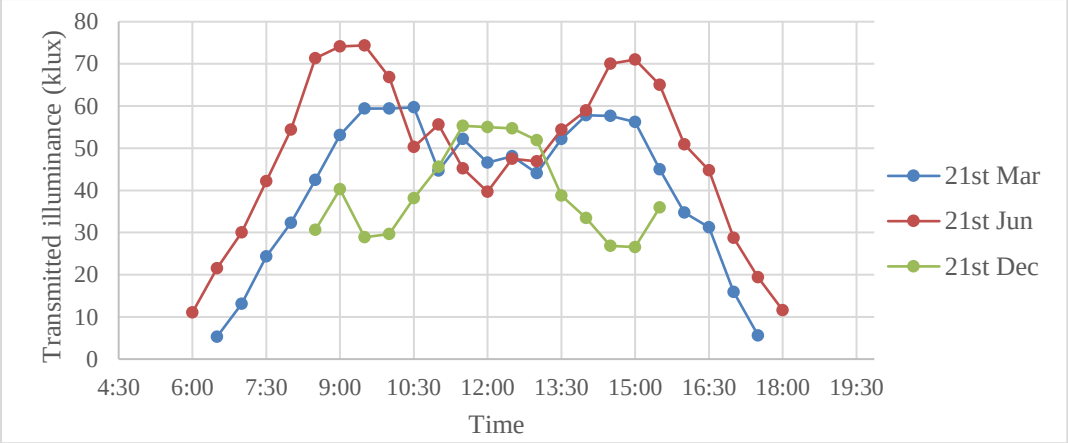


b) Non-coated

Figure 3.3.1.3. Transmitted daylight illuminance of 3D base-coated and non-coated dCCPCs with different tilt angles in spring equinox, summer solstice and winter solstice (Nottingham, south facing, 29 °tilted)



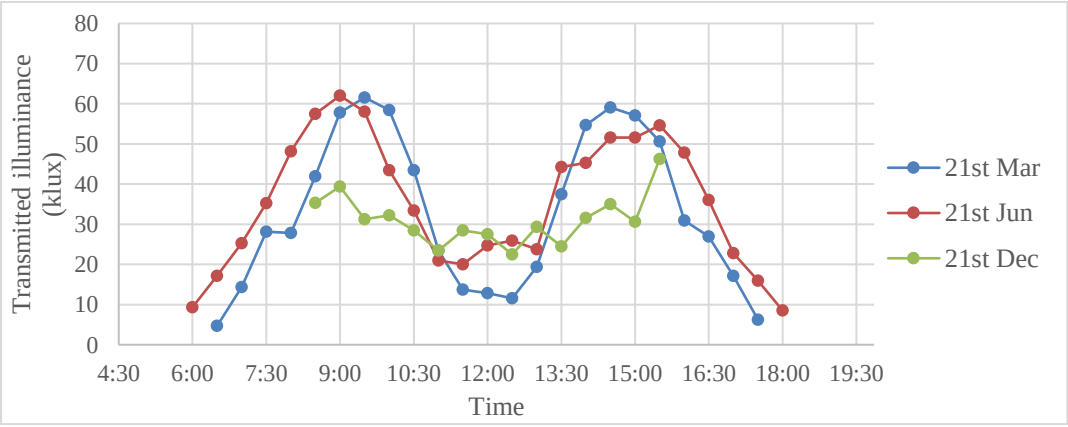
a) Base-coated



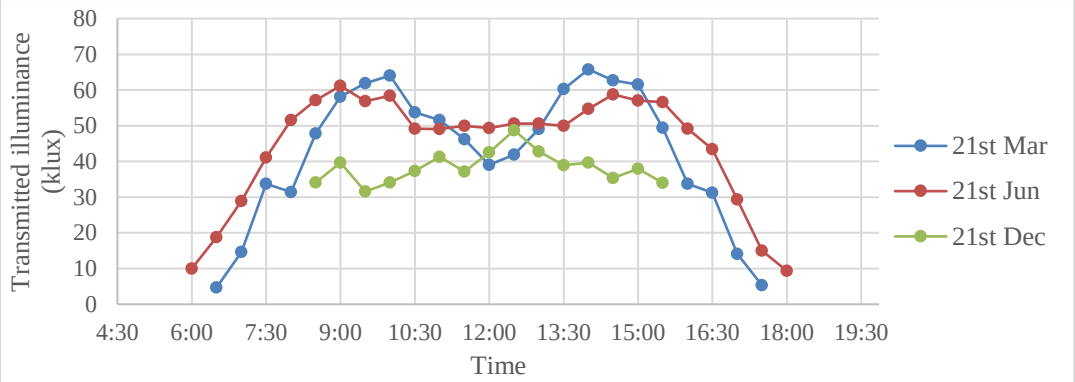
b) Non-coated

Figure 3.3.1.4. Transmitted daylight illuminance of 3D base-coated and non-coated dCCPCs in spring equinox, summer solstice and winter solstice (Nottingham, south facing, 37 °tilted)

The 3D dCCPC tilted to 45 °and 53 °also control sunlight but in different days. For the dCPC with 45 ° tilt angle, the sun light in spring, summer and winter are all prevented to a low level for base-coated type. The CPC with 53 °tilt angle prevents sunlight in winter and spring, but performs high illuminance level in summer which is not appropriate for practical application, and similar to the non-coated type. However, it is worth to mention that for non-coated dCPC with 45 ° tilt angle, the transmitted daylight illuminance is still applicable. The sunlight is not prevented too much in winter solstice and prevented in spring equinox and summer solstice. Although from the transmittance in Figure 4.3 (c) the transmittance of it are almost same in the three specific day, the variable outdoor illuminance results in the practicable transmitted daylight illuminance for it.

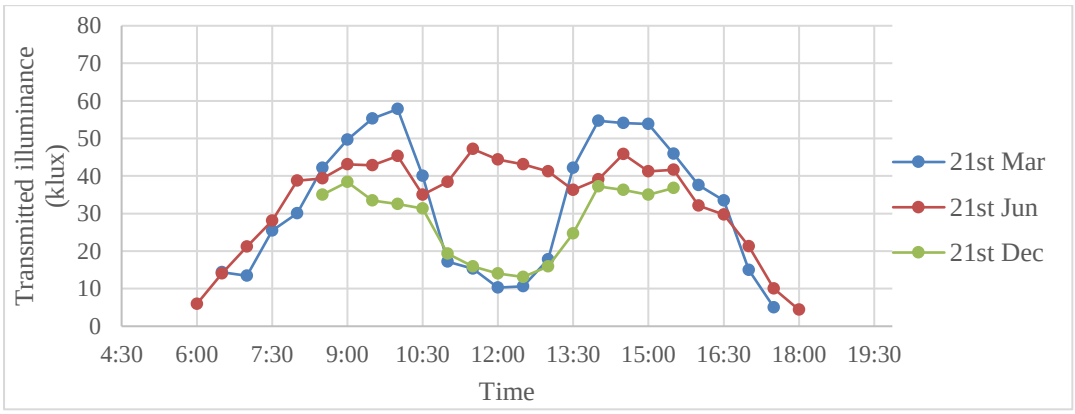


a) Base-coated

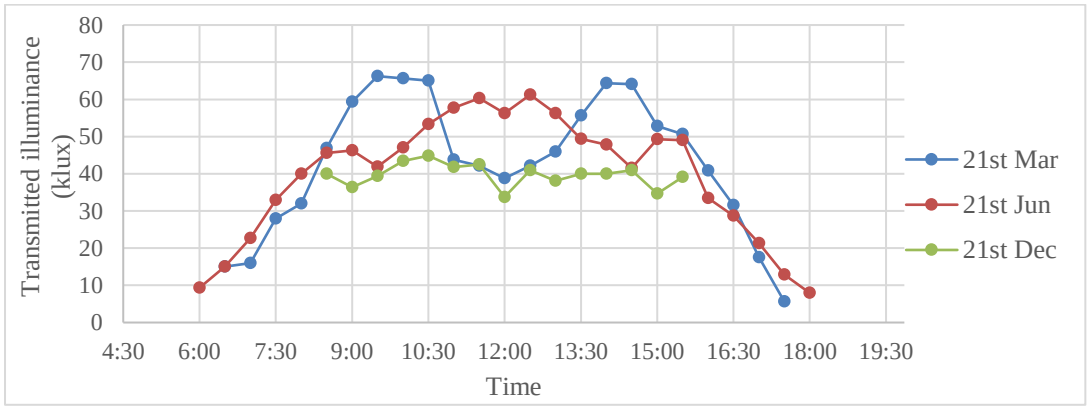


b) Non-coated

Figure 3.3.1.5. Transmitted daylight illuminance of 3D base-coated and non-coated dCCPCs in spring equinox, summer solstice and winter solstice (Nottingham, south facing, 45 °tilted)



a) Base-coated



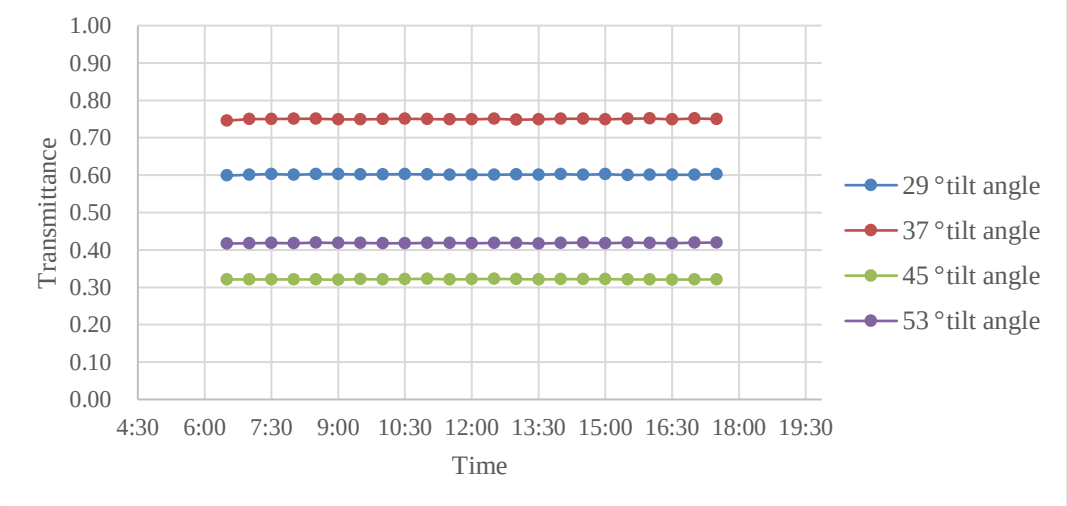
b) Non-coated

Figure 3.3.1.6. Transmitted daylight illuminance of 3D base-coated and non-coated dCCPCs in spring equinox, summer solstice and winter solstice (Nottingham, south facing, 53 °tilted)

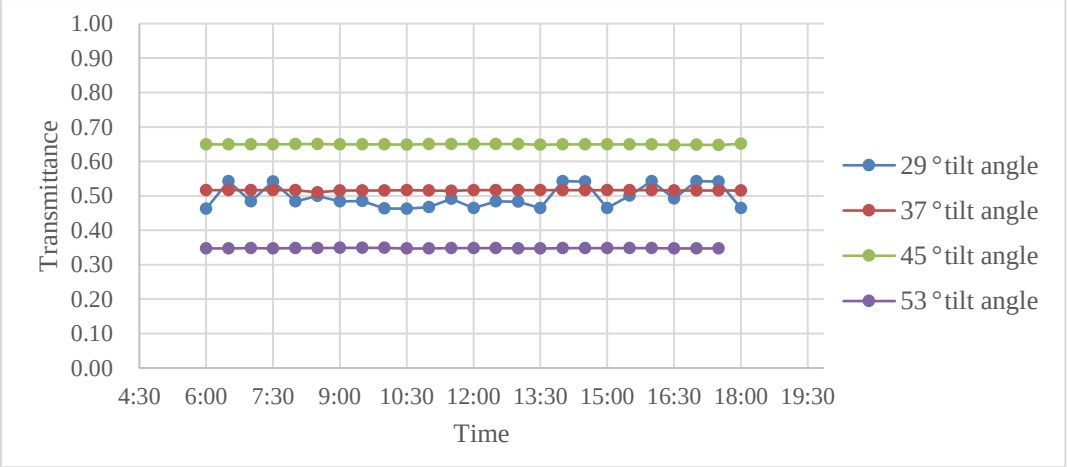
3.3.2. Effect of tilt angle on 3D dCCPC under overcast sky

3.3.2.1. Transmittance

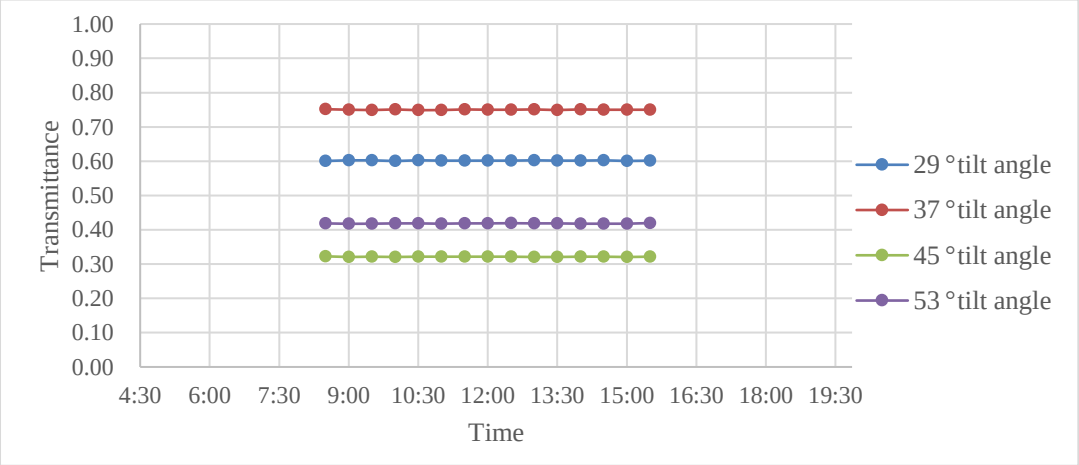
The effects on transmittance by tilt angle under overcast sky is shown in Figure 3.3.2.1 for base-coated dCCPCs. It can be seen that all of the transmittances stay stable in one day for all dCCPCs with different tilt angles. In spring equinox and winter equinox, the transmittances differ a lot on account of different tilt angles. For base-coated dCCPCs, the one with 37 °tilt angle performs highest transmittance which is 0.75 and the one with 45 °provides lowest transmittance which is 0.3. In summer solstice, the dCCPC with 45 °tilt angle has highest transmittance, 0.65 and the lowest one belongs to the dCCPC with 53 °tilt angle. The transmittances of dCCPCs with 29 °and 37 °tilt angle stay at 0.5. The transmittances for non-coated dCCPCs are shown in Figure 3.3.2.2. The changing trends are quite similar to base-coated dCCPCs, but the transmittances are a little bit higher because of the non-absorbing base. In spring equinox and winter solstice, the transmittance for 45 °tilted dCCPCs is around 0.4 and for 37 °tilted dCCPCs is 0.7. In summer solstice, the transmittances of dCCPCs are within 0.55 to 0.75 for all tilt angle.



a) Spring Equinox

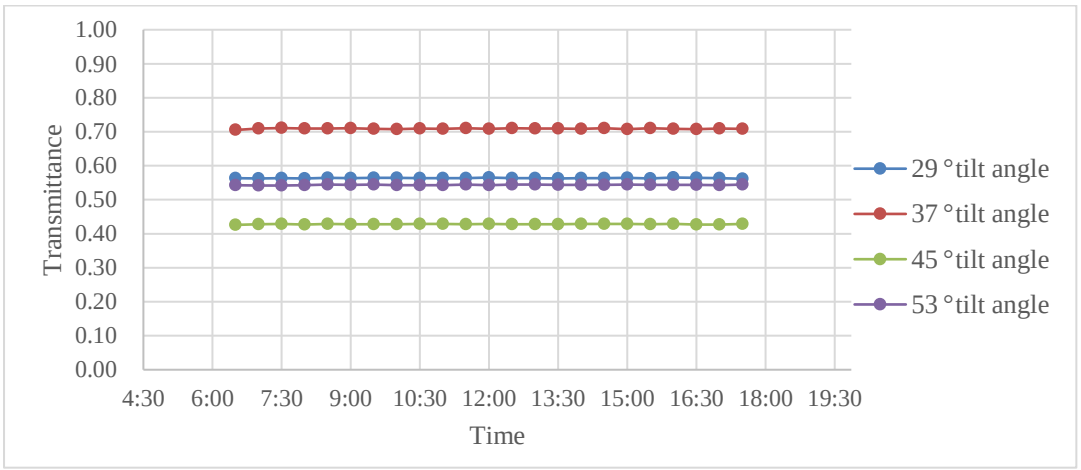


b) Summer solstice

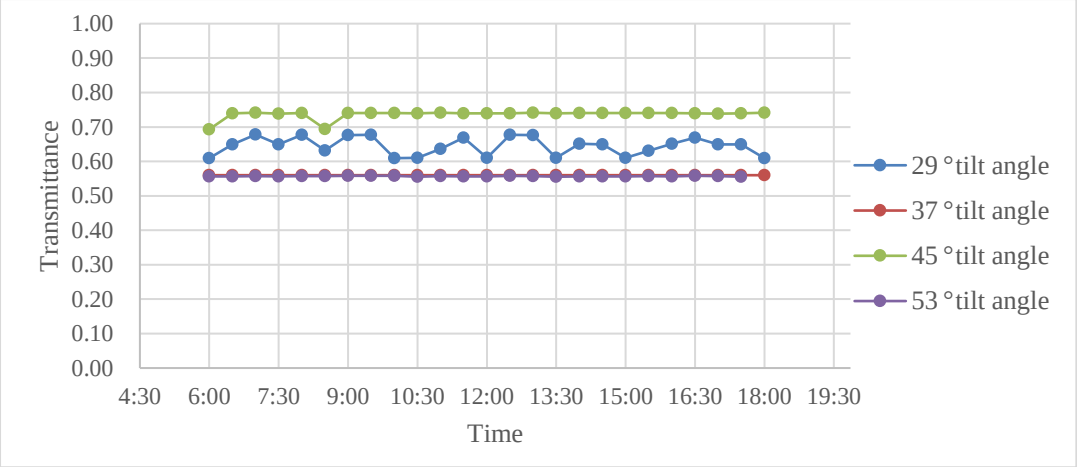


c) Winter solstice

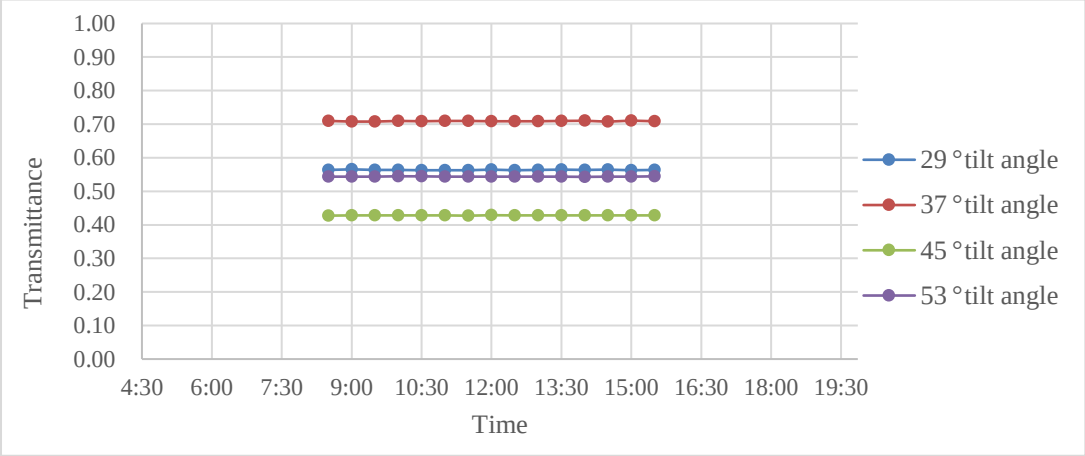
Figure 3.3.2.1. Transmittances of 3D base-coated dCCPC with different tilt angles in spring equinox, summer solstice and winter solstice (Nottingham, south facing)



a) Spring equinox



b) Summer solstice



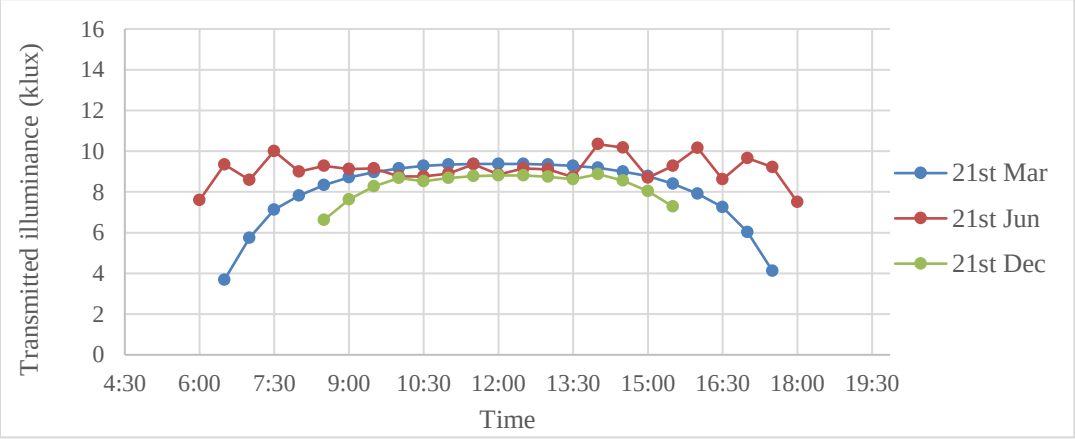
c) Winter solstice

Figure 3.3.2.2. Transmittances of 3D non-coated dCCPC with different tilt angles in spring equinox, summer solstice and winter solstice (Nottingham, south facing)

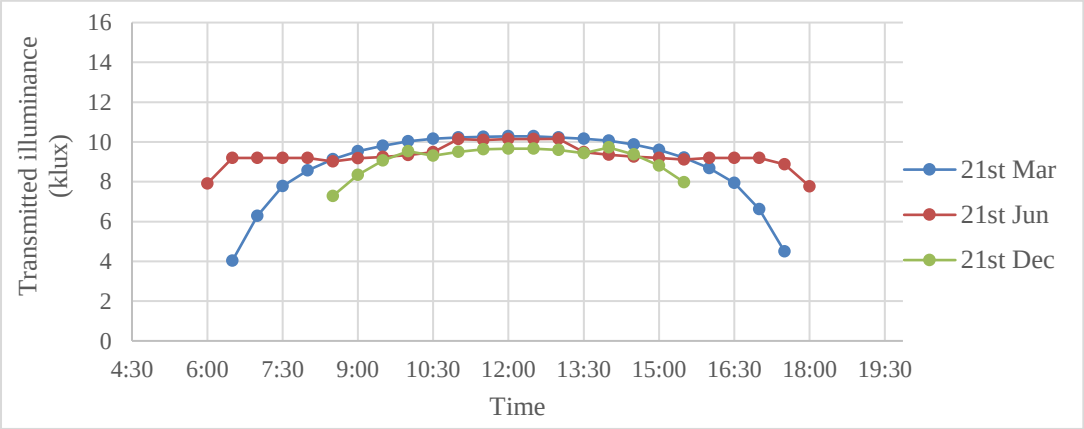
3.3.2.2. Transmitted daylight illuminance

The transmitted daylight illuminance for base-coated and non-coated dCCPCs are shown in Figures 3.3.2.3 and 3.3.2.4. Although the big difference of transmittances discussed in previous section, the transmitted illuminance are close, which is due to the low outdoor illuminance. For base-coated dCCPCs, the transmitted daylight illuminance stays at around 8-10klux for the dCCPCs with 29 ° and 37 ° tilt angle. However, the transmittances for base-coated dCCPCs with 45 ° and 53 ° tilt angle are lower than 8klux which is not enough to provide indoor brightness. In terms of non-coated dCCPCs, the transmittance is 12klux in summer solstice and 8klux in spring and winter for 29 ° tilt angle dCCPC. For the dCCPCs with 37 ° and 45 ° tilt angle, the

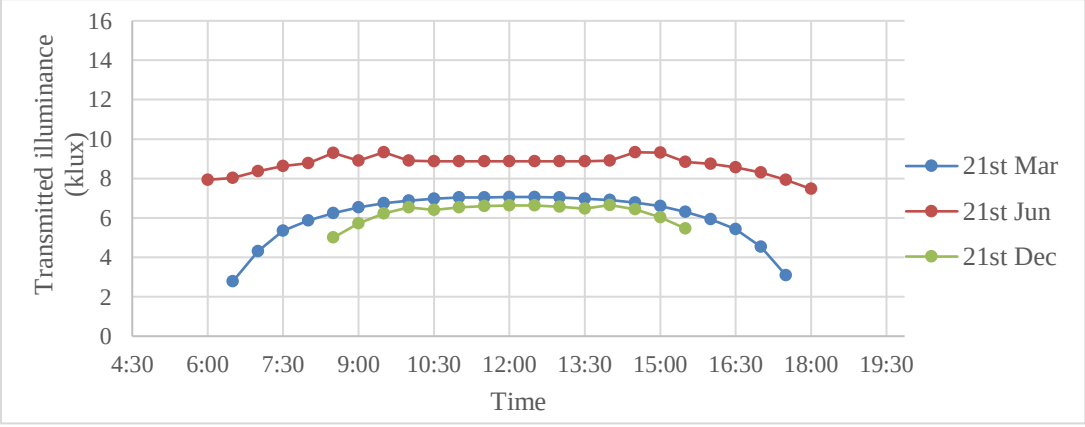
transmitted daylight illuminance ranges from 9klux to 11klux for the three specific days, which means the illuminance should stay in this range during the whole year. For the dCCPC with 53 °tilt angle, the transmittance under overcast sky is within 8-10klux.



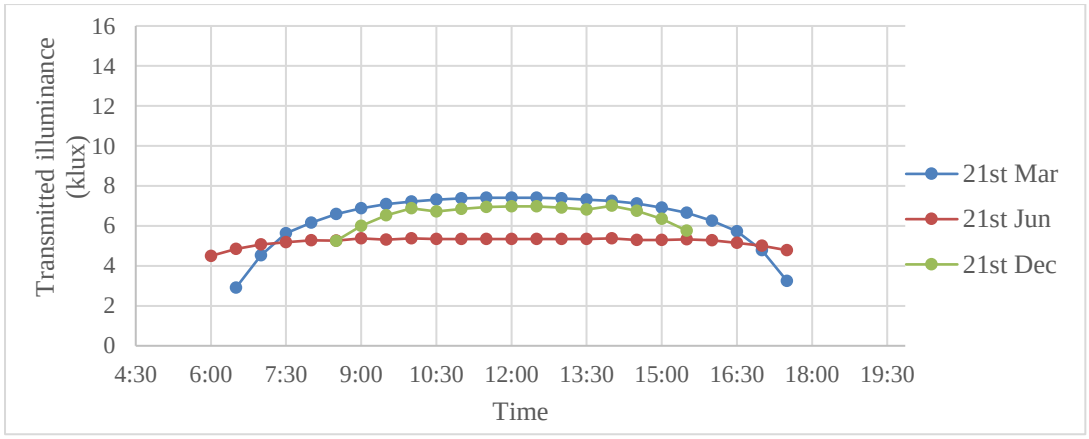
a) 29 °tilt angle



b) 37 °tilt angle

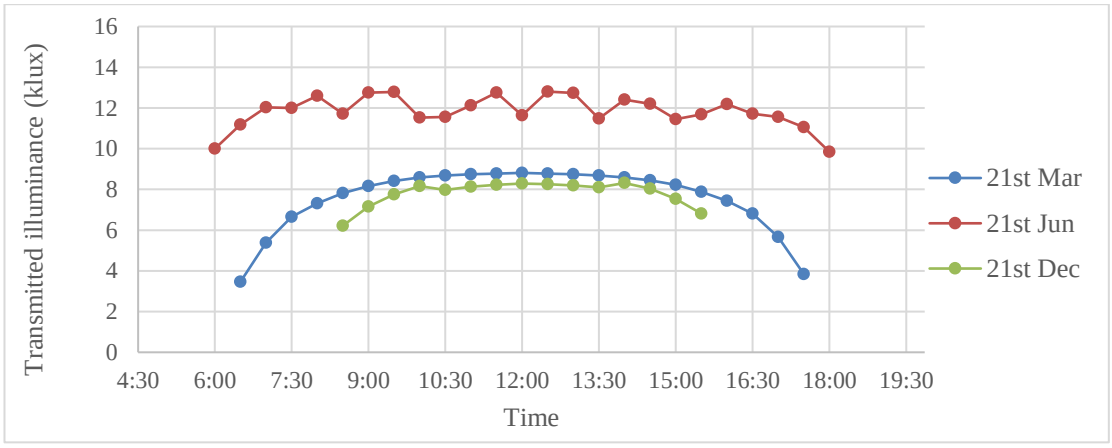


c) 45 °tilt angle

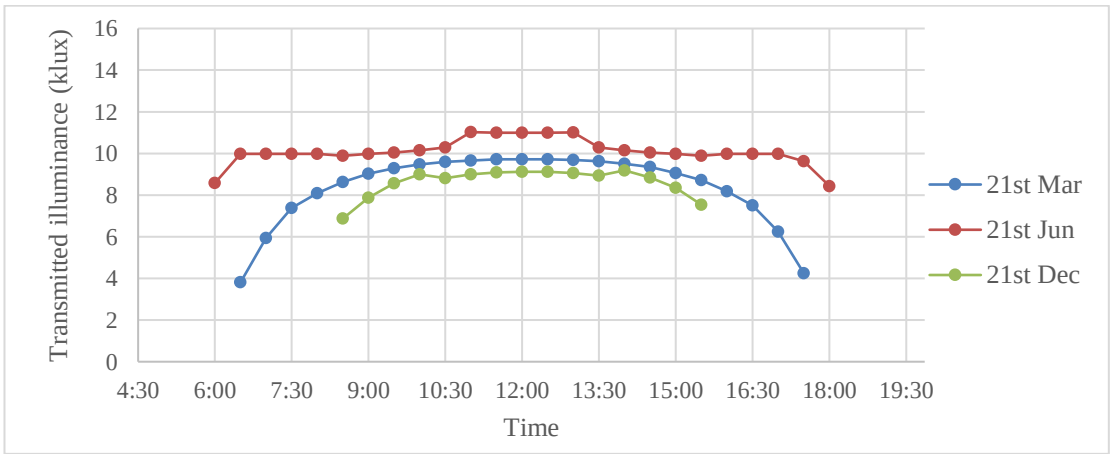


d) 53 °tilt angle

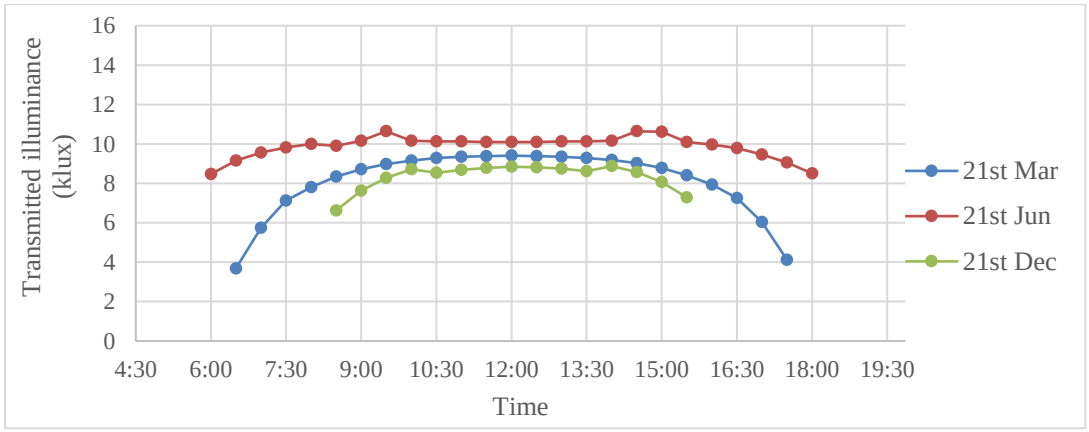
Figure 3.3.2.3. Transmitted daylight illuminance of 3D base-coated dCCPC with different tilt angles in spring equinox, summer solstice and winter solstice (Nottingham, south facing)



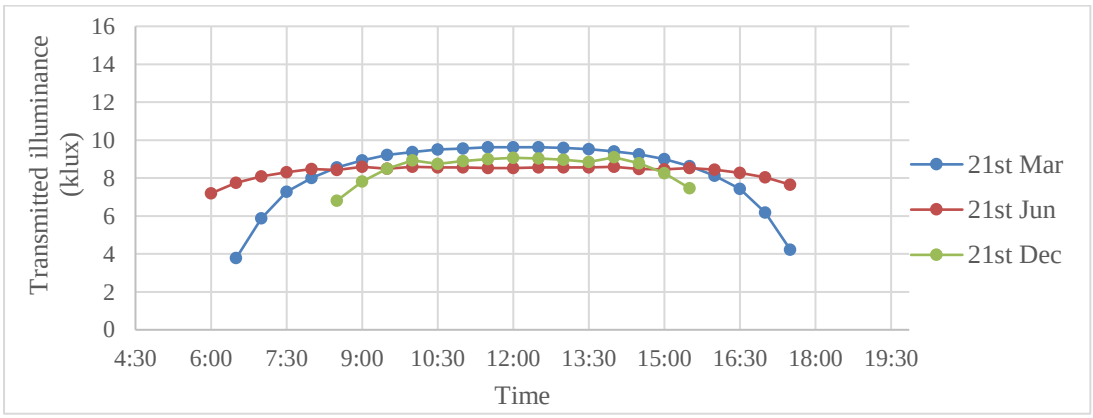
a) 29 °tilt angle



b) 37 °tilt angle



c) 45 °tilt angle



d) 53 °tilt angle

Figure 3.3.2.4. Transmitted daylight illuminance of 3D non-coated dCCPC with different tilt angles in spring equinox, summer solstice and winter solstice (Nottingham, south facing)

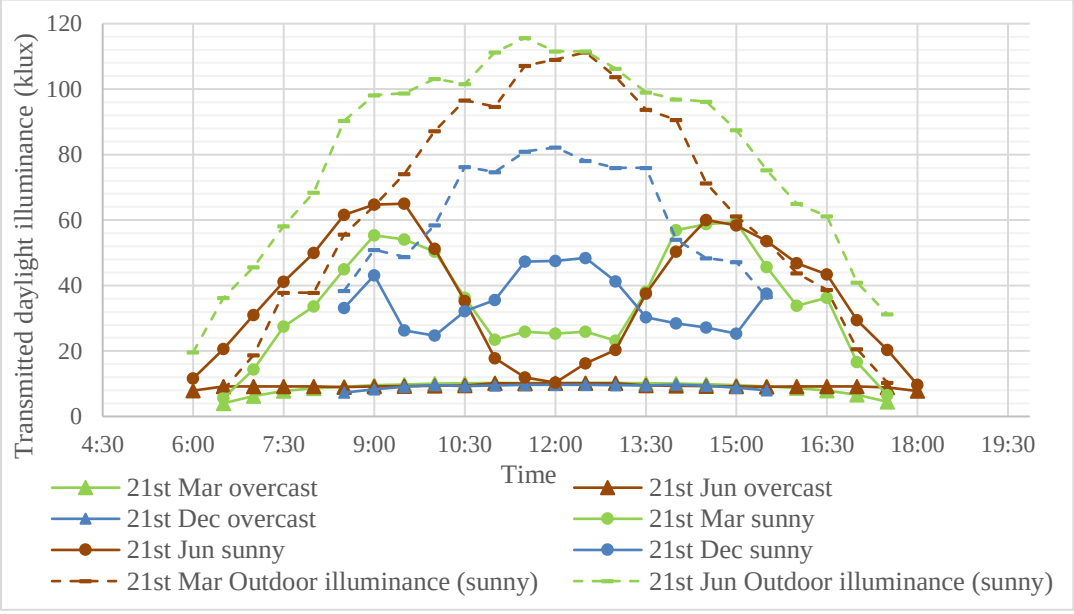
3.3.3. Discussion

This section discuss the influences of tilt angle on 3D base-coated and non-coated dCCPC. Tilt angle is an important factor which relates to the acceptance angle of dCCPC. Four tilt angles, which are 29 °, 37 °, 45 °and 53 °, are selected based on the location of Nottingham, UK (53 °N, 1.2 °W). The sunlight is controlled to different level for spring equinox, summer solstice and winter solstice as results of different tilt angles. For base coated 3D dCCPC, the control of daylight occur from 10:00 to 14:00 roughly. If the transmittances of dCCPC is divided into three levels, which are low (lower than 0.35), medium (0.3-0.65) and high (higher than 0.65), the transmittances could be summarized as shown in Table 3.3.3.1 below. It is obviously shown that as the increase of tilt angle, the transmittance of dCCPCs becomes smaller in spring

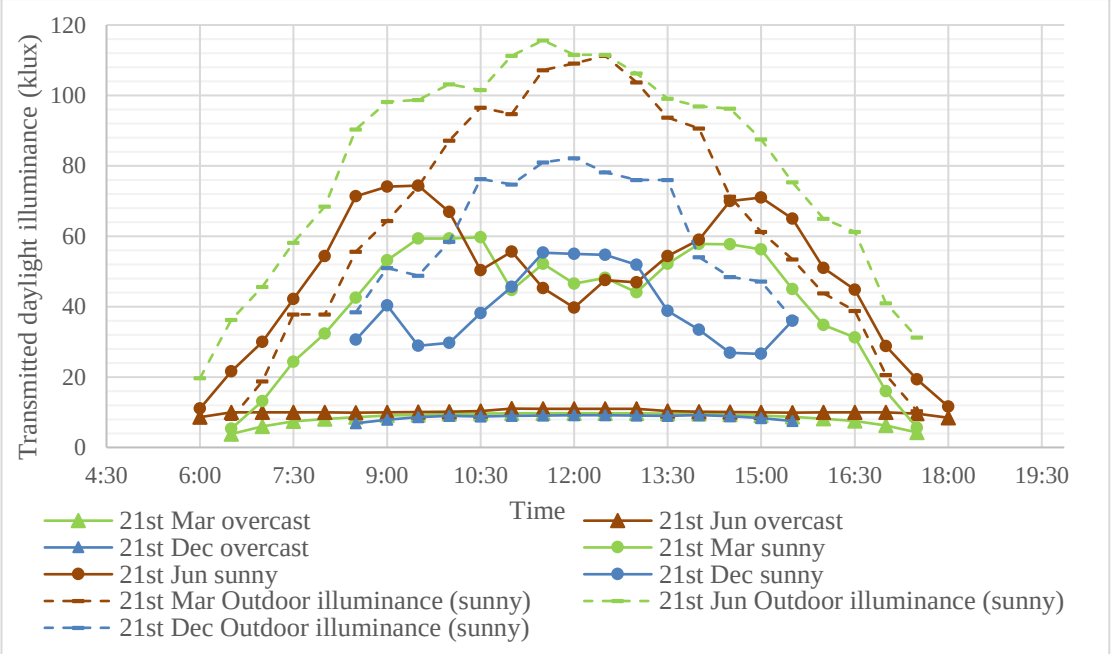
equinox and winter solstice, and increase in summer solstice. Non-coated dCCPC performs higher transmittance than base-coated one in general.

Table 3.3.3.1. Transmittance of 3D dCCPCs with different tilt angles						
	Base-coated			Non-coated		
Tilt angle	21-Mar	21-Jun	21-Dec	21-Mar	21-Jun	21-Dec
29	Medium	Low	High	Medium	Medium	High
37	Low	Low	Medium	Medium	Medium	Medium
45	Low	Low	Low	Medium	Medium	Medium
53	Low	Medium	Low	Low	Medium	Low

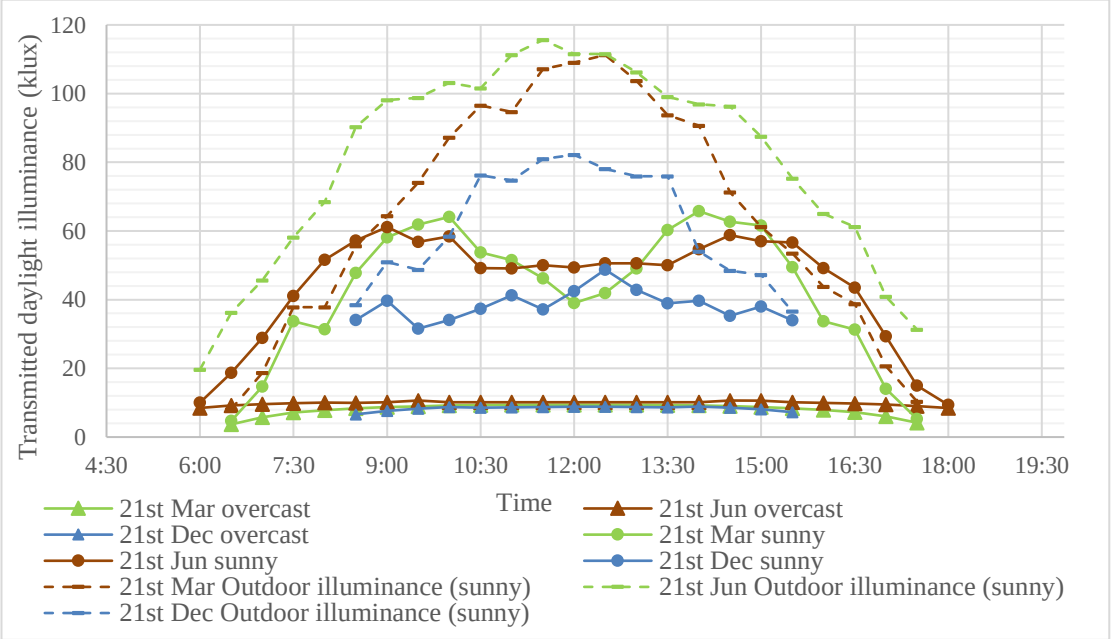
The transmitted daylight illuminance provides similar changing trends under the effects of transmittances. With the consideration of applicability in Nottingham, UK where summer is hot and winter is cold, the dCCPC with higher transmitted illuminance in winter and lower in summer is selected. Comparing with base-coated, non-coated dCCPC, provides more stable illuminance at noon which would benefit the visual comfortable indoors. Under overcast sky conditions, the transmittances differ depends on the various tilt angles, but the transmitted daylight illuminance stay at a low level, around 8-10klux, due to the low outdoor illuminance. Finally, the 3D dCCPC with 37 ° tilt angle is chosen among the base-coated types. For non-coated dCCPCs, the dCCPCs tilted to 37 °and 45 °are all suitable for practical application in Nottingham. The transmitted daylight illuminance of them are summarized in Figure 3.3.3.1.



a) 3D base-coated dCCPC tilted to 37 °



b) 3D Non-coated dCCPC tilted to 37 °



c) 3D non-coated dCCPC tilted to 45 °

Figure 3.3.3.1. Summary of the transmitted daylight illuminance for selected 3D dCCPCs

With the comparison of outdoors illuminance, it is demonstrated that the base-coated dCCPC with 37 ° tilt angle performs the desired performances, of which the lowest transmittance appears in summer, lower transmittance in spring and high transmittance in winter. This could reduce the cooling and heating load in summer and winter time

respectively. However, non-coated dCCPCs have advantages on easy manufacture and low cost. In addition, the dCCPCs tilted to both 37 ° and 45 ° provide considerable results in control daylight, which means the non-coated dCCPC could act on controlling daylight with the tilt angle between 37 ° and 45 °. The difficulty on installation in practice is reduced at the same time. Therefore, the 3D dCCPC is worth to be investigated further for base-coated and non-coated types with 37 ° and 45 ° tilt angles.

3.4. Effects of horizontal rotation angle on 3D dCCPC and r-dCPC

CPC controls light mainly by its curved surfaces. The 3D dCCPC has four curved surfaces which are used to reflect incident light to bottom surface or out of dCPC. It is easy to have deviation of angles in practical installation. Hence the tolerance of horizontal rotation angle of 3D dCCPC will be investigated then. Because 3D dCCPC is symmetry about mid-plane, four angles, which are 0 °, 15 °, 30 ° and 45 ° (Figure 3.4.1), are chosen to compare their transmittances under 37 ° tilt angle and sunny sky conditions. An improvement of 3D dCCPC structure, which is called 3D r-dCPC is compared together to investigate the optical performances. Similar to 3D dCCPC, 3D r-dCPC is divided into base-coated and non-coated types. The comparison will be taken for spring equinox, summer solstice and winter solstice under sunny and overcast sky respectively.

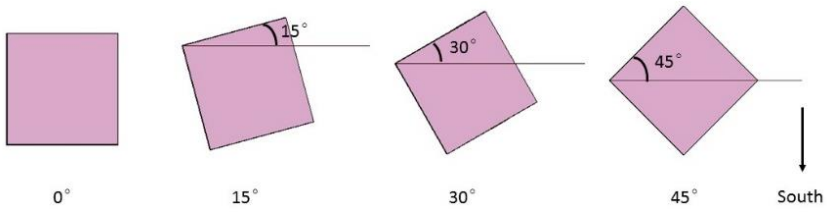


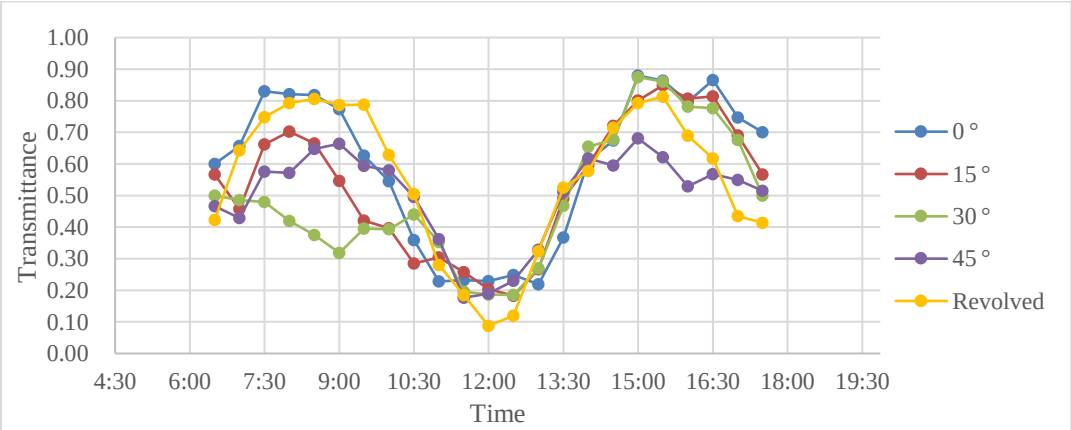
Figure 3.4.1. Top view of 3D dCCPC with different horizontal rotation angle

3.4.1. Effects of horizontal rotation angle of 3D dCPCs under sunny sky

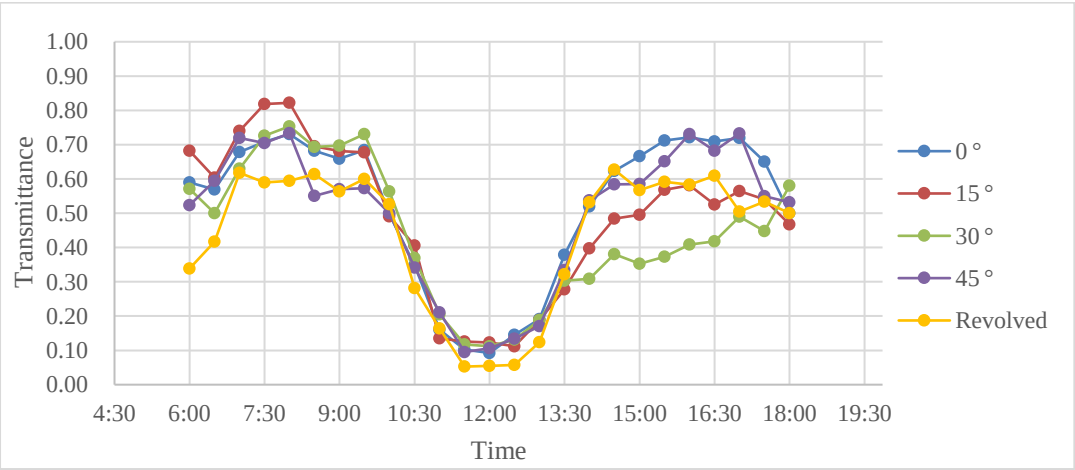
3.4.1.1. Base-coated dCPCs

The horizontal rotation angle does affect the transmittance of 3D base-coated dCCPC according to Figure 3.4.1.1. For the dCPC without horizontal rotation (0 °), the curve of transmittance is almost symmetric about the Y axis at 12:00. However, the transmittances of dCPCs with 15 ° and 30 ° are not symmetric. Both of them perform

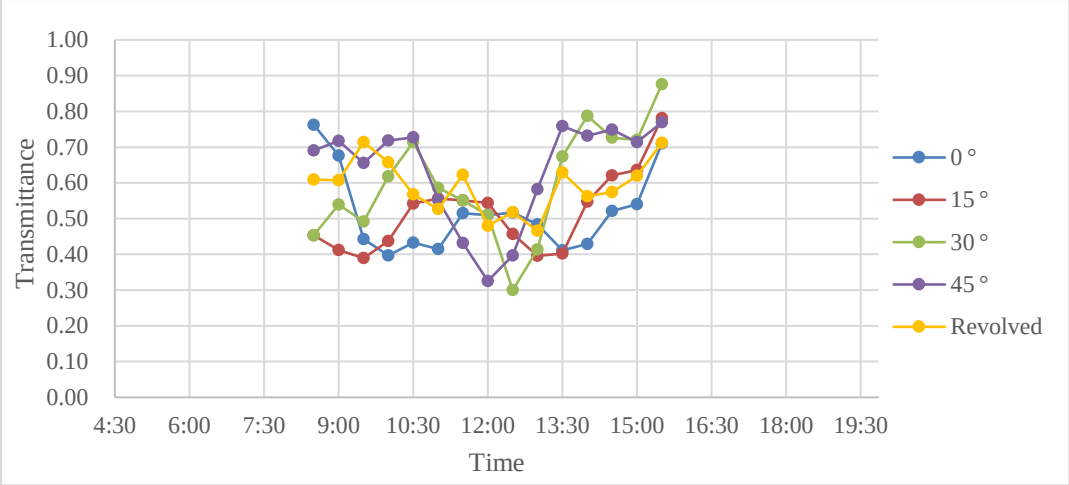
lower transmittances in the morning than that in the afternoon in spring equinox, and lower transmittances in the afternoon than that in the morning in summer equinox. In spring equinox, the dCPC without rotation provides longer control to daylight which is between 10:30 to 13:30, for the other three dCPCs, the period of controlling light at noon is around 11:30 to 1:00. The transmittance of dCPC with 45 °horizontal rotation angle is almost symmetric about the Y axis at noon as well, while it has lower transmittance in the morning and afternoon than the dCPC with 0 °rotation angle in summer solstice. It is worth to point out that this dCPC also provide daylight control at noon in winter solstice which is different from all the other three dCPCs. However, the r-dCPC demonstrates the similar transmittance with non-rotational dCCPC.in spring equinox; the transmittances in summer and winter solstice seems to be close to the average of dCCPCs with different rotation angles. In order to compare the practical performance, the transmitted daylight illuminance through dCPCs are shown in Figure 3.4.1.2.



(a) Spring equinox

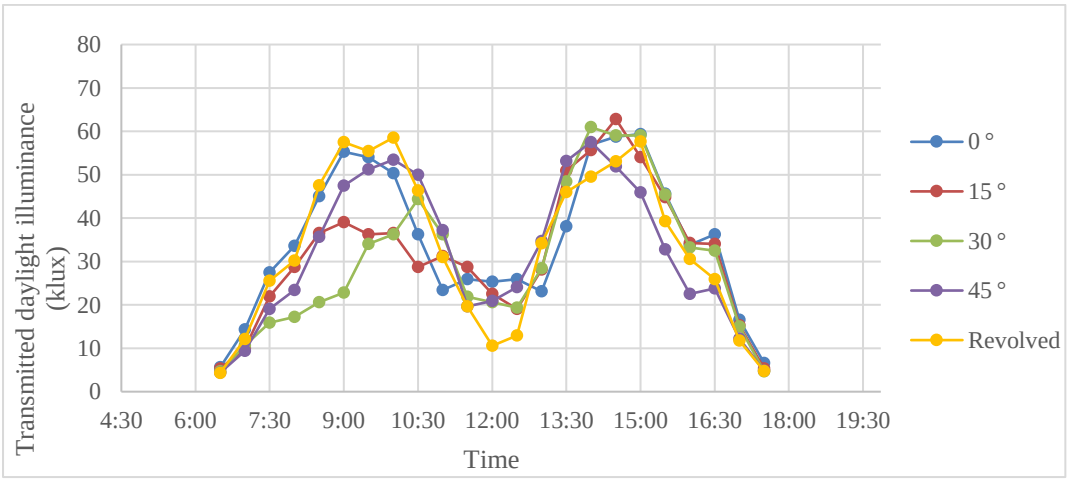


(b) Summer solstice

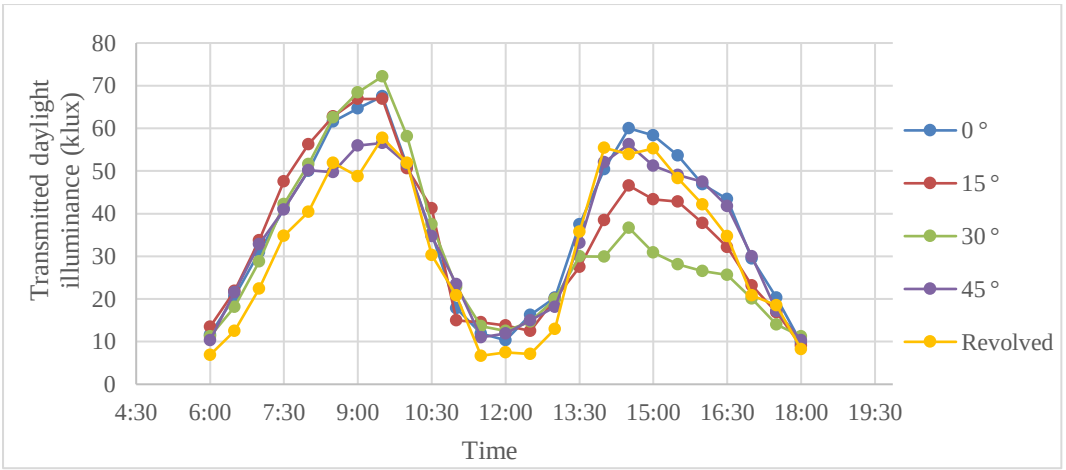


(c) Winter solstice

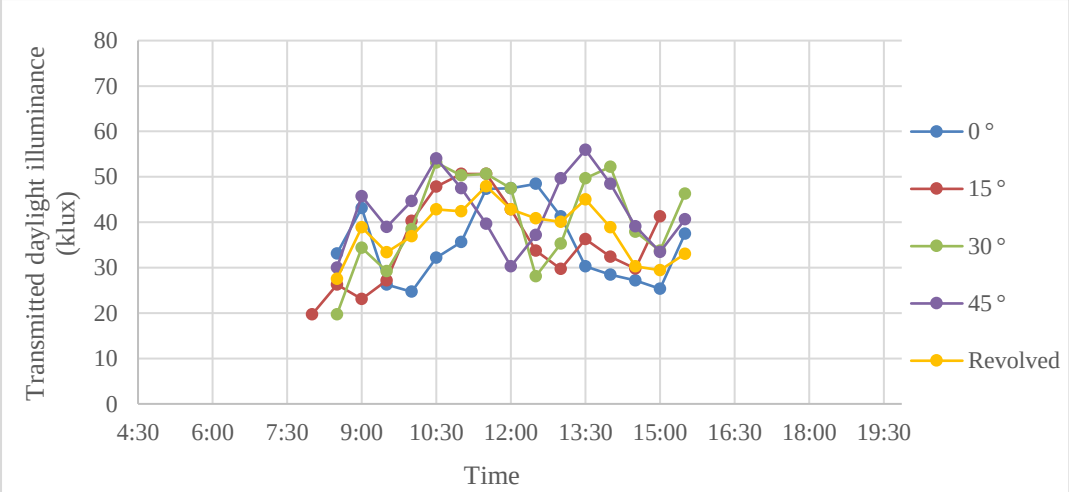
Figure 3.4.1.1. Transmittance of 3d base-coated dCCPC with 0 °, 15 °, 30 °and 45 ° horizontal rotation angle and 3D base-coated r-dCPC under sunny sky (Nottingham, south facing, 37 °tilted)



(a) Spring equinox



(b) Summer solstice



(c) Winter solstice

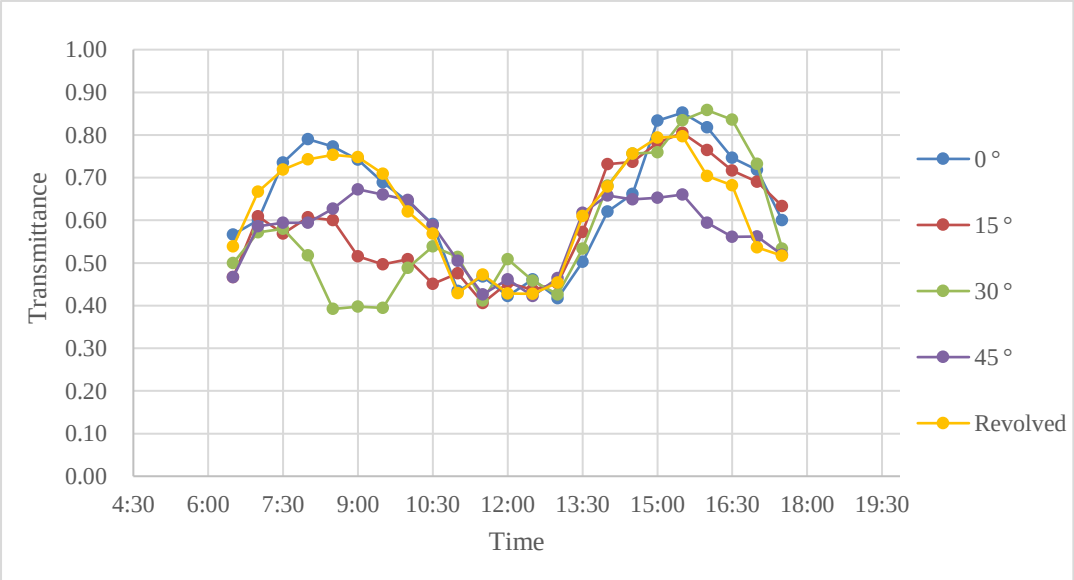
Figure 3.4.1.2. Transmitted daylight illuminance of 3d base-coated dCCPC with 0 °, 15 °, 30 °and 45 °horizontal rotation angle and 3D base-coated r-dCPC under sunny sky (Nottingham, south facing, 37 °tilted)

With the influences of transmittance, the transmitted illuminance shows similar properties. Comparing with the symmetric changing trend of the dCPC without rotation, the transmitted illuminance of dCPCs with 15 °and 30 °rotation angle in the morning are lower than that in the afternoon in spring equinox, and this is reversed in summer solstice. The dCPC without rotation controls the illuminance level under 50klux from 10:00 to 15:00 in spring equinox, while the other three dCPCs have same results between 11:30 and 13:00. The dCPC with 45 ° horizontal angle has better control of daylight during the whole day of summer solstice: the transmitted illuminance is 45klux which is much smaller than the peak illuminance, 60-70klux, provided by other three dCPCs. In winter solstice, it reduces the illuminance to 30klux at noon. For other three dCPCs, the transmitted illuminance is around 50-60klux. Both dCCPC and r-dCPC perform excellent daylight control in spring equinox and summer solstice, which achieve the objective to provide high illuminance level in the morning/afternoon and reduce solar gain at noon. In winter, the relatively stable transmitted illuminance could reduce the heating load.

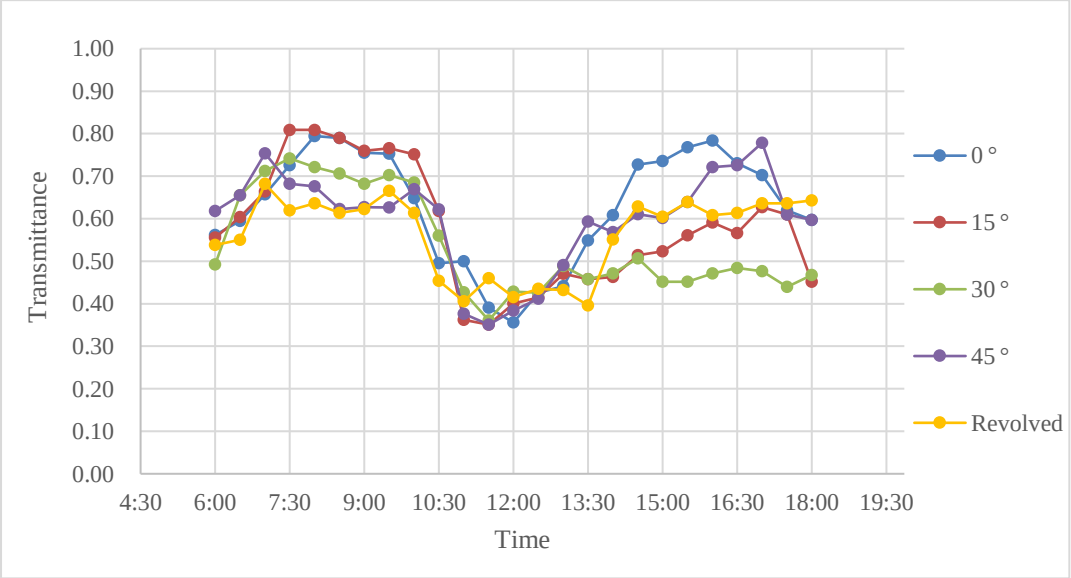
3.4.1.2. Non-coated dCPCs

The properties of transmittances for the 3D non-coated dCCPCs in different horizontal rotation angle are same with the properties for 3D base-coated dCPC. According to Figure 3.4.1.3 and 3.4.1.4, the transmittances of dCPCs with 15 ° and 30 ° in the

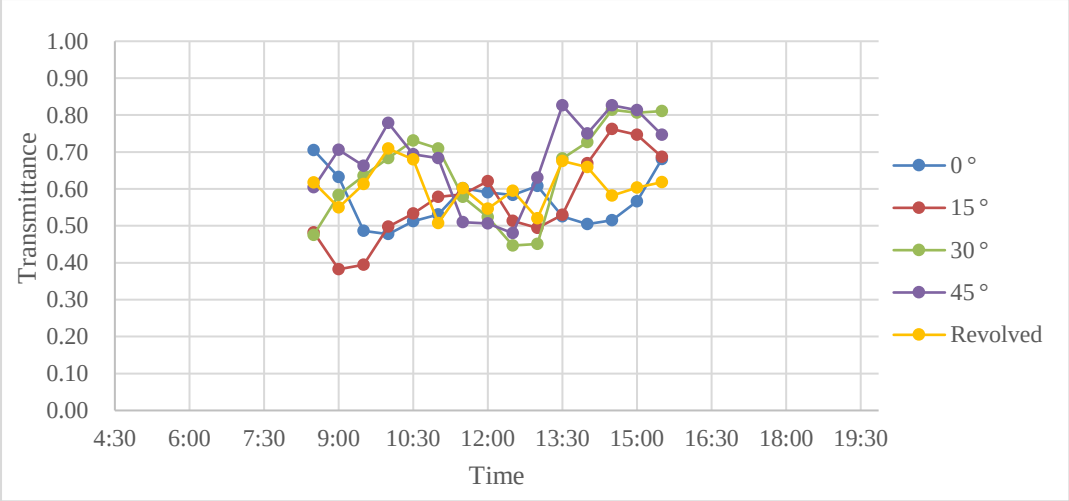
morning are lower than them in the afternoon in spring equinox, and reversed in summer solstice. The dCPC with 45 °rotation angle still has better control on the peak illuminance for the summer solstice day and the lowest transmittance is 30klux which is enough for indoor environment. The transmitted illuminance for winter solstice day are close for the four different types of dCPCs. The transmittance and transmitted illuminance of 3D r-dCPC take the average value of 3D dCCPCs with different rotation angles approximately.



(a) Spring equinox

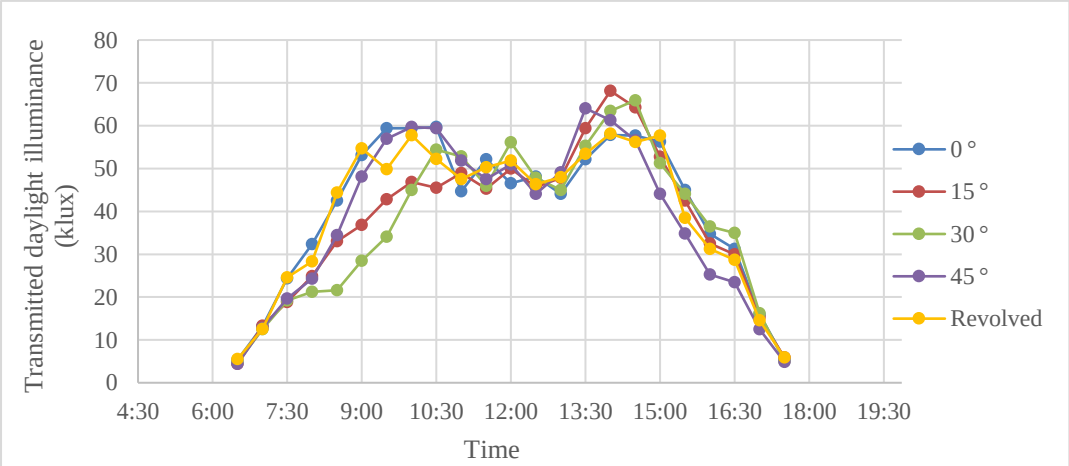


(b) Summer solstice

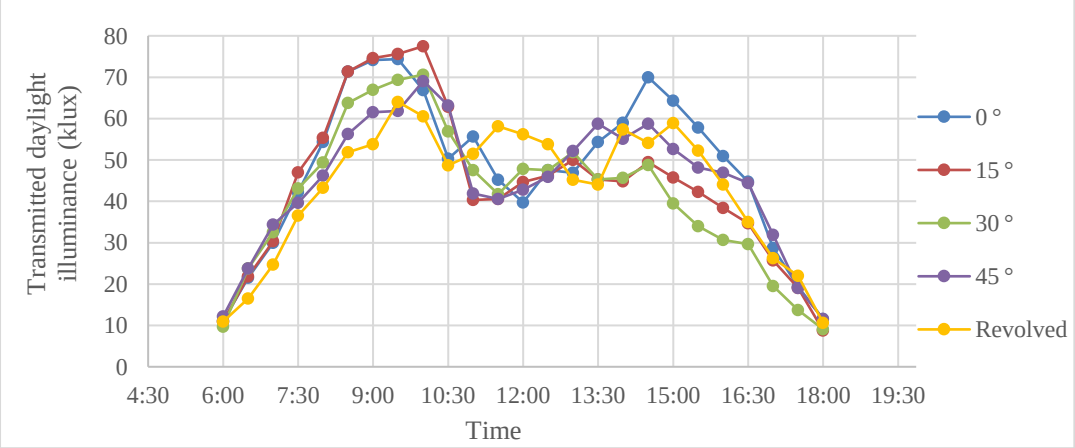


(c) Winter solstice

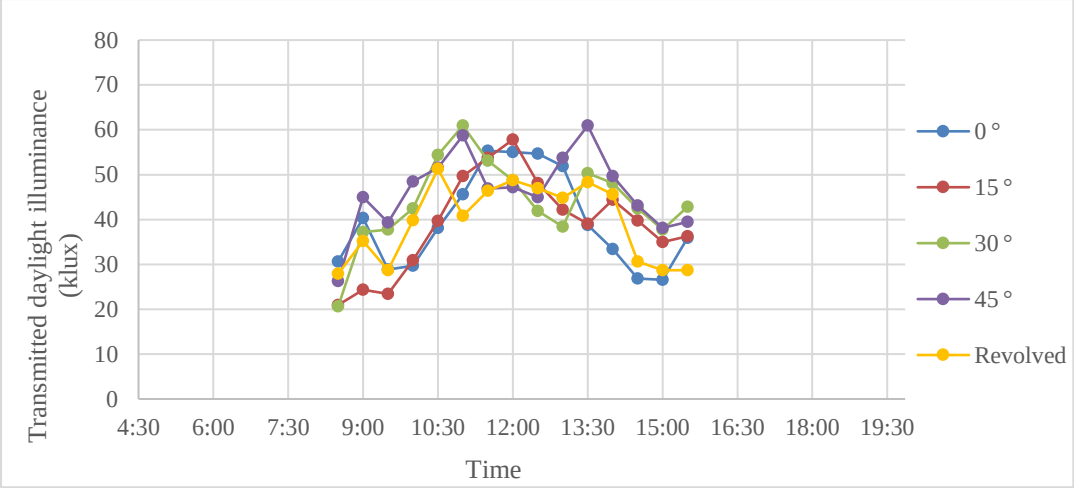
Figure 3.4.1.3. Transmittance of 3D non-coated dCCPC with 0 °, 15 °, 30 °, 45 ° horizontal rotation angle and 3D non-coated r-dCPC under sunny sky (Nottingham, south facing, 37 °tilted)



(a) Spring equinox



(b) Summer solstice



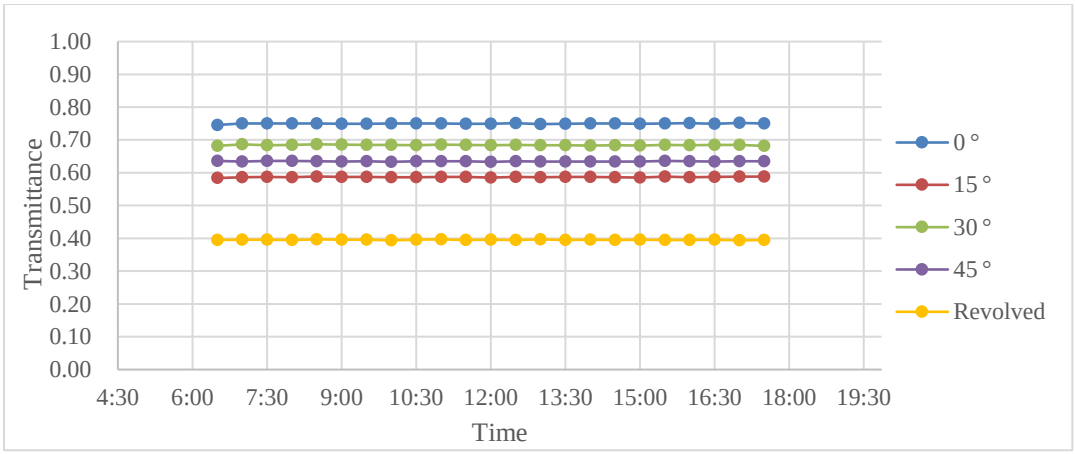
(c) Winter solstice

Figure 3.4.1.4. Transmitted daylight illuminance of 3d non-coated dCCPC with 0 °, 15 °, 30 °, 45 °horizontal rotation angle and 3D non-coated r-dCPC under sunny sky (Nottingham, south facing, 37 °tilted)

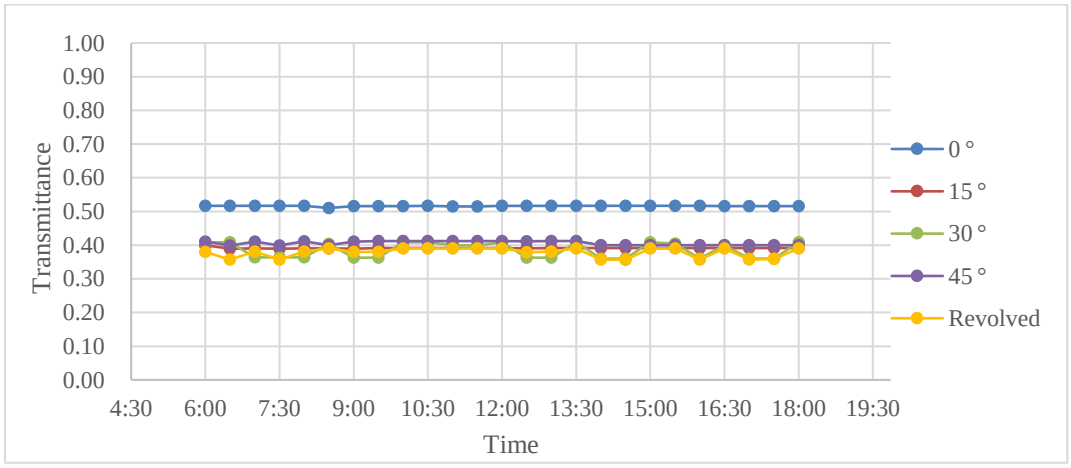
3.4.2. Effects of horizontal rotation angle of 3D dCPCs under overcast sky

3.4.2.1. Base-coated dCPCs

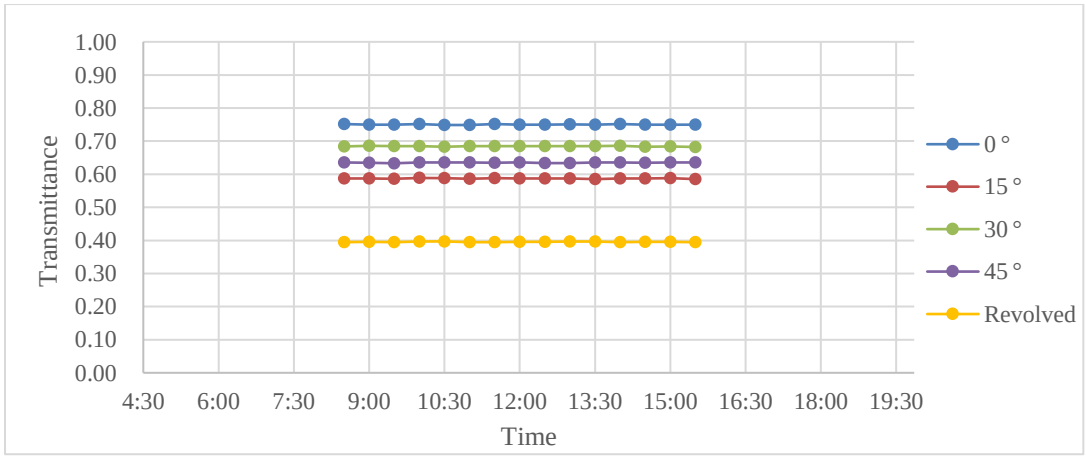
The transmittances of 3D base-coated dCCPC and r-dCPC are shown in Figure 3.4.2.1. Because the diffused daylight takes main proportions under overcast sky condition, the transmittances of dCPCs stay stable in one day approximately. However, the sun position also causes slightly differences in transmittance between dCCPC and r-dCPC. In spring equinox, dCCPC without horizontal rotation performs the highest transmittance which is around 0.75, and dCCPC with 15 °rotation angle has the lowest transmittance, about 0.6, among all the 3D dCCPCs. The transmittance of 3D r-dCPC is 0.4 which is much smaller than dCCPCs. In summer solstice day, the transmittances for all dCPCs keeps at 0.4 except 3D dCCPC without horizontal rotation which transmittance is 0.5. The transmittances of dCCPC and r-dCPC are similar to them in spring equinox due to the lower altitude of the sun comparing with summer solstice.



a) Spring equinox



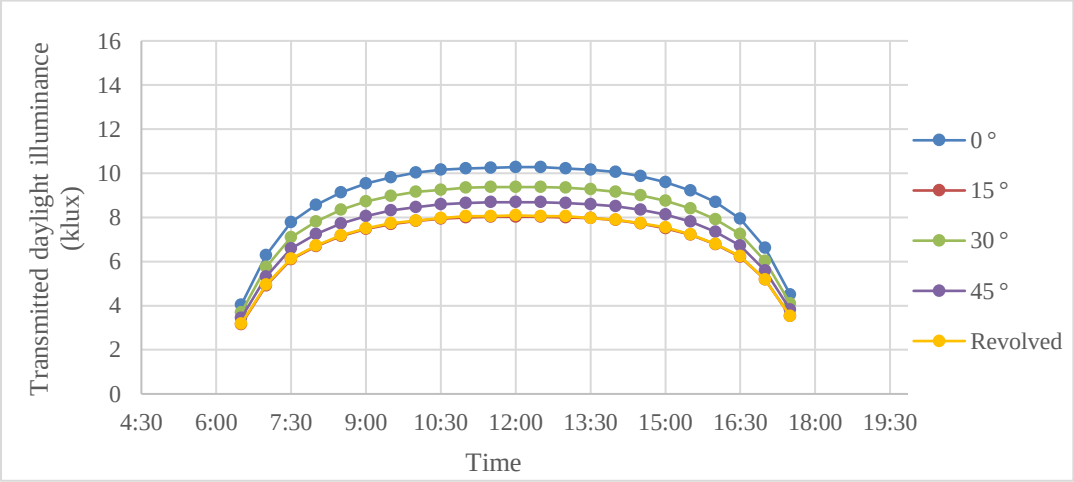
b) Summer solstice



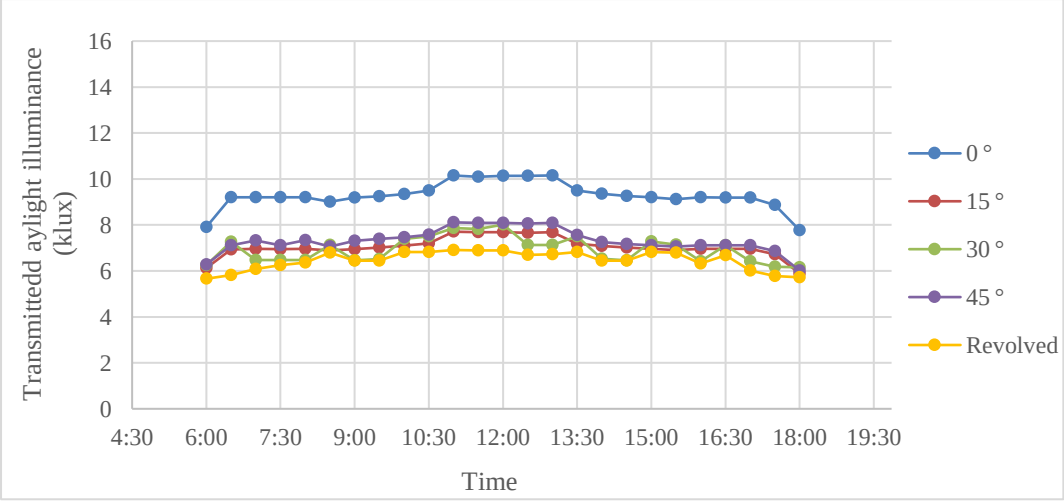
c) Winter solstice

Figure 3.4.2.1. Transmittance of 3d base-coated dCCPC with 0 °, 15 °, 30 °and 45 ° horizontal rotation angle and 3D base-coated r-dCPC under overcast sky (Nottingham, south facing, 37 °tilted)

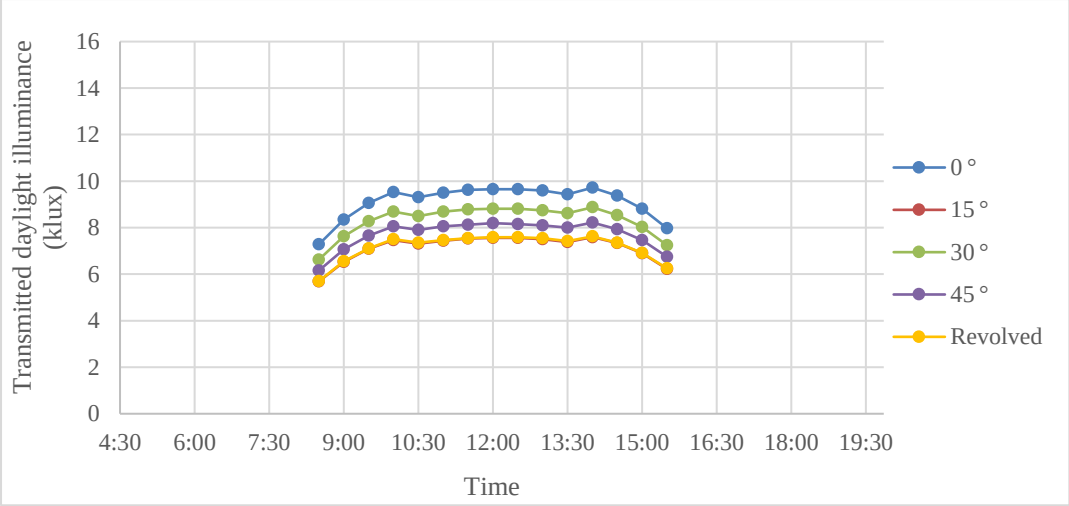
The transmitted daylight illuminance of 3D dCPCs are shown in Figure 3.4.2.2. The low outdoor illuminance results in low transmitted daylight illuminance comparing with sunny sky. The difference between transmitted illuminance of different types of dCPCs are affected by their transmittances. However, the big difference in transmittances only causes small deviations in transmitted illuminance on account of the low outdoor illuminance. For instance, in spring equinox, the biggest gap of transmitted daylight illuminance between 3D dCCPC without rotation and r-dCPC appears at noon is only 2klux, and similar to summer solstice and winter solstice. The transmitted daylight illuminance ranges between 6klux to 10klux in daytime at different seasons.



a) Spring equinox



b) Summer solstice

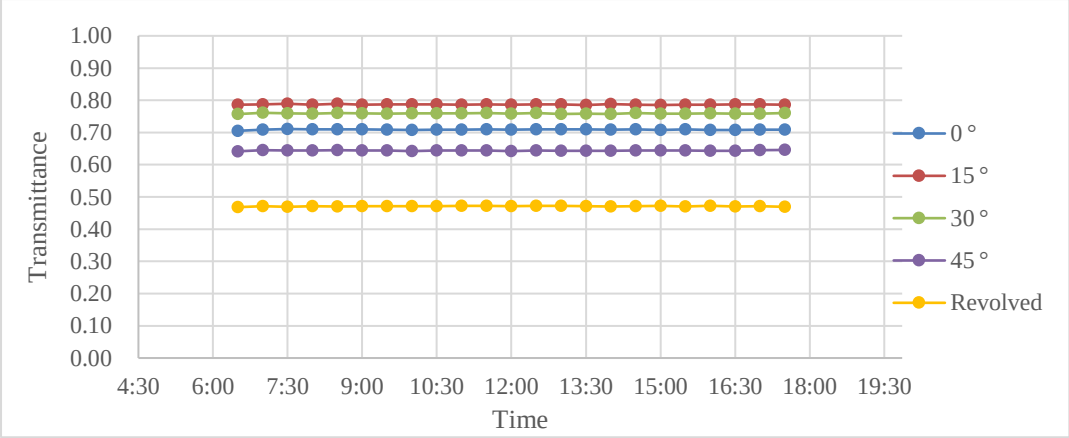


c) Winter solstice

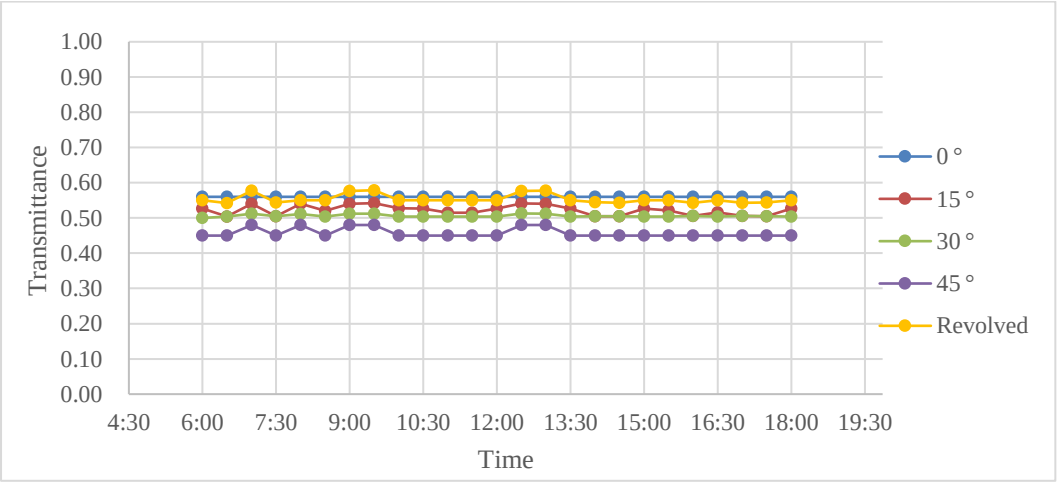
Figure 3.4.2.2. Transmitted daylight illuminance of 3d base-coated dCCPC with 0 °, 15 °, 30 °and 45 °horizontal rotation angle and 3D base-coated r-dCPC under overcast sky (Nottingham, south facing, tilted 37 °)

3.4.2.2. Non-coated dCPCs

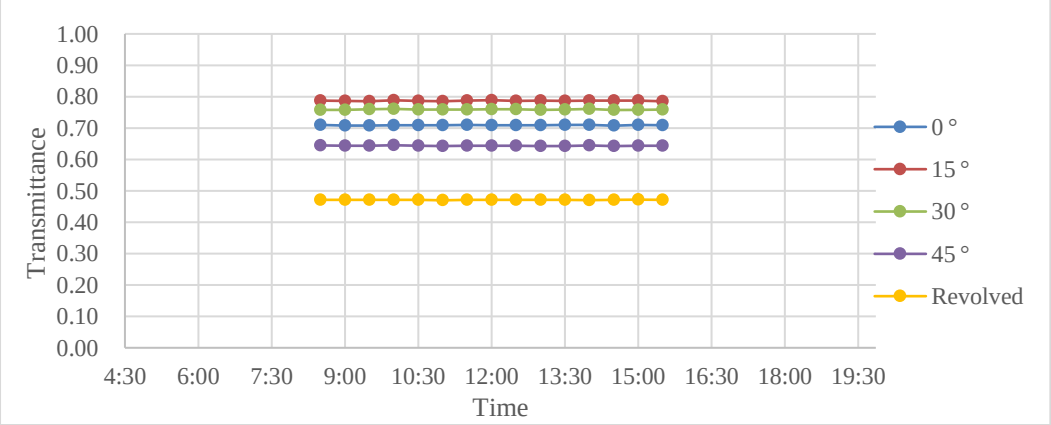
The comparison of transmittances for 3D non-coated dCPCs are shown in Figure 3.4.2.3. Similar to base-coated dCPCs, the transmittances for non-coated dCPCs also stay stable in different time for one day. As a result of the non-absorbing base, the transmittance of non-coated dCPCs are slightly higher than the base-coated ones. In spring equinox and winter equinox, dCPCs perform same transmittances; r-dCPC provides smallest transmittance around 0.5 and dCCPCs provides higher transmittances which ranges from 0.65 to 0.8 differing from the horizontal angles. In summer equinox, the transmittances of them are within 0.45 to 0.6. However, the transmitted daylight illuminance for non-coated dCPCs are close owing to the low outdoor illuminance shown in Figure 3.4.2.4. The biggest gap is 2klux which is same as base-coated dCPCs. The illuminance range for all types of 3D non-coated dCPCs is 7-11klux approximately which is 1klux higher than base-coated dCPCs.



a) Spring equinox

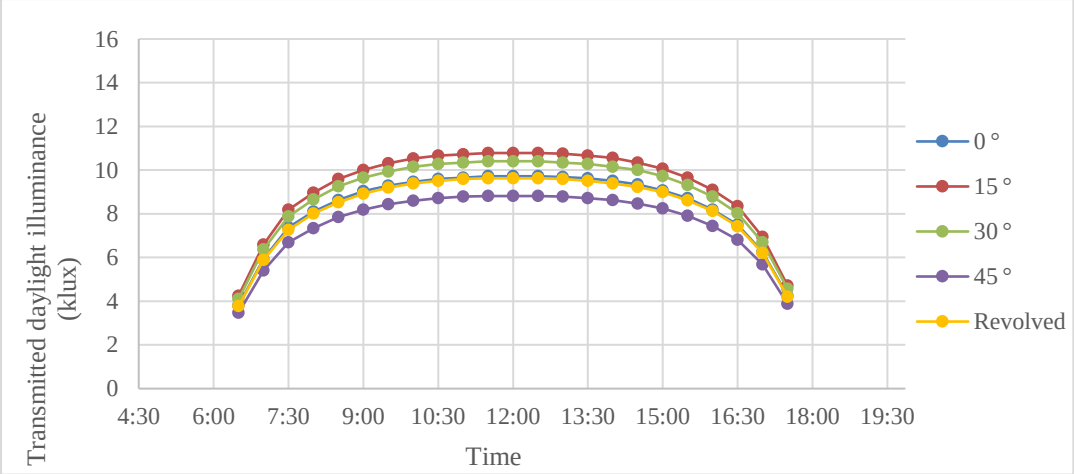


b) Summer solstice

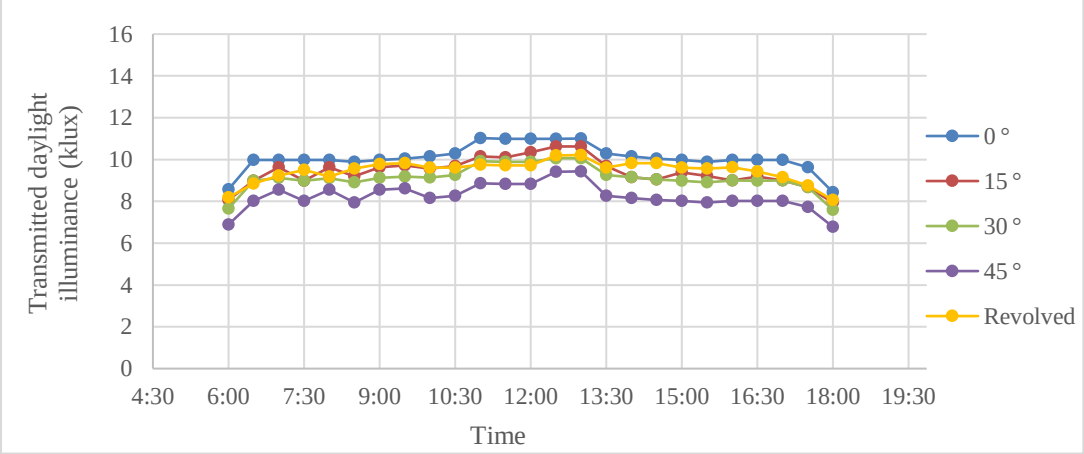


c) Winter solstice

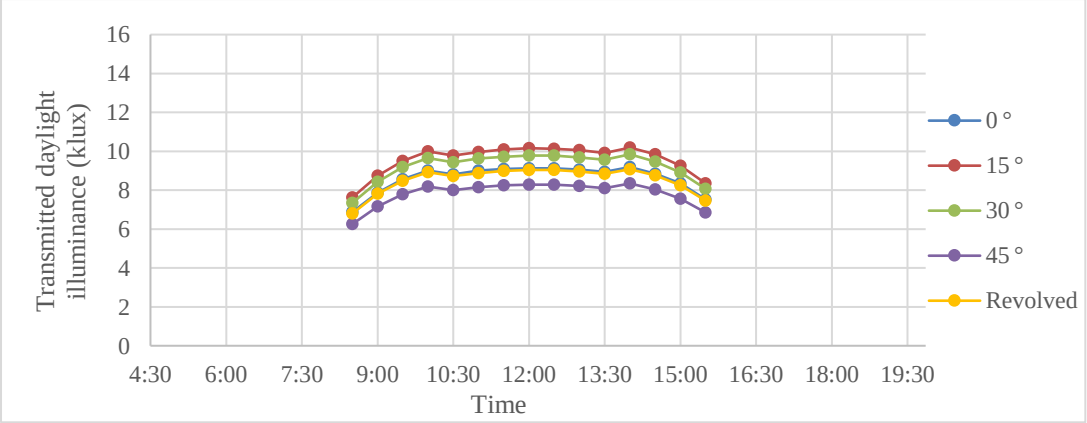
Figure 3.4.2.3. Transmittance of 3D non-coated dCCPC with 0 °, 15 °, 30 °, 45 ° horizontal rotation angle and 3D non-coated r-dCPC under overcast sky (Nottingham, south facing, 37 °tilted)



a) Spring equinox



b) Summer solstice



c) Winter solstice

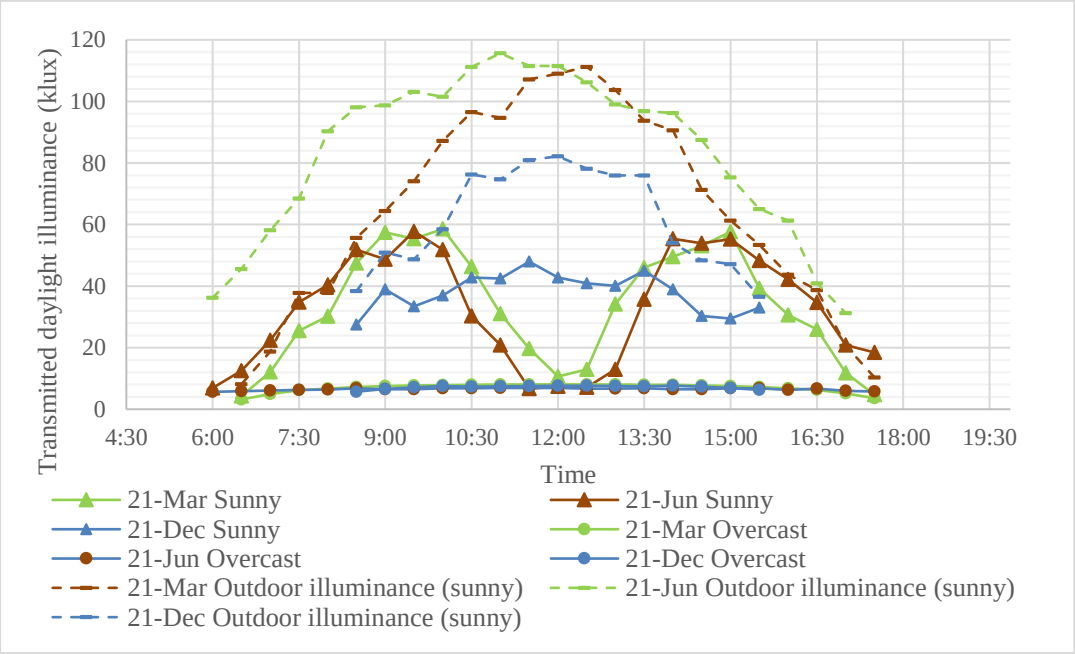
Figure 3.4.2.4. Transmitted daylight illuminance of 3d non-coated dCCPC with 0 °, 15 °, 30 °, 45 °horizontal rotation angle and 3D non-coated r-dCPC under overcast sky (Nottingham, south facing, 37 °tilted)

3.4.3. Discussion

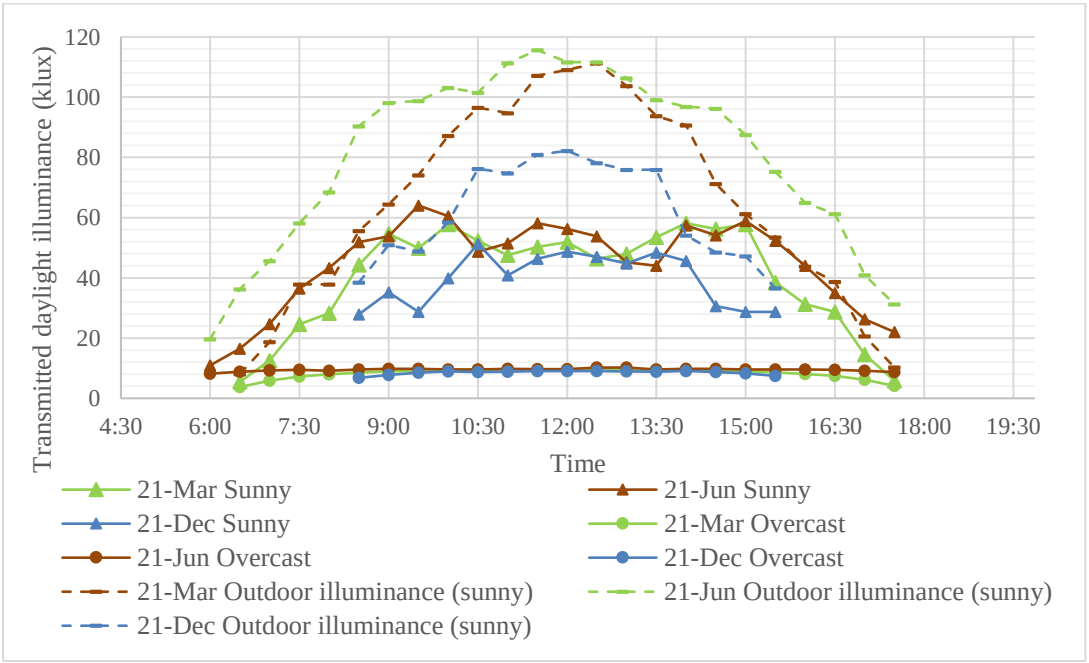
This section investigated the tolerance of horizontal rotation angle for 3D dCCPC and compared it with 3D revolved dCPC (r-dCPC). For both base-coated and non-coated types, results show that 3D dCCPC without horizontal rotation and 45 °has symmetric optical performances in the morning and afternoon about 12:00 while the 3D dCCPCs rotated to 15 ° and 30 ° demonstrate non-symmetric optical properties. 3D r-dCPC has similar optical performances with 3D dCCPC and do not need to concern the effect of horizontal angular deviations. This principle is appropriate not only for dCPCs with 37 ° tilt angle, but also for dCPCs with 29 °, 45 ° and 53 ° tilt angles. In practical installation, it is difficult to control the angular deviations, which may affect the solar distribution in room. The advantages of r-dCPC is stand out. It has similar control ability compared to dCCPC and does not need to concern the angular deviation in practical installation.

Therefore, the potential of application for 3D base-coated and non-coated r-dCPCs tilted to 37 ° are worth to be discussed. Figure 3.4.2.5 compares the transmitted daylight illuminance of this two types of r-dCPCs. The 3D non-coated r-dCPC with 45 ° tilt angle also has high potential in practical application. The results of 3D non-coated r-dCPC with 45 ° tilt angle is demonstrated as well in Figure 3.4.2.6. With the comparison of outdoor illuminance under sunny sky, it can be seen that 3D r-dCPC does perform effective control on daylight. Base-coated r-dCPC provides stronger control on daylight at noon, between 10:30 to 13:30, in spring equinox and summer solstices. During this time, the transmitted daylight illuminance ranges from 10-30klux. For non-coated type, r-dCPCs with 37 ° and 45 ° tilt angles perform almost same results. It could be deduced that the 3D non-coated r-dCPC provides similar transmitted daylight illuminance when the tilt angle ranges between 37 ° and 45 °. The daylight illuminance is within 40-60klux. The optical performances of non-coated and base-coated in winter are almost same. Under overcast sky conditions, base-coated and non-coated r-dCPCs provide similar indoor illuminance level at around 8klux in different seasons. Therefore, the steady illuminance provided by non-coated r-dCPC between 8:00 to 16:00 can bring more comfort experience to occupancies. In addition, base-coated r-dCPC is much more difficult in manufacture and requires higher cost. The 3D non-coated r-dCPC may be the best choice in application with the advantages

of installation, bigger tolerance in tilt angle, more stable illuminance level it provides and lower cost in manufacture.



a) Base-coated 3D r-dCPC



b) Non-coated 3D r-dCPC

Figure 3.4.2.5. Outdoor illuminance and transmitted daylight illuminance of 3D base-coated and non-coated r-dCPC in spring equinox, summer solstice and winter solstice under sunny/overcast sky (Nottingham, south facing, tilted 37 °)

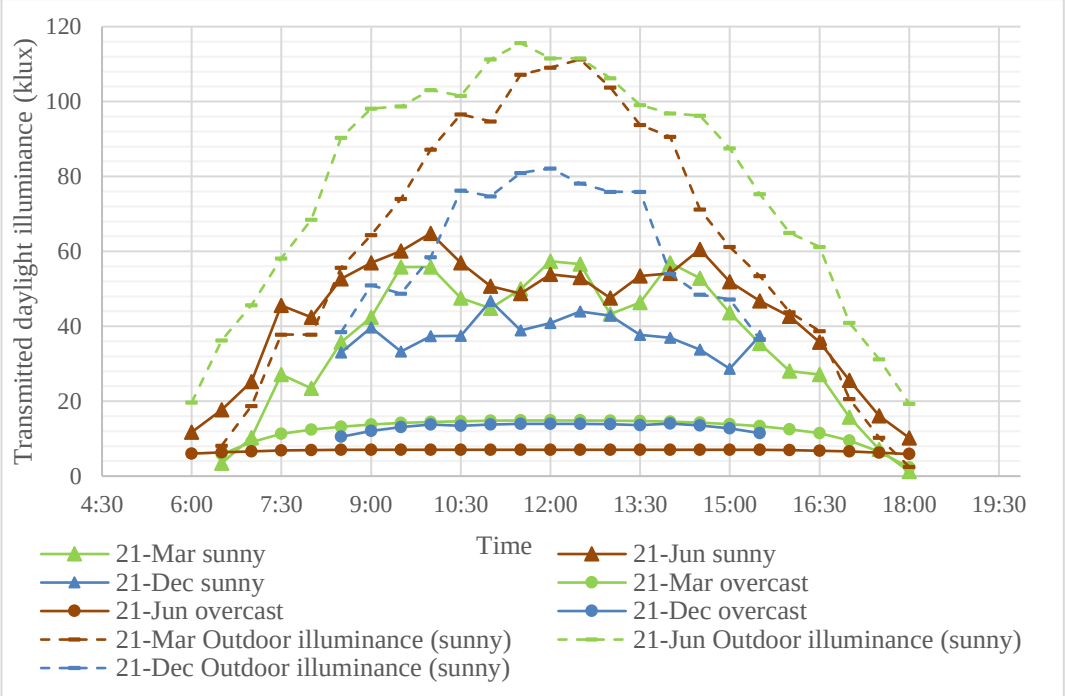


Figure 3.4.2.6. Outdoor illuminance and transmitted daylight illuminance of 3D non-coated r-dCPC in spring equinox, summer solstice and winter solstice under sunny/overcast sky (Nottingham, south facing, tilted 45 °)

3.5. Summary

This chapter is a further research on two dimensional dielectric compound parabolic concentrator (2D dCPC), which provides a general view of the optical performance of using 3D dCPC in daylighting control. Two different three-dimensional (3D) dCPCs are put forward. One is 3D dCCPC with four parabolic surfaces and square apertures, the other is 3D r-dCPC with the curved surface by revolving the parabola and cubic apertures. In addition, each type of dCPC is separated into base-coated and non-coated. The transmittance and transmitted daylight illuminance are selected to compare the optical properties for dCPCs in three specific days which are spring equinox, summer solstice and winter solstice.

Firstly, the optical performances of 2D dCPC, 3D dCCPC and right square pyramid structure are compared with the change of incident angle of light beam. 3D base-coated dCCPC performs almost same optical properties comparing with 2D dCPC for base-coated type while for non-coated dCPCs, 3D dCCPC has better ability on controlling incident light than 2D dCPC but worse than the base-coated 2D and 3D dCPCs. The right square pyramid structure performs poor control on light with the

change of incident angle. Then the control ability of 2D and 3D dCPCs are explored in respect of transmittance and transmitted daylight illuminance. Results demonstrate that 3D dCCPCs have strong control not only in different seasons during whole year, but also at different time in one day.

The influences by tilt angle of 3D dCCPC is investigated as well. Four tilt angles, which are 29 °, 37 °, 45 ° and 53 °, are selected based on the location of Nottingham, UK (53 °N, 1.2 °W). It is demonstrated that as the increase of tilt angle, the transmittance of dCPCs becomes smaller in spring equinox and winter solstice, and increase in summer solstice. The 3D dCPC with 37 ° tilt angle is chosen among the base-coated types, of which the lowest transmittance appears in summer, lower transmittance in spring and high transmittance in winter. For non-coated dCPCs, the dCPCs tilted to 37 ° and 45 ° perform close results in transmitted daylight illuminance, which are all suitable for practical application in Nottingham.

Finally the tolerance of horizontal rotation angle for 3D dCCPC is put forward and compared with 3D r-dCPC. The four selected horizontal rotation angles are 0 °, 15 °, 30 ° and 45 °. Results show that 3D dCCPC without horizontal rotation and 45 ° has symmetric optical performances in the morning and afternoon about 12:00 while the 3D dCCPCs rotated to 15 ° and 30 ° demonstrate non-symmetric optical properties. 3D r-dCPC has similar optical performances with 3D dCCPC and do not need to concern the effect of horizontal angular deviations due to installation, which is a better choice in practical installation.

To conclude, in this chapter, the current solutions got from the results are: 3D base-coated r-dCPC with 37 ° tilt angle is the best choice for the buildings require strong control of sunlight in spring and summer time; 3D non-coated r-dCPC with 37 ° - 45 ° tilt angle are a better solution for controlling daylight in application with the advantages of installation, bigger tolerance in tilt angle, more stable illuminance level it provides and lower cost in manufacture; 3D dCCPC has similar optical performance with 3D r-dCPC. However, because the results given in this chapter is based on the preliminary research of dCPC and aims to show the feasibility of using it for daylighting control, there still are some limitations should be considered here and they would be discussed in the following parts of this thesis. First, because the complexity of 3D dCPC, its optical performance is determined by various criteria which are not

explained in this chapter in detail. In Chapter 5 and Chapter 6, they are investigated and discussed in several novel ways to figure out the relationship between them. Second, this chapter provides a best solution of the type of dCPC for daylighting control, but the practical factors should be considered when it is applied in building. Chapter 4 and Chapter 7 give some new concerns as using it in practice and propose the solutions for further improvements.

Chapter 4

Manufacture and experiment design of dielectric crossed compound parabolic concentrator (dCCPC) panel

4.1. Introduction of 3D dCCPC panel properties

According to the simulation results of individual CPC component in previous chapter, it was found that both base-coated and non-coated dielectric-filled 3D crossed CPC (dCCPC) performs excellent capabilities on control direct sunlight at noon and warm seasons. The CPC discussed in this chapter is 3D dCCPC unless otherwise stated. The simulation results of CPC component were obtained under the ideal design of CPC structure. When designing CPC panel for practical applications, many factors that affect CPC performance should be considered. As CPC panel is used as building facade, especially for skylight, it is expected to be designed as thin as possible to reduce its weight. In addition, the manufacture limitations and sturdiness of CPC panel should be taken into account in practice. Hence, considering the CPC panel structure and design objectives, three criteria were put forward to be investigated their effects on CPC panels, which are conjunction cover, truncation and gap between CPC components as shown in Figure 4.1.1. Conjunction cover is used to integrate CPC components. Truncations on CPC components can reduce the height of CPC in order to reduce the weight of panel effectively. The gap between CPC components come from the limitations of the minimum spacing in manufacture of computer numeric control (CNC) machine.

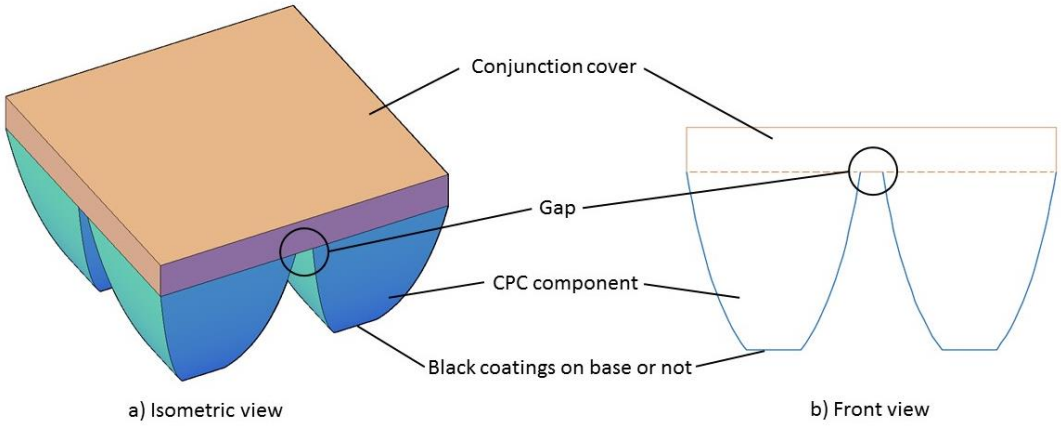


Figure 4.1.1 Schematic diagram of designed CPC panel with four CPC components

In the following parts of this chapter, the three criteria will be discussed one by one to find the best design of CPC panels, which is illustrated in the flow chart as shown in Figure 4.1.2. Original CPC panel is composed of arrayed Individual CPC components. Firstly, the effect of conjunction cover on CPC panel will be investigated. The CPC panels with conjunction cover are compared to the original CPC panel. Then, the CPC

panel consisting of truncated CPCs are simulated to compare its performance with original CPC panel. In order to explore the effect of truncation and conjunction, the performance of truncated CPC panel with conjunction cover is studied. After that, the effect owing to the gap between CPC components is investigated. In addition, the relationships between the three criteria, which are conjunction cover, truncation and gap, are discussed. Finally, the CPC panel is scaled down to further minimize its size. The performance of scaled CPC panel is presented. The optical performances of both base-coated and non-coated CPC panels will be demonstrated. Each CPC panel used for simulation was square and consisted of 900 (30×30) individual CPC components in order to ensure the accuracy of simulation.

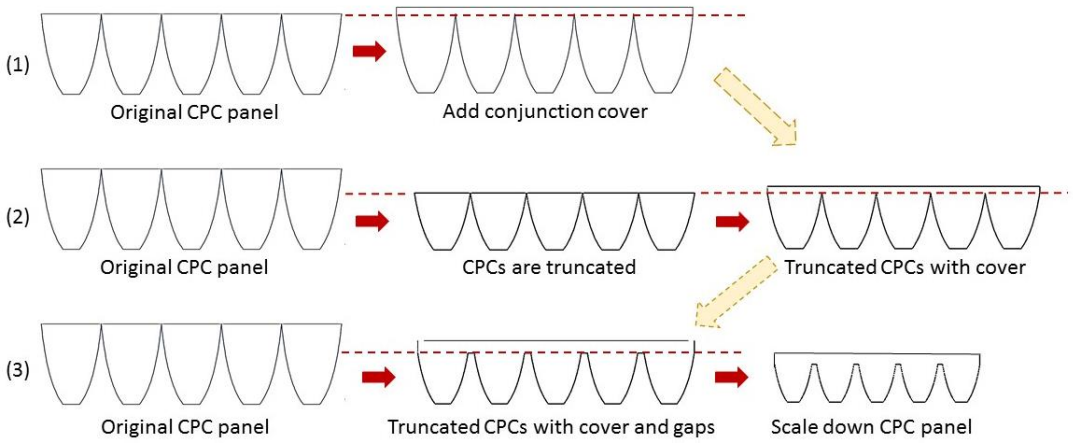


Figure 4.1.2 Flow chart of CPC panel design process (In section view)

4.2. Effects of design criteria on CPC panel performance

4.2.1. Conjunction cover

For either base-coated or non-coated dCPC panels, the cover thicknesses of CPC panels were increased from 1mm to 8mm with 1mm intervals in order to investigate the effects of cover thickness. Figure 4.2.1.1 illustrates the transmittance of covered base-coated and non-coated CPC panels relative to the incident angle. In macro view, effect of cover thickness was quite small. For example, the largest transmittance reduction was 0.0311 for non-coated CPC panel with the cover of 8mm thick at the light incident angle of 70 °which had 4.2% transmission loss comparing with the non-coated CPC panel without cover. However, from Figure 4.2.1.2, it can still be found that the transmittance decreased gradually with the increase of cover thickness for the same incident angle. The reduction of transmittance was the biggest when the incident angle is between 60 °-70 °for each CPC panel.

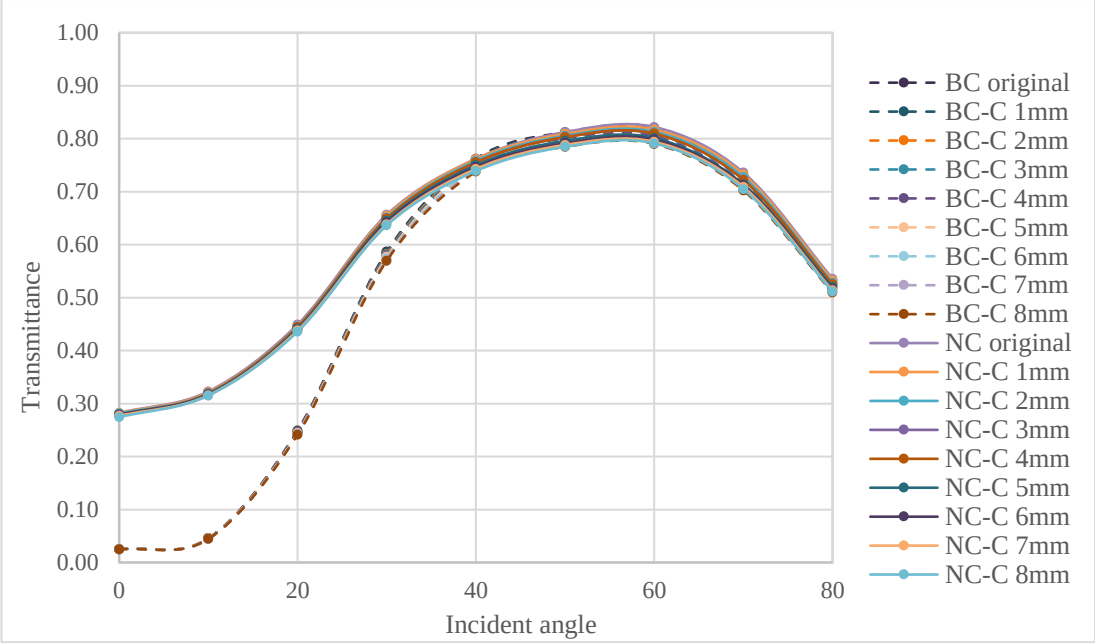


Figure 4.2.1.1. Transmittance of CPC panels with 1-8mm thick covers (BC-C/NC-C *mm: Base-coated/non-coated) CPC panel with *mm thick cover; BC/NC original: base-coated/non-coated CPC panel without cover)

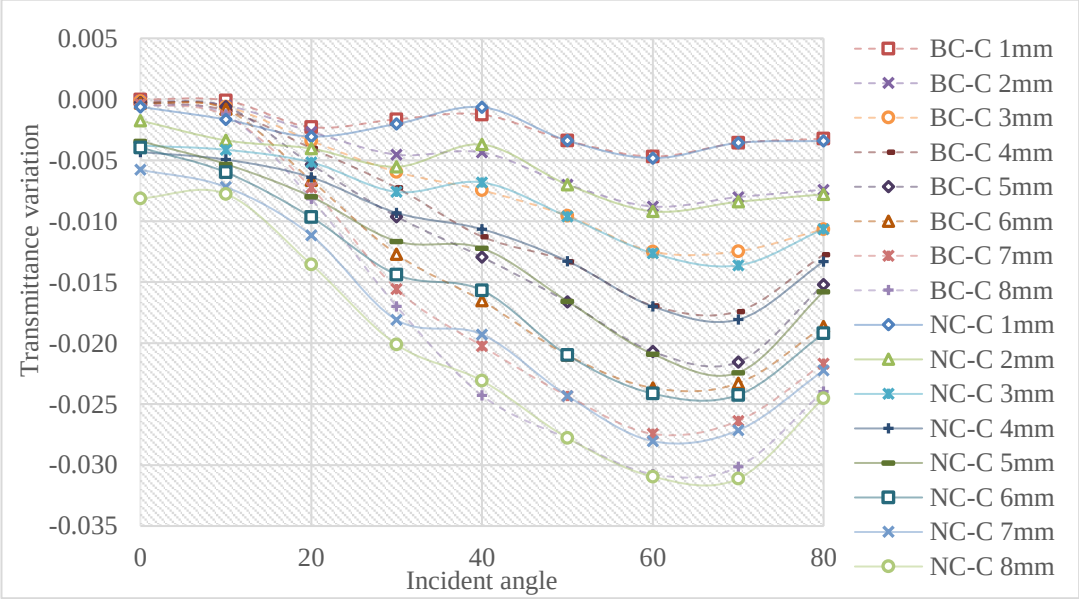


Figure 4.2.1.2. Transmittance variations to incident angle of CPC panels with 1-8mm thick covers compared to CPC panels without covers (BC-C/NC-C *mm: Base-coated/non-coated CPC panel with *mm-thick cover)

4.2.2. Truncation

In order to investigate the truncation effects on CPC panel, the CPC panels truncated by 1mm-8mm with 1mm interval were simulated. Figure 4.2.2.1 demonstrates the

transmittance of base-coated and non-coated CPC panels truncated by 1-8mm based on original CPC panels. The heights of both original base-coated and non-coated CPC panels were 24.2mm. Different from cover effects, the truncation effects on transmittance are much more visible in figure. Figure 4.2.2.2 illustrates the transmittance variations of truncated CPC panels relative to the incident angle. It was interesting to found that comparing with un-truncated CPC panels, when the incident angle was smaller than 20 °and larger than 65 °, truncation resulted in an small increase of transmittance; when the incident angle was between 20 °and 65 °, truncation caused transmittance reductions. For a truncated CPC panel, the truncation had more serious impacts when the light was incident within 30 °-60 °. In other words, truncation weakened the ability of CPC on controlling incident light, especially for the light that was incident between 30-50 °. With the CPC panels being truncated more, the influences were more obvious. For the same truncated thickness, the transmittance of base-coated CPC panel changed more comparing with the transmittance of non-coated CPC panel. The largest decrease of transmittance was 0.1595 for the base-coated CPC truncated by 8mm when light is incident at 40 °, which took 20.9% decrease of the original base-coated CPC panel without truncation.

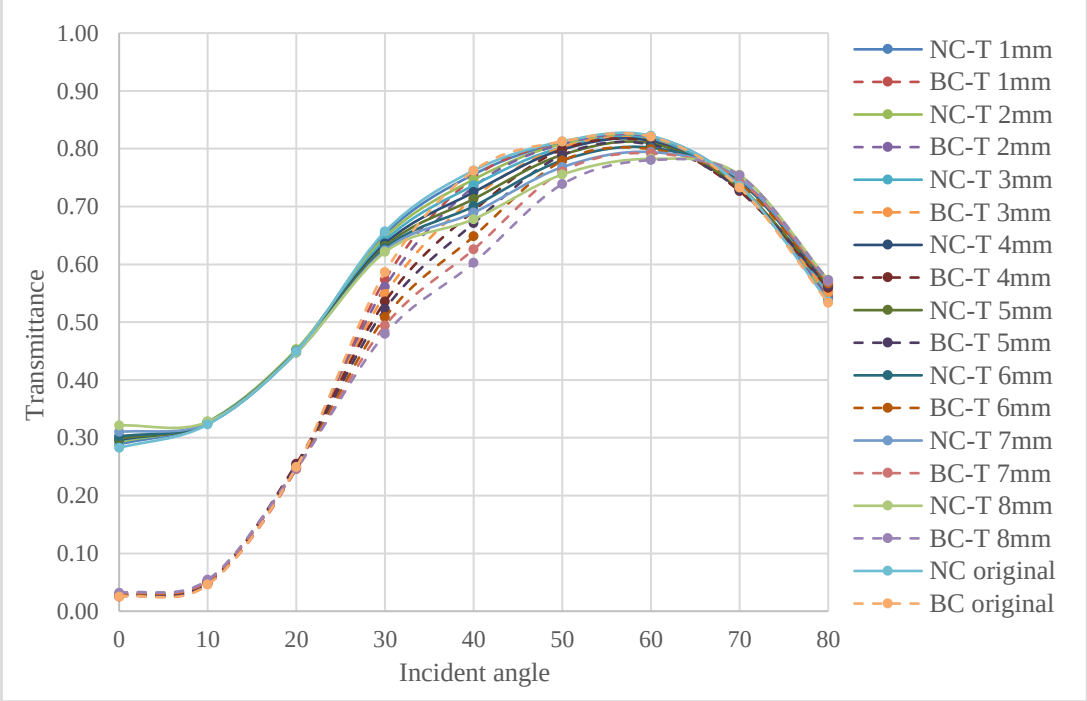


Figure 4.2.2.1. Transmittance of CPC panels which were truncated by 1-8mm (BC-T /NC-T *mm: Base-coated CPC panel truncated by *mm; BC/NC original: the base-coated/non-coated CPC panel without truncation)

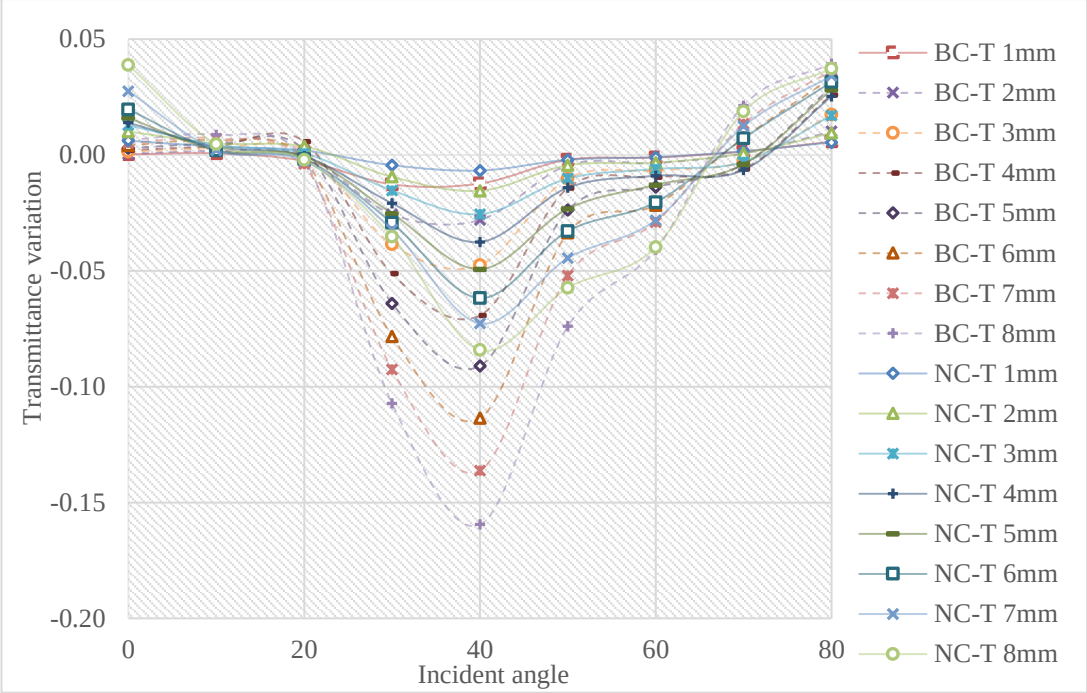


Figure 4.2.2.2. Transmittance variations to incident angle of CPC panels which were truncated by 1-8mm (BC-T/NC-T *mm: Base-coated/non-coated CPC panel truncated by *mm)

Truncation changes light path, and the cover increases transmission loss. Figure 4.2.2.3 shows the transmittance of base-coated and non-coated CPC panels which consisted of truncated CPCs and covers. The thickness of cover was equal to the thickness of truncated part, which guaranteed that the height of truncated CPC panel with cover equals the height of original CPC panel. Owing to the small impacts by cover, the tendencies of transmittance variations were quite similar to that of the truncated CPC panels as shown in Figure 4.2.2.3 and Figure 4.2.2.4. The largest transmission loss, 0.1721, come from the base-coated CPC panel that was truncated by 8mm and had 8mm cover when the light was incident at 40 °. It took 22.6% reduction compared to the original base-coated CPC panel. It can be found that the transmission loss increased under the effect of both truncation and cover, but a small increase of transmittance when the incident angle is smaller than 5 °. Similar to the transmittance variations of truncated CPC panels, for the CPC panels that were truncated and with covers, the transmittance variations of base-coated CPC panels were more obvious than that of non-coated CPC panels.

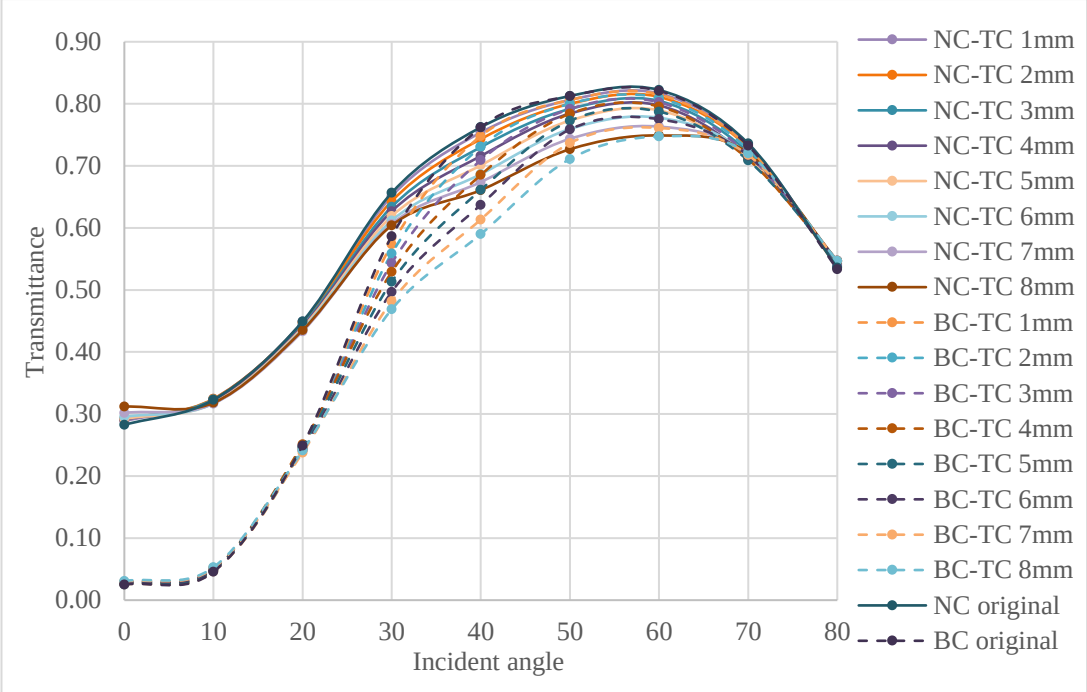


Figure 4.2.2.3. Transmittance of CPC panels which were truncated by 1-8mm and with corresponding 1-8mm covers (BC-TC/NC-TC *mm: Base-coated/Non-coated CPC panel which was truncated by *mm and with *mm-thick cover; BC/NC original: the base-coated/non-coated CPC panel without truncation and cover)

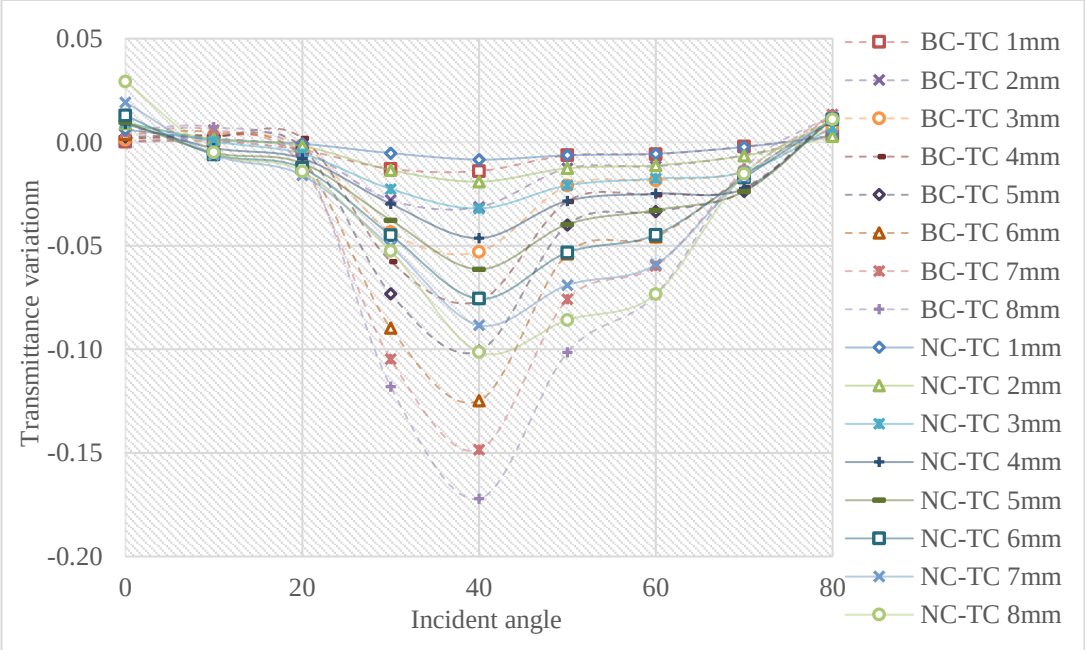


Figure 4.2.2.4. Transmittance variations to incident angle of CPC panels which were truncated by 1-8mm and with corresponding 1-8mm thick covers (BC-T/NC-T *mm: Base-coated/non-coated CPC panel that was truncated by *mm and with *mm-thick cover)

4.2.3. Gaps between CPC elements

The gaps between CPC elements were caused by the truncation of CPC panels in manufacture. Thus the analysis of gap effects were cooperated with the truncation and cover effects. Similarly, the CPC panels being truncated from 1-8mm were simulated. For the designed CPC panel, the gap widths corresponding to the truncated thickness are illustrated in Table 4.2.3.1. The transmittance and its variations of base-coated and non-coated CPC panels, which were truncated, with corresponding covers and gaps, was shown in Figure 4.2.3.1 and Figure 4.2.3.2.

Table 4.2.3.1. Relationship between truncated thickness and gap width

Truncated thickness (mm)	1	2	3	4	5	6	7	8	9	10
Gap width (mm)	0.2	0.4	0.6	0.9	1.1	1.4	1.7	2.0	2.4	2.7

Results implied the gap between individual CPC components was critical to the performances of both base-coated and non-coated CPC panels. Different form the effect of cover and truncation, the demarcation point of incident light changed to 25 °: when the incident angle of light was smaller than 25 °, the increases of gap width, truncation thickness and cover thickness led to the rise of transmittance; as the incident angle of light become larger than 25 °, the increases of the three criteria resulted in the reductions of transmittance. In other words, the larger of the three criteria, the less of the panel capabilities on controlling incident light. It can also be found that the gap width was the key factor that affected the panel performance. It is worth to mention that the gap provided significant influences on CPC panels when the incident angle of light was smaller than the half acceptance angle of CPC, especially when the light was incident perpendicularly on the panel. When the base-coated CPC panel was truncated by 8mm, with 8mm cover and 2.0mm gap width, it performed the largest transmittance increase, 0.1843, at the incident angle is 0 °, which is about 7.4 times larger than the transmittance of the original base-coated CPC panel. The transmittance variations of base-coated CPC panels were more significant comparing with that of non-coated CPC panels.

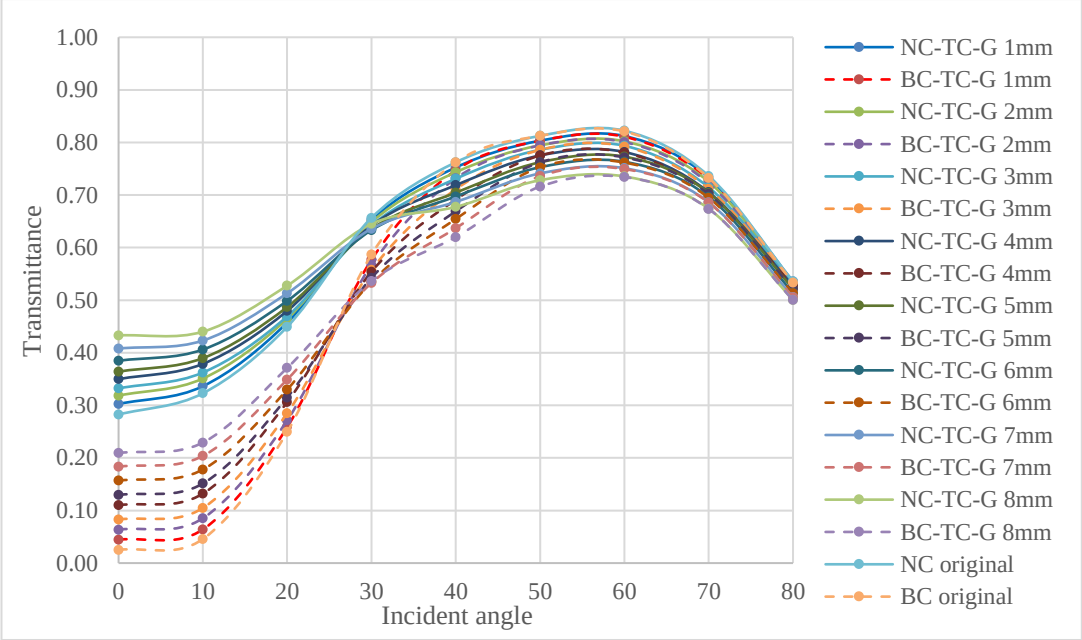


Figure 4.2.3.1. Transmittance of CPC panels which were truncated by 1-8mm, with corresponding 1-8mm covers and gaps between CPC components (BC-TC-G/NC-TC-G *mm: Base-coated/Non-coated CPC panel which was truncated by *mm, with the cover of *mm thick and gap between CPC components corresponding to the truncated thickness *mm; BC/NC original: the base-coated/non-coated CPC panel without truncation and cover)

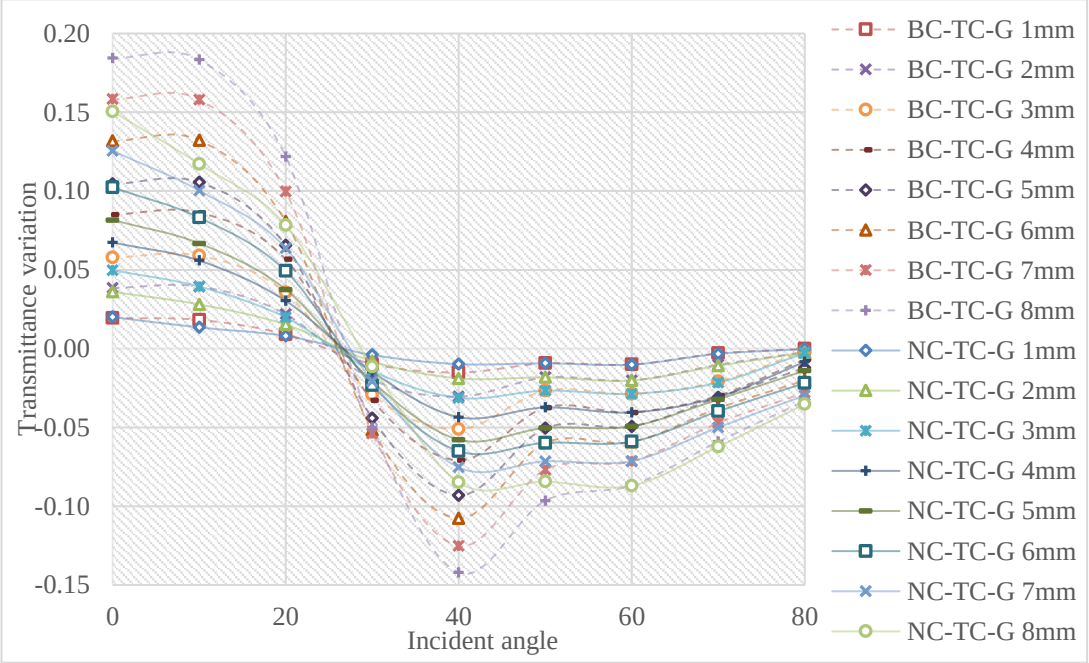


Figure 4.2.3.2. Transmittance variations to incident angle of CPC panels which were truncated by 1-8mm, with corresponding 1-8mm covers and gaps between CPC

components (BC-TC-G/NC-TC-G *mm: Base-coated/Non-coated CPC panel which was truncated by *mm, with the cover of *mm thick and gap between CPC components corresponding to the truncated thickness *mm)

4.3. Discussion

It was investigated that how the three criteria, which are conjunction cover, truncation and gap, affected the performances of CPC panels in section 4.2. In this section, the effect of each criterion are explored further and the relationships between them are investigated.

4.3.1. Conjunction cover

According to simulation results, it was found that the transmittance of CPC panel decreased when the thickness of conjunction cover increased. It was caused by the light attenuation in acrylic which is the gradual loss in intensity of flux through a medium based on Beer-Lambert law. When the light propagates through CPC panel, it is more complex because it consists of several phenomena such as refraction, absorption, and total internal reflection, etc. According to the simulation results of the transmittance for a CPC panel coupled with different conjunction covers, it is expected to figure out a relationship between cover thickness and transmittance.

Figure 4.3.1.1 and Figure 4.3.1.2 illustrate the transmittance variations relative to the cover thickness of covered base-coated and non-coated CPC panels. The base-coated and no-coated CPC panels without conjunction cover were used as references to calculate the variations. It can be seen that under a certain incident angle, the relationship between transmittance variation and cover thickness can be regarded as linear approximately, which corresponds to the Beer's law. Hence for the thicker conjunction cover, its effects on CPC panel can be roughly predicted.

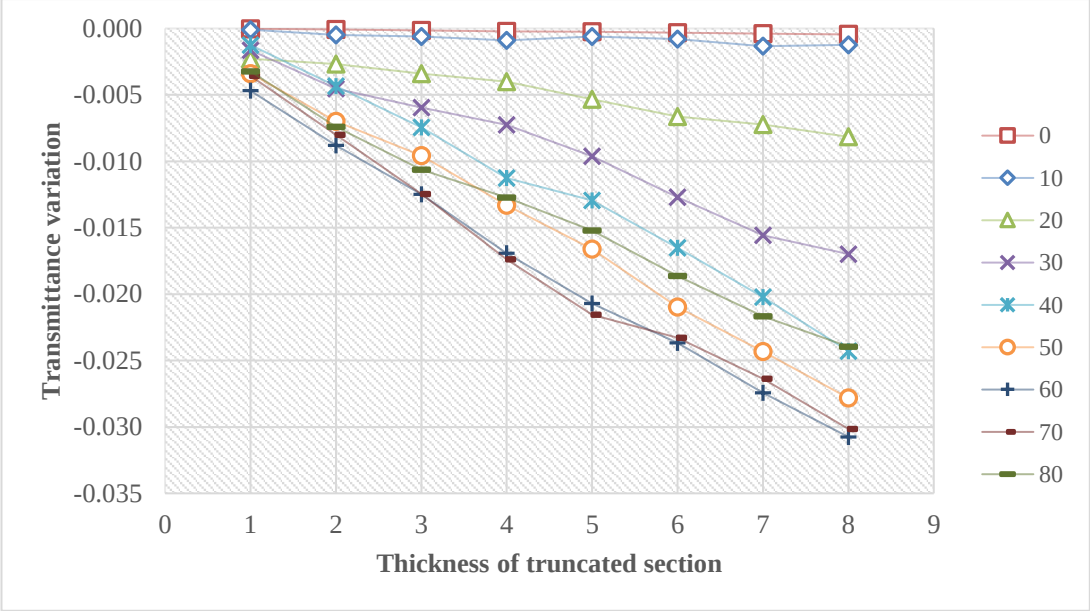


Figure 4.3.1.1. Transmittance variations to cover thickness for base-coated CPC panels with 1-8mm cover at different incident angles comparing with original base-coated CPC panel

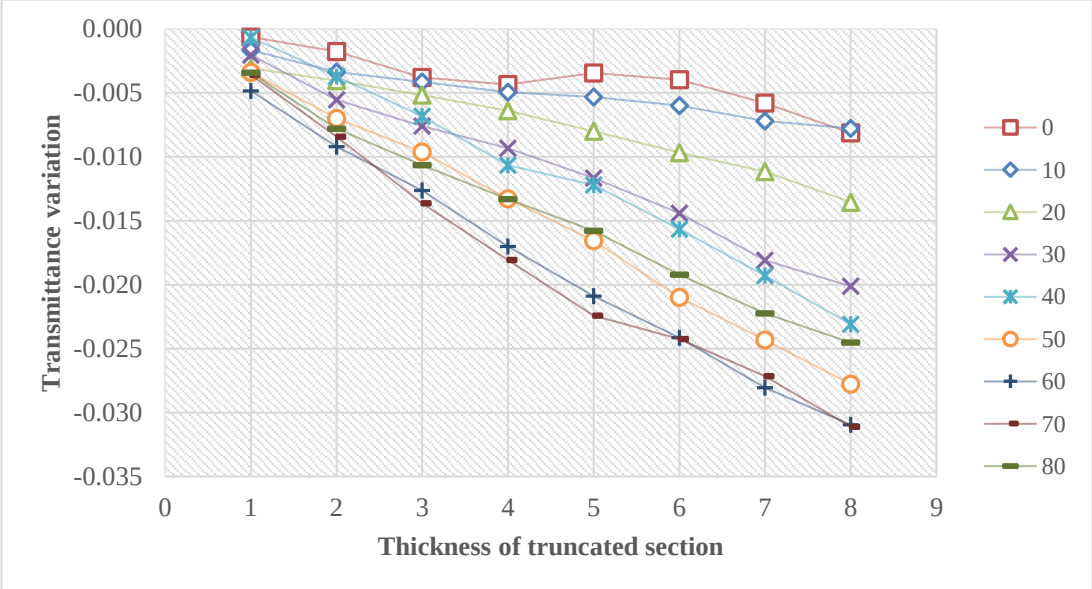


Figure 4.3.1.2. Transmittance variations to cover thickness for non-coated CPC panels with 1-8mm cover at different incident angles comparing with original non-coated CPC panel

4.3.2 Truncation

According to the relationship between transmittance variations and cover thickness, the relationship between transmittance variations and truncation was guessed. According to the simulation results, Figure 4.3.2.1 and Figure 4.3.2.2 demonstrated

their relationships which demonstrated similar tendencies compared to that of cover effects. However, the relationships between them were not linear only. The fitting equations of the relation curves could be quadratic or cubic equations. There were two main aspects when considering the truncation effects on transmittance. When the CPC panel was truncated, the acceptance angle of CPC would increase, so that more light with larger incident angles will be accepted and concentrated. On the other hand, truncation increased the edge effects which led to optical losses for CPC panels [108, 109]. Therefore, different from cover effects, which resulted in transmittance decrease of CPC panels, truncation led to not only increase but decrease of CPC panels depending on the incident angles. In addition, the effects on base-coated and non-coated CPC panels by truncation were not totally same. When the incident angle was 0 °, truncation barely affected the transmittance of base-coated CPC panel, but it caused transmittance increase of non-coated CPC panels. Thus when investigating the effects on CPC panels by truncation, the CPC types should be considered separately.

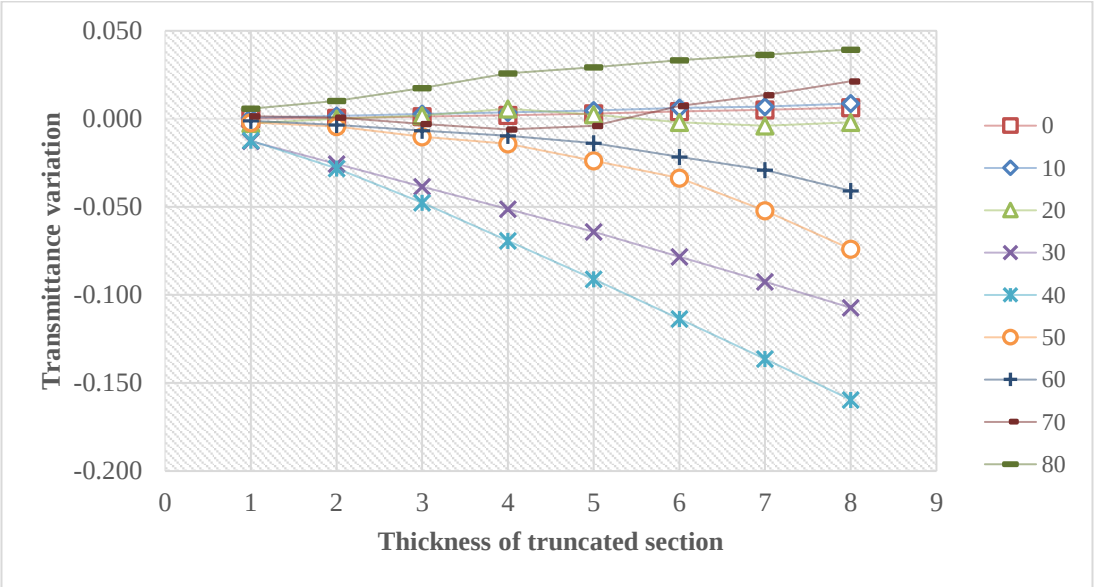


Figure 4.3.2.1 Transmittance variations to truncated thickness for base-coated CPC panels truncated by 1-8mm at different incident angles comparing with original base-coated CPC panel

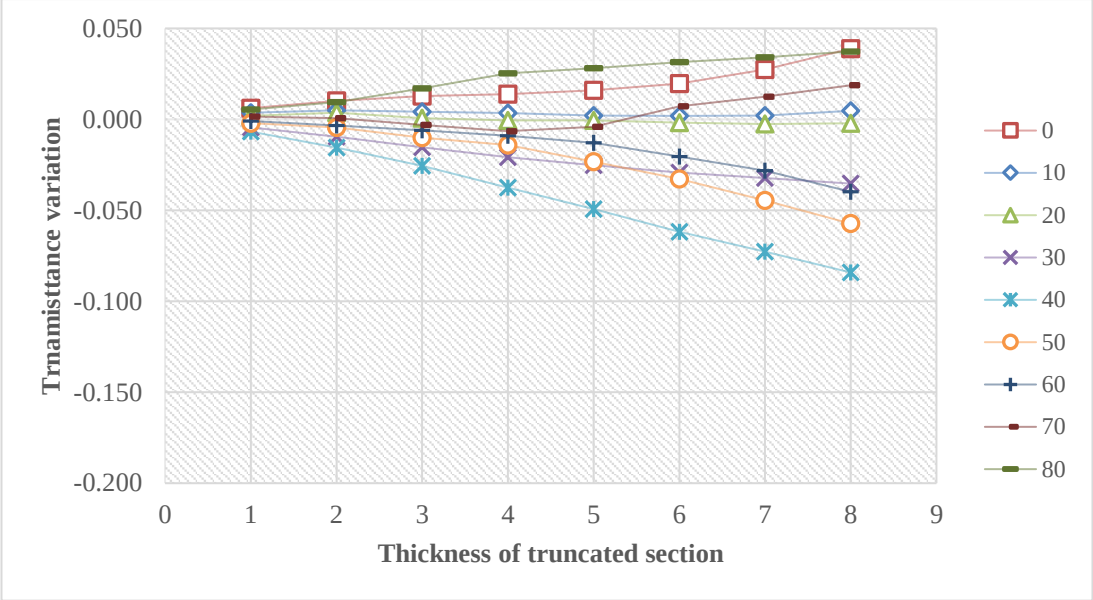


Figure 4.3.2.2. Transmittance variations to truncated thickness for non-coated CPC panels truncated by 1-8mm at different incident angles comparing with original non-coated CPC panel

4.3.3. Gap

When the gap effects were simulated, they were cooperated both of the cover and truncation effects. It is interesting to find that when the three factors, conjunction cover, truncation and gap, interacted with each other, there still were some relationships between the transmittance variations and the three criteria as shown in Figure 4.3.3.1 and Figure 4.3.3.2 for both base-coated and non-coated CPC panels. When the incident angles were 0 °, 10 ° and 20 °, the three factors led to transmittance rise; when the incident angles were larger than 30 °, the criteria caused transmittance drop. This rule applies to both base-coated and non-coated CPC panels, but the transmittance variations were bigger for base-coated CPC panels.

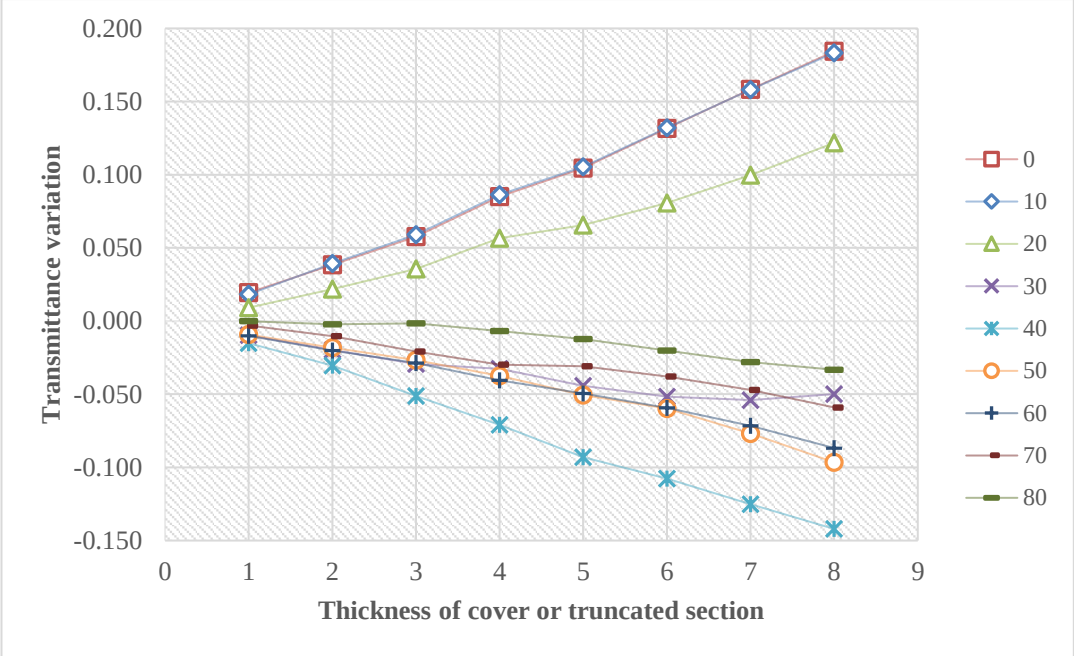


Figure 4.3.3.1. Transmittance variations to cover thickness (or truncated thickness) at different incident angles for base-coated CPC panels truncated by 1-8mm, cooperating with 1-8mm covers and corresponding gaps, at different incident angles comparing with original base-coated CPC panel

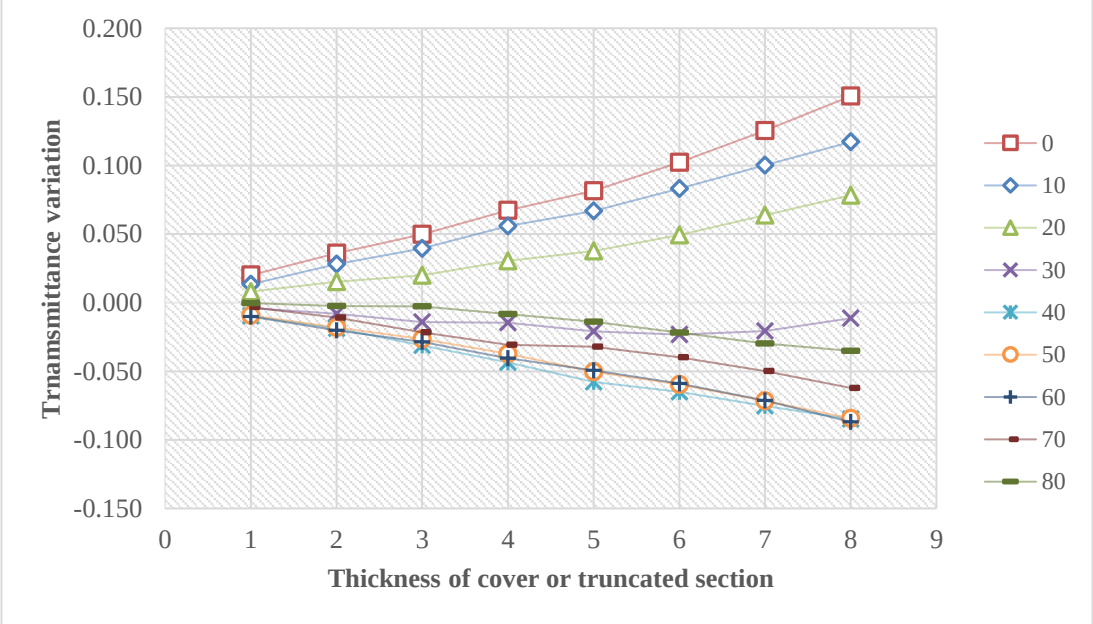


Figure 4.3.3.2. Transmittance variation to cover thickness (or truncated thickness) at different incident angles for non-coated CPC panels truncated by 1-8mm, cooperating with 1-8mm covers and corresponding gaps, at different incident angles comparing with original non-coated CPC panel

4.3.4 Relationship between three criteria

In section 4.2 and 4.3, the effect of conjunction cover and truncation on CPC panels were discussed respectively. Simulations for the CPC panels which were truncated and added conjunction covers were taken as well as demonstrated in section 4.2.2. In order to provide a better estimation of the criteria affecting CPC performance, it is important to figure out how the criteria interact with each other. Based on the results, the effect of conjunction cover and truncation were guessed to be additive. Figure 4.3.4.1 demonstrates the differences between the transmittance of truncated CPC panels with covers and the transmittance obtained by summarizing the transmittance of truncated CPC panels and covered CPC panels. Under the two conditions, the thicknesses of truncated section and cover were same. Results implied that the guess of additive effects was correct. The deviations between the transmittances obtained from two approaches were within -0.012-0.004, which is smaller than 2% of the original transmittance of CPC panels. Generally, the deviations of base-coated CPC panels were a little bit bigger than that of non-coated CPC panels.

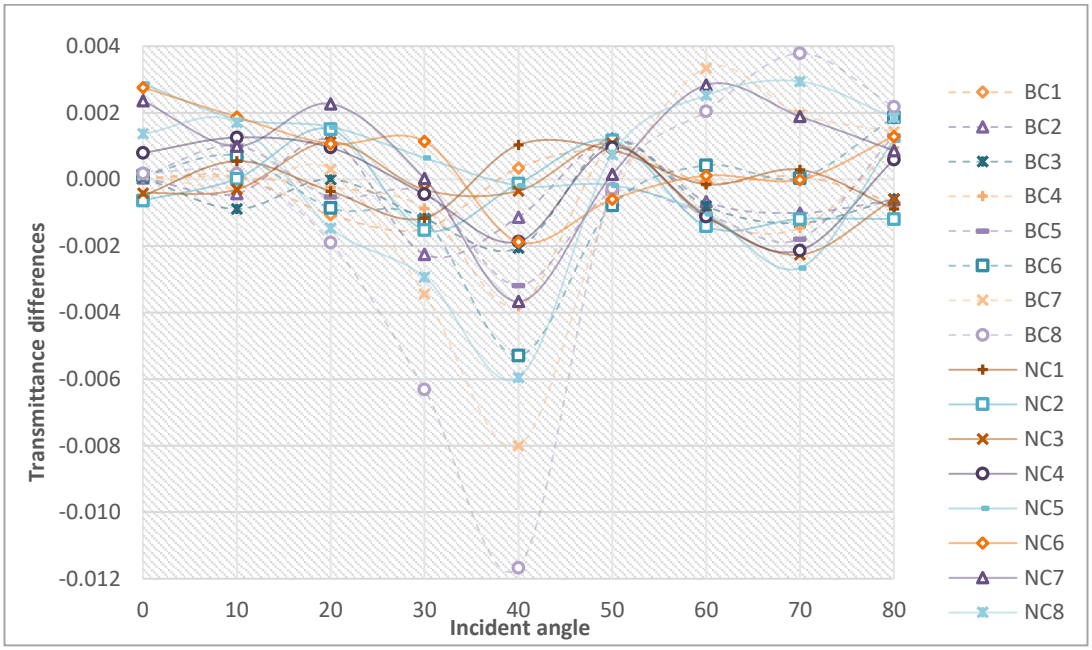


Figure 4.3.4.1. Deviations between the transmittance of truncated-covered CPC panels and the sum of transmittance of truncated CPC panels and covered CPC panels (BC*/NC*: base-coated/non-coated CPC panels truncated by *mm and with *mm cover)

In accordance with the transmittance variations under the effects of cover, truncation and gap shown in Figure 4.3.3.1 and Figure 4.3.3.2, it can be found that there were

also functional relations between transmittance variations and the tree criteria at a certain incident angle. As the additive effect of conjunction cover and truncation were proved, the effect of gaps were assumed to be additive with conjunction cover and truncation for the purpose of investigating the effect of gaps only on CPC panels. Hence, the transmittance variations as a result of gaps only were obtained as shown in Figure 4.3.4.2. The widths of gaps corresponded to the truncated thicknesses of CPC panels according to Table 4.2.3.1. Results indicated that the gaps influenced the performances of CPC panels significantly when the incident angles were small. When the incident angles were smaller than 50 °, gaps caused transmittance rises, and the increases reached the maximum when the light is incident perpendicularly on the CPC panels. For the base-coated CPC panel which was truncated by 8mm, with 8mm cover and 2mm gaps between CPC components, the increase of transmittance was maximum, 0.1785, which was 7 times of the transmittance performed by original base-coated CPC panel. When the light was incident larger than 60 °, gaps resulted in a small reduction on transmittance of CPC panels. Similar to the other two criteria, the gap effects on base-coated CPC panels were more obviously than that on non-coated CPC panels.

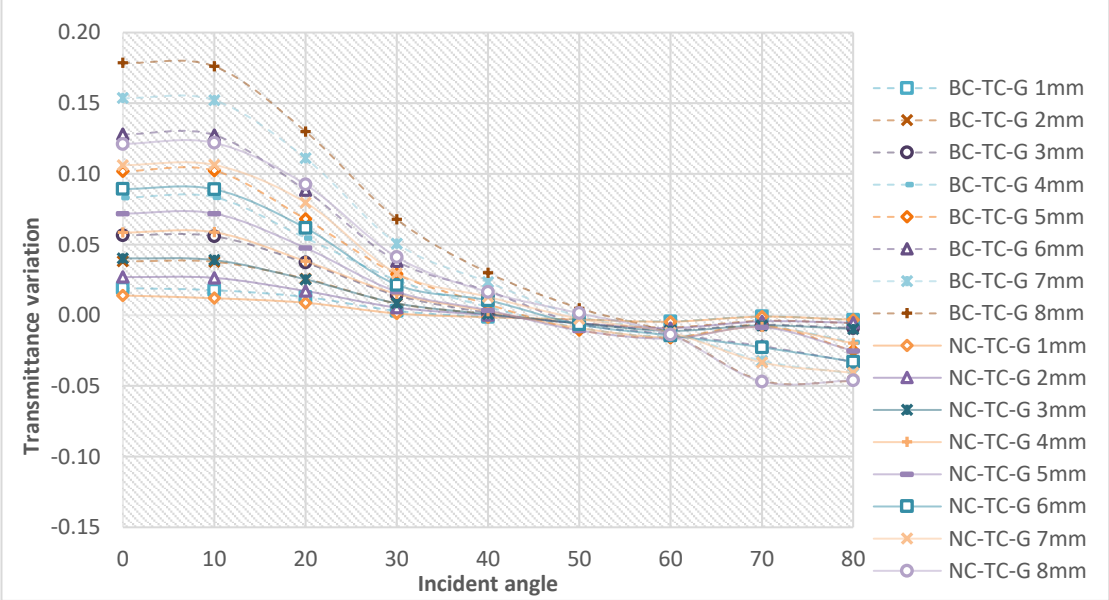


Figure 4.3.4.2. Transmittance variations affected by gaps only on CPC panels with 1-8mm covers, 1-8mm truncations and corresponding gaps, compared to original CPC panel (BC-TC-G/NC-TC-G *mm: base-coated/non-coated CPC panel that was truncated by *mm, with *mm cover and with gap between CPC components, and the gap width corresponds to the truncated thickness)

4.4 Further modifications

4.4.1 Design requirements

In section 4.2 and 4.3, the effects on CPC panels by three criteria, conjunction cover, truncation and gaps, were discussed. The influences of them can be summarized as shown in Table 4.4.1.1. The CPC panels designed for practical applications are required to be light weight, thin, and accurate in order to integrate with building facade and control daylight well. Thus some modification suggestions were put forward based on the properties of three criteria for CPC panels. Conjunction cover is used to connect and fix individual CPC components. For the purpose of reduce panel weight, conjunction cover was expected to be designed as thin as possible. For an acrylic panel, a 2mm conjunction cover is strong enough for sturdiness. The transmission loss due to the cover who is thinner than 2mm is lower than 1% compared to original CPC panel. When CPC panel is utilized as building facade, it works on prevent direct sunlight at noon. The half acceptance angle of designed CPC is 22.5 °which means it mainly control the direct sunlight with the incident angles that smaller than 22.5 °. It was found that truncation mainly affects the light whose incident angles are larger than 20 °. Considering the objective of light weight, the truncation effects should be investigated further to find a good tradeoff between truncated thickness and control capability on sunlight for CPC panels. In terms of gap effect, results demonstrated that it provided critical influences on the performance of CPC panels. It was intended to be reduced to not only decrease weight but increase accuracy of CPC panels. On account of the manufacture limitation of CNC, the minimum of gap width could be 1mm.

Table 4.4.1.1. Summary and suggestions of three design criteria of CPC panel

Design criteria	Impact level	Affected ranges of incident angles	Effects on base-coated and non-coated CPC panels	Modification suggestions	Modification purposes
Conjunction cover	Low (<4.2%)	20°-60°	Almost same	As thin as possible	Reduce panel weight
Truncation	Medium (<20.9%)	20°-70°	greater effects on base-coated CPC panels	Truncating as more as possible	Reduce panel weight

Gap	High (up to 700%)	<40° and >60°	greater effects on base-coated CPC panels	As small as possible	Increase panel accuracy

4.4.2 Prediction of truncation effects

The relationships between truncation effects on transmittance will be investigated in this section. According to Figure 4.3.2.1 and 4.3.2.2, the fitting equations can be obtained for each curve, in order to estimate the transmittance variations of two types of CPC panels. The fitting equations are cubic functions as shown in Eq. 4.4.2.1.

$$T_v(x) = ax^3 + bx^2 + cx + d \qquad (4.4.2.1)$$

Where T_v is transmittance variation, x is the thickness that the CPC is truncated, a,b,c,d are constants. The values of constants corresponding to different incident angles are shown in Table 4.4.2.1.

Table 4.4.2.1. Values of constants for fitting equations 4.4.2.1

Incident angle	base-coated CPC panel				non-coated CPC panel			
	a	b	c	constant	a	b	c	constant
0	0	6×10^{-5}	0.0003	-3×10^{-4}	0.0002	-0.002	0.0098	-0.002
10	7×10^{-6}	-6×10^{-5}	0.0012	-5×10^{-4}	0.0001	-0.001	0.0043	0.0006
20	0.0002	-0.0025	0.0116	-0.013	5×10^{-5}	-7×10^{-4}	0.0014	0.0016
30	0	-0.0002	-0.012	-0.001	0	0.0003	-0.0069	0.0026
40	0.0001	-0.0018	-0.012	0.0016	0	0	-0.0113	0.0067
50	-0.0002	0.0009	-0.005	0.0024	0	-9×10^{-4}	8×10^{-5}	-0.001
60	-8×10^{-5}	0.0004	-0.003	0.0016	0	-8×10^{-4}	0.0016	-0.003
70	-6×10^{-6}	0.0013	-0.009	0.0104	-4×10^{-5}	0.0018	-0.0102	0.0117
80	0	-0.0004	0.0085	-0.004	0	-4×10^{-4}	0.0084	-0.004

Base on the fitting equations for the relationships between transmittance variations and truncated thicknesses, the transmittance of both base-coated and non-coated CPC panels which were truncated by 1-14mm with 1mm interval was demonstrated in Figure 4.4.2.1 and Figure 4.4.2.2. It can be found that for both two CPC panels, the transmittance of the CPC panels truncated by 9-14mm performs similar tendencies with the CPC panels truncated by 1-8mm, but the transmittance variations were much bigger.

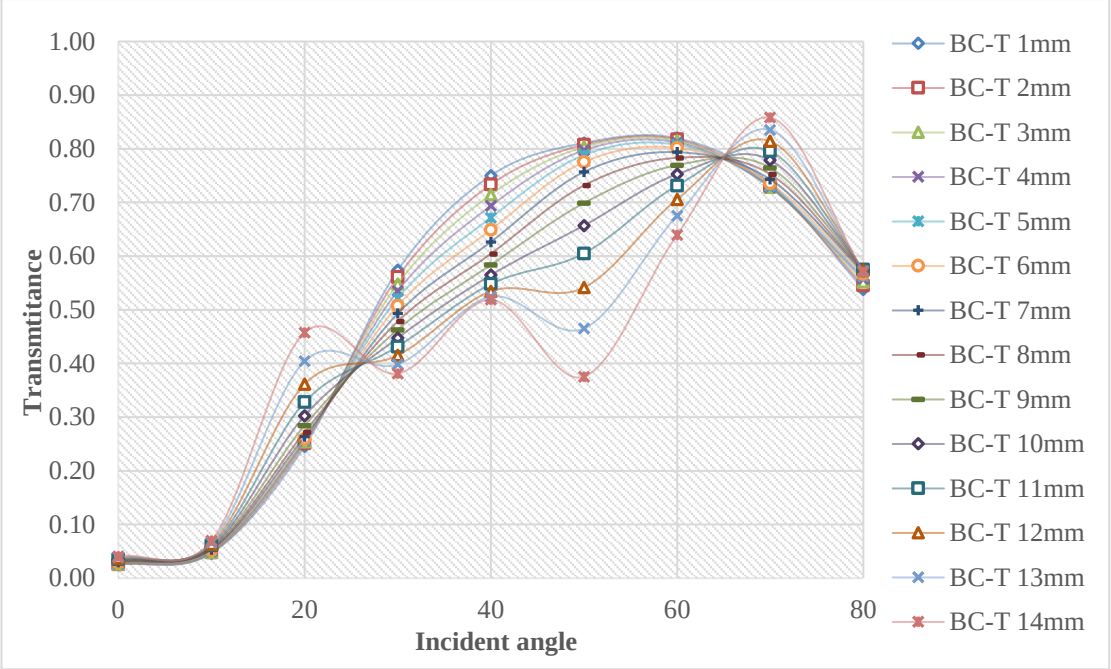


Figure 4.4.2.1. Predicted transmittance of base-coated CPC panels truncated by 1-14mm (BC-T *mm: base-coated CPC panels truncated by *mm)

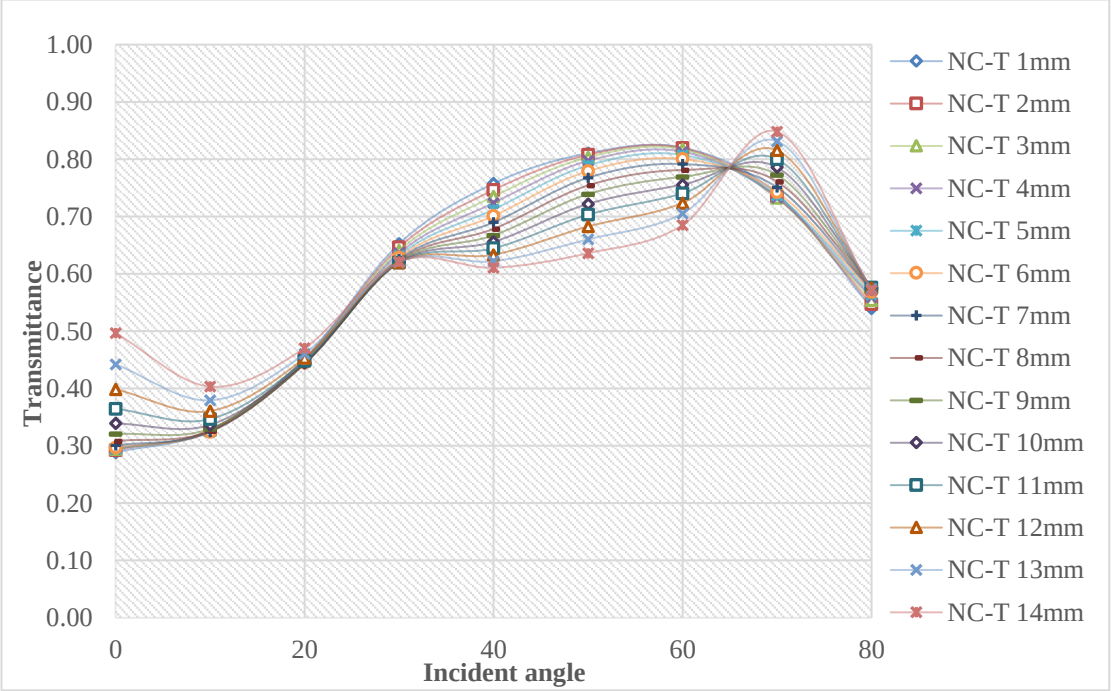


Figure 4.4.2.2. Predicted transmittance of non-coated CPC panels truncated by 1-14mm (NC-T *mm: non-coated CPC panels truncated by *mm)

4.4.3 Validations of truncation predictions

In this section, three examples which are the CPC panels truncated by 10mm, 12mm and 14mm are selected to validate the predicted transmittance calculated in section

4.4.2. Figure 4.4.3.1-4.4.3.3 demonstrate the deviations between the predicted values obtained by fitting equations and simulated values. It can be found that compared to simulation results, the predicted results performed more obvious fluctuations. For both base-coated and non-coated CPC panels, when the truncated thicknesses were shorter than 12mm, the differences were within 10%, which indicated that the fitting equations were feasible to predict the truncation effects on CPC panels when the truncated thicknesses were smaller than 12mm. In addition, considering the CPC properties on controlling incident light, 12mm truncation was about 50% of the thickness of original CPC panels. Therefore, the truncated thickness that is bigger than 12mm was not suggested.

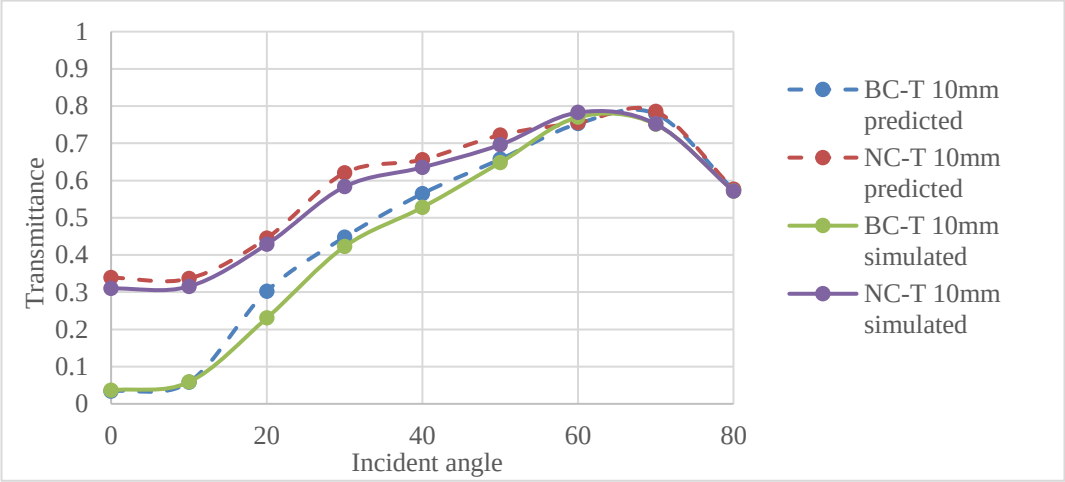


Figure 4.4.3.1. Validations of predicted and simulated transmittance for CPC panels truncated by 10mm

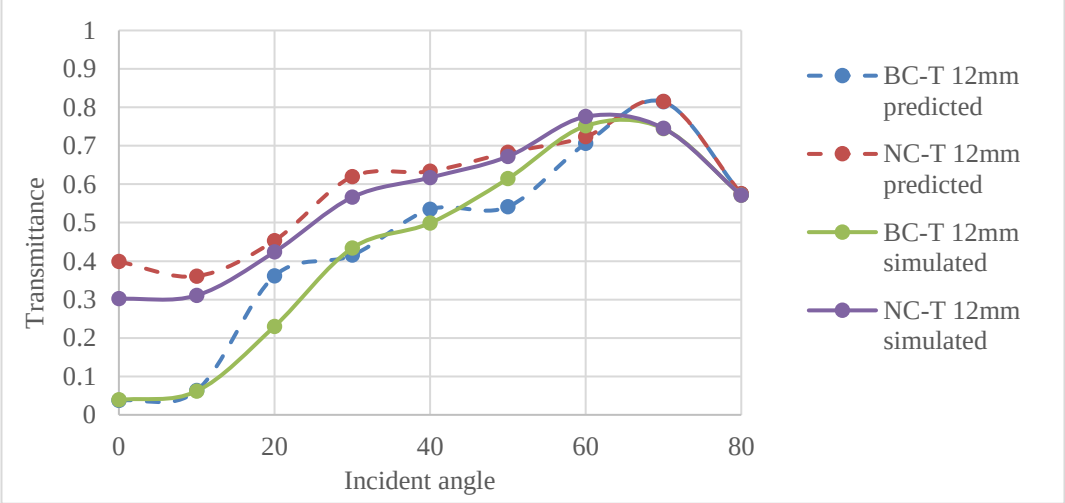


Figure 4.4.3.2. Validations of predicted and simulated transmittance for CPC panels truncated by 12mm

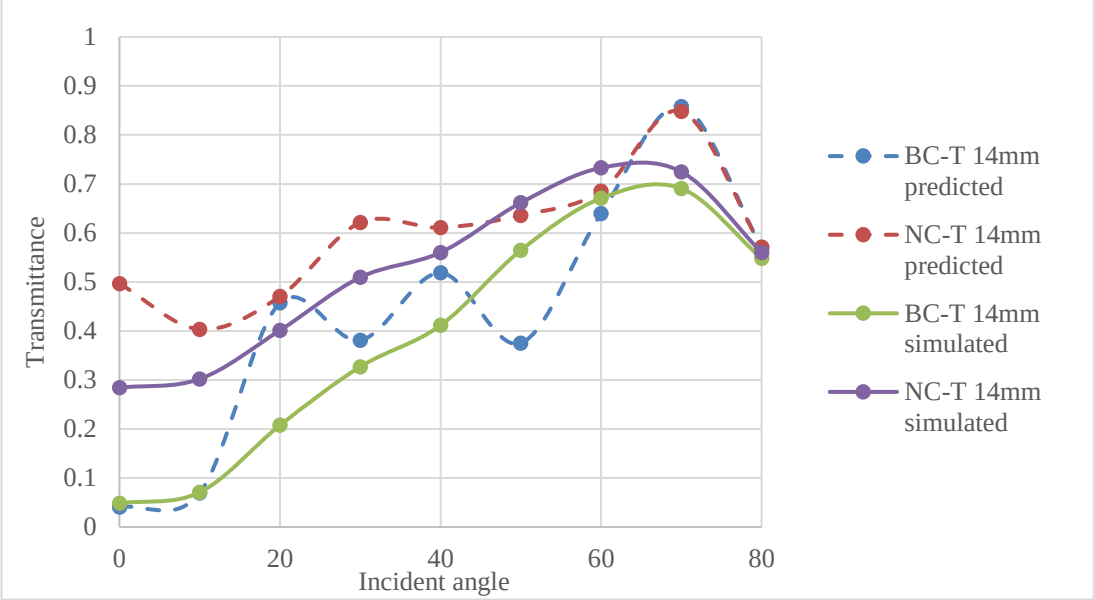


Figure 4.4.3.3. Validations of predicted and simulated transmittance for CPC panels truncated by 14mm

4.4.3. Scaling

After investigating the effect of the three critical criteria, which are conjunction cover, truncation and gap, scaling is considered to further minimize the size of CPC panel. It was known that scaling of CPC can minimize its size and keep its optical properties approximately. Results demonstrated in Figure 4.4.3.1 verified this assumption. The original base-coated and non-coated CPC panels selected were truncated by 8mm and with 4mm conjunction covers; the thicknesses of CPC panels were 16mm and the gaps between CPC components were 2mm wide. The CPC panels used for comparison come from scaling down original CPC panels by 0.5. Thus the sizes of the CPC panels that were scaled down were 8mm thick, with 2mm conjunction covers and 1mm-wide gaps. It can be found that for both base-coated and non-coated CPC panels, the scaled CPC panels almost kept the optical performances compared to original CPC panels. When the incident angle was larger than 30 °, the scaled CPC panels perform a little bit higher transmittance comparing with original CPC panels. However, the transmittance variations were quite small which can be accepted if the size of CPC panel were half minimized.

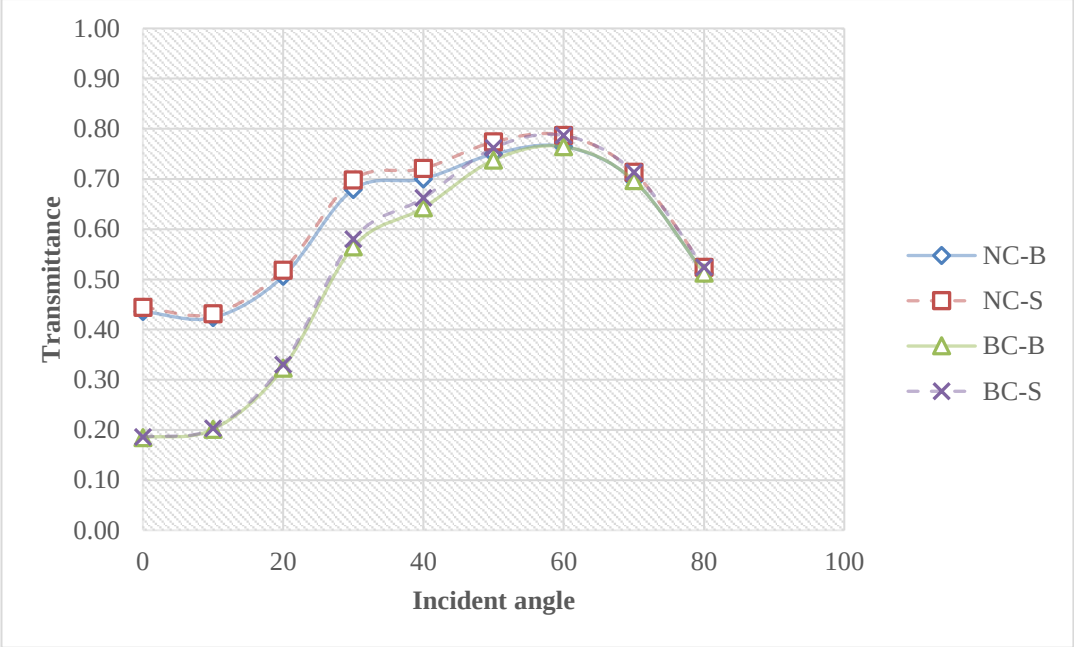


Figure 4.4.3.1. Transmittance comparisons of scaling CPC panels (NC-B/BC-B: non-coated/base-coated CPC panel before scaling; NC-S/BC-S: non-coated/base-coated CPC panel that is scaled down by 0.5)

4.5 Experiment methodology

4.5.1 Design of dCCPC panel

In accordance to the analysis in previous sections, the CPC panels with the best trade-off among its control capability, manufacture requirements and weights was obtained, which was truncated by 8mm, with 2mm gap between CPC components and 4mm conjunction cover on top. Then the CPC panel was scaled down by 0.5 to further reduce its weight. The dimensions of the final CPC panel for experiment is shown in Figure 4.5.1.1, which was a 215.1×215.1mm square panel consisting of 24×24 individual CCPC components. The width of each CCPC component was 8mm with a 1mm gap between each other. The height of CCPC component was 8.1mm with a 2mm conjunction cover. The height of the CPC panel was 10.1mm. The panel is made of dielectric material acrylic with refraction index of ~1.5. The general and detail views are presented in Figure 4.5.1.2. The panel is manufactured by computer numeric control (CNC) machine.

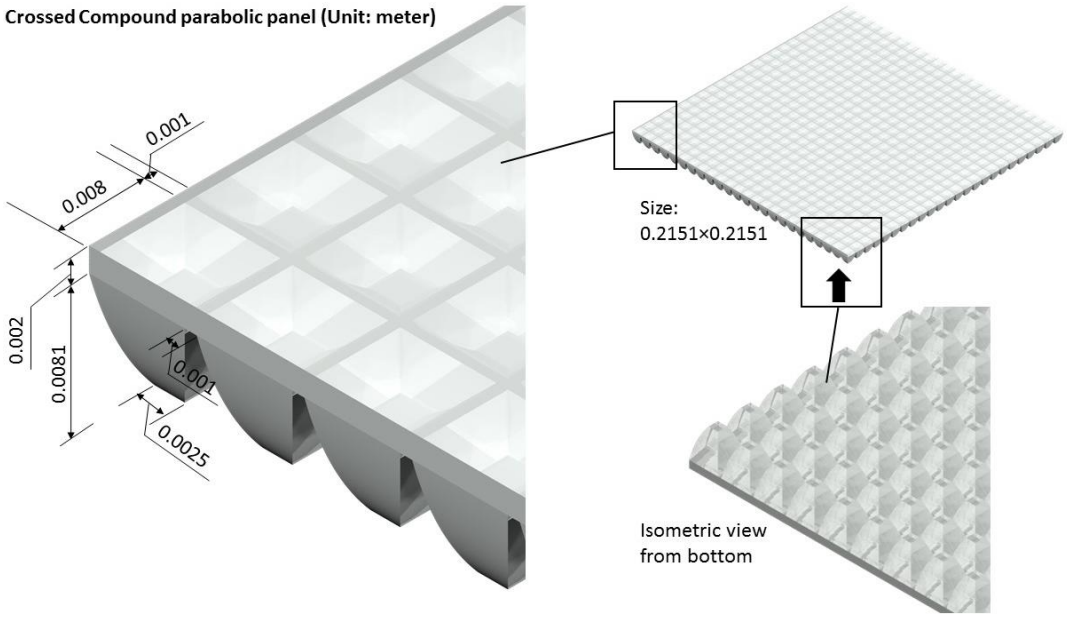


Figure 4.5.1.1. Dimensions of designed CPC panel for experiment

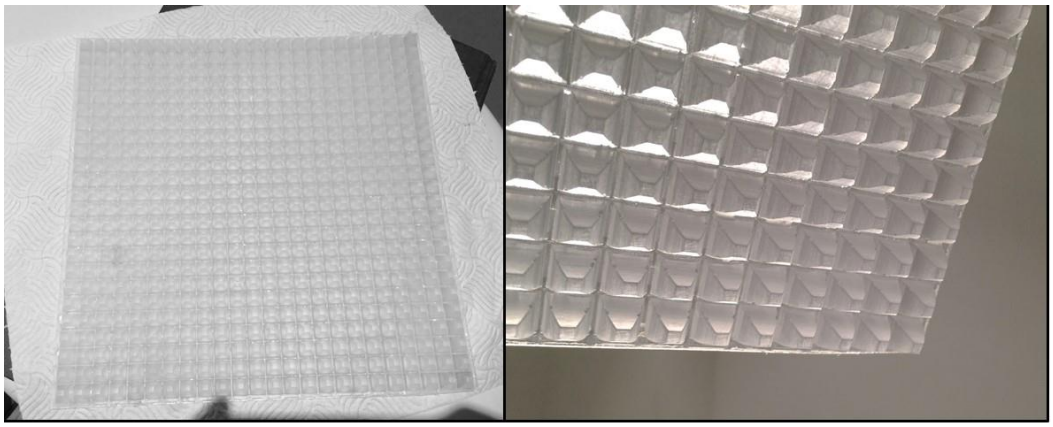


Figure 4.5.1.2. Photos of the dCCPC panel used in experiment (left: general view; right: detail view)

4.5.3 Test PV output to estimate transmittance

The transmittance of CPC could be regarded as the ratio of the solar radiation passed through CPC to the solar radiation incidence received by aperture. Generally, the short circuit current of PV can be assumed that it is directly proportional to the solar radiation on PV when testing the PV performance. Therefore the transmittance of CPC panel can be calculated by Eq. 4.5.3.1. This is a fast and simple way to determine the optical performance of CPC with a relatively high accuracy, and it has been widely used in estimating the light that passing through the concentrators of PV. By this calculation method, Li, G., et al. [78] found the deviations between simulation and experiment results are less than 5% when investigating the transmittance of PV/T-

CPC; Tina, G. M., et al. [173] and Li, G., et al. [76] found good matches between their simulation and experiment findings .

$$T_{cpc} = \frac{I_{PV-CPC}}{I_{PV}} \times \frac{1}{C} \qquad \text{(Eq. 4.5.3.1)}$$

where I_{PV-CPC} is the short circuit current of PV with CPC panel; I_{PV} is the short circuit current of PV without CPC panel; C is the concentration ratio of CPC panel.

Figure 4.5.3.1 illustrates a schematic diagram of the experiment which utilizes PV to test CPC properties. A light beam with a certain irradiation density was provided by solar simulator. During the experiment, changing the load resistance R from zero to infinity. At the same time, the output voltage *V* would change from zero to open circuit voltage and the output current *I* will be change from the short circuit current to zero. Hence the output curve of PV can be obtained. Then the transmittance of CPC could be calculated by comparing the PV performances of two prototypes based on Eq. 4.5.3.1.

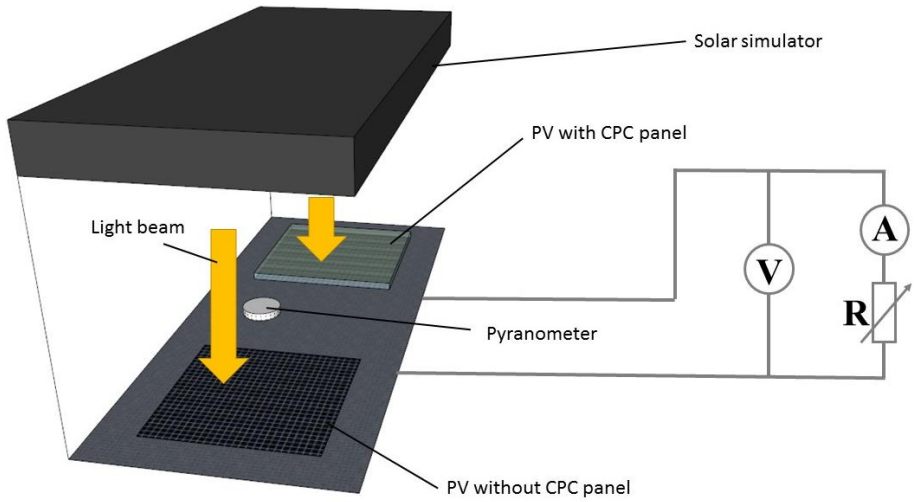


Figure 4.5.3.1. Configurations of CPC experiment by using PV

The equipment demonstrated in Figure 4.5.3.2 is used to take the measurements of PV output. It consists of a 450W Xenon solar simulator 94043A (beam uniformity ≤ 2%, beam size 101.6×101.6mm, ray intensity 1000W/m^2) [174] and a Keithley 2420 digital source meter [175]. The performance of the solar simulator complies the requirements of the Class AAA which indicates it provides excellent spectral match, spatial non-uniformity of irradiance and temporal instability to provide one to one correspondence of real world situations and test conditions [176]. Light sensor is the most popular tool

to measure the illuminance. Figure 4.5.3.3 compares the relative spectral sensitivity of light sensor and the spectral response of a silicon solar cell. It can be found that both of the light sensor and PV can respond to the light with the wavelength ranging between 300nm and 1000nm, and PV is also sensitive to the light with the wavelength within 1000-1200nm. The wavelength provided by solar simulator ranges from 400nm to 1100nm. Therefore, utilizing solar simulator to test the electrical performance of PV can be used to measure the light transmitted through CPC and indicate the performance of CPC to some extent.



Figure 4.5.3.2. Experiment rigs for PV-I testing

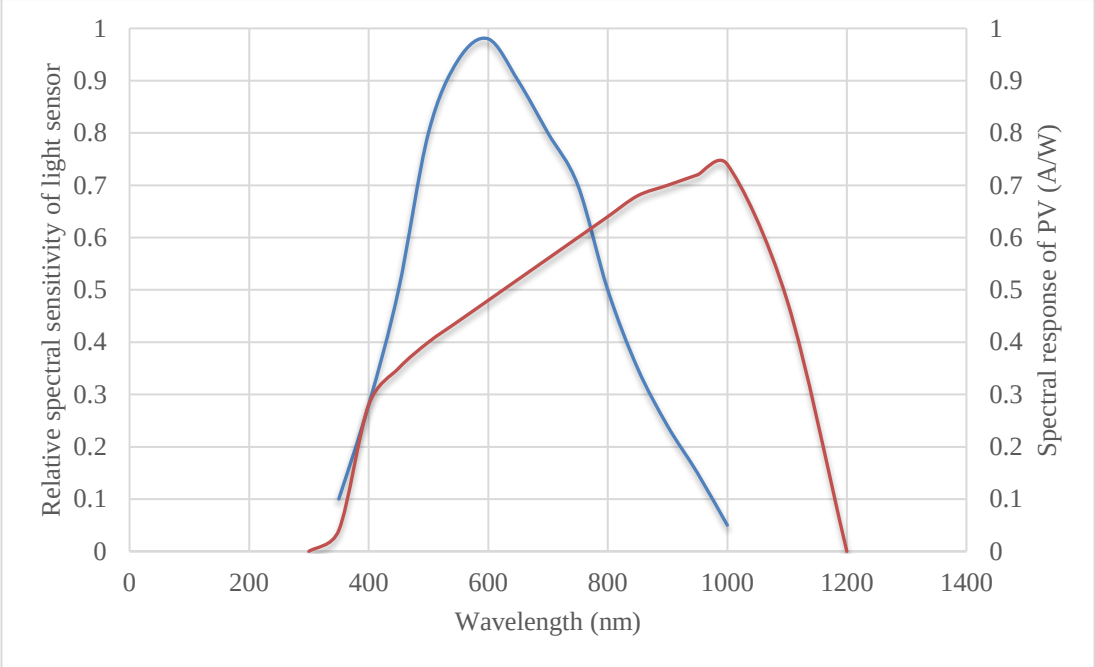


Figure 4.5.3.3. Relative spectral sensitivity of light sensor and spectral response of PV [177, 178]

When the PV is used to test CPC performance, it is important to consider the effect of temperature on PV. Ideally the surrounding temperature should be kept at room temperature during experiment. The concentrating properties of CPC would result in non-uniform flux distribution and high temperatures on PV, which reduces the fill-factor of PV and causes power losses [76, 80, 81, 179, 180]. This should be taken into account when the accuracy of experiment is discussed. In addition, the uncertainty of measuring apparatus should be considered as well. The relative uncertainties of was ±2% of pyranometer, ±3.8% for ammeter, and ±1.1% for photovoltaic cell analyzer.

4.6 Results and discussion

As investigated in previous study, the horizontal rotation angle also affects the transmittance of dCCPC. In the experiment, two typical horizontal rotation angle is tested which are 0 °and 45 °. The incident angle of light beam ranges from 20 °to 90 ° with 10 °interval. Two groups of data was tested in the experiment, one is attaching PV cell onto the base of dCCPC panel, the other is keeping a 2mm gap between PV and dCCPC panel. The results obtained from experiments are summarized in Fig. 4.6.1 below. It can be found that when PV is attached on the base of dCCPC, it absorbs some rays that is incident onto the base of dCCPC so that the transmittance of dCCPC tested in this moment is higher than the transmittance without attaching PV under the

same incident angle. The horizontal rotation angle of dCCPC does not have significant effects on the transmittance of dCCPC.

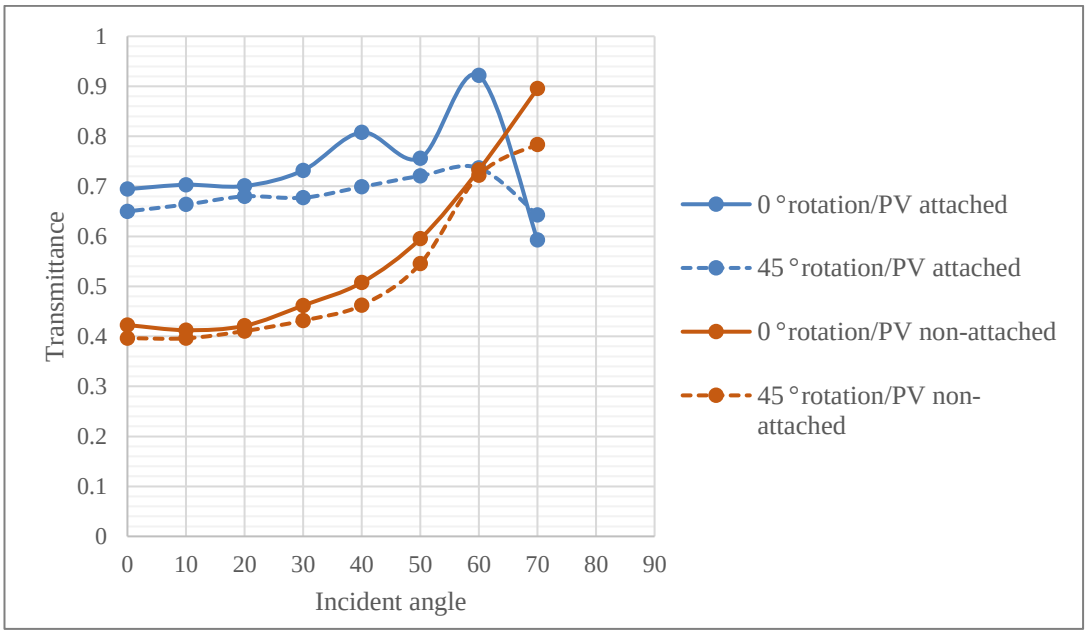


Fig. 4.6.1. Tested transmittance of dCCPC with the horizontal rotation angle of 0 ° and 45 °by experiments

The results of simulations and experiments are compared in Fig. 4.6.2 and 4.6.3. In terms of the dCCPC with a gap between dCCPC and PV, the experiment results demonstrate almost same values for the dCCPC with 0 ° and 45 ° horizontal rotation angles. However, the simulation results provide different tendencies. For the dCCPC with the rotation angle of 0 °, experiment and simulation results perform similar tendencies: the transmittance is low at about 0.4 as the incident angle is large and it becomes higher reaching 0.7-0.8 when the incident angle is small. The deviations between simulation and experiment are relatively large when the incident angle is between 40 °-60 °. For the dCCPC with 45 ° horizontal rotation angle, the simulation result is different from the experiment result when the incident angle is smaller than 60 °. For the simulation results, the transmittance is increased to 0.6 and then dropped back to 0.4 as the incident angle becoming small. The experiment results show that the transmittance is increased with the reduction of incident angle. Similar to the dCCPC without attaching PV on base, the dCCPC with PV attached provides same tendencies with simulation results when the horizontal rotation angle is 0 ° and provides relatively large deviations when the horizontal rotation angle is 45 °.

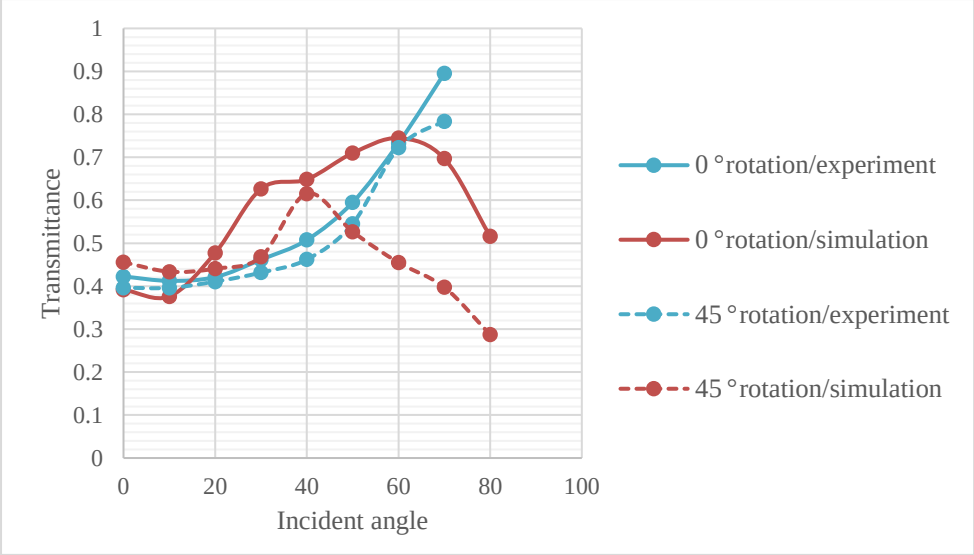


Fig. 4.6.2. Comparisons between the transmittances obtained from experiment and simulation of the dCCPC without PV attached on base

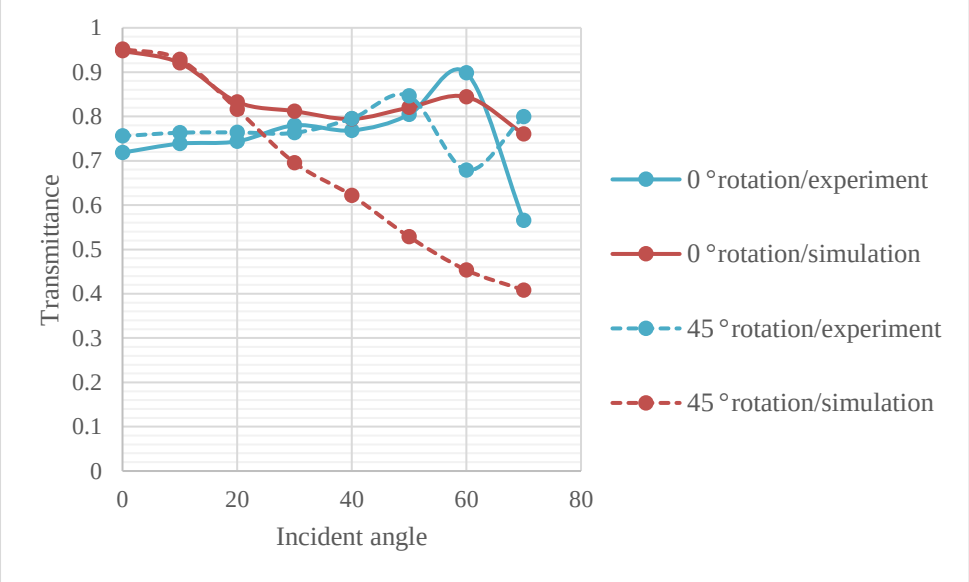


Fig. 4.6.3. Comparisons between the transmittances obtained from experiment and simulation of the dCCPC with PV attached on base

Considering the errors between simulation and experiment results, the deviations may be caused by the following reasons. Firstly, the manufacture accuracy should be the main problem causing the differences. The dCCPC panel is made through CNC machine, and the polish is difficult to be covered for all its surfaces due to the small gap between each dCCPC component. Some small area should not be clear enough for perfect reflection. The escaping of light from the edges of curved surfaces should also be considered. Due to the high temperature during manufacture, some tiny cracks

occur near the edges of curved surfaces which may increase the amount of incident rays escaping from the edges. It can be seen that in experiment results, the variation of transmittance due to horizontal rotation angle is not as sensitive as that in simulation, which may be caused by the accuracy of geometry and the structure of PV cell. In PV cell, the bus-bar on PV cannot receive incident light and transfer it to electricity. The missing energy due to bus-bar may result in some small deviations on results. In addition, some errors may be caused by the uneven light distribution on PV and the temperature increase on PV. Many studies proposed that the uneven irradiance distribution on PV would cause the reduction of fill-factor (FF) [180, 181]. Finally, the manual measurement should also be considered.

4.7 Summary

In this chapter, the feasibility of using dCCPC in practice was investigated. Firstly, the dimension of dCCPC was minimized as much as possible through scaling and truncation in order to reduce its thickness and weight. Four factors, which are the scale ratio, thickness of truncation, thickness of conjunction cover, and the width of gap between dCCPC components, relating to dimension of dCCPC that would affect the performance of dCCPC were investigated. It was found that the dCCPC provides less effects on controlling incident light with the thicker of the truncated part. Scaling does not affects the performance of dCCPC approximately. In order to connect each component of dCCPC, a conjunction cover needs to be added on the top of dCCPC. The influence by the conjunction cover on dCCPC performance is negligible. The gap between each dCCPC component is considered for manufacture process. The width of gap should be as small as possible to weaken its effect on dCCPC transmittance. Thus, in order to reducing the weight of dCCPC and maintaining its performance at the same time, a tradeoff among these criteria was found and the final dimension of dCCPC is: 8mm of truncated thickness, 2mm of the thickness of conjunction cover, 2mm of gap width, and 0.5 of scale ratio.

Following the new results of design criteria, the dimension of dCCPC used for manufacture is 215.1×215.1mm square panel consisting of 24×24 individual CCPC components. The total height of dCCPC panel is 10.1mm comprising the dCCPC part with the thickness of 8.1mm and conjunction cover with the thickness of 2mm. The gap between each dCCPC component is 1mm. Experiment was taken for testing the transmittance of dCCPC under different incident angle of light beam provided by solar

simulator. PV cell was used to receive the transmitted light trough dCCPC and the short circuit current was applied to calculate the transmittance of dCCPC. Two groups of experiment were taken, one is attaching PV cell on the base of dCCPC panel, the other is keeping a 2mm gap between PV cell and the base of dCCPC. It was found that the experiment results provides same tendencies but the transmittance was not sensitive to the horizontal rotation angle Compared to the simulation results. The deviations between experiment and simulation results were supposed to be caused by the accuracy of dCCPC geometry, the polishing performance on the curved surface of dCCPC panel, the non-uniform distribution of light on PV and the measurement errors. For the further works, simulation could provide detailed and precise results and predictions of the performance of dCCPC, which is suggested for investigating the properties of dCCPC; the experiment is limited by the processing technics of manufacture, it is recommended to be applied for validate the simulation results, and test the relatively accurate performance of dCCPC in practice.

Chapter 5

Multiple nonlinear regression model for predicting the optical performances of dielectric Crossed Compound Parabolic Concentrator (dCCPC)

5.1. Introduction

The compound parabolic concentrator (CPC) is one type of the nonimaging optics, which has great potential in solar energy concentration, daylighting control and illumination. CPC is a non-tracking concentrator to collect solar energy in concentrating photovoltaic (CPV) and solar thermal systems, which has been verified by many research studies [13, 88, 99, 105]. In terms of traditional two-dimensional (2D) CPC, Sun and Shi [80] tested the maximum short circuit current of a CPV system which was higher than twice of the flat PV panel. In the experiment conducted by Bahaidarah et al. [81], the CPV system with cooling generated 61.9% higher electricity compared to the flat PV panel with cooling. For the lens-walled CPC proposed by Su et al. [74] and Li et al.[76-78], it was found that the solar energy collected by the lens-walled CPC is 20-30% more than traditional 2D CPC. For crossed CPC (CCPC), the maximum optical efficiency could reach 95% [106]. The maximum power ratio was up to 2.67 for the dielectric filled crossed CPC [86]. In a system integrating CPC, PV and tubular absorber, the total energy conversion efficiency was 20% higher than the independent PV module [128].

The advantages of CPC in daylighting control has been also proposed by some researchers [15, 84, 85, 143, 145] in recent years. Due to its specific structure, CPC can receive or reject sunlight depending on the incident angle. Ulavi et al. [141, 142] designed a hybrid solar window with CPC and tubular absorber; the annual thermal efficiency ranged from 21% to 26% when it was used as skylight and 15-24% when it was used as south or east-facing windows. Yu et al. [15] investigated the feasibility of using 2D dielectric CPC as skylight in daylighting control. It was found that the CPC provided lower transmittance at noon and higher transmittance in the morning and afternoon under clear sky, which could reduce solar heat gain significantly. PRDIEs is a smart window applied on building facade integrating CPC and photovoltaic to provide daylighting and electricity at the same time. It has been extensively investigated by many researchers [82, 87, 90, 144, 145] . The average electrical conversion efficiency was 9.43% and it could reduce up to 20% in the cost of per unit power output comparing with the conventional PV module [90].

Two-dimensional (2D) trough CPC has a longitudinal axis and two parabolic-curved surfaces, which is the most common one in all CPCs [70]. For the most common east-west orientation of 2D trough CPC in practice, the incident light projected on the

north-south meridian forms a so-called south projection angle, which could be compared with the acceptance angle of CPC to determine its optical performance. However, this would be not suitable for a three-dimensional CPC, for example, typical crossed CPC (CCPC), also called orthogonal CPC, consists of four parabolic surfaces and two square apertures. Different from 2D CPC, the optical performance of CCPC is more complicated so that it cannot be determined using a simple south projection angle directly. Due to the complex ray path of incident light, the optical performance of CCPC can be obtained only by raytracing simulation.

The dielectric CPC (dCPC) is an alternative to the mirror CPC and has an enlarged acceptance angle owing to the refraction on air-dielectric interface and also allows transmission of light beyond its acceptance angle. As a result, the dCPC has been widely used in CPV and daylighting control systems. Welford and Winston [70] proposed that the actual acceptance angle of a dCPC needs to be adjusted by a certain degree for nonmeridional incident rays due to the refraction. For 2D dCPC, Yu and Su [94] proposed a concept of inner projection angle which is the refracted projection angle of incident light inside dCPC. They found strong correlations between inner projection angles and optical performance at different solar azimuth angles of 2D dCPC based on simulation results. However, for 3D dielectric crossed compound parabolic concentrator (dCCPC), the refraction and total internal reflection owing to dielectric material should also be considered, which causes the prediction of optical performance of dCCPC becomes more complicated.

To date, no research has been published in the literature that proposes a relatively fast and simple model to predict the optical performance of dCCPC except for simulation. In this chapter, several mathematical models are proposed through multiple nonlinear regression based on a mass of simulation results, in order to predict the optical performance for base-coated and non-coated dCCPC from the given solar azimuth angle, altitude angle and sky clearness factor. The validation and limitations of the models are given to discuss the feasibility and reliability of the models as well. On basis of the regression models proposed in this study, the transmittance of using dCCPC can be calculated in a fast and accurate way rather than using long time ray-tracing simulations. Similarly, in terms of the CPV application, the amount of light received by the PV panel attached on the base of dCCPC can also be determined in a much more convenient way.

5.2. Methodology

5.2.1. Models of dCCPC

The optical performance of dCCPC can be evaluated in two aspects: the optical efficiency and transmittance. According to previous studies [182, 183], it was found that the transmittance and optical efficiency of a dCCPC are related to its dimension, sun position and sky condition. In this research, the dCCPC demonstrated in Fig. 5.2.1.1 is selected as an example to investigate the correlations between its performance and influencing factors. It consists of four parabolic surfaces and two square apertures, which is transformed by crossed interception of two tough dielectric CPCs. For the purpose of applying CPC to windows or facades, the dCCPC is a miniature optical structure, for example, with a height of 24.2mm and an entry aperture of 18mm*18mm. The dCCPC may be filled with acrylic material, which has a refractive index of 1.5. The inner and outer half acceptance angles of the dCCPC are 14.47 ° and 22.02 °, respectively. Two kinds of the dCCPCs in this dimension will be investigated in this study: one is non-coated dCCPC which is the normal dielectric CCPC, the other is base-coated dCCPC having black material attached on its exit aperture to simulate solar absorption.

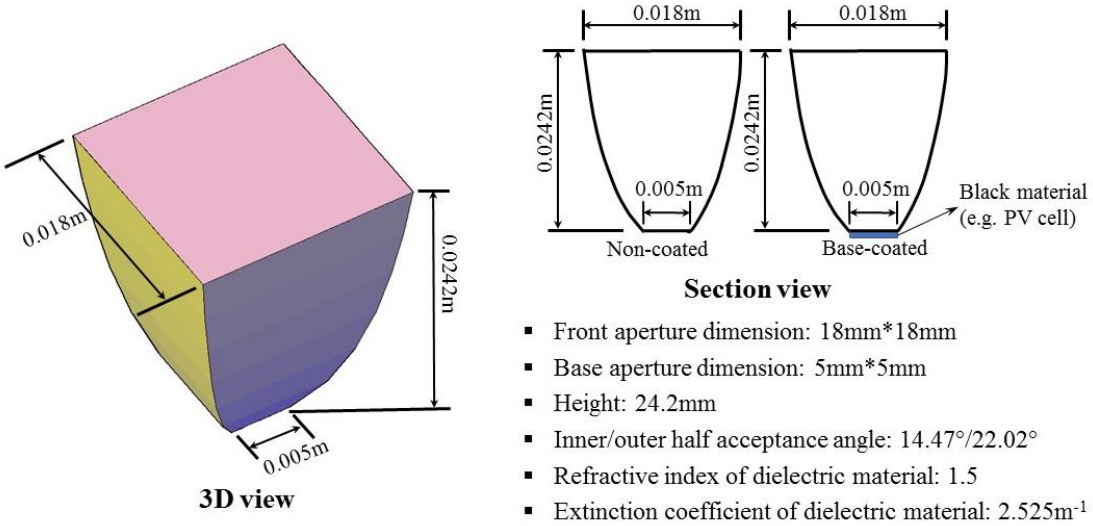


Figure 5.2.11. Schematics, dimensions and physical properties of dielectric CCPC

5.2.2. Software settings

The optical performance of dCCPC was simulated by Photopia. It is a fast and accurate photometric analysis software which can provide liable and comprehensive evaluation for non-imaging optical systems. The calculation is based on probabilistic raytracing

under numerous defined optics and light source models in its library [162]. The light source models for modelling daylight input offered by Photopia are based on the IESNA RP-21 daylight equations. The luminance distribution of sky dome varies across the hemisphere as described in IESNA RP-21. The absolute illuminance from the sun (solar disk) and sky are provided automatically depending on the altitude angles and sky conditions, but they can also be adjusted manually. Both of the sun and sky model emit light onto the optical systems in order to simulate real outdoor conditions. It is worth to mention that the real sky changes all the times and the RP-21 equations represent standard conditions.

Sky clearness factor (ε) proposed by Perez et al. [184] is a popular way to determine the sky condition which has been used in EnergyPlus simulation [185] and daylight calculations [186, 187]. It is calculated from the horizontal diffuse irradiance, normal direct irradiance and solar zenith angle in order to describe the sky condition as shown in Eq. 5.2.2.1. It has been validated using data from various climate environment which accounts for the environment effects such as temperature, humidity, weather, and etc. [184]. Eight categories corresponding to the different value intervals were proposed to describe the sky conditions from overcast to very clear sky [184].

$$\varepsilon = \frac{\frac{(I_h + I)}{I_h} + kZ^3}{1 + kZ^3} \qquad \text{(Eq. 5.2.2.1)}$$

where I is direct normal solar irradiance; I_h is diffuse horizontal irradiance; k is a constant and equals 1.041; Z is solar zenith angle in radians.

However, in the optical simulation using Photopia, it is not a setting option to choose a sky clearness factor, but it allows to change the lumen or radiative outputs from the sun disk and sky dome in its sky model. The horizontal irradiance or illuminance can be then obtained from the sun and sky with complex light distribution for different solar altitudes, and the sky clearness factor can be hence calculated. It would offer a convenience in data analysis by defining a term called sunlight lumen ratio (φ_{lumen}), which is a ratio of the direct normal output from the sun disk to the diffuse output from the sky dome in the sky model, as expressed in Eq. 5.2.2.2. The output from the sun and sky can be set as required in Photopia. The values of sunlight lumen ratio can be controlled as constant in order to investigate the relationships among other criteria.

$$\varphi_{lumen} = \emptyset_{sun} : \emptyset_{sky} \quad \text{(Eq. 5.2.2.2)}$$

where $\emptyset_{sun}$ is the total light output from the sun (direct light output); $\emptyset_{sky}$ is the total light output from the sky (diffuse light output).

In addition, it is important to note that each sunlight lumen ratio corresponds to an interval of sky clearness factor. Table 5.2.2.1 illustrates the sunlight lumen ratios used in simulation for this study, and corresponding horizontal sunlight illuminance ratio, sky clearness factors and sky conditions. The horizontal sunlight illuminance ratio is the ratio of direct horizontal illuminance and global horizontal illuminance, which can indicate the percentage of sunlight illuminance to the total illuminance on a horizontal surface. According to the classification of clearness factor, it is overcast condition when ε < 1.2, intermediate to clear for $\varepsilon \approx 2-3$, and then becomes clearer towards very clear conditions as ε > 6.2. This research focuses on clear sky condition. Therefore the sky clearness factor is controlled above 3 by adjusting the sunlight lumen ratio. Three lumen ratios were selected corresponding to three intervals. It can be seen that with the increase of sky clearness factor, the horizontal sunlight illuminance ratio rises from 0.55 to nearly 1. It is important to mention that the sunlight lumen ratio will be used to demonstrate simulation results for better comparison and illustration, but the sky clearness factor would be used in data regression for the purpose of practical application.

Table 5.2.2.1. Comparisons of sunlight lumen ratio, horizontal sunlight illuminance ratio and sky clearness factor and corresponding sky conditions

Sunlight lumen ratio (φ_{lumen})	Horizontal sunlight illuminance ratio	Sky clearness factor (ε)	Sky condition
1:9	0.55~0.75	3~3.6	Clear sky
1:4	0.75~0.85	3.6~6.6	Clear sky - Very clear sky
1:1	0.85~1	>6.6	Very clear sky

5.2.3. Multiple nonlinear regression

Multiple nonlinear regression is a kind of regression analysis by which the relationship between observation data can be described using a function. The dependent variable is determined by several independent variables through nonlinear combinations in a

multiple nonlinear regression model. XLSTAT is a powerful and intuitive data analysing and statistical add-in integrated into Microsoft Excel, which provides user-friendly interface by Visual Basic Application (VBA) and mathematical and statistical computations by C++ [188]. More than 100 statistical procedures for data analysis, regression, visualization and forecasting are offered by this program. In addition, it was claimed by the Addinsoft SARL that the results by XLSTAT are reliable due to the intensive tests against other software [188]. In order to find the relations between several independent variables, the nonlinear regression using least-squares method would be applied to find the equation with the assumption of homoscedasticity which means the standard errors of regression is independent of the constant variance. The Levenberg-Marquardt and other complex but efficient algorithm would be used.

The criteria utilized to offer the goodness of regression are the coefficient of determination (R^2), the sum of squared errors (SSE) and the mean square error (MSE) as shown in Eq. 5.2.3.1-Eq. 5.2.3.4. There is no absolute criteria for a good value of R^2, MSE and SSE, and all of them should be considered when comparing the prediction data [189]. Generally speaking, the closer to 1 of R^2, the more accurate of prediction; the value of MSE smaller than 10% could be considered as the 'high' of accuracy preference [189, 190].

$$R = \frac{n\sum y_i\hat{y}_i - (\sum y_i)(\sum \hat{y}_i)}{\sqrt{n(\sum y_i^2) - (\sum y_i)^2}\sqrt{n(\sum \hat{y}_i^2) - (\sum \hat{y}_i)^2}} \qquad (Eq.\,5.2.3.1)$$

Where R is correlation coefficient; R^2 is coefficient of determination; $\hat{y}_i$ is the value of the dependent variable predicted by the model; y_i is the true value of the dependent variable; n is the number of samples.

$$SSE = \sum_{i=1}^{n} e_i^2 \qquad (Eq.\,5.2.3.2)$$

$$e_i = y_i - \hat{y}_i \qquad (Eq.\,5.2.3.3)$$

Where SSE is the sum of squared errors of prediction; e_i is the residual.

$$MSE(XLSTAT) = \frac{SSE}{DF} \qquad (Eq.\,5.2.3.4)$$

Where DF is the degree of freedom.

5.2.4. Independent variables

According to the optical properties of dCCPC, it is known that the transmittance of dCCPC is only affected by the path of incident light, that is, the position of incident light source, for a certain dCCPC. Hence, in terms of independent variables, sun position is the most important factor that affects dCCPC performance, which can be described by both azimuth (γ) and altitude (θ_h). In order to find a more accurate and relatively complete result of how the sun influences the performance of dCCPC, the sky models with different sun locations were used in simulations in order to cover the likely incident angles as many as possible. Fig. 5.2.4.1 illustrates the schematic of dCCPC and sun positions used in simulations. The dCCPC was assumed to be positioned as the two perpendicular median planes are along the east-west and north-south directions. With the considerations of the symmetry of dCCPC and simplifying simulation, the solar azimuth was chosen from 0 ° to 45 ° with interval of 5 °. When the sun is at very low altitude, the incident light entering dCCPC is quite few so that this condition does not need to be considered. Thus the solar altitude was chosen from 10 ° to 90 ° in every 5 °. The combinations of the total 17 altitude angles and 10 azimuth angles give 170 sun locations in total which cover an eighth of the hemisphere of sky dome. For the incident ray whose azimuth or altitude is beyond its range, the azimuth or altitude angle can be converted to equivalent angle based on the symmetry of dCCPC for calculation. For example, for an incident ray having the azimuth of 243 ° and the altitude of 73 °, the equivalent azimuth and altitude should be 27 ° and 73 °.

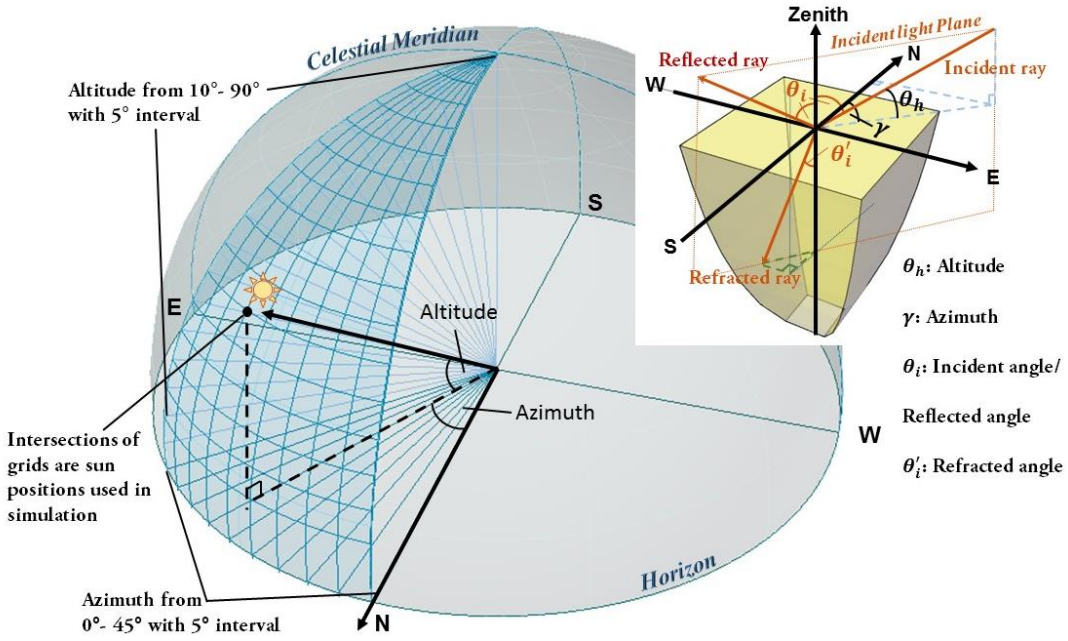


Figure 5.2.4.1. Schematic of azimuth, altitude and selected sun positions for simulation

The performance of dCCPC under overcast sky can be calculated by its geometric properties directly and it is almost constant for diffuse solar radiation [75, 191]. The sky condition being focused on in this study is clear sky only. According to the realistic weather data [192], the skylight and sunlight illuminance change all the time depending on the sun position and sky condition as well. In order to investigate the effects on CPC performance from sky conditions, sky clearness factor was applied as another independent variable. For each of the three ranges of sky clearness factor shown in Table 5.2.2.1, simulations were taken for total 170 sun positions as mentioned before. Therefore there were 510 sets of data in total were used to derive every mathematical model in this study.

5.2.5. Dependent variables

Transmittance and optical efficiency are two main properties to evaluate the performance of dCCPC, and they will be the dependent variables in regressions. Transmittance indicates the amount of incident light passed through dCCPC. Optical efficiency reveals how much irradiance is received by the base of dCCPC, and it is for base-coated dCCPC only. They are expressed by Eq. 7 and Eq. 8 as follows:

$$T = \frac{E}{E_0} \quad \text{(Eq. 5.2.5.1)} \quad \text{and} \quad \eta_{opt} = \frac{I_{obs}}{I_0} \quad \text{(Eq. 5.2.5.2)}$$

Where E is the transmitted daylight illuminance; E_0 and I_0 are the illuminance and irradiance incident onto the entry aperture of dCCPC; T is the transmittance of dCCPC; η_{opt} is the optical efficiency of dCCPC; I_{obs} is the irradiance received by dCCPC base.

5.3. Results and regression

In this section, the simulation results will be presented and data regression will be put forward. There are three regressors which are altitude (θ_h), azimuth (γ) and sky clearness factor (ε), and two dependent variables that are transmittance (T) and optical efficiency (η_{opt}). Fig. 5.3.1 shows the flow chart of the regression models that will be introduced in this section. There are three regression models in total and each of them has three independent variables and one dependent variable. For each model, 510 groups of simulation data obtained from Photopia are provided. The investigation of regression model begins from non-coated dCCPC. Then the model will be adapted to base-coated dCCPC to see whether it is capable to predict its transmittance and optical efficiency.

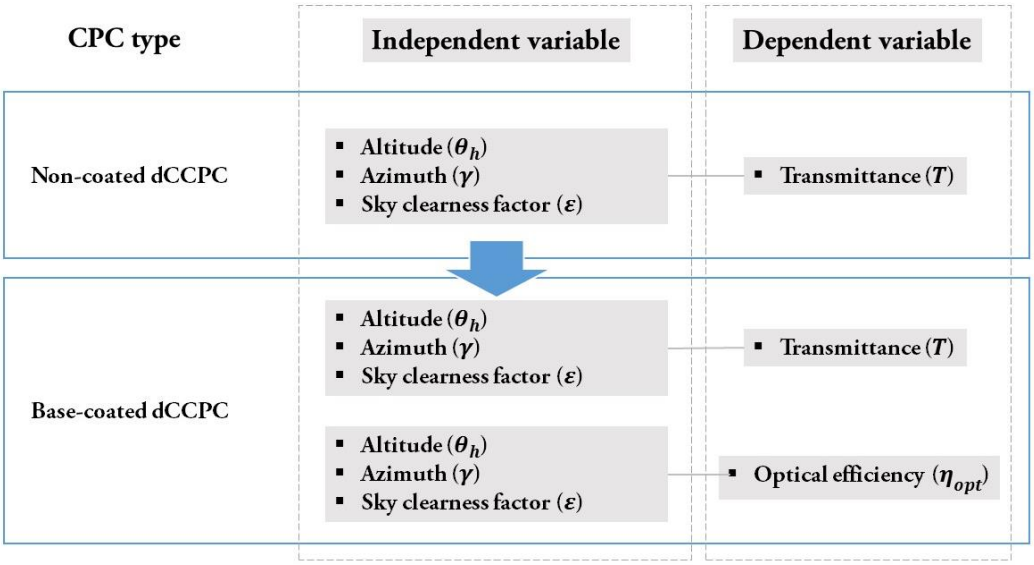


Figure 5.3.1. Independent and dependent variables used in data regression and prediction

5.3.1. Transmittance prediction model for non-coated dCCPC

5.3.1.1. Simulation results

In accordance with different variables, massive simulation results were obtained by Photopia. Fig. 5.3.1.1 presents 3D contour plots of the transmittance of non-coated

dCCPC varying with solar azimuth and altitude for sunlight lumen ratio of 1:9, 1:4, and 1:1 respectively; the transmittance under only direct sunlight condition is also presented in Fig. 5.3.1.1 a) as an ideal condition for comparison. It is verified that the transmittance does relate to these three criteria. When the incident light is direct sunlight only, the curved surface is the smoothest which is the best data set to investigate the relations between transmittance and sun position. When the dCCPC is under the both sun and sky dome, the transmittance becomes more and more uneven as the sunlight illuminance takes less and less percentage of total illuminance. Small peaks and valleys begin to occur on the curved surfaces of transmittance variation when the sunlight lumen ratio are 1:4 and 1:9. This is caused by the diffuse light emitted by sky dome in various directions.

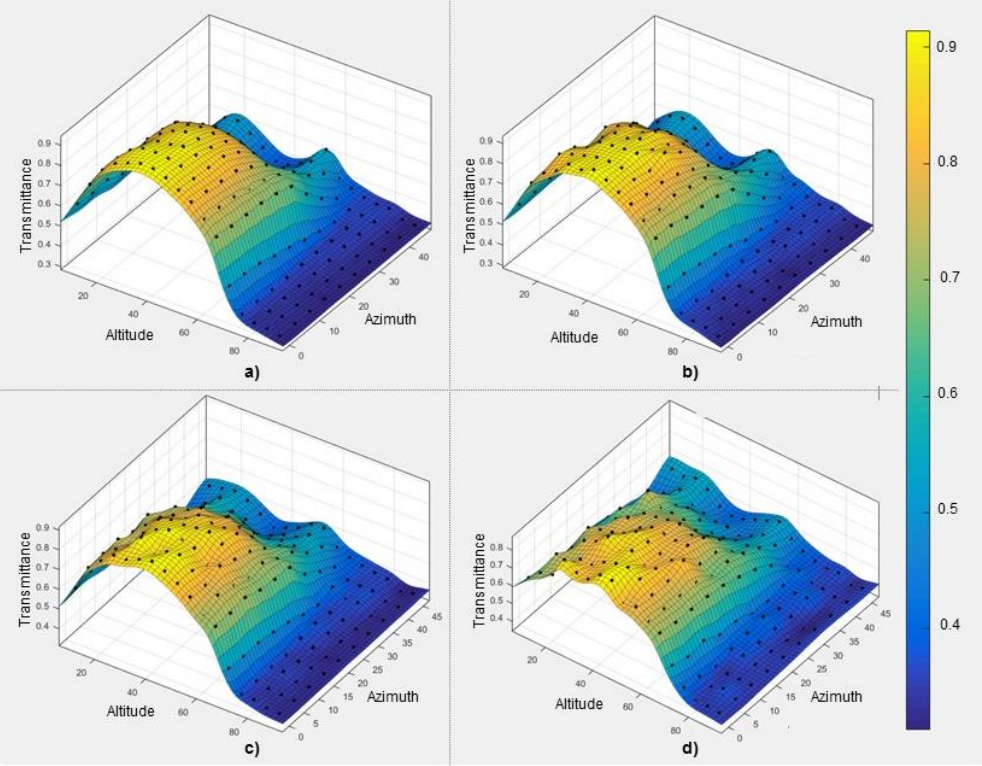


Figure 5.3.1.1. 3D contour plots of transmittance versus solar altitude and azimuth under clear sky with different sunlight lumen ratios in sky model (φ_{lumen}): a) only direct sunlight; b) $\varphi_{lumen} = 1{:}1$ ($\varepsilon \geq 6.6$) ; c) $\varphi_{lumen} = 1{:}4$ ($\varepsilon \approx 3.6{\sim}6.6$) ; d) $\varphi_{lumen} = 1{:}9$ ($\varepsilon \approx 3{\sim}3.6$) (2D contour plot is shown in Appendix Figure B-1)

Fig. 5.3.1.2 demonstrates how the sunlight lumen ratio in sky model affects transmittance and how transmittance varies with the two criteria more intuitively. The horizontal axis is divided into ten parts, and each part refers to a certain azimuth angle. In every part of azimuth, the curves show the transmittance changing with the altitude

from 10 ° to 90 °. The colours of curves distinguish different sunlight lumen ratios. It can be found that the peak values of transmittance decrease generally when the azimuth changes from 0 ° to 45 °. When the azimuth ranges between 0 ° and 30 °, for a certain azimuth angle, the transmittance increases as the altitude rises from 10 ° to 35 ° and reaches the maximum value; then it drops with the altitude increasing from 35 ° to 90 °; the transmittance is at the lowest value when the altitude is 90 °. This performance presents how dielectric CCPC controls transmission of incident light. CCPC can receive incident light with an incident angle smaller than its half acceptance angle. Part of the light refracted into CCPC is escaped from the curved surfaces and edges causing transmittance; the rest of light is reflected out of CCPC again after total internal reflection. When the incident light is located at higher altitude angle (45 °-90), more incident light will be reflected out so that the transmittance decreases. When the azimuth angle of incident light is within 35-45 °, the transmittance declines slightly on the original tendency as the altitude is at 20-55 °. Because CCPC consists of only four parabolic surfaces, there is no parabolic surface facing the direction from which the azimuth of incident light is close to 45 °. More complicated total internal reflections occur inside CCPC which may cause the fluctuation of transmittance variation. In addition, it can be observed that the effect of sunlight lumen ratio in sky model are not significantly. It mainly changes the peak and lowest values of transmittance but does not influence the tendencies of transmittance variation. Comparing with the two curves of only direct sunlight and sunlight lumen ratio of 1:9 in sky model, the maximum difference of transmittance is ± 0.1 approximately. It is important to mention that the altitude and azimuth are the critical criteria affecting transmittance of non-coated CCPC; the sky clearness factor does not has significant influence on it: It changes the peak and valley values regardless of the variation tendency.

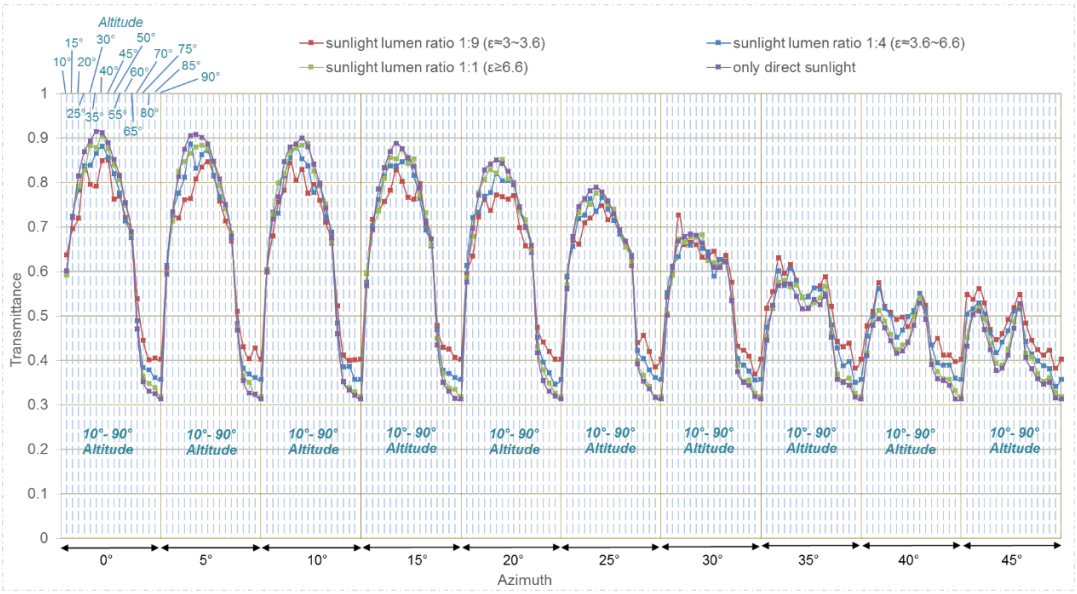


Figure 5.3.1.2. Transmittance of non-coated CCPC under clear sky with different sunlight lumen ratios in sky model (Altitude of sun ranges from 10 °-90 °; Azimuth of sun ranges from 0 °-45 °)

5.2.1.2. Regression prediction model

Based on the simulation results, twelve regression equations that are likely to provide strong correlations are proposed as shown in Table 5.3.1.1 below. The goodness of each regression equation is demonstrated in Table 5.3.1.2. In every regression, the independent variables are altitude (θ_h), azimuth (γ) and sky clearness factor (ε); the dependent variable is transmittance (T). The regression starts from the most common way, the first order polynomial equation, as expressed by Eq. 5.3.1.1-1. It is obvious that this equation does not fit well according to the low R^2 of 0.572 in this regression. It was found that the variations of transmittance are periodic with the change of azimuth and altitude. Thus the terms including altitude (θ_h) and azimuth (γ) in polynomial equation are replaced by trigonometric functions in Eq. 5.3.1.1-2, 5.3.1.1-3 and 5.3.1.1-4. The goodness of these equations indicates the trigonometric functions make the regressions fit simulation data better. For Eq. 5.3.1.1-4, the coefficient of determination R^2 reaches 0.836. However the sum of squared errors (SSE) of predictions for this equation is not good enough. Then the quadratic polynomial functions as shown by Eq. 5.3.1.1-5 and 5.3.1.1-6 are attempted but the fittings are almost the same as the first order polynomial equation. In regression equation, the main effect and interaction effect should be taken into account [193]. Up to now each independent variable has been incorporated into the regression equation as a main-

effect term however the regressions are not satisfied. The interactions among these variables are considered beginning with Eq. 5.3.1.1-7. In Eq. 5.3.1.1-7 and 5.3.1.1-8, the functions with the multiplication of independent variables are tried but they still do not provide satisfactory regression results. However, when plotting the regression results of Eq. 5.3.1.1-8 it was found that this equation provides comparable tendencies of transmittance variation compared to simulation results although it does not perform acceptable goodness of regression. Then, Eq. 5.3.1.1-9 is proposed which contains the interactions between only two independent variables: azimuth and altitude. This equation provides relatively good fittings with the high R^2 of 0.915. It also inspired the authors to fit data in a new way. Because the variations of transmittance are mainly determined by azimuth and altitude, and the sky clearness factor does not affect the variation of tendencies. In regression equation, the multiplication of two terms with trigonometric functions of altitude and azimuth are applied to determine the general variations of predicted values; then another term with sky clearness factor is multiplied by them as correction. Therefore Eq. 5.3.1.1-10, 5.3.1.1-11 and 5.3.1.1-12 are put forward. The third term of interaction is polynomial function. It was found that the regressions coincide with simulated data well when the correction term contains all of the three independent variables. Comparing with the fitting goodness of these three equations, it can be seen that when the order of polynomial function in correction term is higher, the regression fits the simulated data better. When the order of polynomial function is higher than 3, the goodness stays stable. Based on the goodness and simplification of regression, Eq. 5.3.1.1-12 is decided to be the regression equation to forecast the transmittance of non-coated dCCPC. Because there is no skylight in the models simulating the data set of 'only direct sunlight', it is important to mention that this data set was not used for the regression in Eq. 5.3.1.1-12.

Table 5.3.1.1. Regressing equations attempted for the correlations of altitude, azimuth and sky clearness factor to the transmittance of non-coated dCCPC

Eq. 5.3.1.1-1	$T = a_1\theta_h + a_2\gamma + a_3\varepsilon + a_4$
Eq. 5.3.1.1-2	$T = a_1 \cos\theta_h + a_2 \cos\gamma + a_3\varepsilon + a_4$
Eq. 5.3.1.1-3	$T = a_1 \cos(b_1\theta_h) + a_2 \cos(b_2\gamma) + a_3\varepsilon + a_4$
Eq. 5.3.1.1-4	$T = a_1 \cos(b_1\theta_h + b_2) + a_2 \cos(b_3\gamma + b_4) + a_3\varepsilon + a_4$
Eq. 5.3.1.1-5	$T = a_1\theta_h^2 + a_2\gamma^2 + a_3\varepsilon^2 + a_4$
Eq. 5.3.1.1-6	$T = a_1 \cos^2(b_1\theta_h + b_2) + a_2 \cos^2(b_3\gamma + b_4) + a_3\varepsilon^2 + a_4$

Eq. 5.3.1.1-7	$T = a_1\theta_h \cdot \gamma \cdot \varepsilon + a_2$
Eq. 5.3.1.1-8	$T = a_1 \cos(b_1\theta_h + b_2) \cdot \cos(b_3\gamma + b_4) \cdot \varepsilon + a_2$
Eq. 5.3.1.1-9	$T = a_1 \cos(b_1\theta_h + b_2) \cdot \cos(b_3\gamma + b_4) + a_2$
Eq. 5.3.1.1-10	$T = a_1 \cos(b_1\theta_h + b_2) \cdot \cos(b_3\gamma + b_4) \cdot (c_1 + c_2\varepsilon + c_3\gamma + c_4\theta_h + c_5\theta_h\gamma + c_6\varepsilon\gamma + c_7\theta_h\varepsilon + c_8\varepsilon\theta_h\gamma) + a_2$
Eq. 5.3.1.1-11	$T = a_1 \cos(b_1\theta_h + b_2) \cdot \cos(b_3\gamma + b_4) \cdot (c_1 + c_2\varepsilon + c_3\gamma + c_4\theta_h + c_5\theta_h\gamma + c_6\varepsilon\gamma + c_7\theta_h\varepsilon + c_8\varepsilon^2\theta_h\gamma + c_9\theta_h^2\varepsilon\gamma + c_{10}\gamma^2\varepsilon\theta_h + c_{11}\varepsilon^2\theta_h^2\gamma^2) + a_2$
Eq. 5.3.1.1-12	$T = a_1 \cos(b_1\theta_h + b_2) \cdot \cos(b_3\gamma + b_4) \cdot (c_1 + c_2\varepsilon + c_3\gamma + c_4\theta_h + c_5\theta_h\gamma + c_6\varepsilon\gamma + c_7\theta_h\varepsilon + c_8\varepsilon^2\theta_h\gamma + c_9\theta_h^2\varepsilon\gamma + c_{10}\gamma^2\varepsilon\theta_h + c_{11}\varepsilon^2\theta_h^2\gamma^2 + c_{12}\varepsilon^2 + c_{13}\theta_h^2 + c_{14}\gamma^2) + a_2$
θ_h is altitude (expressed in radian measure); γ is azimuth (expressed in radian measure); ε sky clearness factor; T is transmittance; a_n, b_n, c_n are regression coefficients.	

Table 5.3.1.2. Goodness of regressions (Eq. 5.3.1.1-1 – Eq. 5.3.1.1-12) for non-coated dCCPC

Eq. No.	R^2	SSE	MSE	RMSE	Eq. No.	R^2	SSE	MSE	RMSE
Eq. 5.3.1.1-1	0.572	6.346	0.013	0.112	Eq. 5.3.1.1-7	0.174	12.241	0.024	0.155
Eq. 5.3.1.1-2	0.676	4.799	0.009	0.097	Eq. 5.3.1.1-8	0.476	7.771	0.015	0.124
Eq. 5.3.1.1-3	0.695	4.517	0.009	0.095	Eq. 5.3.1.1-9	0.915	1.840	0.003	0.052
Eq. 5.3.1.1-4	0.836	2.434	0.005	0.070	Eq. 5.3.1.1-10	0.933	0.995	0.002	0.045
Eq. 5.3.1.1-5	0.696	4.502	0.009	0.094	Eq. 5.3.1.1-11	0.937	0.938	0.002	0.044
Eq. 5.3.1.1-6	0.838	2.405	0.005	0.069	Eq. 5.3.1.1-12	0.944	0.825	0.002	0.041
R^2: coefficient of determination					SSE: sum of squared errors of prediction				
MSE: mean squared error					RMSE: root mean square error				

For the simulated non-coated dCCPC, Table 5.3.1.2 illustrates the parameter values obtained for regression Eq. 5.3.1.1-12. The parameter values for Eq. 5.3.1.1-1 to Eq. 5.3.1.1-11 are presented in Table B-1 in Appendix for the purpose of reproducing the outcomes in this paper. The coefficient of determination (R^2) of this regression model is 0.944 which indicates the regression is relative accurate and acceptable. In addition,

it is important to mention that the altitude and azimuth angle used in this equation should be in radian measure. This equation is suitable when the altitude ranges between 10 °-90 ° and the azimuth ranges from 0 ° to 45 °. If the dCCPC is tilt or the incident light coming from other angles beyond the acceptable ranges of angles, this equation is still applicable by converting the angle of incident light to equivalent angles within the acceptable ranges on the basis of the symmetry of dCCPC. In addition, this equation should also be suitable for other designs of non-coated dCCPC but the parameter values would be different.

Table 5.3.1.3. Parameter values of Eq. 5.3.1.1-12 for predicting the transmittance of non-coated dCCPC

a_1	1.496188	c_2	0.002828	c_9	0.000495
a_2	0.406272	c_3	0.280238	c_{10}	-0.036059
b_1	2.036185	c_4	0.536357	c_{11}	0.000658
b_2	1.932737	c_5	-0.010543	c_{12}	-0.000065
b_3	1.564716	c_6	0.001939	c_{13}	-0.350158
b_4	3.308904	c_7	0.000824	c_{14}	-0.326153
c_1	0.100193	c_8	0.000047		

The simulation results and the values predicted by Eq. 5.3.1.1-12 with determined parameter values for transmittance of non-coated dCCPC are compared in Fig. 5.3.1.3. It can be seen that the regression data fits simulated data perfectly in no matter what interval of azimuth and transmittance. All of the predicted values are located within the region of $\pm$20% deviation, which implies that this mathematical model is reliable to predict the transmittance of non-coated dCCPC. It can be also seen that different from the incident light at 0 °-30 ° azimuth angle, the transmittance of non-coated dCCPC is always lower than 0.6 when the light is incident at the azimuth angle within 30-45 °. The transmittance of non-coated dCCPC is larger than 0.3 for all incident angle of light.

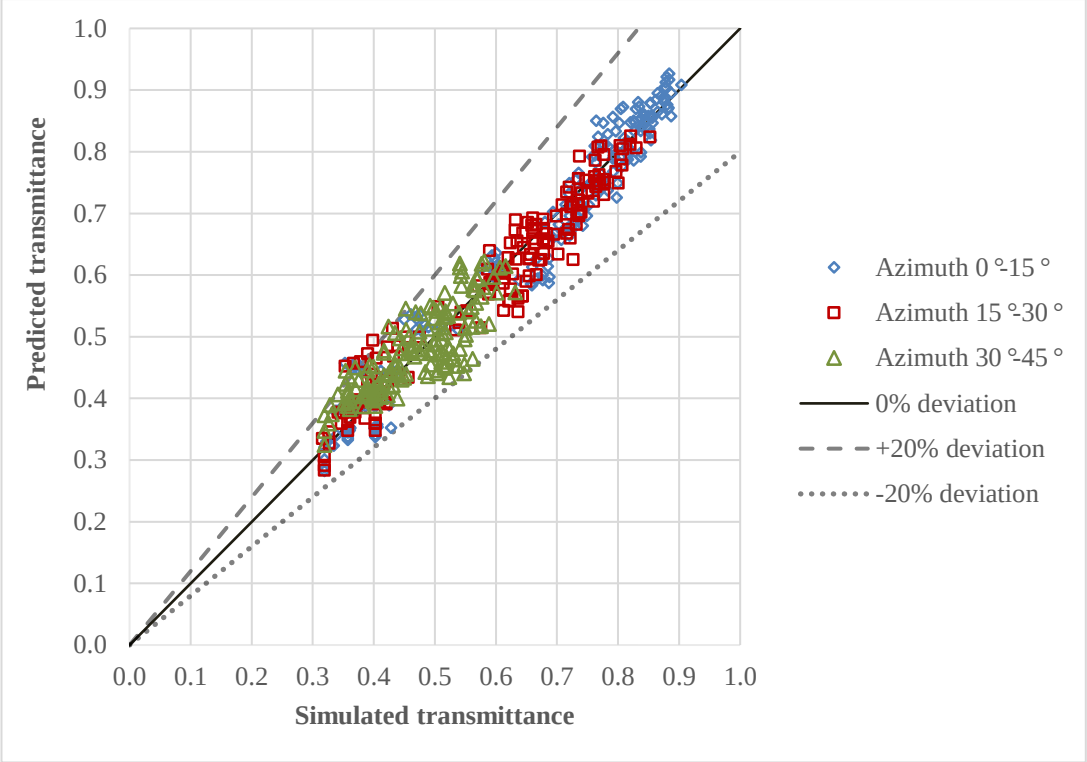


Figure 5.3.1.3. Comparisons between predicted and simulated transmittance of non-coated dCCPC (Regression: Eq. 5.3.1.1-12)

The absolute values of the residuals between predicted and simulated transmittance are quantified in Fig. 5.3.1.4. It can be found that all of the values are smaller than 0.12 and more than 80% of them are smaller than 0.06. For different azimuth and altitude angles, the residuals distribute relatively uniformly. When the altitude ranges from 10 °to 50 °, most of the residuals are smaller than 0.06. Larger residuals also occur when the altitude is between 55 °and 75 °for different azimuth angles.

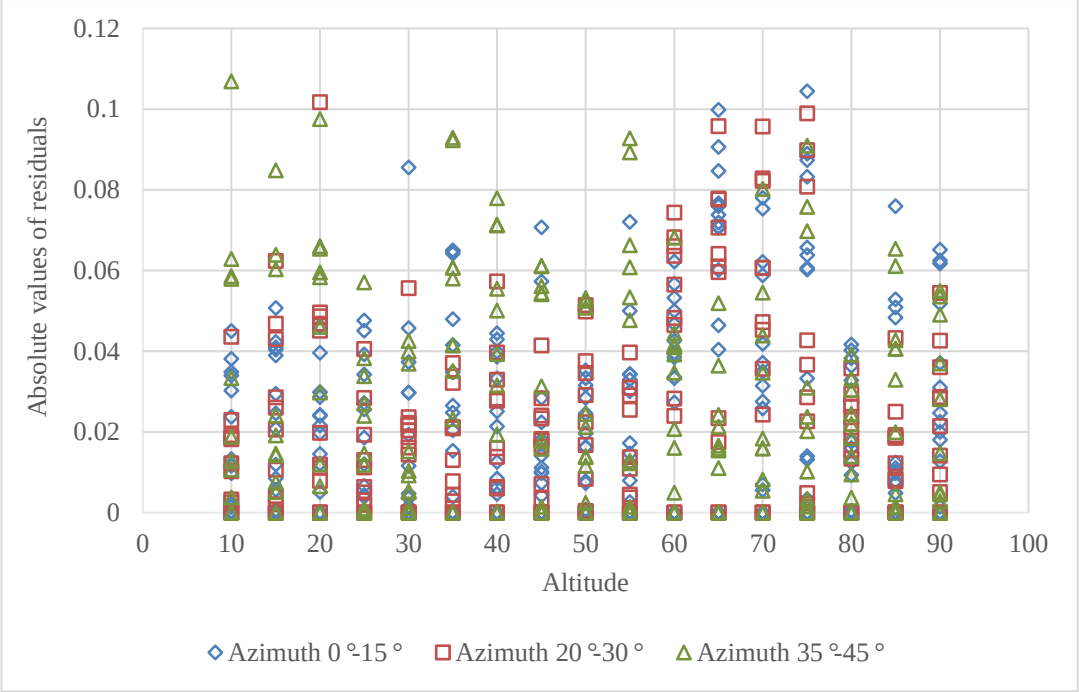


Figure 5.3.1.4. Absolute values of the residuals of predicted and simulated transmittance for non-coated dCCPC (Regression: Eq. 5.3.1.1-12)

5.3.2. Transmittance prediction model for base-coated dCCPC

Base-coated dCCPC has totally the same structure as non-coated dCCPC but possessing an absorbing surface attached on its base (exit aperture). The relationships obtained from ray-tracing simulation among transmittance, azimuth, altitude and sunlight lumen ratio in sky model of base-coated dCCPC are illustrated in Fig. 5.3.2.1. It can be seen that the tendencies of curves are almost same as those of non-coated dCCPC, but base-coated dCCPC performs similar maximum values and lower minimum values of transmittance. The maximum difference between transmittance for the two curves of only direct sunlight and sunlight lumen ratio of 1:9 in sky model is ± 0.2 approximately.

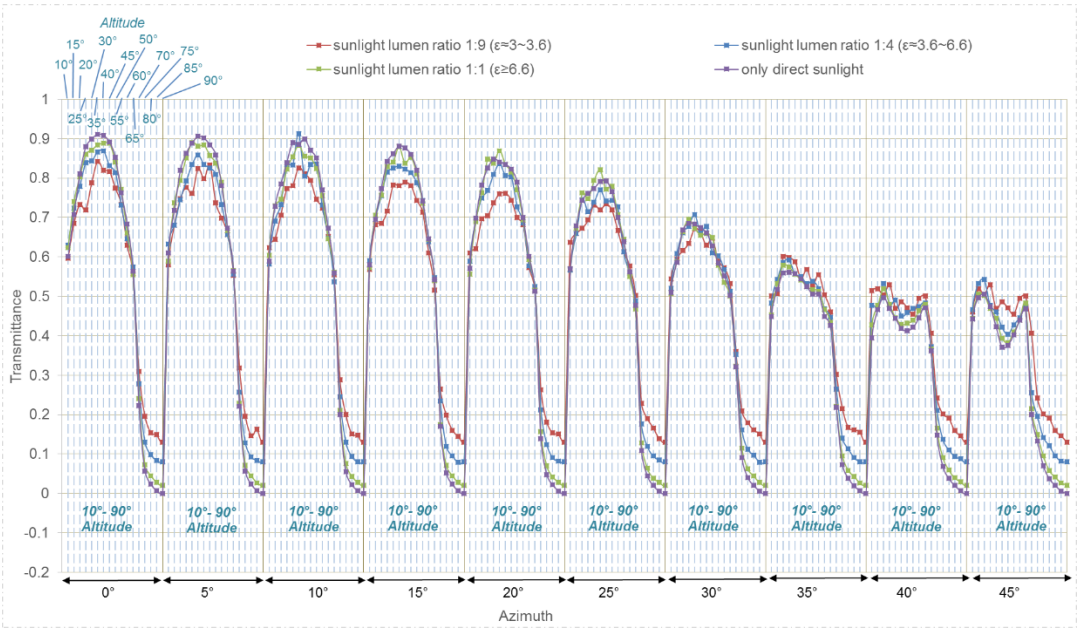


Figure 5.3.2.1. Transmittance of base-coated dCCPC under clear sky with different sunlight lumen ratios in sky model (Altitude of sun ranges from 10 °-90 °; Azimuth of sun ranges from 0 °-45 °)

Considering the similarities of the tendency and the periodicity between the transmittance for base-coated and non-coated dCCPC, it is supposed that the regression model for non-coated dCCPC is likely to predict the transmittance of base-coated dCCPC as well. Thus the simulation results for base-coated dCCPC were regressed using Eq. 5.3.1.1-12 and the correlations between simulation and prediction results are presented in Fig. 5.3.2.2. It can be seen that most of the predicted values are located within the region of ±20% deviation. The goodness of this regression model provides the 0.967 of R^2 and 1.234 of SSE, which indicates that the regression Eq. 5.3.1.1-12 is still suitable to predict the transmittance for base-coated dCCPC, but big deviations appear when the transmittance is smaller than 0.3 regardless of azimuth angle. Based on the research by Yu and Su [94], the relationship between inner perpendicular projection angle and transmittance is validated and presented in Appendix D.

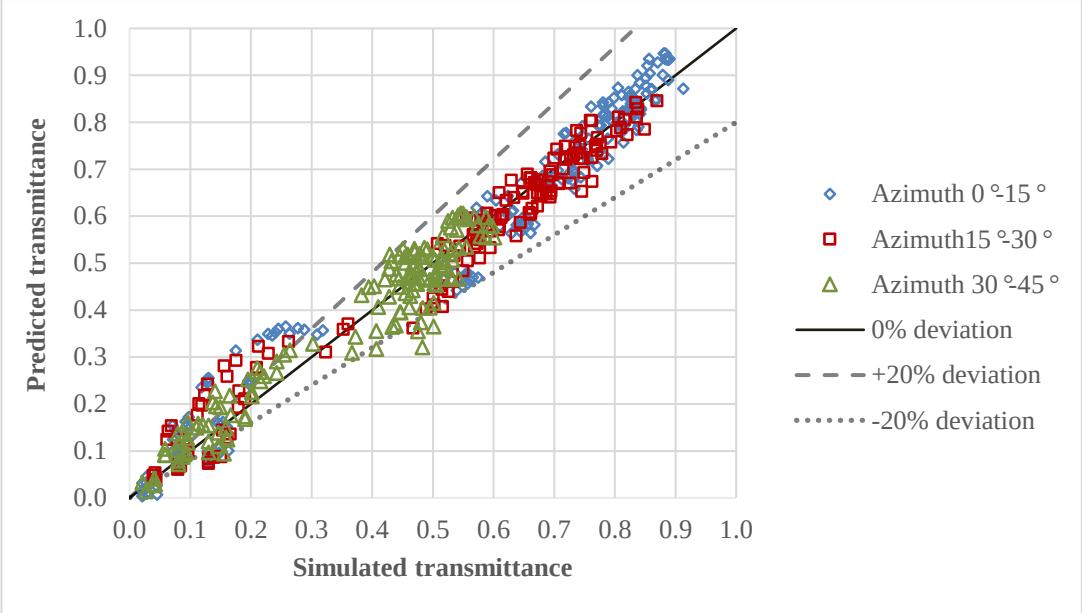


Figure 5.3.2.2. Comparisons between predicted and simulated transmittance of base-coated dCCPC (Regression: Eq. 5.3.1.1-12)

According to the transmittance results shown in Fig. 5.3.2.3, it can be seen that for each different azimuth angle, the transmittance of base-coated dCCPC is lower than 0.3 when the altitude of incident light ranges from 70 ° to 90 °. The reason of larger errors occurring at lower transmittance may be because the regression parameters are not perfectly suitable for the whole range of the data. Thus, it is attempted to divide all of the transmittance results into two groups: one is that the altitude is smaller than 70 ° the other is that the altitude is equal to or larger than 70 °, then two groups of parameter values are regressed according to Eq. 5.3.1.1-12. The value of each parameter is obtained as shown in Table 5.3.2.1 and the comparisons between predicted and simulated values are illustrated in Fig. 5.3.2.3. It can be found that with the new parameter values, almost all of the deviations for predicted transmittance are within the range of -20% - 20% compared to the original simulation results. A few large errors occur when the transmittance is within 0.4-0.5 and the azimuth angle ranges between 30 ° and 45 °. This is caused by the transmittance having the slightly different tendencies compared to the transmittance of other azimuth angles, which can be found in Fig. 8. For all of the data in two groups, the goodness of prediction is 0.986 of R^2 and 0.531 of SSE, which is better than the regression by using only one group of parameter values. It is suggested that using two groups of parameter values for more accurate transmittance prediction of base-coated dCCPC.

Table 5.3.2.1. Parameter values of Eq. 5.3.1.1-12 for predicting the transmittance of base-coated dCCPC

Parameter values of Eq. 5.3.1.1-12 ($\theta_h \geq 70°$)					
a_1	15.438580	c_2	0.000189	c_9	0.000041
a_2	0.272134	c_3	0.028146	c_{10}	0.001606
b_1	3.172319	c_4	0.156169	c_{11}	-0.000020
b_2	1.971506	c_5	-0.020172	c_{12}	-0.000003
b_3	1.376607	c_6	-0.000187	c_{13}	-0.042172
b_4	3.076578	c_7	0.000103	c_{14}	0.005846
c_1	-0.128884	c_8	-0.000001		
Parameter values of Eq. 5.3.1.1-12 (θ_h<70 °)					
a_1	1.103238	c_2	0.015591	c_9	-0.039893
a_2	-0.437428	c_3	-2.844649	c_{10}	-0.008916
b_1	1.567036	c_4	-0.589013	c_{11}	0.000383
b_2	2.297709	c_5	-0.825488	c_{12}	-0.000403
b_3	0.584756	c_6	-0.015636	c_{13}	1.138829
b_4	1.968326	c_7	0.005027	c_{14}	1.331796
c_1	2.870284	c_8	0.001094		

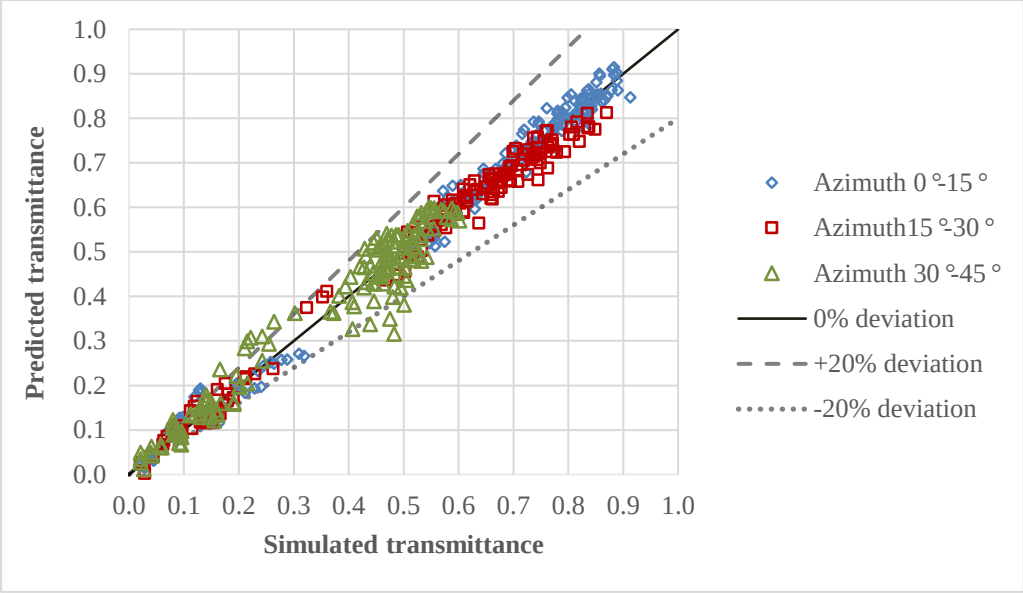


Figure 5.3.2.3. Comparisons between predicted and simulated transmittance of base-coated dCCPC (Regression: Eq. 5.3.1.1-12, separate parameter values for $\theta_h \geq 70°$ and θ_h<70 °)

5.3.3. Optical efficiency prediction model for base-coated dCCPC

For base-coated dCCPC, another important characteristic is optical efficiency except for transmittance. In order to find whether the optical efficiency has similar relations

with these criteria, they are plotted in Fig. 5.3.3.1 in the same way. It is interesting to see that the optical efficiency is mainly determined by solar altitude, in other words, the incident angle of light. The optical efficiency does not change as obviously as transmittance with variation of azimuth. When the solar altitude is at around 70 °, there is a steep increase of optical efficiency which indicates that most of the light is concentrated onto the base of dCCPC when the light is incident within the half acceptance angle of dCCPC. The sunlight lumen ratio in sky model has similar influences on it compared to transmittance. The differences of the optical efficiencies under 1:9 sunlight lumen ratio and only direct sunlight range from -0.2 to +0.05 approximately.

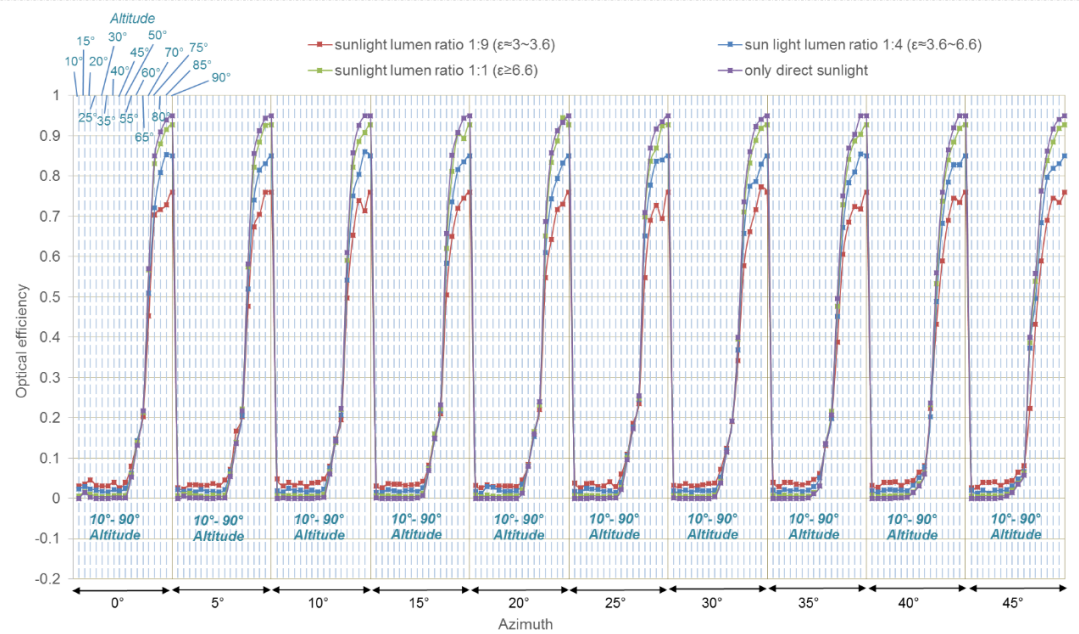


Figure 5.3.3.1. Optical efficiency of base-coated dCCPC under clear sky with different sunlight lumen ratio in sky model (Altitude of sun ranges from 10 °-90 °; Azimuth of sun ranges from 0 °-45 °)

In accordance with the relationships among optical efficiency, altitude, azimuth and sky clearness factor shown in Fig. 5.3.3.1, it was found that the optical efficiency of base-coated dCCPC has the same periodicity with transmittance: the optical efficiency varies in similar tendencies for different altitudes, and it changes with altitude for a certain azimuth. Thus, Eq. 5.3.1.1-12 is also attempted to predict the optical efficiency and the new expression formula is written as Eq. 5.3.1.1-13. The goodness of regression provides the R^2 of 0.969 and SSE of 1.760 which shows the regression is satisfactory in general. Fig. 5.3.3.2 illustrates the scatterplot comparing the predicted

and simulated values for the regression. Similar to the regression for transmittance of base-coated dCCPC, the predicted optical efficiency has relatively larger deviation when the optical efficiency is smaller than 0.3. Thus, all of the results are attempted to be divided into two groups for separate regressions.

$$\eta_{opt} = a_1 \cos(b_1\theta_h + b_2) \cdot \cos(b_3\gamma + b_4) \cdot (c_1 + c_2\varepsilon + c_3\gamma + c_4\theta_h + c_5\theta_h\gamma + c_6\varepsilon\gamma + c_7\theta_h\varepsilon + c_8\varepsilon^2\theta_h\gamma + c_9\theta_h^2\varepsilon\gamma + c_{10}\gamma^2\varepsilon\theta_h + c_{11}\varepsilon^2\theta_h^2\gamma^2 + c_{12}\varepsilon^2 + c_{13}\theta_h^2 + c_{14}\gamma^2) + a_2 \quad (\text{Eq. } 5.3.1.1 - 13)$$

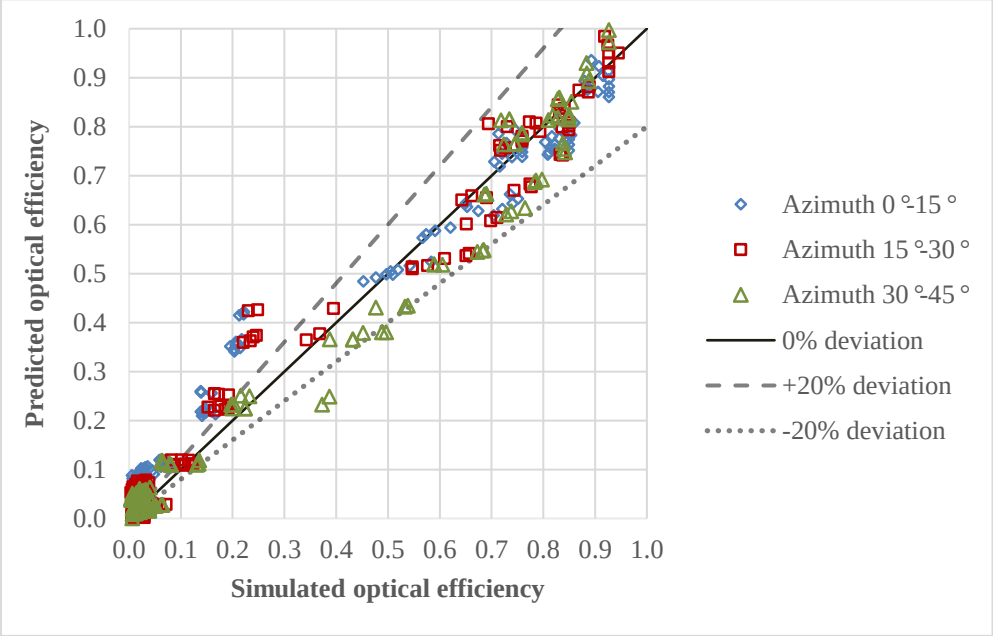


Figure 5.3.3.2. Comparisons between predicted and simulated optical efficiency of base-coated dCCPC (Regression: Eq. 5.3.1.1-13)

According to the variations of optical efficiency shown in Fig. 5.3.3.1, it was found that the 70 ° of altitude is the boundary determining whether the optical efficiency is less than or higher than 0.3 for most of the data. The regressions are conducted for the data that with the altitude equal to or larger than 70 °, and less than 70 °. The parameter values of regressions are listed in Table 5.3.3.1 and the comparisons between predicted and simulated results are illustrated in Fig. 5.3.3.3. For the new regression results, the R^2 is 0.994 and the SSE is 0.349, which implies the regression fits better when separating the data into two groups for regressions. Almost all of the predicted values are located within the range of ±20% deviation. The regression results indicate that the derived mathematical model can be applied for not only transmittance, but optical

efficiency for dCCPC. In addition, the relationship between inner perpendicular projection angle and optical efficiency was investigated as well and demonstrated in Appendix D.

Table 5.3.3.1. Parameter values of Eq. 5.3.1.1-13 for predicting the optical efficiency of base-coated dCCPC

Parameter values of Eq. 5.3.1.1-12 ($\theta_h \geq 70°$)					
a_1	5.232485	c_2	-0.002435	c_9	-0.000384
a_2	-0.355704	c_3	-0.311694	c_{10}	-0.000638
b_1	2.121739	c_4	0.415850	c_{11}	0.000010
b_2	2.812218	c_5	0.213677	c_{12}	0.000010
b_3	0.581986	c_6	-0.003565	c_{13}	-0.114970
b_4	3.322576	c_7	0.000789	c_{14}	-0.066297
c_1	-0.594695	c_8	0.000065		
Parameter values of Eq. 5.3.1.1-12 ($\theta_h < 70°$)					
a_1	0.365010	c_2	0.068264	c_9	-0.162943
a_2	0.046430	c_3	2.316287	c_{10}	0.135648
b_1	4.133090	c_4	4.273429	c_{11}	-0.008014
b_2	1.081834	c_5	-1.633847	c_{12}	-0.002401
b_3	0.382385	c_6	-0.151169	c_{13}	-3.873164
b_4	1.776869	c_7	-0.001518	c_{14}	-0.661668
c_1	-1.801165	c_8	0.012119		

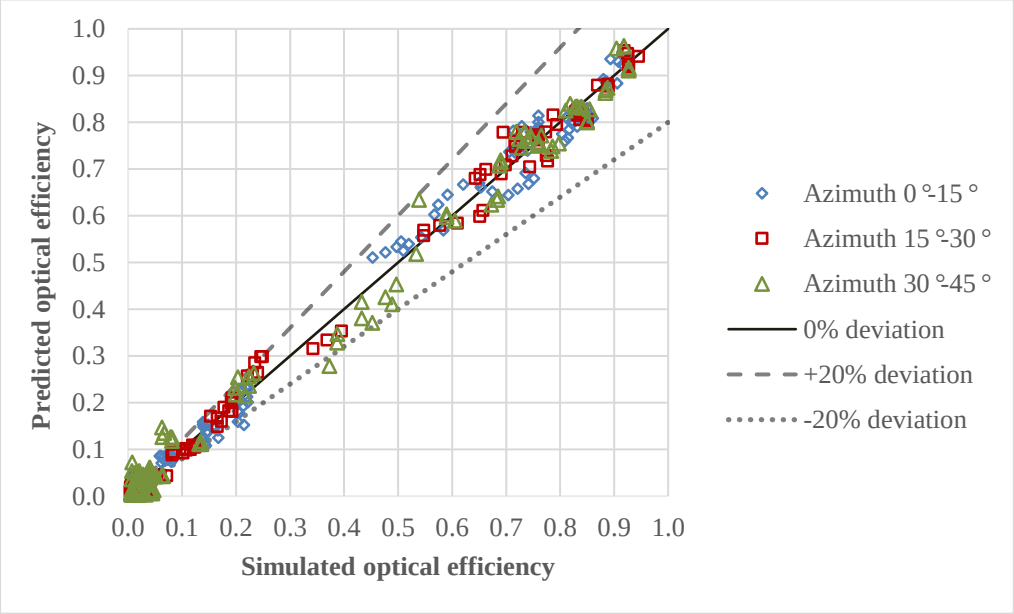


Figure 5.3.3.3. Comparisons between predicted and simulated optical efficiency of base-coated dCCPC (Regression: Eq. 5.3.1.1-12, separate parameter values for $\theta_h \geq 70°$ and $\theta_h < 70°$)

5.4. Discussion

5.4.1. Verification of prediction models

In this section, several examples of predicting the optical performance for the simulated dCCPC will be presented to show using derived regression models in practice, as well as to verify the feasibility of the prediction method. The location of Nottingham, UK (53.0 °N, 1.2 °W) will be used as an example. The time and date selected are the 10am and 12pm for spring equinox (21st Mar), summer solstice (21st Jun) and winter solstice (21st Dec). The dCCPC is assumed to be located facing south with the tilt angle 37 °, which can collect the most sunlight. The comparisons between predicted and simulated values for the selected date and time are demonstrated in Table 5.4.1.1. For the three regression models, the predicted results are close to the simulated results. The deviations between them are mostly smaller than 0.1. The biggest error of 0.14 occurs in the transmittance prediction at 10am on 21st Dec. It can be seen that the prediction models are reliable to predict the optical performance for dCCPC in practical conditions.

Table 5.4.1.1. Verification of predicted optical performance to simulation results for dCCPC on various dates and times

Local time			**21 Mar**		**21 Jun**		**21 Dec**	
			10am	**12pm**	**10am**	**12pm**	**10am**	**12pm**
Solar altitude (θ_h)			29.9 °	36.5 °	52.0 °	60.4 °	9.1 °	13.6 °
Solar azimuth (γ)			141.0 °	176.2 °	128.7 °	177.1 °	151.8 °	179.5 °
Tilt angle (β)			37 °	37 °	37 °	37 °	37 °	37 °
sky clearness factor (ε)			4.42	3.04	5.58	6.56	5.29	8.48
Non-coated dCCPC	transmittance	predicted	0.68	0.47	0.67	0.37	0.57	0.81
		simulated	**0.73**	**0.44**	**0.71**	**0.37**	**0.50**	**0.84**
Base-coated dCCPC	transmittance	predicted	0.63	0.28	0.55	0.12	0.59	0.78
		simulated	**0.64**	**0.23**	**0.61**	**0.09**	**0.45**	**0.83**
	optical efficiency	predicted	0.08	0.61	0.24	0.79	0.08	0.04
		simulated	**0.09**	**0.74**	**0.22**	**0.83**	**0.02**	**0.02**

5.4.2. Model limitations

The regressions in this study are all based on the results simulated by Photopia which is an accurate raytracing tool. In order to introduce the feasibility of the obtained regression equation, it is important to describe the sky model used in simulations. The light distribution in sky model is calculated by IESNA RP-21 daylight equations [162, 194]. There are two kinds of sky models provided by Photopia lamp library, one is overcast sky and the other is clear sky. In the new sky standard published by the British Standard Institution, there are 15 luminance distributions for different sky conditions that are determined by the gradation (I-VI) and indicatrix (1-6) parameter numbers [195]. The luminance distribution of the overcast sky model used in Photopia is the same as CIE Standard Overcast Sky model I.1 which has steep luminance gradation towards zenith, azimuthal uniformity. The clear sky model in Photopia is similar to the type V.4 (CIE Standard Clear Sky with low luminance turbidity) in CIE standard. For the clear sky model, part of sky that is near the sun would be brighter. The intensive light beams are emitted from the solar disk. Therefore, the sunlight would be the main factor that affects dCCPC performance in the simulations using clear sky model. Hence, the main limitation of the regression equations obtained is that they are suitable for the clear sky condition in which the sunlight illuminance is predominant.

In addition, it is important to mention that the regression model proposed in this chapter is based on the certain dCCPC introduced in Section 5.2.1. Although the optical performance of dCCPC varies with its own geometry and dielectric material, the optical performances of them still follow the same rules and have similar tendencies. This chapter aims to investigating the feasibility of proposing a mathematical model for predicting the optical performance of dCCPC. The dCCPC used in this part is regarded as an example and the results imply that the performances of the dCCPCs in other dimensions and materials are very likely to be predicted by the regression model. The characters of dCCPC itself, such as the type of dielectric material, the transparency of dCCPC, the accuracy of geometry, and the dust deposition on the surface are not considered in this study, but they are recommended to be added to improve the prediction model for future work.

5.4.3. Significance of prediction models

The results obtained from the best regression models for non-coated and base-coated dCCPCs are illustrated in Table 5.4.3.1 below. For the models forecasting the optical efficiency and transmittance, the high values of R^2 indicate their feasibility but few of predictions may have relatively large errors. The coefficient of determination (R^2) of all models are higher than 0.94 and the MSE are smaller than 0.002, which indicates they are capable to predict the nonlinear relationship reliably for the optical performance of both non-coated and base-coated dCCPCs.

Table 5.4.3.1. Summary of multiple nonlinear regression models

CPC type	Independent variables	Dependent variables	Regression		
			R^2	SSE	MSE
Non-coated	$\theta_h, \gamma, \varphi_{sun}$	T	0.944	0.825	0.0017
Base-coated	$\theta_h, \gamma, \varphi_{sun}$	T	0.986	0.531	0.0011
Base-coated	$\theta_h, \gamma, \varphi_{sun}$	η_{opt}	0.994	0.349	0.0007

The derived regression models provide a fast and simple approach to predict the optical performance of base-coated and non-coated dielectric dCCPC for the light coming from arbitrary directions accurately, which means the transmittance and optical efficiency of dCCPC can be determined directly under clear sky without running simulations by software when the tilt angle of dCCPC, sky clearness factor, time, longitude and latitude of location are given in practice. For example, for the solar concentrating photovoltaic (CPV) and solar thermal systems, they can be used to estimate the optical efficiency of dCCPC and then calculate the collected solar energy rapidly; in the daylighting control system integrated with dCCPC, the energy saving due to daylighting can be predicted accurately without the long-time simulations. On the other hand, the regression models proposed are suitable for not only the dCCPCs used in in this study, but also other CPCs with different dimensions owing to the similar structures and working principle of CPC. For other CPC of different geometries, the new parameter values of the proposed prediction equations can be obtained in the same way and then the specific model for it could be built.

5.5. Summary

The mathematical models for calculating the optical performance of dielectric crossed compound parabolic concentrator (dCCPC) have been proposed in this chapter through multiple nonlinear regression method in accordance to a mass of simulation results. The independent variables for each model are solar altitude, azimuth and sky clearness factor, which are used to determine both of the transmittance and optical efficiency of base-coated dCCPC and the transmittance of non-coated dCCPC. The coefficient of determination (R^2) for every model obtained by regression is higher than 0.94 and the deviations of most predicted data are less than 20% compared to simulation data, which indicates the accuracy and reliability of prediction models.

It is significant to establish the mathematical models for calculating the optical performance of dCCPC. The most common way to determine the optical performance of dCCPC is by raytracing simulation currently which requires a long time. The derived models can help to forecast the optical performance of dCCPC accurately and rapidly from the given solar altitude, solar azimuth and sky clearness factor, which saves a lot of time for running simulation. In addition, the regression models provide visualized equations that can be validated, optimized and it is friendly to be incorporated with other software. Meanwhile, it should be mentioned that the regression models proposed in this chapter are only suitable for the clear sky condition. In Chapter 6, the prediction models are modified to fit more different sky types. In addition, this study only explored the prediction models for dCCPC, it is promising to adopt these models to predict the optical performance for other types of CPCs owing to the similar structure and working principles for the future work.

Chapter 6

Comparison between multiple nonlinear regression and artificial neural network for predicting the transmittance of dCCPC under standard sky conditions

6.1. Introduction

With the consideration of raised problems in building design, such as visual comfort, overheating, human health and energy saving, daylighting control has become an essential part in building design for the purpose of sustainability. In a survey conducted by Reinhart and Fitz [196], 91% of 185 interviewees related to architecture and building energy from 27 countries had considered daylighting aspects in their building design.

As a representative type of nonimaging optics, the compound parabolic concentrator (CPC) has been widely applied in solar concentration for generating electricity and heat for many decades [80, 86-88, 105]. In recent years, its potential in daylighting control has been discovered by many researchers. As a result of its specific structure, a CPC can receive or reject sunlight and diffuse skylight depending on the incident angle of light so as to control daylighting in different incident angles.

Walze et al. [85] proposed a smart window coated with a microstructure in shape of two-dimensional (2D) CPC array on its surface. The micro CPC was manufactured by interference lithography in PMMA and can allow a selective transmission of daylight with smaller or larger incident angle depending on the coating position. Ulavi et al. [141, 142] put forward a hybrid solar window consisting of transparent 2D CPCs and tubular absorbers. The CPC is coated with a wavelength selective film in order to concentrate the sunlight in infrared range onto absorber and transmit the sunlight in visible range into interior spaces. The annual thermal efficiency of this window ranges between 15-26% in the climate of Minneapolis. Similarly, another hybrid window called PRIDE, which is the abbreviation of photovoltaic facades of reduced costs incorporating devices with optically concentrating elements, was also introduced with the integration of 2D asymmetric CPC and PV cell. After several improvements on PRIDE by many researchers [84, 87, 90, 143, 145], the typical type of PRIDE having 2D asymmetric dielectric CPC and PV attached on the base of CPC can provide the maximum power output which is 3.27 times as high as a flat PV of the same area [145]. Meanwhile, PRIDE also controls daylighting by its parabolic surfaces.

The dielectric CPC (dCPC) is regarded as a type of CPC which enlarges its acceptance angle due to the refraction on air-dielectric interface [70], so it can receive more sunlight comparing with conventional mirror CPC. As a result, it has become more

popular in CPC application, especially in daylighting control. Yu et al. [15] investigated the feasibility of a 2D dielectric CPC (dCPC) in daylighting control when it is used as skylights for atrium. It was found that the transmittance provided by dCPC is lower in summer and higher in winter, which can prevent overheating in the summer effectively. The transmittance is relatively high under overcast sky condition so that the indoor illuminance level can be maintained. Tian and Su [182] investigated the potential of three-dimensional (3D) dielectric crossed compound parabolic concentrator (dCCPC) on daylighting control. Comparing with 2D dCPC, it presents better capability on controlling daylight not only in different seasons during a whole year, but in different times through a whole day. For example, on the summer solstice, the transmittance of 3D dCCPC is higher at about 0.8 in the morning and afternoon, and lower at 0.4 at noon; in winter solstice, the transmittance is at around 0.4 in the morning and at 0.6 at noon.

As more and more studies have been conducted to investigate the feasibility of CPC in daylighting control, an accurate and reliable model for calculating or predicting the transmittance of CPC becomes significant. Using raytracing software is the most common way to determine the optical efficiency of CPC, for instance, Matlab [152], LightTools [153], Radiance [159], Photopia [162], and COMSOL Multiphysics [157], etc. They combine the advantages of illuminance calculation and interior visualization. Many studies have proved the reliability and accuracy of raytracing simulations [74, 77, 110, 147, 148]. However, raytracing simulation takes a long time for complex light path and is impracticable for a performance analysis on an annual basis. Except simulation, few of researches have brought forward simple, fast and accurate mathematical models or other approaches to predict the optical performance of CPC, especially for dCPC which has complex light reactions including reflection, refraction and total internal reflection.

For calculating the optical performance of 2D dCPC, Yu and Su [94] put forward a concept of inner projection angle, which refers to the refracted angle of incident light inside dCPC. After analysing the CPC performance under light beam with various incident angles, strong correlations between inner projection angle and optical efficiency, and between inner projection angle and the sum of transmittance and surface reflection were found for the 2D dCPC with a coating on its base. As regards 3D dCPC, our previous work [197] derived new mathematical models to predict the

transmittance and optical performance of dielectric crossed CPC (dCCPC) under clear sky condition.

Artificial neural network (ANN), usually called neural network, is an alternative to traditional simulation method, which is a self-learning and self-training programme. A neural network can be considered as a network of neurons which interact with each other in a specific order through mathematical functions. It has been widely applied to various disciplines, such as renewable energy, heat exchange, refrigeration, chemical process control, and building design, etc., for data analysis and prediction [198-201].

ANN has also been used as a powerful forecasting tool in aspect of daylighting including luminance value, daylighting performance, energy saving for building and daylighting control system [202-206]. Navada et al. [207] attempted to predict outdoor and indoor illuminance level through ANN in order to control the position of blinds, and the predicted results matched the experiment values very well. Kazanasmaz et al. [208] predicted the daylighting levels inside an local office building by ANN and obtained the results that were close to the measured values. Hu and Olbina [209] used ANN to calculate the optimum slat angles of split blinds for the purpose of adjusting indoor illuminance. Results demonstrated that the errors were less than 10% of illuminance and less than 5% for slat angles for about 90% of the time in a year.

As a continuous work of our previous research [197], the multiple nonlinear equation predicting the transmittance of 3D dielectric crossed compound parabolic concentrator (dCCPC) is modified to be appropriate to calculate the transmittance of dCCPC under all standard sky conditions for the purpose of daylighting application in this chapter, with the input variables of solar azimuth, solar altitude and sky clearness factor. In addition, ANN model is attempted to be created to forecast the transmittance of dCCPC. Finally, the two models are compared and discussed focusing on their accuracy, feasibility, pros and cons.

6.2. Methodology

6.2.1. Model description

Two types of dCCPC will be discussed in this study, one is non-coated dCCPC, the other is base-coated dCCPC. Non-coated dCCPC represents the conventional CPC filled with dielectric material that is acrylic usually. Each surface of non-coated dCCPC is transparent. Base-coated dCCPC is the same as non-coated dCCPC but

having a black surface attached on its base, which is used to absorb the light reflected onto it. The dCCPC attached with a PV cell on its base is considered as base-coated dCCPC in most cases. Fig. 6.2.1.1 illustrates the dimensions of the sample dCCPC used in this study, which consist of four parabolic surfaces and two square apertures. The performance of dCCPC is simulated by PHOTOPIA, which is a professional and precise optical analysis software [162]. Three standard sky models, clear sky, intermediate sky and overcast sky, are used to cover all typical sky conditions. All sky models are based on the equations defined in CIE standard [195] and IES RP-21 [194].

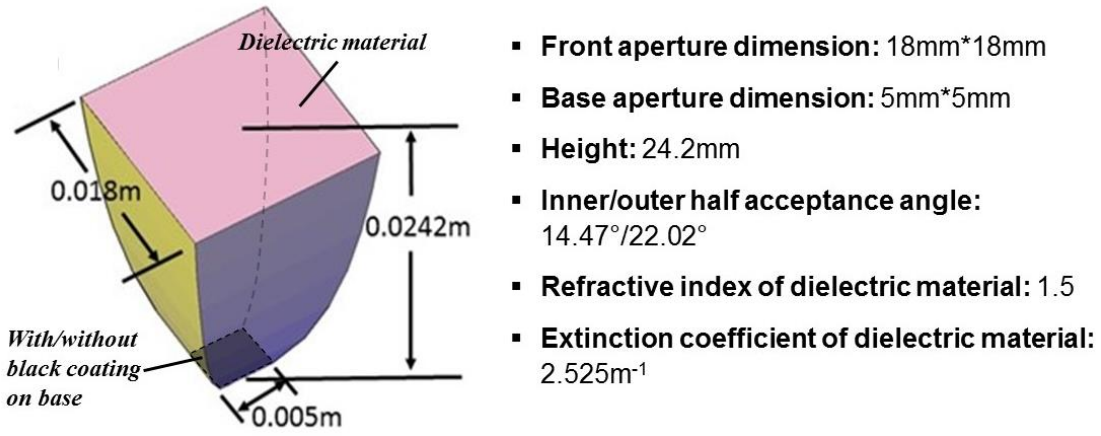


Fig. 6.2.1.1. Schematic and dimensions of dCCPC

Similar to the previous study, the independent variables for prediction models are solar altitude (θ_h), solar azimuth (γ), and sky clearness factor (ε). For the input data set, the solar altitude ranges from 10 ° to 90 °, and the solar azimuth ranges from 0 ° to 45 ° considering the symmetry of dCCPC. The sky clearness factor is equal or greater than 1. According to the sky model proposed by Perez, et al. [184], when $1 \leq \varepsilon \leq 1.2$, it refers to overcast sky; ; $\varepsilon \approx 1.2{\sim}2$ represents overcast to intermediate sky; $\varepsilon \approx 2{\sim}3$ indicates intermediate to clear sky; when $\varepsilon > 3$, it implies clear sky. The sky clearness factor is defined by Eq. 6.2.1.1 [185] in detail.

$$\varepsilon = \frac{\frac{(I_h + I)}{I_h} + kZ^3}{1 + kZ^3} \qquad \text{(Eq. 6.2.1.1)}$$

where I is direct normal solar irradiance; I_h is diffuse horizontal irradiance; k is a constant and equals 1.041 for solar zenith angle Z in radians.

The dependent variable, that is, the output of prediction model is the transmittance (T) of dCCPC, which indicates the amount of incident light passed through dCCPC as shown in Eq. 6.2.1.2.

$$T = \frac{E}{E_0} \quad \text{(Eq. 6.2.1.2)}$$

Where E is the transmitted daylight illuminance

E_0 is the illuminance received by the entry aperture of dCCPC

T is the transmittance of dCCPC

6.2.2. Multiple Nonlinear Regression (MNLR)

In respect of data-based prediction, the traditional way is to use statistical models. Multiple nonlinear regression (MNLR) is probably the most common approach for dealing with nonlinear relationships with several variables. It is assumed that the relationship between the dependent variable $\boldsymbol{y}$ and the $\boldsymbol{p}$ vector of regressors $\boldsymbol{x_i}$ is nonlinear in MNLR models. The MNLR models for predicting the optical performance of dCCPC were developed by XLSTAT which is an accurate statistical add-in integrated into Microsoft Excel [188].

The input variables were used to train and test the MNLR models are: solar altitude (θ_h), solar azimuth (γ), and sky clearness factor (ε). According to the previous study [197], the best NMLR model for predicting the transmittance of dCCPC under clear sky is as shown by Eq. 6.2.2.1 below:

$$\begin{aligned} T = {} & a_1 \cos(b_1\theta_h + b_2) \cdot \cos(b_3\gamma + b_4) \\ & \cdot (c_1 + c_2\varepsilon + c_3\gamma + c_4\theta_h + c_5\theta_h\gamma + c_6\varepsilon\gamma + c_7\theta_h\varepsilon + c_8\varepsilon^2\theta_h\gamma \\ & + c_9\theta_h^2\varepsilon\gamma + c_{10}\gamma^2\varepsilon\theta_h + c_{11}\varepsilon^2\theta_h^2\gamma^2 + c_{12}\varepsilon^2 + c_{13}\theta_h^2 + c_{14}\gamma^2) \\ & + a_2 \qquad \text{(Eq. 6.2.2.1)} \end{aligned}$$

Where θ_h is altitude (expressed in radian measure); γ is azimuth (expressed in radian measure); ε is sky clearness factor; T is transmittance; a_n, b_n, c_n are regression coefficients.

6.2.3. Artificial Neural Network (ANN)

Artificial Neural Network (ANN) is an alternative way to extract the nonlinear relationships between the variables by self-training and self-learning through black-

box modelling [210]. It is good at solving multi-variable problems and extracting the non-linear relationship by means of training data.

The multi-layer perceptron (MLP) is the most commonly used neural network, in which every neuron organized in different layers interacts with the neurons in contiguous layers. A typical feedforward artificial neural network consists of three layers of neurons which are input layer, hidden layer and output layer. The input layer contains all of the input parameters, and then they are processed through the network in a forward direction, layer by layer until the output information is computed by the output layer.

Fig. 6.2.3.1 demonstrates the ANN frame utilized in this study. The ANN model is composed of an input layer with two or three input parameters depending on different models, a hidden layer, and an output layer containing one output parameter. The mathematical form of this three-layer feedforward ANN is expressed as Eq. 6.2.3.1 [211].

$$O = g_2\left[\sum_j Z_j v_j \, g_1\left(\sum_i w_{ji} I_i + w_{j0}\right) + v_0\right] \qquad \text{(Eq. 6.2.3.1)}$$

Where I_i is the value of node i in the input layer; Z_j is the value of node j in the hidden layer; O is the value output from the node in the output layer; w_{j0} are the weights of bias input node $I_0 = 1$ and v_0 is the weight of bias input from hidden unit $Z_0 = 1$; w_{ji} is the weight going to hidden node j from input node i, and v_j is the weight going into the output node from hidden node j; g_1 and g_2 are the transfer functions for the hidden layer and the output layer.

The training algorithm applied in this study for ANN model is Levenberg-Marquardt (LM) by which the weight and bias values are updated. The LM algorithm is an optimization of the Newton algorithm which improves second-order training speed without computing the exact Hessian matrix, and provides stable and fast convergence [212]. Many studies have demonstrated the advantages of the LM algorithm comparing with other training algorithms [213-216]. The LM algorithm is defined by Eq. 6.2.3.2 [217].

$$X_{k+1} = X_k - [J^T J + \mu I]^{-1} J^T \mathrm{e} \qquad \text{(Eq. 6.2.3.2)}$$

Where X is the criteria of the neural network that would be optimized; J is the Jacobian matrix that contains first derivatives of the network errors in terms of weight and bias; e is the vector of all error terms; μ is the combination coefficient controlling the learning process; I is the identity matrix.

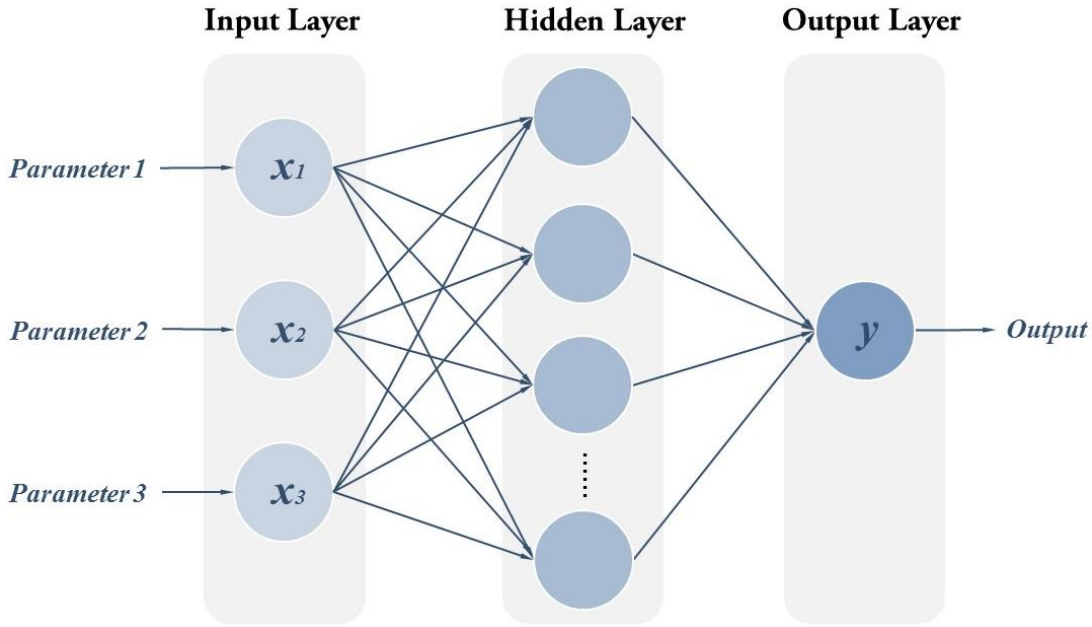


Fig. 6.2.3.1. Feedforward ANN architecture with one hidden layer

The Neural Network Toolbox in MATLAB 2016b was chosen to build ANN model in this study. All of the ANN models utilize Levenberg-Marquardt back propagation (BP) training algorithms due to its reliability and simplicity [218]. In each ANN model, the total 1050 dataset are randomly divided into three parts: 70% of them was used for training, 15% for validation and 15% for testing. The number of neurons in the hidden layer is optimized based on the available data through the trial and error procedure. It was found that the hidden layer with 20 neurons would result in the best performance for the ANN models used in this study. Tansig and purelin functions are selected as the first and second transfer functions after various attempts, which can lead to the best results. Similarly, the input variables are solar altitude (θ_h), solar azimuth (γ), and sky clearness factor (ε), and the output variable is transmittance (T).

6.2.4. Evaluation criteria

The criteria used to evaluate the goodness of regression are the coefficient of determination (R^2), the sum of squared errors (SSE) and the mean square error (MSE) as defined by Eq. 6.2.4.1-Eq. 6.2.4.3.

$$R = \frac{n\sum y_i\hat{y}_i - (\sum y_i)(\sum \hat{y}_i)}{\sqrt{n(\sum y_i^2) - (\sum y_i)^2}\sqrt{n(\sum \hat{y}_i^2) - (\sum \hat{y}_i)^2}} \qquad \text{(Eq. 6.2.4.1)}$$

Where R is correlation coefficient; R^2 is coefficient of determination; $\hat{y}_i$ is the value of the dependent variable predicted by the model; y_i is the true value of the dependent variable; n is the number of samples.

$$SSE = \sum_{i=1}^{n}(y_i - \hat{y}_i)^2 \qquad \text{(Eq. 6.2.4.2)}$$

Where SSE is the sum of squared errors of prediction.

$$MSE = \frac{SSE}{n} \qquad \text{(Eq. 6.2.4.3)}$$

Each of the criteria refers to a specific property of regression data. There is no absolute criteria for a good value of R^2, MSE and SSE. [189]. Generally speaking, the closer to 1 of R^2, the more accurate of prediction; the value of MSE smaller than 10% could be considered as highly accurate [189, 190].

6.3. Modification of Multiple Nonlinear Regression (MNLR) model

As is known that dCCPC accepts light with larger incident angle, and rejects light with smaller incident angle. For a sky, the incident light consists of direct light from the sun and diffuse light from the sky. The optical performance including transmittance and optical efficiency of dCCPC is sensitive to the incident angle of direct sunlight, which implies that the transmittance varies more significantly under clear sky and less obviously under intermediate sky even constant under overcast sky [75, 191]. Therefore, a modified mathematical model (Eq. 6.3.1a and Eq. 6.3.1b) was proposed on the basis of previous work [197] aiming at determining the transmittance of both non-coated and base-coated dCCPC under all standard sky conditions: Eq. 6.3.1a is suitable for the clear and intermediate skies and Eq. 6.3.1b is for overcast condition. The results of predicting the optical efficiency by MNLR model are shown in Appendix A and the corresponding results from ANN model are demonstrated as well.

$$T(\theta_h, \gamma, \varepsilon) = \begin{cases} a_1 \cos(b_1\theta_h + b_2)\cos(b_3\gamma + b_4)(c_1 + c_2\varepsilon + c_3\gamma + c_4\theta_h \\ +c_5\theta_h\gamma + c_6\varepsilon\gamma + c_7\theta_h\varepsilon + c_8\varepsilon^2\theta_h\gamma + c_9\theta_h^2\varepsilon\gamma + c_{10}\gamma^2\varepsilon\theta_h, & \varepsilon > 1.2 \\ +c_{11}\varepsilon^2\theta_h^2\gamma^2 + c_{12}\varepsilon^2 + c_{13}\theta_h^2 + c_{14}\gamma^2) + a_2 \\ \\ T_0, & 1 \le \varepsilon \le 1.2 \end{cases}$$

Where θ_h is altitude (expressed in radian measure), $0° < \theta_h \le 90°$; γ is azimuth (expressed in radian measure), $0° \le \gamma \le 45°$, and $\gamma = 0°$ when the projected light on the top surface of dCCPC is normal to either side of its entry aperture; ε is sky clearness factor; T is transmittance; a_n, b_n, c_n are regression coefficients; T_0 is the transmittance of dCCPC under overcast sky.

The simulation results of dCCPC transmittance under clear sky, intermediate sky and overcast sky are applied to the regression of Eq. 6.3.1a-6.3.1b. The values of parameters are illustrated in Table 6.3.1 for base-coated and non-coated dCCPC respectively. According to our previous research [197], the regression of base-coated dCCPC is divided into two parts by altitude in order to get better regression results. Fig. 6.3.1 and Fig. 6.3.2 compares the simulated values with the predicted values generated by Eq. 6.3.1a. Because the transmittance of dCCPC is regarded as constant under overcast condition, that is when $1 \le \varepsilon \le 1.2$, Eq. 6.3.1b is excluded in comparison.

Table 6.3.1. Parameter values of Eq. 6.3.1a-6.3.1b for non-coated and base-coated dCCPC

non-coated dCCPC					
a_1	1.92522	c_2	0.01374	c_9	-0.00474
a_2	0.56370	c_3	-0.45392	c_{10}	0.01027
b_1	1.80728	c_4	-0.00785	c_{11}	-0.00026
b_2	1.36934	c_5	0.48689	c_{12}	-0.00014
b_3	2.01738	c_6	-0.02002	c_{13}	-0.21601
b_4	2.31492	c_7	-0.00734	c_{14}	-0.23176
c_1	0.30229	c_8	0.00058	T_0	0.63267
base-coated dCCPC (θ_h<70 °)					
a_1	1.51451	c_2	0.02316	c_9	0.01683
a_2	0.17648	c_3	-0.66508	c_{10}	-0.04433
b_1	1.09774	c_4	-0.53359	c_{11}	-0.00057
b_2	2.18317	c_5	-0.23800	c_{12}	-0.00058
b_3	2.19941	c_6	0.00115	c_{13}	0.16767
b_4	1.79765	c_7	-0.03045	c_{14}	0.65415
c_1	0.79983	c_8	0.00191	T_0	0.52864

base-coated dCCPC (θ_h>70 °)					
a_1	8.24190	c_2	0.00530	c_9	-0.00587
a_2	0.33604	c_3	-0.01065	c_{10}	-0.00129
b_1	0.18880	c_4	0.08257	c_{11}	0.00012
b_2	4.32194	c_5	-0.05855	c_{12}	-0.00006
b_3	4.88711	c_6	-0.00045	c_{13}	0.00010
b_4	-0.72973	c_7	0.02421	c_{14}	0.04963
c_1	-0.05998	c_8	-0.00036	T_0	0.52864

It can be seen that the regression of Eq. 6.3.1a provides very strong fittings for non-coated dCCPC. The coefficient of determination (R^2) reaches 0.93 and the MSE is 0.0016. More than 82.5% of the residuals deviations are within ±10%, and 98.5% of the deviations are within ±20%. The goodness of regression for base-coated dCCPC seems not as good as the non-coated one, but still a satisfactory result. It offers a higher R^2 of 0.97 and a relatively lower MSE of 0.0030 which proves its reliability and accuracy. The percentage of the deviations of residuals that is within ±20% is 80.1%. In addition, most of the large deviations occur when the transmittance is smaller than 0.35, because the smaller reference values cause larger percent deviations for the same residuals.

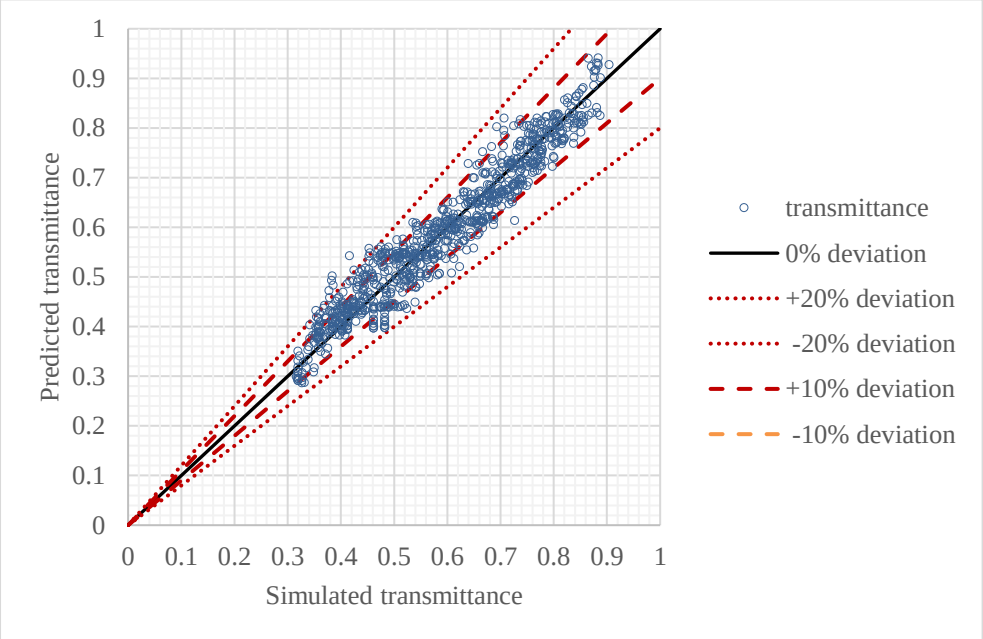


Fig. 6.3.1. Comparison between simulated and predicted transmittance of non-coated dCCPC under clear and intermediate skies (MNLR, Eq. 6.3.1a)

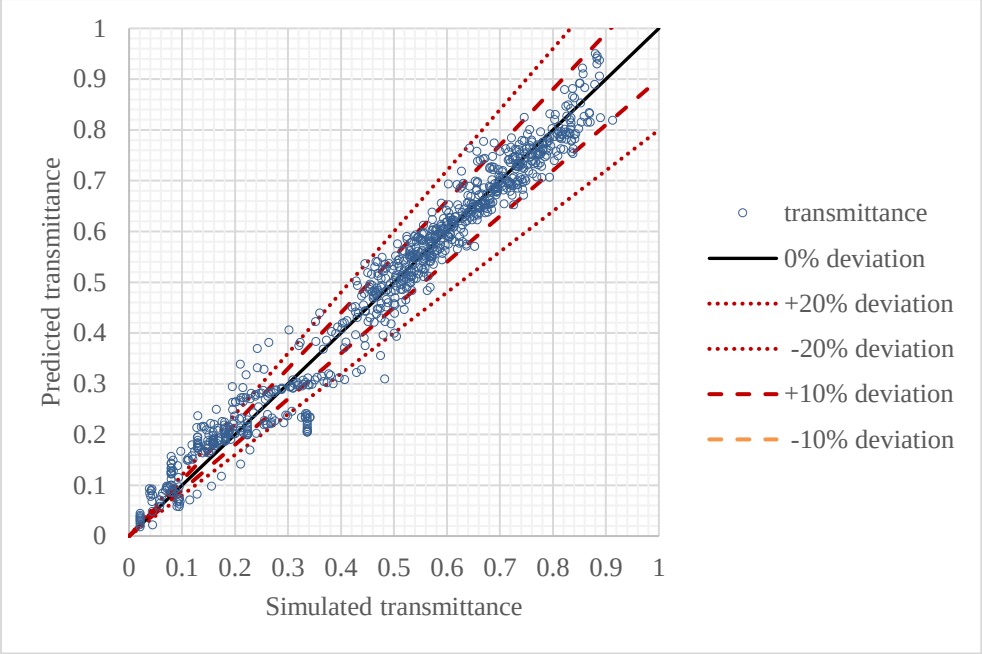


Fig. 6.3.2. Comparison between simulated and predicted transmittance of base-coated dCCPC (MNLR, Eq. 6.3.1a)

6.4. Development of Artificial Neural Network (ANN) model

As artificial neural network (ANN) is a data-driven process consisting of a flexible mathematical algorithm, the ANN models were trained, tested and validated based on the same combinations of input variables including both dependent and independent variables as they were in regression in Section 6.3 in order to verify and compare with the obtained regression equations. For all input data in each ANN model, 70% was randomly selected to be used for training, 15% was for test and the rest of 15% was for validation. Fig. 6.4.1 demonstrates an example of the ANN model results that predict the transmittance (T) of non-coated dCCPC. It is important to mention that the data used for training each ANN model include all the three sky types: clear sky, intermediate sky and overcast sky. For verifying and comparing with regression results, the results of all data (100%) obtained from ANN models would be processed and applied in this section.

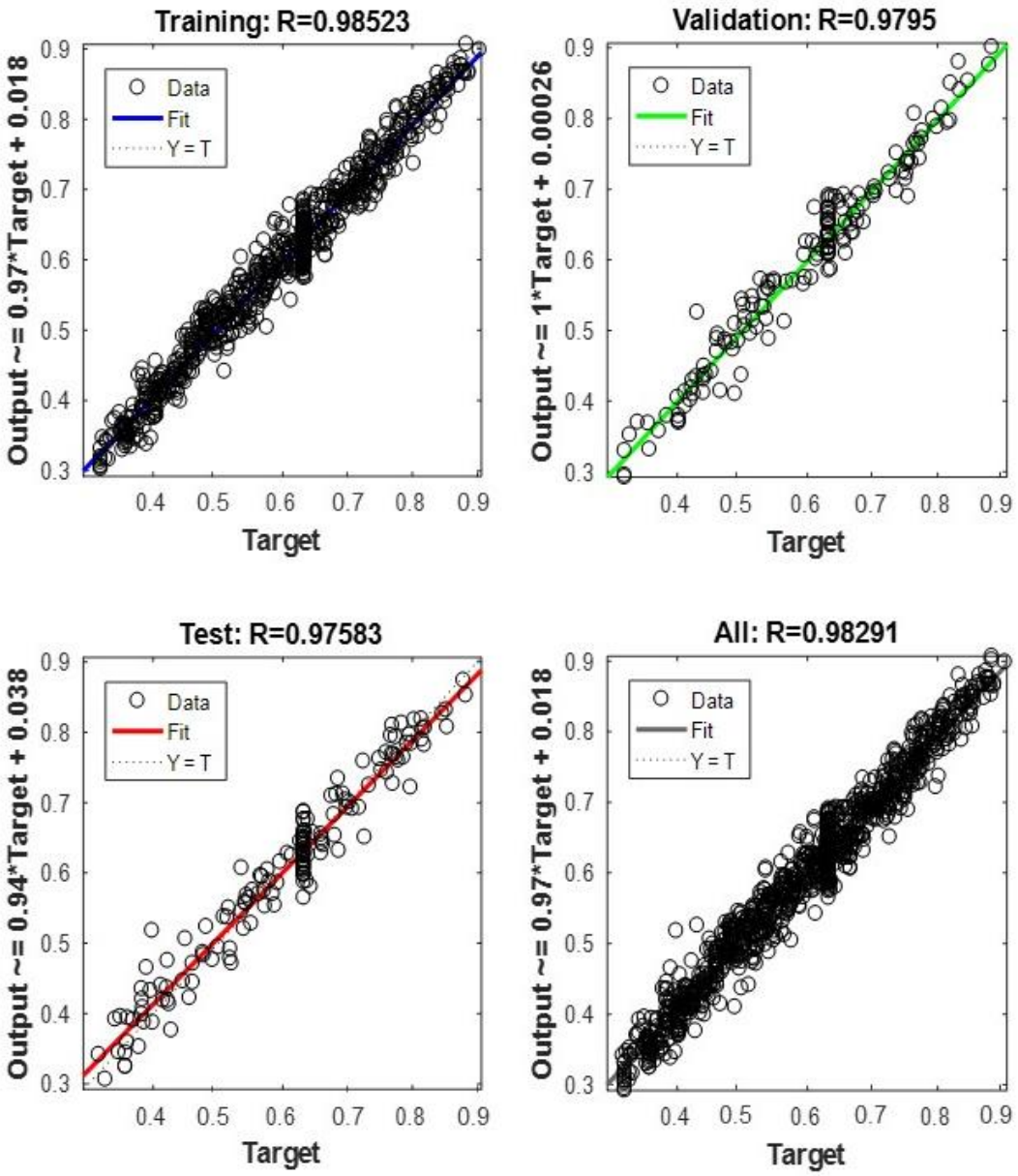


Fig. 6.4.1. Comparison between predicted values and simulation values (target) obtained in training, validation and test processes of ANN (Independent variables: θ_h, γ, ε; Dependent variable: T for non-coated dCCPC)

Similar to regression model, the group of independent variables are altitude, azimuth, sky clearness factor (θ_h, γ, ε), and the dependent variables is transmittance (T). All of the angles used as input parameters in ANN models are in radian measure. Table 6.4.1 summarizes the correlation coefficients (R) and mean square errors (MSE) of ANN models aiming at the combinations of independent and dependent variables of obtained regression equations. It can be found that all of the correlation coefficients are higher than 0.99 and MSEs are less than or equal to 0.0006, which mean the ANN

models provide reliable predictions that are very close to input values. The results of each model would be discussed in details in the following parts.

Table 6.4.1. Correlation coefficients of trained ANN models

CPC type	Independent variables	Dependent variables	R				MSE (for all data)
			Training (70%)	Validation (15%)	Test (15%)	All (100%)	
Non-coated	$\theta_h, \gamma, \varepsilon$	T	0.9852	0.9795	0.9758	0.9829	0.0006
Base-coated	$\theta_h, \gamma, \varepsilon$	T	0.9936	0.9905	0.9906	0.9927	0.0007

The simulated and ANN-predicted results of transmittance for non-coated dCCPC are shown in Fig. 6.4.2. Comparing with the predicted results gained from regression demonstrated in Fig. 3, it can be seen that more results, up to 96%, are located within the regions of ±10% deviations. The coefficient of determination R^2 reaches 0.966 which is higher than that of regression. Similar to the ANN predictions of transmittance for non-coated dCCPC, the ANN prediction model are slightly better than the regression model for base-coated dCCPC. The coefficient of determination R^2 is 0.986. More than 86% of predicted values are within the region of ±20% deviations as shown in Fig. 6.4.3. Compared to the regression results in Fig. 6.3.2, it is interesting to see that the deviations of these two models have something in common: relatively large deviations occur when the transmittance is less than 0.5. Results reveal that ANN is a relatively accurate and reliable approach to predict the transmittance of non-coated dCCPC with a certain group input of altitude, azimuth and the sky clearness factor. It also can be found that although the deviations of ANN model are smaller than that of regression model generally, the tendencies or error occur of both regression and ANN models are the same. Owing to the high accuracy of ANN prediction model, other combinations of dependent and independent variables are attempted to predict the performance of dCCPC in a different way, which are shown in Appendix D.

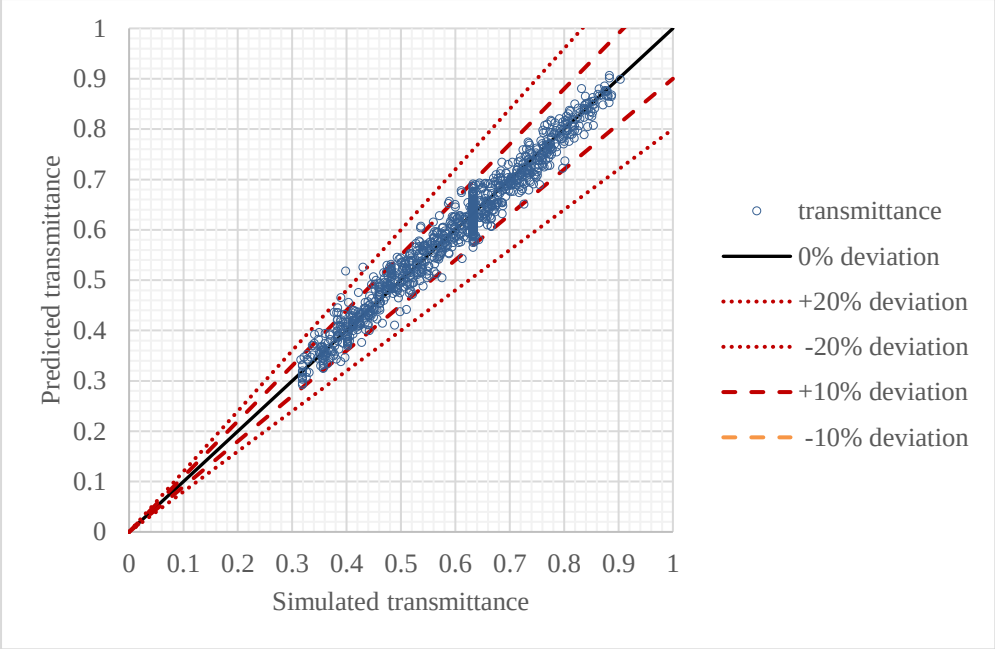


Fig. 6.4.2. Comparison of predicted and simulated transmittance of non-coated dCCPC (ANN)

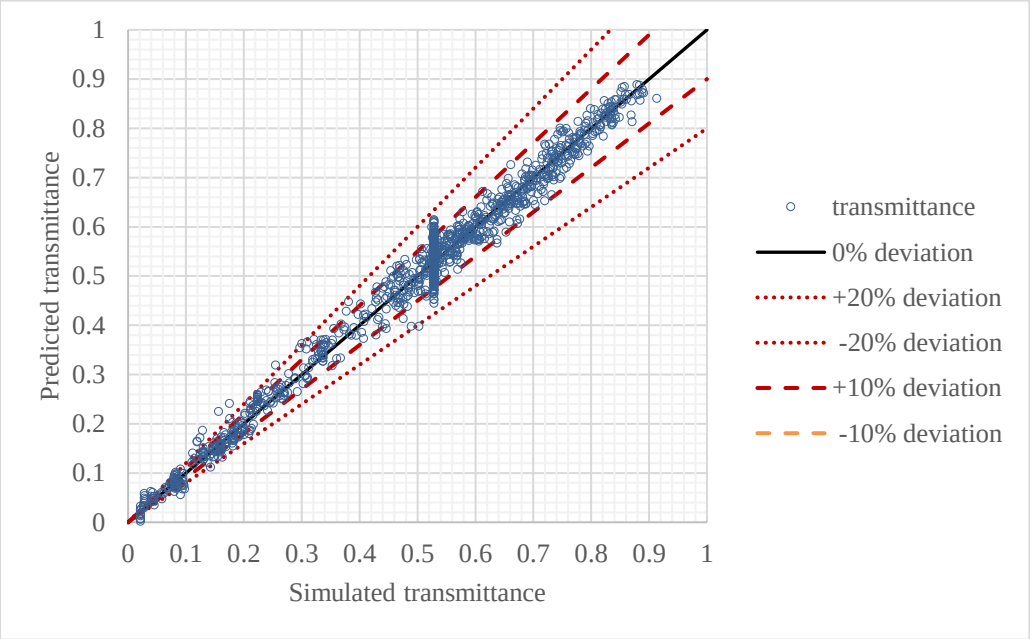


Fig. 6.4.3. Comparison of predicted and simulated transmittance of base-coated dCCPC (ANN)

6.5. Advantages and limitations

6.5.1. Comparison between ANN and MNLR

The results obtained from the best regression and ANN models for different CPC types are illustrated in Table 6.5.1.1 below. The coefficient of determination (R^2) of all

models are higher than 0.93. ANN models performs higher R^2 and lower MSE comparing with corresponding regression models. It can be found that both of regression and ANN models are capable to predict the nonlinear relationship accurately but ANN models always perform slightly better accuracy.

Table 6.5.1.1. Comparison between the correlations of regression formula and ANN model

CPC type	Independent variables	Dependent variables	Regression		ANN	
			R^2	MSE	R^2	MSE
Non-coated	$\theta_h, \gamma, \varepsilon$	T	0.931	0.0016	0.966	0.0006
Base-coated	$\theta_h, \gamma, \varepsilon$	T	0.969	0.0030	0.986	0.0007

Both of ANN and regression are fast and feasible methods for data prediction, but they have their own specific advantages and drawbacks. ANN is a data-driven process based on flexible algorithms and it can provide more precise forecast as a result of its specific neural network. Its main drawback is black-box modelling, which means it cannot provide available formula or visualized calculation procedures. On the contrary, regression model give a specific formula which demonstrates the relationships among variables clearly. It is easy for people to understand and formula is more likely to be accepted when cooperating with other software. In addition, dCCPC is designed for controlling daylight for the purpose of saving energy for building. Many software related to building energy simulation are capable to cooperate with customized input formula for specific devices, while not that many platforms support the ANN program. In aspect of the improvement and simplification of models, ANN is more flexible than MNLR models. MNLR model is good at dealing with the variables having obvious and regular relationships, like the relationships among sky clearness factor, sun position and transmittance referred to in this study. ANN is not limited in specific criteria and can build prediction model for the variables without obvious correlations. Many studies [202, 219, 220] have attempted to forecast the daylight such as sky illuminance or luminous efficacy through ANN successfully, which implies it is highly possible to build the ANN model to predict the dCCPC performance with other input variables relating to sun and sky, for example, solar radiation, direct sunlight illuminance, and global horizontal illuminance, etc. The advantages and drawbacks of MNLR and ANN models are summarized in Fig. 6.5.1.1. Both of the ANN and

regression present promising results in predicting optical performance of dCCPC, the selection of these two methods should be determined by the requirements under different conditions.

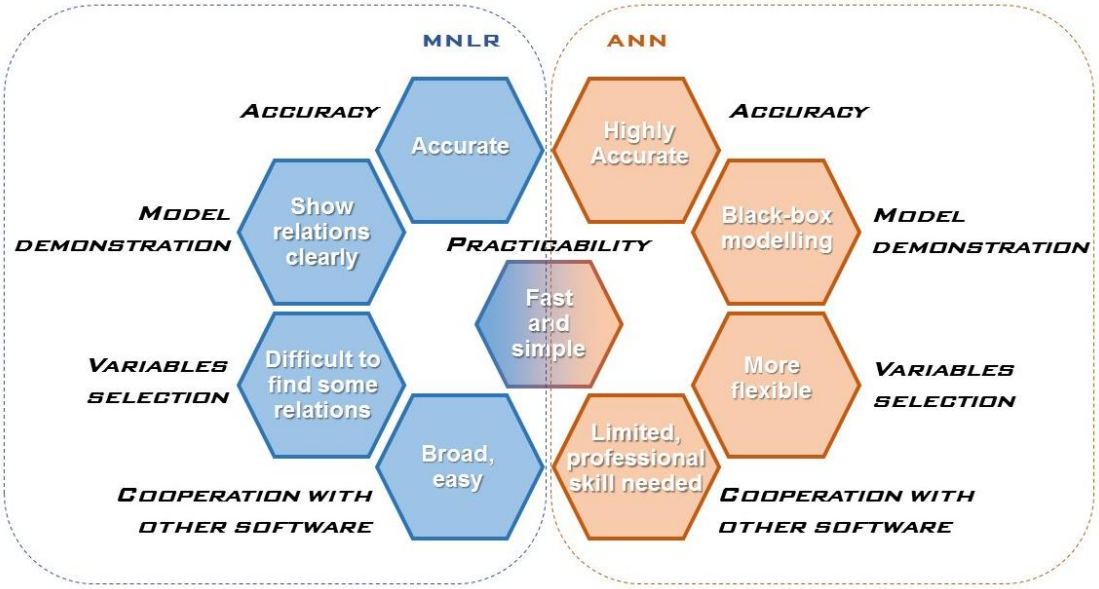


Fig. 6.5.1.1. Summary of pros and cons for MNLR and ANN models

6.5.2. Significance and limitation of prediction models

This research investigated two ways to predict the transmittance for base-coated and non-coated dCCPC. The input data used for setting models are obtained from the simulations by PHOTOPIA which is an accurate optical analysis tool. The data includes the transmittance of base-coated and non-coated dCCPCs under three typical skies: clear sky, intermediate sky, and overcast sky. The three sky models are based on the standard sky models defined in CIE Standard [195] and IES RP-21 [194] and they are assumed to cover all typical sky conditions. However, the actual sky changes all the time leading to various luminance distribution, i.e. 15 sky types are proposed in CIE Standard in total. Also, considering the errors of these empirical sky models, small errors may occur when using prediction models in practice. However, this can be improved by using data obtained from actual conditions as input. In this study, both MNLR and ANN models are data-driven models, which means the basic input data set are required when building the prediction models. Generally speaking, the more referenced data is input, the more accurate the forecasting models will be. The input data could be simulation or experiment data.

Based on the proposed prediction models, the transmittance of dCCPC under arbitrary sky conditions can be determined rapidly with the known of local sun position, dCCPC orientation and sky clearness factor, which saves the time on optical simulations. The energy saving on building from dCCPC can also be calculated under the cooperation with software simulating the energy consumption of building. On the other hand, the MNLR and ANN models put forward are not appropriate for not only the specific dCCPC used in this study, but for the dCCPCs with different dimensions. On account of the similar structures and working principles of all CPCs, like dCCPC, 2D CPC, and mirror CPC, etc., both the two types of prediction models have great potential to be applied for other types of CPC. Finally, as discussed before about the advantages of ANN, it is highly probable that the input variables could be more simple and straightforward, e.g. sky illuminance and direct radiation, etc., to determine the transmittance of dCCPC through ANN.

6.6. Summary

In order to investigate the CPC properties in daylighting control, the multiple nonlinear regression (MNLR) and artificial neural network (ANN) models for calculating the transmittance of base-coated and non-coated dCCPC have been proposed in this chapter on account of a mass of simulation results. The models covered all standard sky conditions including overcast, intermediate and clear skies. Three key parameters, which were solar altitude, solar azimuth and sky clearness factor were selected as the independent variables. The coefficients of determination (R^2) are higher than 0.93 for the MNLR models and higher than 0.96 for the ANN models. The deviations of most predicted values were less than 20% compared to input data.

It was found that both of MNLR and ANN models are accurate and reliable to determine the transmittance of dCCPC. The two models have their specific advantages and drawbacks. ANN models provide slightly better results than MNLR models owing to its special mechanism of network. Regression models present clear relationships among variables while ANN is black-box modelling process. MNLR models easier to incorporate with other software but ANN models are more powerful when building complex and irregular relations among variables. Therefore, it is suggested to choose different models depending on the requirements and the features of these two methods. All of the proposed models also implies its great potential. It could save a lot of time

for running raytracing analysis by optical simulation software, and it can fit dCCPC in different dimensions. In addition, it is promising to adopt these models to predict the optical performance for other types of CPC under real sky condition, and explored more straightforward input variables for simplifying models in future works.

Chapter 7

Energy and visual performance of building with dCCPC panel as skylights

7.1. Introduction

The energy consumption related to building takes more than one-third of total global energy consumption [221]. The electricity required by artificial lighting is one of the main parts of the energy demand for buildings. Lighting energy took 19% (1900 TWh) of the total global electricity consumption approximately, and it is estimated to reach 4250 TWh by 2030 under current policies [222]. Daylighting design is a popular choice in modern building design with the considerations of energy saving, human health and comfort visual environment. The combination of direct sunlight and diffuse skylight are regarded as daylight whose quality and intensity of daylight varies depending on the location, season, time, weather, sky condition, building geometry and so forth. With the appropriate daylight design, about 40% lighting energy could be saved [223]. In addition, the saved energy could reach 70% with the proper designs of space type and control type [224]. The cost on energy can be saved with the reduction on lighting consumption. As a passive solar energy design, daylighting also causes space heating which can reduce the heating load to some extent. It was also found by many researchers that daylight is good for human health: it can cure medical ailments, reduce psychological sadness related to the seasonal affective disorder [5, 225, 226]. In a survey conducted by Hourani et al. [9], More than 80% of the working staffs were willing to sit by windows and similar results were obtained from the student and patient groups. Daylight also results in the better perception and higher productivity for human [10, 227].

As one of the nonimaging optics, compound parabolic concentrator has been attempted to be utilized in building facade for daylighting application in the past decades. Walze et al. [85] proposed two kinds of smart windows with the microstructure of two dimensional (2D) compound parabolic concentrator (CPC) array on the surface, which focused on preventing unnecessary solar radiation and improving light-guiding abilities. Yu et al. [15] investigated the feasibility of 2D dielectric CPC in daylighting control as it is used as a skylight; it was found that the transmittance of the stationary CPC varies with the sun locations, which is lower at noon and larger in the morning and afternoon. Ulavi et al. [141, 142] designed a hybrid solar window integrating tubular absorber and 2D CPC for the purpose of transmitting daylight to the interior and concentrate solar ration onto the absorber at the same time. Another hybrid window called PRIDE (Photovoltaic Facades of Reduced Costs

Incorporating Devices with Optically Concentrating Elements) also works in the similar way but replacing the tubular absorber by photovoltaic (PV) panel to generate electricity. With the improvements by many researchers [82, 84, 87, 90, 143-145], the electricity generated by the latest generation of PRIDE is 2.17 times higher than that from flat PV and it also provides daylighting to the interior simultaneously.

Glare is the result of extreme contrast within the vision filed leading to uncomfortable for human eyes. Although the visual environment provided by daylight is preferred by occupancy, the glare caused by direct sunlight is a key point that should be considered in daylighting design. Based on our previous research [182, 183], it was found dielectric crossed compound parabolic concentrator has outstanding performance in controlling daylighting when it is used as a skylight. Due to its specific structure, it also has great potential in preventing glare comparing with common skylights and diffuse panels.

In this chapter, the performance of dCCPC will be investigated when it is used as a skylight for a standard office building. Firstly, the indoor illuminance distribution of dCCPC is compared with other types of skylights, and the roof type that is suitable for installing dCCCP is investigated. Then, the energy consumption for building is simulated based on the best types of skylight and roof structure. Fourteen locations selected all over the world for the simulation, and the dCCPC will be compared with traditional double-glazing and low-E double glazing. Three main criteria will be evaluated for dCCPC, which are its effects on lighting usage, effects on total thermal load, and effects on indoor visual environment. The well-known parametric design software Grasshopper and optical analysis software Photopia, will be utilized for the simulations. Finally, the economic analysis is presented to investigate the economic benefits and payback period after installing dCCPC. The advantages and drawbacks of dCCCP are discussed, and the feasibilities of practical application are summarized at the end of this part.

7.2. Calculation of equivalent altitude angle and equivalent azimuth angle for dCCPC in any south-facing tilt angle

When the dCCPC is used in practice, the tilt angle of it should be adjusted based on the location to take full advantage of it. According to the multiple nonlinear regression

model, the equivalent altitude and azimuth angles should be used instead for a tilted dCCPC to determine the correct transmittance of it. This section introduces how to calculate the equivalent angles and an calculation example is given.

For the purpose of calculating the equivalent altitude and azimuth angles of dCCPC, a coordinate system is applied as illustrated in Fig. 7.2.1. The south, east and zenith directions are represented by x, y and z axis respectively. The incident sunlight is denoted by vector $\boldsymbol{S}$. The actual altitude and azimuth are indicated by θ_h and γ. To obtain the best result of controlling daylight by dCCPC, the dCCPC would be tilted to the south when it is applied in the northern hemisphere. The entry aperture (top surface) of dCCPC, which is also the interface between air and dielectric material receiving incident rays, is denoted by the plane ABCD. The plane ABCD is tilted by β to south from the horizontal plane, which stands for the tilt angle β of dCCPC, and the line NN', which is normal to the plane ABCD and passes through point O, is tilted by β to the z axis. M is the point lying on the surface ABCD and the direction of $\overrightarrow{OM}$ refers to the equivalent north direction of the plane ABCD; the projection of $\overrightarrow{OM}$ on the horizontal plane coincides exactly with the x axis. The vector $\overrightarrow{SO}$ refers to the incident ray and the vector $\overrightarrow{OS_1}$ indicates the refracted ray. S' is the projection of point S onto the horizontal, and E is the projection of point S onto the plane ABCD. Thus, in terms of the sun position, γ is the actual azimuth and the angle between $\overrightarrow{OM}$ and $\overrightarrow{OE}$ is the equivalent azimuth γ' for the tilted dCCPC; the angle between $\overrightarrow{OS}$ and $\overrightarrow{OS'}$ is the actual solar altitude θ_h and the angle between $\overrightarrow{OS}$ and $\overrightarrow{OE}$ is the equivalent altitude θ_h'. The surface NSN'O is the plane of incidence, and the line OS_1 lies on this plane. The angle between the vector $\overrightarrow{OS}$ and the vector $\overrightarrow{ON}$ is the incident angle θ_i of dCCPC.

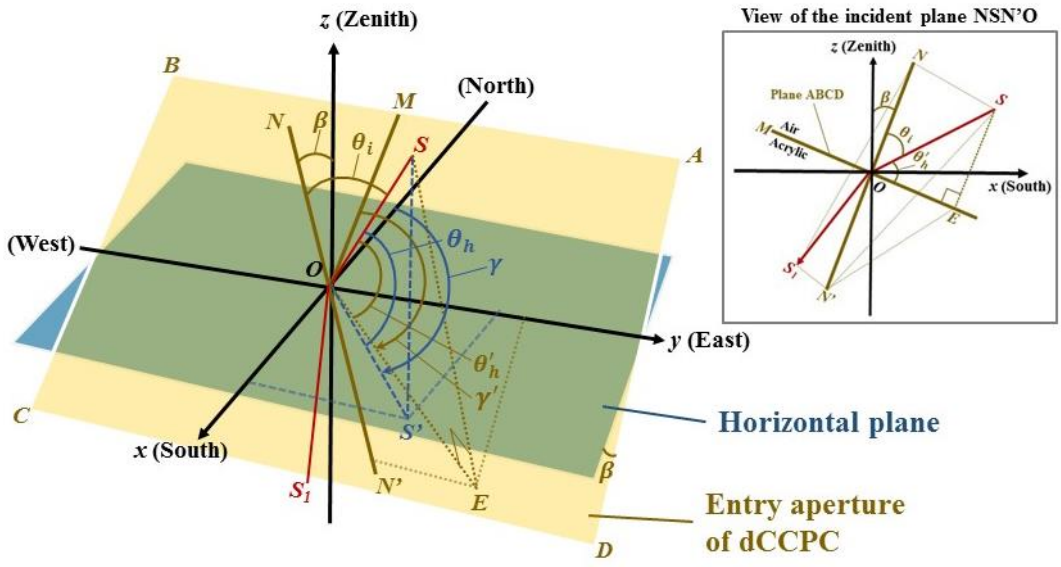


Fig. 7.2.1. Coordinate system of an optical path through a south-facing tilted dCCPC. S: sun position; $\overrightarrow{SO}$: incident ray; $\overrightarrow{OS_1}$: refracted ray; ABCD: top surface of tilted dCCPC; β: tilt angle; NON': normal of the plane ABCD; E: projection of point S onto the plane ABCD; S': projection of point S onto the horizontal plane; $\overrightarrow{OM}$: equivalent north direction of the plane ABCD; θ_h: solar altitude; γ: solar azimuth angle; θ_h': equivalent solar altitude; γ': equivalent solar azimuth angle.

7.2.1. Calculation of equivalent altitude angle

It is assumed that the lengths of the vector $\overrightarrow{OS}$ and $\overrightarrow{ON}$ are 1. The coordinates of point S and N can be expressed by:

$S(-\cos\theta_h \cos\gamma\,, \cos\theta_h \sin\gamma\,, \sin\theta_h)$ and $N(\sin\beta\,, 0, \cos\beta)$;

The vector $\overrightarrow{OS}$ and $\overrightarrow{ON}$ can be defined as:

$\overrightarrow{OS} = (-\cos\theta_h \cos\gamma\,, \cos\theta_h \sin\gamma\,, \sin\theta_h)$ and $\overrightarrow{ON} = (\sin\beta\,, 0, \cos\beta)$;

Then angle between $\overrightarrow{OS}$ and $\overrightarrow{ON}$, that is, the incident angle θ_i, can be calculated by:

$$\cos\theta_i = \frac{\overrightarrow{OS}\cdot\overrightarrow{ON}}{\left|\overrightarrow{OS}\right|\cdot\left|\overrightarrow{ON}\right|} = -\cos\theta_h \cos\gamma \sin\beta + \sin\theta_h \cos\beta \qquad \text{(Eq. 7.2.1.1)}$$

Hence, the incident angle is

$$\theta_i = \arccos(\cos\theta_i) \qquad \text{(Eq. 7.2.1.2)}$$

And the equivalent altitude of tilted dCCPC is:

$$\theta_h' = \frac{\pi}{2} - \theta_i \qquad \text{(Eq. 7.2.1.3)}$$

7.2.2. Calculation of equivalent azimuth angle

In the right triangle SOE in which SO is the hypotenuse,

$$\left|\overrightarrow{ES}\right| = \left|\overrightarrow{OS}\right| \cdot \cos\theta_i = \cos\theta_i$$

In addition, because $\overrightarrow{ON}$ and $\overrightarrow{ES}$ are two parallel vectors, the vector of $\overrightarrow{ES}$ can be expressed as:

$$\overrightarrow{ES} = (\cos\theta_i \sin\beta\,, 0, \cos\theta_i \cos\beta)$$

The vector $\overrightarrow{EO}$ can be calculated by:

$$\overrightarrow{EO} = \overrightarrow{ES} + \overrightarrow{SO}$$

Where $\overrightarrow{SO} = (\cos\theta_h \cos\gamma\,, -\cos\theta_h \sin\gamma\,, -\sin\theta_h)$

Thus,

$$\overrightarrow{EO} = (\cos\theta_h \cos\gamma + \cos\theta_i \sin\beta\,, -\cos\theta_h \sin\gamma\,, \cos\theta_i \cos\beta - \sin\theta_h)$$

The vector $\overrightarrow{OM}$ is the equivalent north direction of tilted dCCPC and the length of it is assumed to be 1. The coordinates of point M is:

$$M(-\cos\beta\,, 0, \sin\beta)$$

The angle $\angle MOE$ is the equivalent azimuth angle γ' of the tilted dCCPC, which is defined by

$$\cos\angle MOE = \frac{\overrightarrow{EO} \cdot \overrightarrow{OM}}{\left|\overrightarrow{EO}\right| \cdot \left|\overrightarrow{OM}\right|}$$

$$\cos\angle MOE = \frac{-\cos\theta_h \cos\gamma \cos\beta - \sin\theta_h \sin\beta}{\sqrt{(\cos\theta_h \cos\gamma + \cos\theta_i \sin\beta)^2 + \cos^2\theta_h \sin^2\gamma + (\cos\theta_i \cos\beta - \sin\theta_h)^2}}$$

(Eq. 7.2.2.1)

Considering the symmetry of dCCPC and for the purpose to calculate the transmittance of dCCPC, the equivalent azimuth angle γ' should be within the range of 0 °- 45 °. Thus the equivalent azimuth angle γ' can be calculated by

$$\gamma' = \text{arc}(\cos\gamma') \qquad (Eq.\ 7.2.2.2)$$

$$\gamma' = \begin{cases} \text{arc}(\cos\angle MOE) & if \quad \text{arc}(\cos\angle MOE) \leq 45° \\ 90° - \text{arc}(\cos\angle MOE) & if \quad 45° < \text{arc}(\cos\angle MOE) < 90° \\ \text{arc}(\cos\angle MOE) - 90° & if \quad 90° \leq \text{arc}(\cos\angle MOE) \leq 135° \\ 180° - \text{arc}(\cos\angle MOE) & if \quad 135° < \text{arc}(\cos\angle MOE) \leq 180° \end{cases} \qquad \text{(Eq. 7.2.2.3)}$$

7.2.3. Example of calculating transmittance of dCCPC for random location, time and sky condition

An example of calculating the transmittance of a non-coated dCCPC will be presented in this section in detail. The location of Birmingham, UK(52.45 °N, 1.73 °W) and the local time 11am in 21st Dec are selected as an example. According to the EnergyPlus weather data [192], the solar altitude θ_h is 12.8 °, solar azimuth γ is 164.7 °, and the direct normal irradiance I is 294W/m^2. The total irradiance I_{total} on the top surface of dCCPC is 273 W/m^2 which is obtained by the simulation in DAYSIM using actual weather data.

In order to get the best use of dCCPC for daylighting control, the tilt angle of dCCPC is

$$\beta = 90° - Latitude = 37.55°$$

From Eq. 7.2.1.1-7.2.1.3, the equivalent altitude θ_h' is

$$\theta_h' = 90° - \text{arc}[\cos(-\cos\theta_h \cos\gamma \sin\beta + \sin\theta_h \cos\beta)] = 48.48°$$

From Eq. 7.2.2.1-7.2.2.3, the equivalent azimuth γ' can be calculated as 22.86 °.

In order to calculate the transmittance of dCCPC, the equivalent sky clearness factor ε' is also required. According to the equation of calculating the sky clearness factor introduced in Chapter 5, the equivalent sky clearness factor can be expressed as

$$\varepsilon' = \frac{\frac{(I_h{}' + I')}{I_h{}'} + kZ'^3}{1 + kZ'^3} \qquad \text{(Eq. 7.2.3.1)}$$

where I' is equivalent direct normal solar irradiance; $I_h{}'$ is equivalent diffuse horizontal irradiance; k is a constant and equals 1.041 for Z' in radians; Z' is equivalent solar zenith angle in radians.

$$Z' = 90° - \theta_h' = 41.52°$$

The equivalent direct normal solar irradiance is

$$I' = I \cos\theta_i = 220.13\,\mathrm{W/m^2}$$

The equivalent diffuse horizontal irradiance is

$$I_h{}' = I_{total} - I' = 52.87\,\mathrm{W/m^2}$$

The equivalent sky clearness factor ε' is 3.98 according to Eq. 7.2.3.1, which implies the sky condition is clear sky. Therefore, the transmittance of dCCPC can be calculated by Eq.7.5.1.1 which is 0.72. In addition, the transmittance obtained by Photopia simulation is 0.75, which provides good coincidence with calculated result.

7.3. Comparison of indoor illuminance distribution of dCCPC and other diffuse panels

Before the energy and visual environment simulation, the types of skylights and roof structure are investigated in this section. In the first part, the non-coated dCCPC will be compared with double glazing and another two typical skylight diffusers, which consist of miniature prism and hemisphere. In the second part, the indoor illuminance distribution is explored when dCCPC skylight is mounted in different types of roofs. The results of illuminance distribution is provided by the ray tracing simulations in Photopia that is a fast and accurate optical analysis software.

In each part of simulation, two sky types are selected as examples of extreme conditions: the clear sky model in which the sun position is altitude 60 °and azimuth 180 ° indicates the sky with strong sunlight during midday; the overcast sky model without solar disk indicates the cloudy sky conditions or the sky during dawn and dusk. The average global horizontal illuminance of the clear sky model is 92klux and 3klux for the overcast sky model. Based on the historical weather data of London (51.3 °N, 0.7 °W), 11.8% of the global horizontal illuminance is lower than 3lux and 6% of it is higher than 90klux throughout the whole year, which implies these two models are

capable to be used as typical models to simulate the extreme sky conditions, sunny and overcast, in terms of total outdoor illuminance level [228].

The reflectance of roof, wall and floor were taken into account when simulating the illuminance distribution of the work plane in test room. The typical reflectance values of room surfaces are: 70-80% for white acoustic-tiled ceilings, 40-60% for light-coloured walls and 15-30% for carpeting [229]. The reflectance values of the room surfaces set in simulation are 50% for wall, 80% for ceiling and 20% for floor. In order to simulate the illuminance distribution accurately, the illuminance of working plane is divided into 400*400 grids whose size ($0.000256m^2$) is much smaller than the maximum grid size ($0.73m^2$) for illuminance grid specified by European Standard BS EN12464-1 [230] as shown by Eq. 7.3.1.

$$p = 0.2 \times 5^{\log_{10}(d)} \quad \text{(Eq. 7.3.1)}$$

Where p is the maximum grid cell size; d is the longer dimension of the illuminance plane (m).

The illuminance level in contour map is divided into several ranges according to the standard recommended illuminance level provided by CIBSE [231]: 0-250lux is the range of low illuminance level and artificial lighting is required; 250lux-500lux indicates the environment that is suitable for visual tasks, e.g. office, libraries, and retail shops; 500-1,000lux refers to brighter visual environment but it is appropriate for some detailed work such as drawing offices, general inspection and supermarket; 1,000lux-2,000lux provides bright visual environment and low contrasts; when the illuminance ranges between 2,000lux-20,000lux it is still able for working but the contrast becomes very low; the illuminance level higher than 20,000lux is beyond the comfortable range of human eyes and shading device is suggested.

7.3.1. Comparison between dCCPC, prismatic and hemispheric panels

Four different skylight types, which are dCCPC panel, prismatic panel, hemispheric panel and double glazing will be compared when they are mounted on the roof of test room in this section. Fig. 7.3.1.1 presents the dimensions of the test room and the different skylights. The test room is a common square room with the length of 6.4m and height of 3m. The skylight locating in the middle of roof is the only opening of

the room. The skylight occupies 5% of floor area that follows the general rule of thumb which indicates the skylight-to-floor area ratio (SFAR) ranges from 3% to 7% [232]. The reflectance values of internal surfaces are 0.2 of floor, 0.5 of wall and 0.8 of ceiling. The work plane whose illuminance distribution would be simulated is taken as 0.8m above floor level.

Except for double glazing, the dimensions of other three diffusers, dCCPC, prism and hemisphere, are shown in Fig. 7.3.1.1 b). The dimension of the entry aperture for each component is 0.018m × 0.018m. A top cover with the thickness of 1mm is used to connect the individual component into a panel. Both of the width and length of the diffuser panel are 1.44m so that each panel consists of 80×80 individual components. The panel of dCCPC is the thickest one whose thickness is 24.3mm. For the prismatic diffuser, each element is in right square pyramid structure and the thickness of it is 12.8mm. For last diffuser with hemispherical component, the thickness equals the radius of entry aperture which is 10mm including the cover. The material of the three diffusers are acrylic with the refractive index of 1.49. The transmittance of double glazing is 0.75.

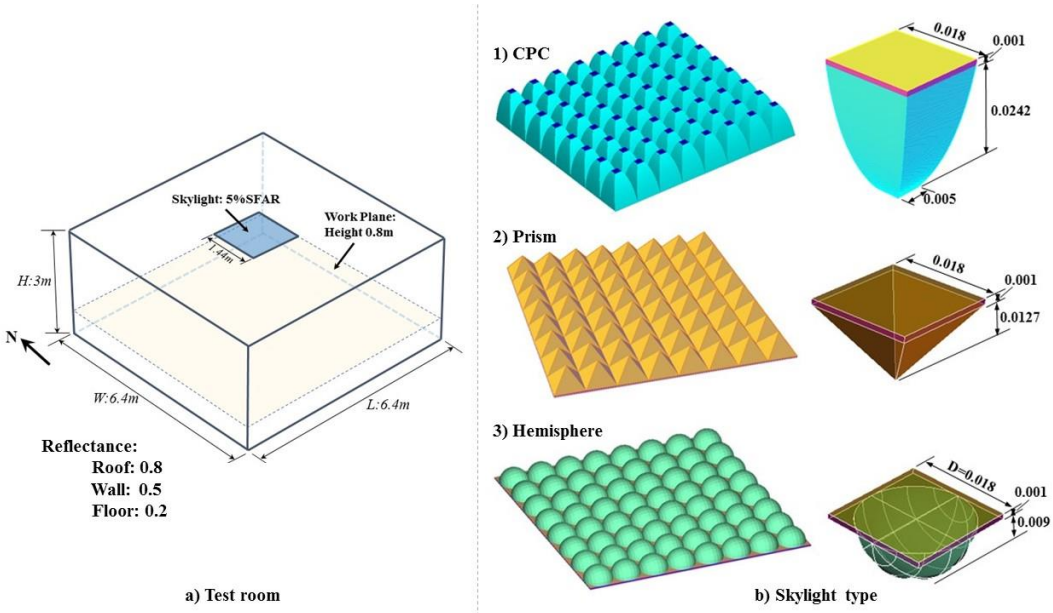


Fig. 7.3.1.1. Dimensions of the test room and different skylight diffusers

The illuminance distributions of work plane for the test room with different skylights under clear sky are illustrated in Fig. 7.3.1.2. The average outdoor global horizontal illuminance is 92klux. For the skylight utilizing dCCPC, the maximum illuminance indoor is 20,481lux. It can be seen that the incident light was strongly scattered into

the room and the illuminance of more than 70% area is higher than 1,000lux. In terms of prismatic diffuser, there is a small area with extreme bright light where the highest illuminance reaches 42,386lux. A bright area occurred under the skylight with the illuminance higher than 20,000lux. The incoming daylight is scattered on to the working plane causing lots of bright spots. For the hemispherical diffuser, the diffuse effect is much weaker than that of dCCPC and prism. The proportion of the area with the illuminance higher than 1,000lux is reduced to 40%. A bright area with the illuminance ranging between 20,000lux-40,000lux that is similar to the size of skylight is occurred on the work plane and the illuminance decreases progressively outward the bright area. The indoor illuminance distribution when double glazing is utilized as skylight is worse than other three diffusers. An extremely bright area in the same size of skylight is occurred whose average illuminance is about 75,000lux. The illuminance is rapidly dropped to 2,000lux beyond the bright area, which is easy to result in glare and uncomfortable visual environment. The proportion of the area where the illuminance higher than 1,000lux is about 35%.

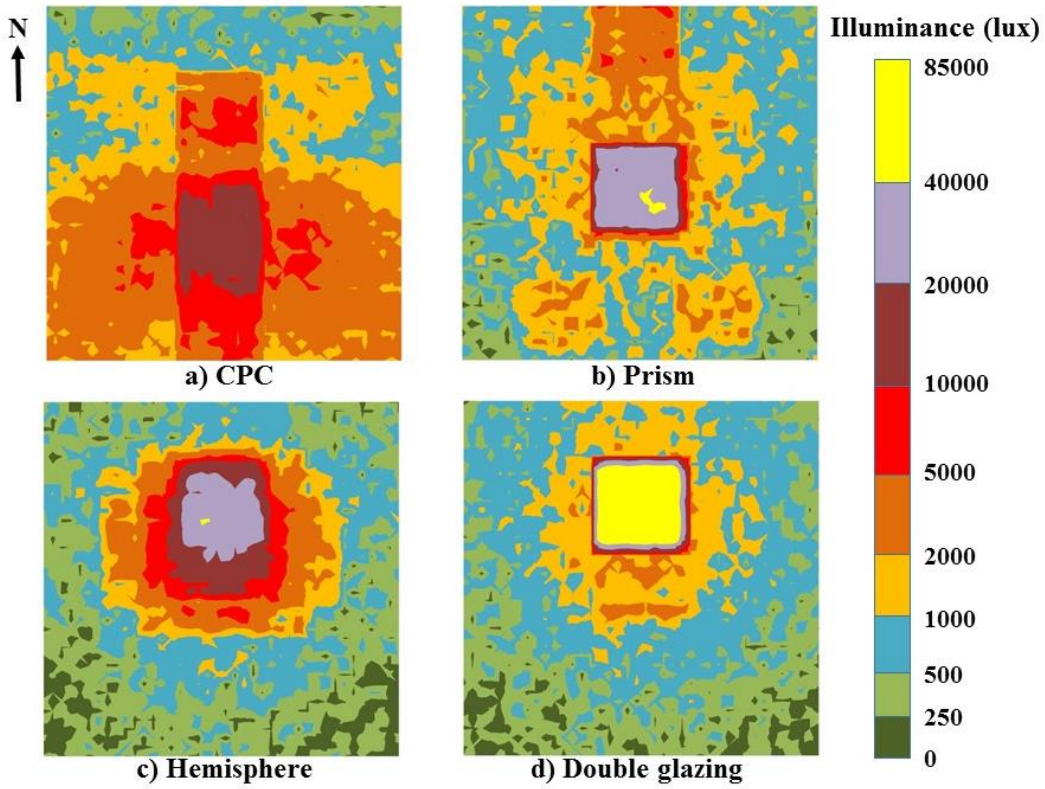


Fig. 7.3.1.2. Illuminance distribution on work plane of example room (Sky type: Clear sky; Solar altitude: 60 °; Solar azimuth: 180 °; Outdoor average illuminance: 91,922lux)

Fig. 7.3.1.3 illustrates the comparisons of illuminance distribution on work plane for different skylights under overcast sky of which the average global horizontal illuminance is 3klux approximately. It can be seen that the lit area is the smallest when the skylight is dCCPC due to its specific structure. It also corresponds to our previous simulation result, which indicates the transmittance of dCCPC under overcast sky is about 0.63 which is smaller than that of double glazing. Similar to clear sky, sporadic light spots with higher illuminance level are distributed on work plane in respect of prismatic diffuser. The illuminance distribution of work plane for hemispherical diffuser and double glazing are similar, but the double glazing provides larger lit area due to the high transmittance. In addition, artificial lighting are required for all of the four skylight types due to the low outdoor illuminance.

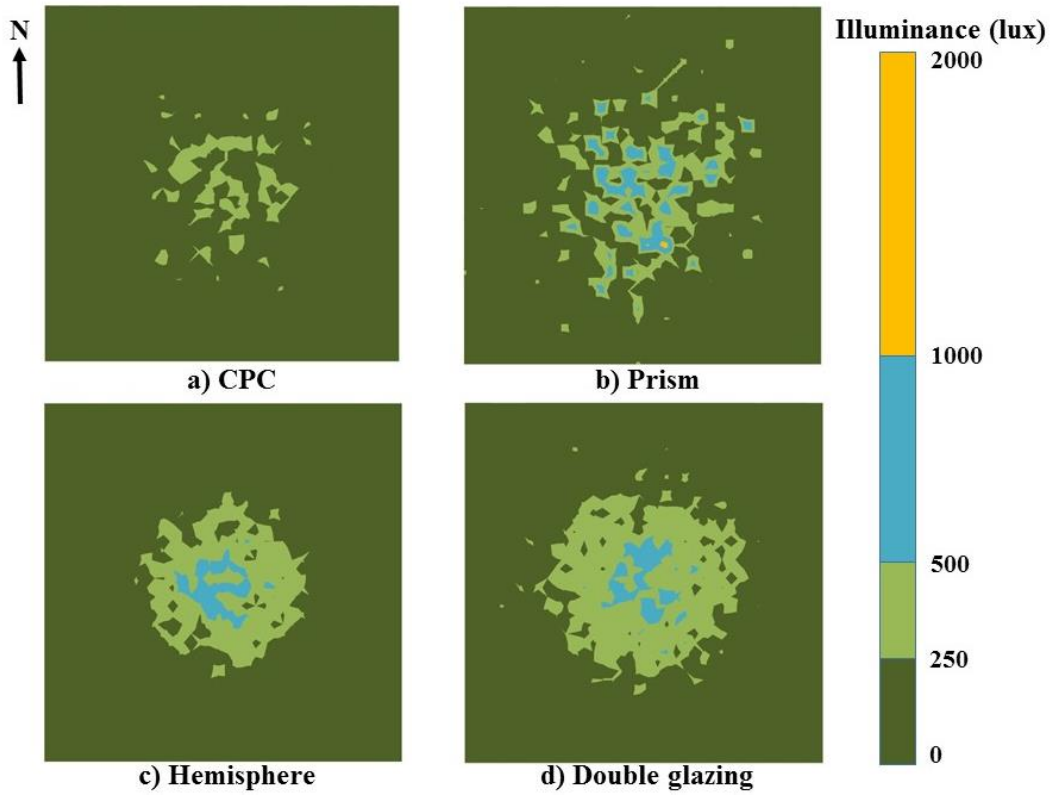


Fig. 7.3.1.3. Illuminance distribution on work plane of example room (Sky type: Overcast sky; Solar altitude: 10°; Solar azimuth: N/A; Outdoor average illuminance: 3,692lux)

7.3.2. Comparison between tilted roof and flat roof

It was found that the dCCPC provides excellent performance in controlling strong sunlight and diffusing incident light. In order to make the best use of its advantages,

dCCPC should be tilted to the south when it is mounted on roof. The tilt angle is the complementary angle of local latitude. In the simulations used in this part, the location of Birmingham, UK (52.45 ℃N, 1.73 ℃W) is applied as an example. Thus the dCCPC is tilted by 37 °to the south. Two typical roof types are selected for the test room, one is slanted roof, the other is flat roof as shown in Fig. 7.3.2.1. This two kind of roofs can take full advantage of dCCPC: the dCCPC should be faced south and the area of dCCPC is espected to be as small as possible to provide enough daylight and prevent heat loss from skylight at the same time. The test room retains same dimension of 6.4m×6.4m×3m and the skylight also retains the same dimension of 1.44m×1.44m (5% SFAR). For the room with slanted roof, the inclined angle of roof is 37 ° facing south. With respect to the test room with flat roof, the 37 °tilted dCCPC is mounted in the middle and the other three sides of the raised skylight are set to the same material with roof whose reflectance of internal surface is 80%. For the four surfaces of the raised skylight, each surface is perpendicular to another two adjacent surfaces.

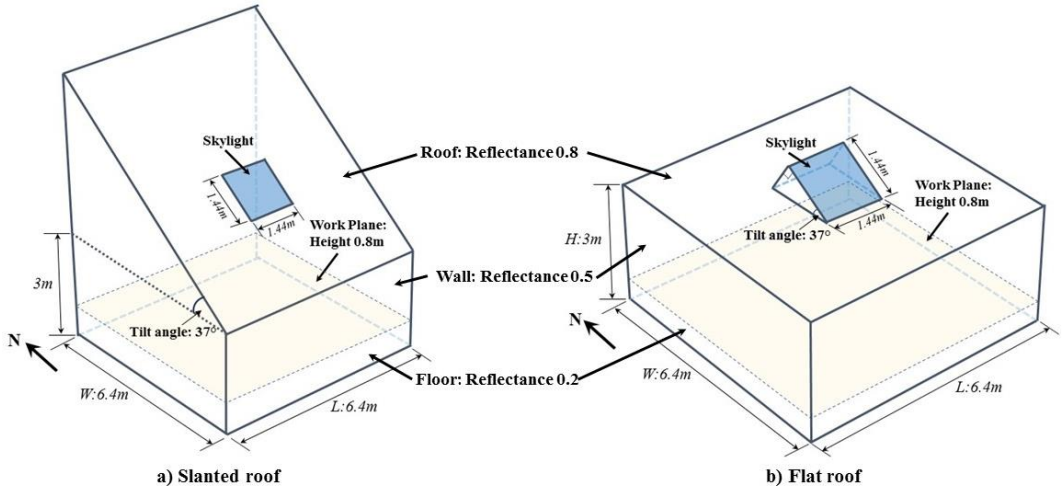


Fig. 7.3.2.1. Dimensions of test room with slanted roof and flat roof

The illuminance distribution of work plane for the test room with slanted and flat roof under clear sky and overcast sky are illustrated in Fig. 7.3.2.2. It can be found that the illuminance distribution are quite similar for both rooms under clear sky, which performs a bright area of about 10,000lux in skylight size and less bright areas along east, south and west directions. However, the bright area are more intensive of flat roof which may be resulted by the height of skylight and roof. The slanted roof increases the total height of room, e.g. for the test room with 37 °tilted roof, the height of north wall is increased by 4.8m from 3m. The position of skylight is also higher

than that of flat roof, which results in darker indoor environment. Similarly, the illuminance of work plane for the room with slanted roof is lower than 250lux but it is higher for the roof with flat roof. In addition, because the tilt angle of dCCPC should be changed based on the local latitude, the slanted roof is not practical for the room located in the area with low latitude. Therefore, flat roof is recommended for practical application.

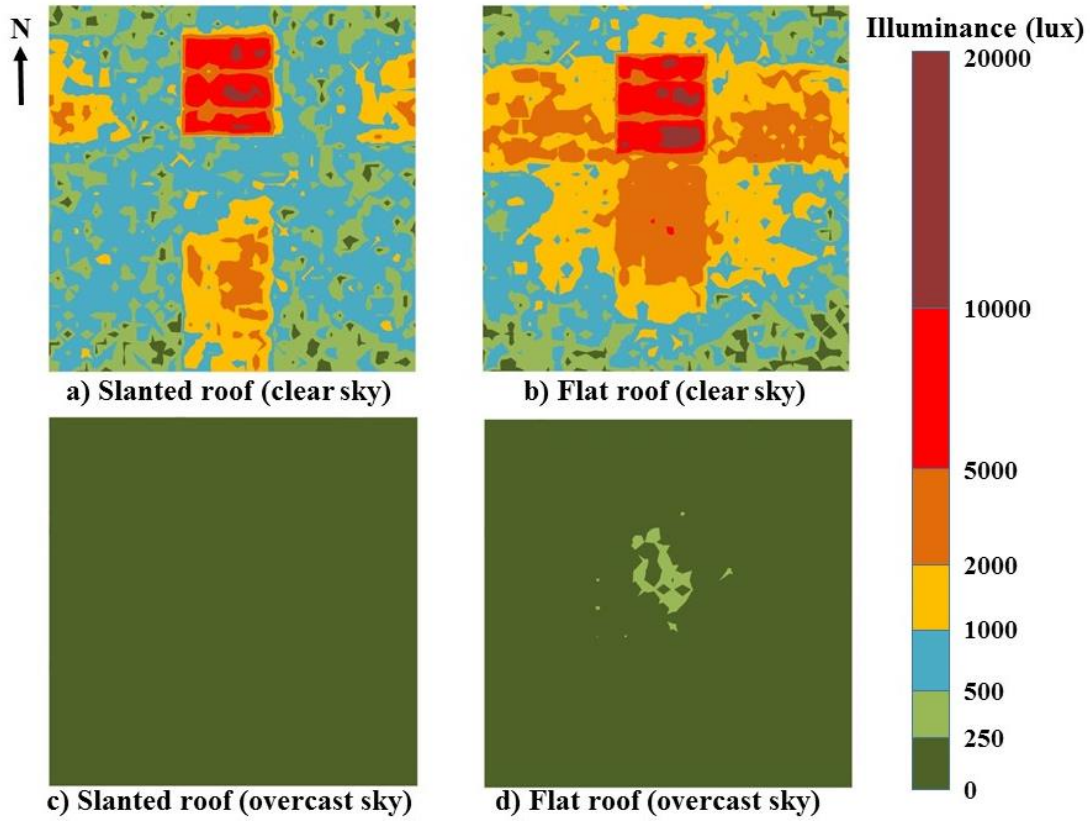


Fig. 7.3.2.2. Illuminance distribution on work plane of example room (Sky type: Clear sky (Altitude: 60 °; Azimuth: 180 °; Outdoor average illuminance: 91,922lux)/Overcast sky (altitude: 10 °; azimuth: N/A; Outdoor average illuminance: 3,692lux); Roof pitch of slanted roof: 37 °; Tilt angle of dCCPC: 37 °)

7.3.3. Summary of indoor illuminance distribution of different skylights

The illuminance distribution of work plane in the test room with different skylights and roof types are discussed in previous sections. The dCCPC is compared with prismatic diffusers, hemispherical diffusers and common double glazing. Table 7.3.3.1 summarizes their performances in several aspect such as peak illuminance value,

extreme bright area, uniformity of illuminance distribution, and capability on preventing direct sunlight, etc. It can be found that dCCPC performance well in controlling daylighting under clear sky conditions. The average and total illuminance values of work plane are relatively high but the peak values are quite low compared to prismatic and hemispherical diffusers. The percentage of the area with illuminance higher than 1,000lux indicates that when dCCPC is used as skylight, more indoor area would be lit up, which can reduce the requirement of artificial lighting effectively. Double glazing provides high sum and average values as well but an extremely bright area would occur and the lit area is small. In addition, dCCPC also provides better uniformity of light distribution which improves the visual comfort for occupancies. For overcast sky, the visual environment of the room with dCCPC is darker due to its especial structure. However, partial artificial lighting is also required for other diffusers and double glazing to guarantee the indoor illuminance level.

In second part, the indoor illuminance of the test room with two types of roofs, slanted and flat roofs, are investigated. The results implies that the illuminance distributions are similar but differ in the extent of intensive. The room with slanted roof is much higher so the lit areas are more scattered. For the flat roof with tilt dCCPC mounted in middle, the lit areas are continuous which provides natural gradient of illuminance change. Moreover, because the tilt angle of dCCPC changes with the local latitude, the flat roof is much more practical in actual applications.

Table 7.3.3.1. Summary of the performances for different skylights

Clear sky (outdoor illuminance 91,922lux)						
Skylight type	Work plane illuminance (lux)		Area% higher than 1000lux	Extreme bright area	uniformity of distribution	Avoid strong direct sunlight
	average	peak				
dCCPC	3,056	20,482	80%	none	good	good
Prism	2,707	42,386	60%	small	medium	medium
Hemisp-here	2,884	42,090	40%	small	good	medium
Double glazing	4,462	84,180	30%	big	bad	bad
Overcast sky (outdoor illuminance 3,692lux)						
Skylight type	Work plane illuminance (lux)		Area% higher than 250lux	Extreme bright area	uniformity of distribution	artificial lighting required
	average	peak				
dCCPC	98	505	10%	none	medium	yes

Prism	90	1,276	15%	small	medium	partial
Hemisp-here	100	680	20%	none	good	partial
Double glazing	141	805	25%	none	good	partial

7.4. Introduction of software for energy simulation

7.4.1. Software overview

Rhinoceros 3D is a three-dimensional (3D) computer graphics and computer-aided design application software that is good at modelling curves and freeform surfaces in computer graphics [233]. Grasshopper is one of the key plugins running within the Rhinoceros 3D, which is a visual programming language and environment to build generative algorithms [234]. Programs can be created by dragging provided components onto a canvas and connecting each component. Ladybug and Honeybee are two plugins for Grasshopper to import and analyse standard weather data, and run simulations for building energy, occupant comfort, daylighting usage and lighting consumption with the simulation engines like EnergyPlus, Radiance, Daysim and OpenStudio, etc. as shown in Fig. 7.4.1.1. Radiance is a widely used optical simulation tool for analysing the distribution of visible radiation in illuminated spaces based on the backward ray-tracing from the image plane to the sources [235]. Daysim is a RADIANCE-based simulation engine in Rhinoceros for predicting the annual daylight in building, analysing complex shading and lighting control system [236]. EnergyPlus and OpenStudio are the console-based software which is good at simulating the energy consumption including heating, cooling, ventilation, lighting and water usage in buildings [237]. Therefore, a building can be modelled and analysed in Grasshopper parametrically for both comprehensive design and accurate energy evaluation.

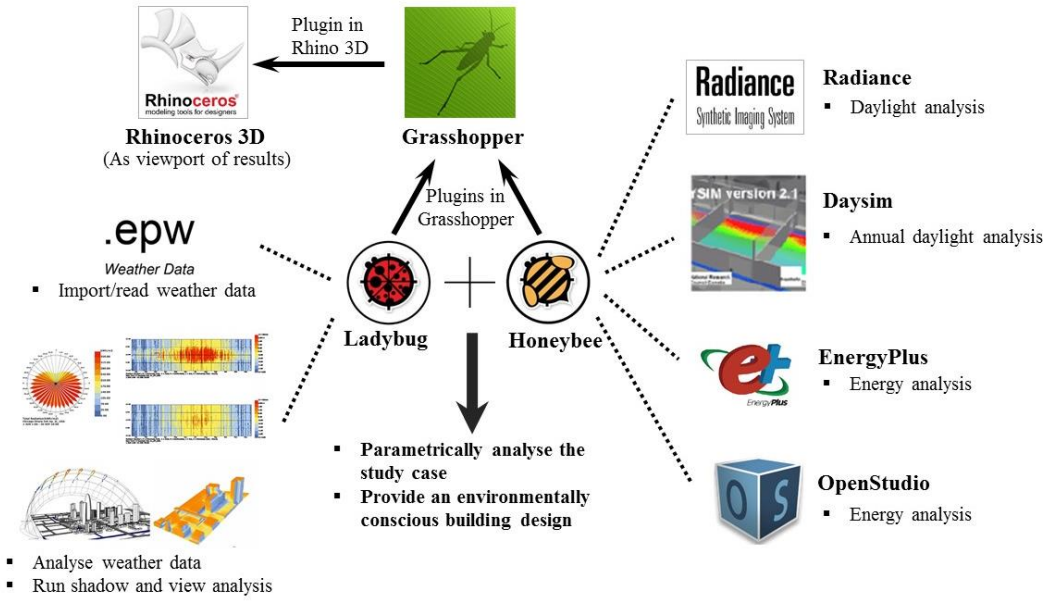


Fig. 7.4.1.1. Relations among Rhinoceros, Grasshopper, Ladybug and Honeybee in building simulations

In this study, several plugins are used for simulating the energy consumption of test building as shown in the workflow diagram in Fig. 7.4.1.2. The weather data is imported through Ladybug plugin and the sun path, location and sky condition are obtained and demonstrated as required. The building model is built in Rhinoceros 3D. For the energy simulation, the indoor light distribution, skylight material setting and glare analysis are done by the Radiance engine in Honeybee plugin. Then, the annual daylight analysis is conducted by Daysim engine and the detailed annual lighting control schedule would be generated. Finally, the lighting control schedule will be applied for the annual energy consumption through the EnergyPlus engine in Honeybee.

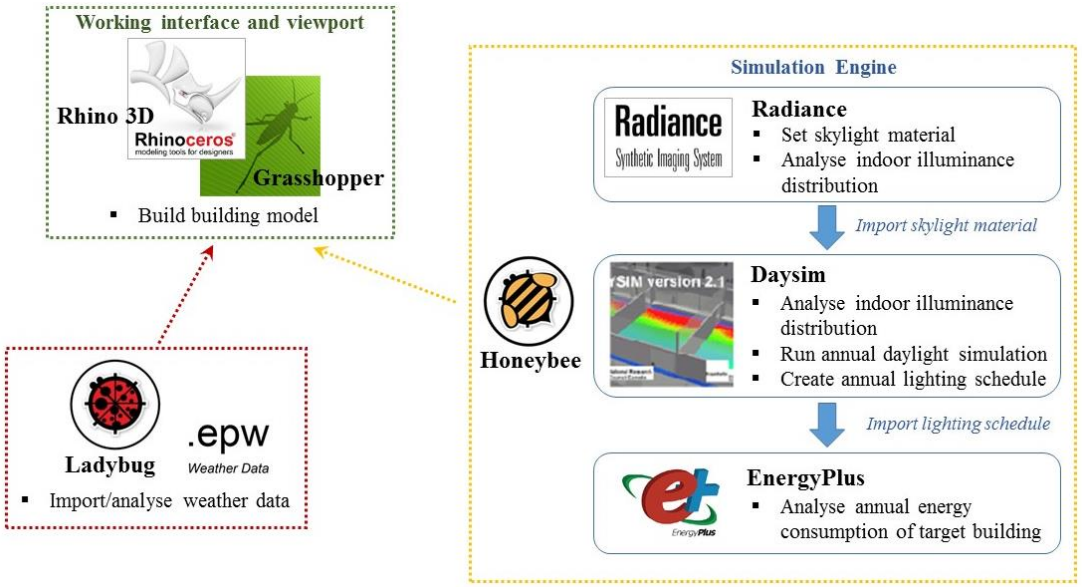


Fig. 7.4.1.2. Workflow diagram of running daylighting and energy simulation for target building in Grasshopper

7.4.2. Selection of skylight material used in Grasshopper

According to the research about dCCPC in previous chapters, the structure of dCCPC is too complex to be built for energy consumption simulations in Grasshopper and EnergyPlus. In addition, it is also difficult to build Radiance BSDF (bidirectional scattering distribution function) materials file for dCCPC due to its complicated structure. In order to simulating the effects of dCCPC on energy consumption for building, a Radiance translucent material is set and applied as a vicarious material for skylight instead of dCCPC. The reflectance in R, G, B channels, specular reflection, diffuse transmission, specular transmission and surface roughness of this material can be adjusted as required [238]. In order to investigate the indoor performance, the reflection properties of the vicarious material do not affect the illuminance distribution so that it can be ignored. The diffuse transmission, specular transmission and roughness are the three main factors that should be investigated. To make the performance of translucent material as similar as possible to dCCPC, it will be run in Grasshopper and compared with the performance of dCCPC run in Photopia for the same room model as shown in Fig. 7.4.2.1. Based on the best types of roof structure found in Section 7.3, the test room is a square room whose length and width are much longer than that of the skylight, which aims to reduce the reflectance effect of wall. There is no other openings except the skylight. The skylight is in the middle of roof

and tilted by 37 °to the south. The surface reflectances of roof, wall and floor are 0.8, 0.5 and 0.2 respectively.

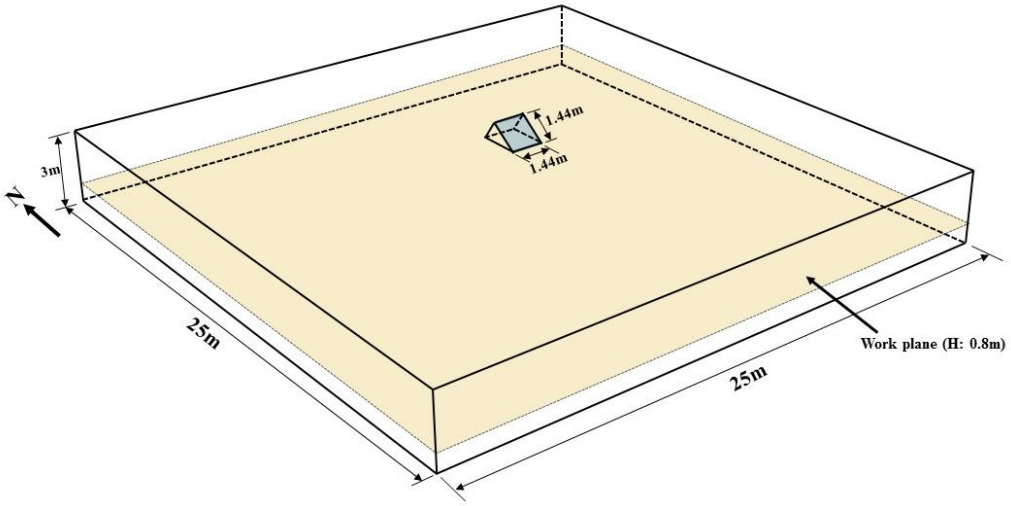


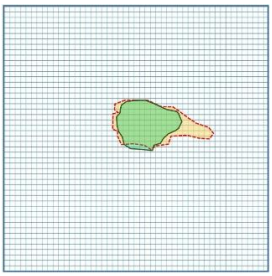
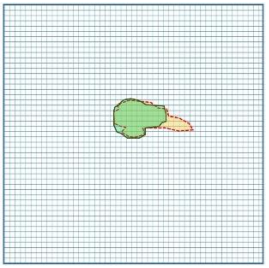
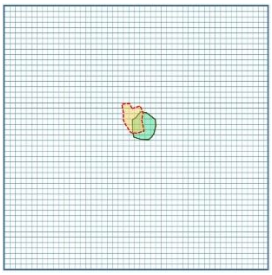
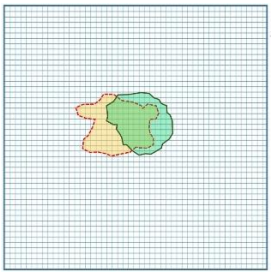
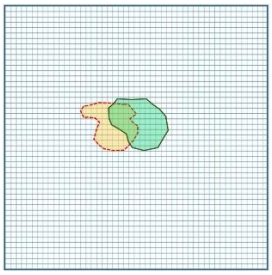
Fig. 7.4.2.1. Dimension of the test room for simulating illuminance distribution of work plane

The location and weather data used for test room is Birmingham, UK (52.45 °N, 1.73 °W). Three local time corresponding to different sky types are selected, which are 3pm on 21st Jun, 12pm on 21st Mar and 10am on 15th Aug. The sky conditions are determined by the sky clearness factor ε proposed by Perez, et al. [184], which are clear sky with the ε of 5.64, overcast sky (ε=1.03) and intermediate sky (ε=2.46). For each sky type, the percentages and the illuminance maps of the lit area with the illuminance higher than 300lux and 500lux are demonstrated. Results are obtained by the raytracing simulation through Photopia and the simulation through Radiance engine in Grasshopper. The settings of the translucent material in Grasshopper has been adjusted until the best result is obtained, that is, the lit area fractions and the shapes of lit area maps are as similar as possible to the results obtained by the simulations of dCCPC in Photopia.

The results of the translucent material having the closest results with dCCPC are demonstrated in Table 7.4.2.1. It can be found that the lit areas with the illuminance higher than both 300lux and 500lux for vicarious material and dCCPC are quite similar. For the clear sky, the dCCPC lit more area than that by vicarious material. However, the excessive part is small and lathy, which can be ignored when considering the artificial lighting. For overcast and intermediate skies, the lit area fractions and shapes

are same but the positions of lit areas have slight offsets compared to dCCPC. This small offsets can also be accepted for calculating indoor artificial lighting. Therefore, the translucent material is capable to be used as the replaced material of dCCPC for lighting and energy simulations of building. The final settings of the Radiance translucent material are also shown in Table 7.4.2.1.

Table 7.4.2.1. Simulated illuminance distribution on work plane under different sky conditions

Information	Lit area >300lux	Lit area >500lux
Test date: 21st Jun 3pm Sky type: Clear (ε=5.64) Transmittance of dCCPC: 0.60 Lit area fraction (>300lux): Photopia: 4.04% Grasshopper: 3.08% Lit area fraction (>500lux): Photopia: 2.24% Grasshopper: 2.00%		
Test date: 21st Mar 12pm Sky type: overcast (ε=1.03) Transmittance of dCCPC: 0.63 Lit area fraction (>300lux): Photopia: 0.64% Grasshopper: 0.72% Lit area fraction (>500lux): Photopia: 0.04% Grasshopper: 0.00%		N/A
Test date: 15th Aug 10am Sky type: intermediate (ε=2.46) Transmittance of dCCPC: 0.81 Lit area fraction (>300lux): Photopia: 4.32% Grasshopper: 4.08% Lit area fraction (>500lux): Photopia: 2.60% Grasshopper: 2.88%		
Legend: Lit area simulated by Grasshopper; Lit area simulated by Photopia.		
Settings of translucent material: R/G/B reflectance: 0.01; Specular reflection: 0.07; Diffuse transmission: T ×0.2; Specular transmission: T ×0.2; Roughness: 0.07 (T: transmittance of dCCPC).		

7.5. Methodology

7.5.1. Model description

The model of example building is set as a single-storey office building with skylights and windows as shown in Fig. 7.5.1.1 below in which the target building is located in the middle of the sun path model of Birmingham, UK (52.45 ℃N, 1.73 ℃W) and the yellow circles refer to the sun positions from 4am to 8pm with 1hr interval on 21st June. The building has the dimension of 80m (L) × 30m (W) × 3m (H) belonging to the typical size of standard air-conditioned office building [239], and the long sides of the building are in south-north direction. The window-to-wall ratio (WWR) is set to be 0.35 for the walls in south, north, east and west directions, which is within the optimal range of WWR for most office buildings in different climates [240, 241]. The total area of skylights follow the rule of thumb which occupies 5% of roof area. The total amount of skylights are 84 and located on the roof regularly in a 14×6 array. The skylight is mounted on the flat roof and tilted to the south. The tilt angle and the solar latitude angle at 12:30pm in 21st June are complementary to achieve the best performance.

The interior of the office building is open plan. In the following energy simulations in Grasshopper, the 'OpenOffice' schedules are used for occupancy, activities, heating, cooling, equipment and infiltration. The envelopes of wall, window, roof and floor are set as the default exterior wall, clear double glazing window, exterior roof and exterior floor constructions provided by EnergyPlus, respectively. The default constructions are not the best selections for the purpose of energy saving for building, but can be considered as the constructions with average performances that are more suitable for analysing the effect of skylights in different climates. Similarly, the heating and cooling load in simulations are calculated by the ideal load air system, which aims to focus the variation of thermal load caused by skylight and reduce the effect of the efficiency of different air-conditioning systems. The heating set point is set as 21 ℃ and cooling set point is set as 24 ℃. It is important to mention that, the control types of artificial lighting for all models are the same, which is auto dimming and it will be switched off when there is no occupancy in the room. The set point of lighting is 500lux. Shading system and glare control are not considered for windows and skylights.

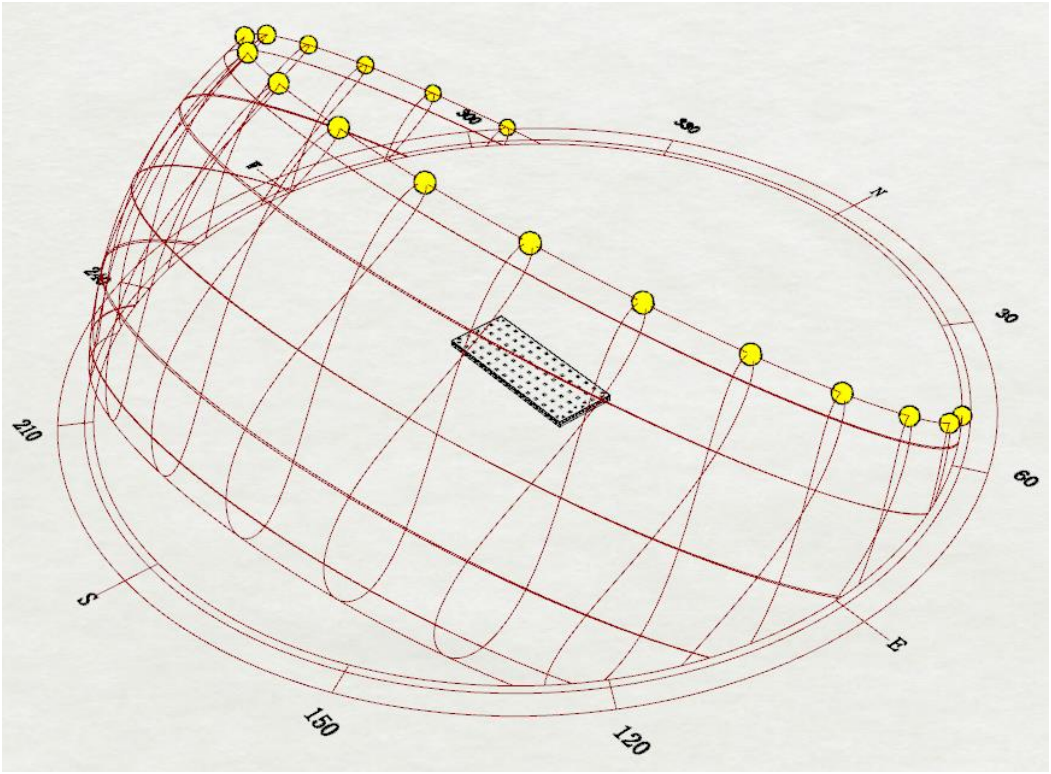


Fig. 7.5.1.1. Test building and sun path of Birmingham on 21st June from 4am to 8pm in Rhino 3D

Three different skylights are chosen for comparison in the following simulations in this section as shown in Table 7.5.1.1. The basic window type which is regarded as the reference is clear double glazing window (DB) whose visible transmittance (VT) is 0.79, solar heat gain coefficient (SHGC) is 0.70 and U-value is 2.669 W/m^{2}K [242]. As introduced in previous parts, dCCPC is used as a layer in window which provides the control of daylight and prevents glare. Two types of windows with dCCPC layer are set for simulations, one is clear double glazing (dCCPC-DB) and the other is double glazing with low-E coatings (dCCPC-lowE). The U-value, VT and SHGC for typical low-E double glazing is 1.420 W/m^{2}K, 0.69 and 0.27 respectively [242]. The properties of the windows with dCCPC are assumed to be similar as the original window types, but the transmittance (VT) and solar heat gain coefficient (SHGC) are varied with the transmittance of dCCPC (T_{dCCPC}). The type of dCCPC discussed in this section is non-coated dCCPC. The transmittance of it is calculated by Eq. 7.5.1.1 below, which is determined by the sun position and sky conditions. An example of hourly transmittance for a whole year when the dCCPC is used in Birmingham, UK (52.45 ℃N, 1.73 ℃W) are shown in Fig. 7.5.1.2. It can be found that the transmittance is

lower in the morning and afternoon and higher at noon from November to February, and the transmittance variations are reversed from March to Oct.

$$T_{dCCPC} = \begin{cases} a_1 \cos(b_1\theta'_h + b_2)\cos(b_3\gamma' + b_4)(c_1 + c_2\varepsilon' + c_3\gamma' + c_4\theta'_h \\ +c_5\theta'_h\gamma' + c_6\varepsilon'\gamma' + c_7\theta'_h\varepsilon' + c_8\varepsilon'^2\theta'_h\gamma' + c_9\theta'^2_h\varepsilon'\gamma' + c_{10}\gamma'^2\varepsilon'\theta'_h, & \varepsilon' > 1.2 \\ +c_{11}\varepsilon'^2\theta'^2_h\gamma'^2 + c_{12}\varepsilon'^2 + c_{13}\theta'^2_h + c_{14}\gamma'^2) + a_2 \\ T_0 & 1 \le \varepsilon' \le 1.2 \end{cases}$$

(Eq. 7.5.1.1)

Where θ'_h is equivalent altitude (expressed in radian measure), $0° < \theta'_h \le 90°$; γ' is equivalent azimuth (expressed in radian measure), $0° \le \gamma' \le 45°$, and $\gamma' = 0°$ when the projected light on the top surface of dCCPC is normal to either side of its entry aperture; ε' is equivalent sky clearness factor; T is transmittance; a_n, b_n, c_n are regression coefficients; T_0 is the transmittance of dCCPC under overcast sky.

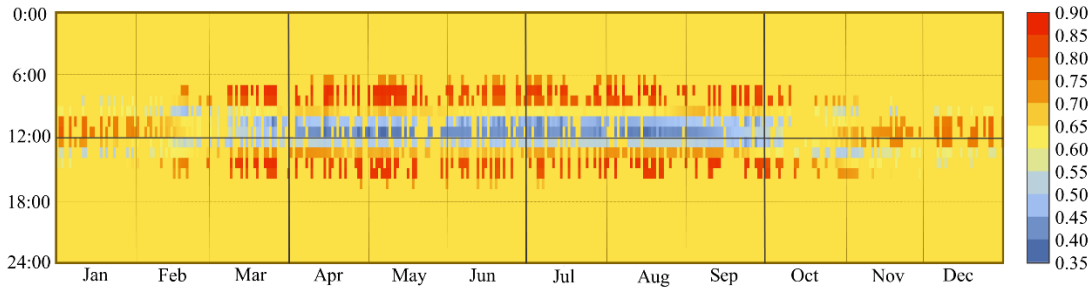


Fig. 7.5.1.2. Hourly transmittance of dCCPC for a whole year in Birmingham

Table 7.5.1.1. Properties of skylight materials (DB, dCCPC-DB and dCCPC-lowE)

	Clear double glazing (DB)	Clear double glazing with dCCPC (dCCPC-DB)	Low-E double glazing with dCCPC (dCCPC-lowE)
U-value (W/m^2K)	2.669	2.669	1.420
SHGC	0.70	$T_{dCCPC} \times 0.70$	$T_{dCCPC} \times 0.27$
VT	0.79	$T_{dCCPC} \times 0.79$	$T_{dCCPC} \times 0.69$
T_{dCCPC}: Transmittance of dCCPC			

7.5.2. Location

In order to investigate the performance of dCCPC in different locations and climates, 14 cities as illustrated in Table 7.5.2.1 are applied for the energy simulations of the target office building. The 14 cities includes the locations from the eastern hemisphere to western hemisphere on earth. Two of them are in America, six of them are in Europe

and the rest of six is in Asia. According to the Köppen-Geiger climate classification, the climates of the fourteen cities cover four main categories which are tropical climate, dry climate, temperate climate and continental climate. Among all cities, some locations need either only cooling or heating such as Bangkok and Kiruna, and others require both during the whole year like Beijing and Istanbul. Some cities have strong direct sunlight like Lhasa, and some cities are covered by clouds in most of the time like Aberdeen. As is introduced that the sky conditions is one of the key factor determining the performance of dCCPC, the percentages occupied by different sky conditions during the daytime of whole year for each location are demonstrated in Fig. 7.5.2.1. The sky conditions are calculated based on the annual weather data and categorized by sky clearness factor proposed by Perez, et al. [184]. Because the performance of dCCPC is determined by sky conditions, it is important to point out that the sky conditions are calculated for the daytime simulations; the sky conditions are assumed as overcast sky in the night, that is, the transmittance of dCCPC under overcast sky is used as the transmittance of dCCPC for night time in simulation. It can be found that the percentages of clear sky are around or less than 10% for most cities, except Lhasa, Los Angeles and Miami. Aberdeen has the longest time of overcast sky. The overcast and overcast to intermediate sky take about 90% time of the whole year.

Table 7.5.2.1. Locations and climates of simulated cities

Location		Latitude	Longitude	Köppen-Geiger climate classification	
Asia	China-Beijing	39.80 °	116.47 °	Dwa	Continental dry winter and hot summer climate
	China-Hong Kong	22.32 °	114.17 °	Cfa	Hot summer temperate without dry season climate
	China-Shanghai	31.17 °	121.43 °	Cfa	Hot summer temperate without dry season climate
	China-Lhasa	29.67 °	91.13 °	BSK	Arid steppe cold climate
	Philippines-Manila	14.52 °	121.00 °	Aw	Tropical savanna wet climate
	Thailand-Bangkok	13.92 °	100.60 °	Aw	Tropical savanna wet climate
Europe	Finland-Helsinki	60.32 °	24.97 °	Dfb	Warm summer continental without dry season climate
	UK-Aberdeen	57.20 °	-2.22 °	BSK	Arid steppe cold climate
	UK-Birmingham	52.45 °	-1.73 °	Cfb	Warm summer temperate without dry season climate

	Italy-Rome	41.80 °	12.58 °	Csa	Temperate dry and hot summer climate
	Sweden-Kiruna	67.82 °	20.33 °	Dfc	Hot summer continental without dry season climate
	Turkey-Istanbul	40.97 °	28.82 °	Csa	Temperate dry and hot summer climate
America	USA-Los Angeles	33.93 °	-118.40 °	Csa	Temperate dry and hot summer climate
	USA-Miami	25.80 °	-80.27 °	Aw	Tropical savanna wet climate

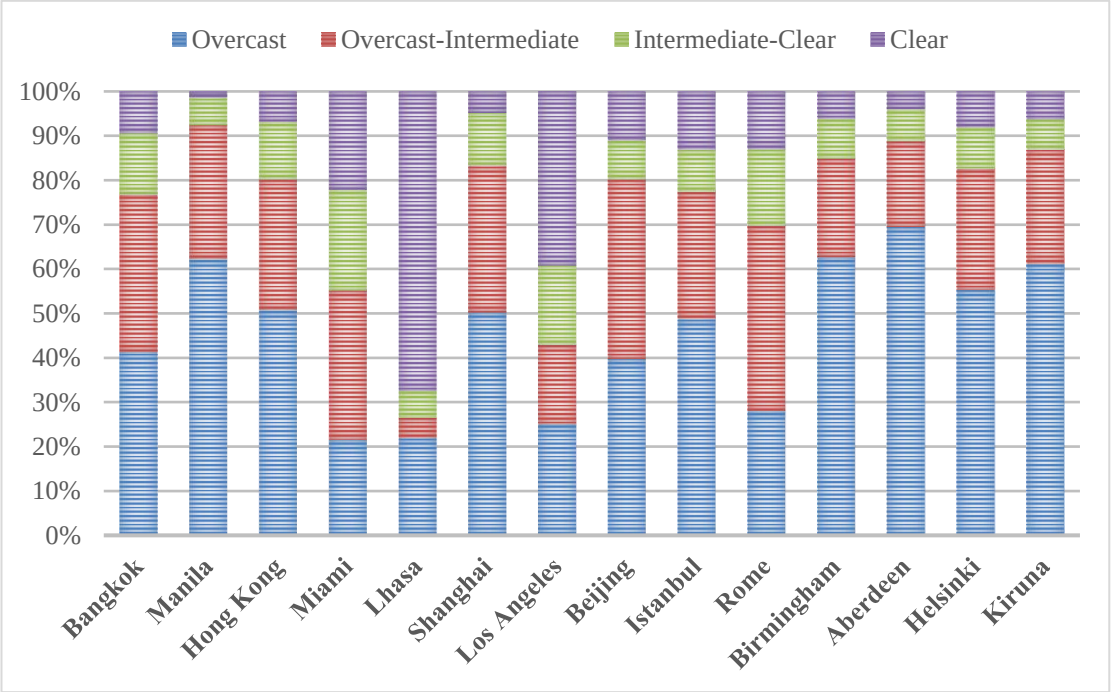


Fig. 7.5.2.1. Percentages of daytime sky conditions during the whole year for selected locations

7.5.3. Glare analysis

The criteria to evaluate the glare is daylight glare probability (DGP), which is proposed by Wienold and Christofferson [243] to describe the satisfaction of occupancy on visual environment. The equation of DGP is expressed by Eq. 7.5.3.1 [243]. The ratings of DGP ranges are defined as follows: Imperceptible glare (DGP ≤ 0.35); perceptible flare (0.35 < DGP ≤ 0.40); disturbing glare (0.40 < DGP ≤ 0.45); intolerable glare (DGP > 0.45) [244].

$$DGP = 5.87 \times 10^{-5} E_v + 9.18 \times 10^{-2} \log\left(1 + \sum_{i=1}^{n} \frac{L_{s,i}^2 \omega_{s,i}}{E_v^{1.87} P_i^2}\right) + 0.16 \quad \text{(Eq. 7.5.3.1)}$$

Where E_v is the vertical eye illuminance (lux); L_s is the luminance of source (cd/m^2); ω_s is the solid angle of source; P is the position index.

The glare analysis was taken by the Radiance engine in Grasshopper to investigate the indoor luminance environment of target building. It was tested that for a certain building and viewpoint, the values of DGP are close for the different locations under same sky conditions. Thus, the glare analysis was focused on the indoor visual environment of target building under different sky conditions for an example location in this study. The location of Birmingham, UK (52.45 °N, 1.73 °W) was selected for simulating the performance of dCCPC under different sky conditions. The local times chosen are 3pm on 21st Jun for clear sky, 10am on 15th Aug for intermediate sky and 12pm on 21st Mar for overcast sky. The corresponding sky clearness factors (ε) of these three times are 5.64, 2.46 and 1.03 respectively. The viewpoint of HDRI is facing east from the west wall inside the building. Three skylights are compared in simulations, which are double glazing, double glazing with low-E coating, and double glazing with a dCCPC layer (dCCPC-DB).

7.6. Results and discussion

7.6.1. An example of variations of hourly energy consumption

The particular characteristic of dCCPC is that the transmittance of it varies with the sun position and sky condition. Before demonstrating the annual thermal load of target building, an example of the selected 14 cities are provided to show the hourly variations of energy consumption, solar gain, skylight transmittance and sky conditions. In Fig. 7.6.1.1 and Fig. 7.6.1.2, it can be found how the transmittance of dCCPC varies with the sun position and sky clearness factor, and how the dCCPC affects the solar gain and thermal load of building in detail. The example city chosen is Birmingham, UK (52.45 °N, 1.73 °W), and the date is 22nd Jun which is a typical day in summer. Three kinds of skylights are compared, which are standard double glazing (DB), double glazing with a dCCPC layer (dCCPC–DB) and double glazing with low-E coating and a dCCPC layer (dCCPC–LowE).

Based on the sky clearness factor shown in Fig. 7.6.1.2, the sky is clear from 9am to 3pm, and the sky is intermediate or overcast in the morning and afternoon. In Fig. 7.6.1.1, the transmittance of dCCPC-DB and dCCPC-lowE varies as time goes on: the transmittance is higher in the morning and afternoon, and it becomes low at noon. For

double glazing, the transmittance stays constant. The total solar gain from skylight is affected by the transmittance significantly. For DB, the solar gain becomes higher from morning to noon, and then drops down in the afternoon. For dCCPC-DB, the solar gain also goes higher from morning to noon and decreases in the afternoon, but the solar gain is reduced at 11am, 12pm and 1pm due to the low transmittance at noon. In terms for dCCPC-lowE, the total solar gain is less than 10kWh for all the time and has similar tendencies with dCCPC-DB. In terms of hourly solar gain, dCCPC-DB reduces more than half of the solar gain through DB. The solar gain by dCCPC-lowE is about a quarter of dCCPC-DB owing to the lower transmittance and SHGC. The solar gain also affects the total thermal load. In Birmingham on 22nd Jun, only cooling load is required. From Fig. 7.6.1.2, the demand of cooling starts from 11am and becomes high in the afternoon. Due to the less solar gain through dCCPC-DB and dCCPC-lowE, the cooling load of using these two skylights are less than that of using DB except 7pm. At 19:00, the temperature of outdoor becomes low and solar gain can offset some requirement on cooling load. For 12pm, 1pm and 2pm, when the solar gain from dCCPC-DB and dCCPC-lowE are much less than DB, more than 1/3 of cooling requirement are saved by dCCPC-DB and dCCPC-lowE compared to DB.

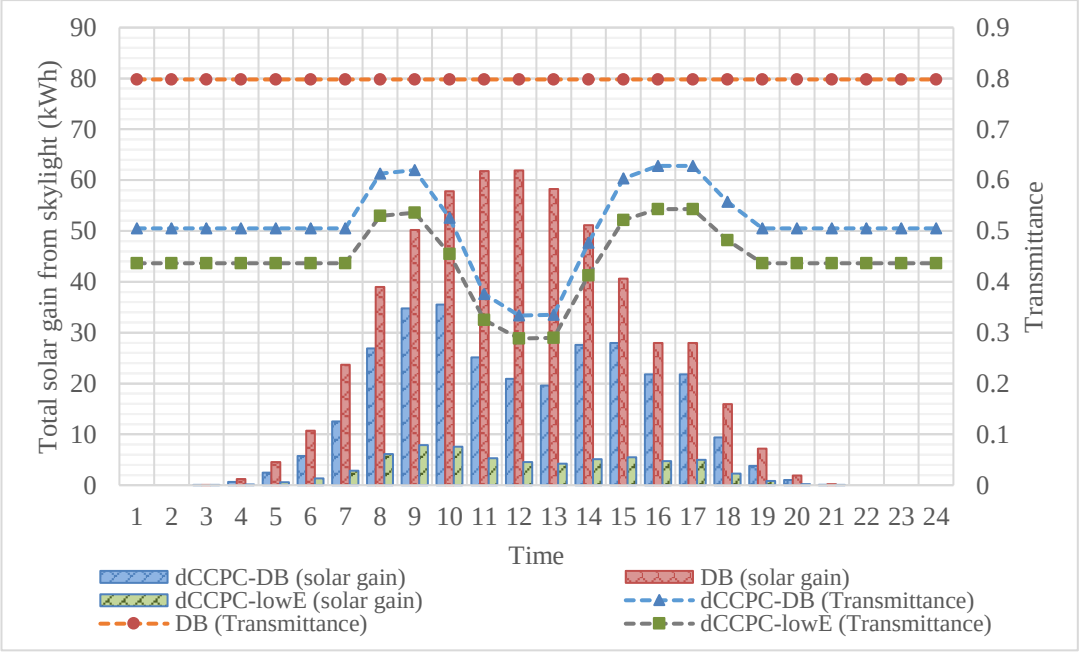


Fig. 7.6.1.1. Hourly solar gain from skylights and transmittance of skylights on 22nd Jun in Birmingham, UK (52.45 ℃N, 1.73 ℃W)

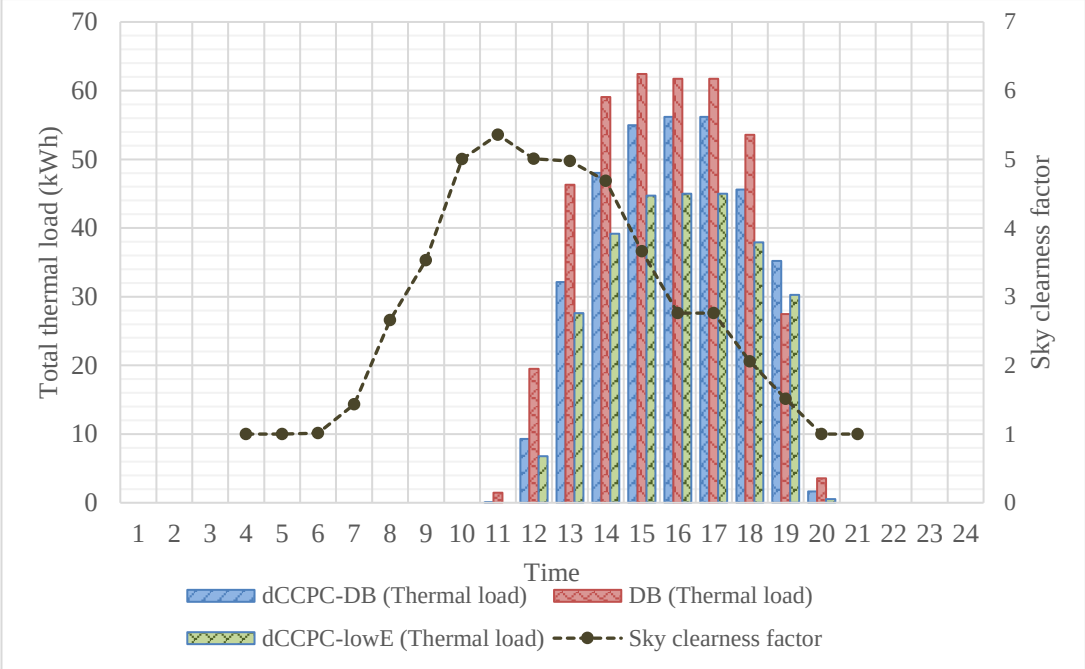


Fig. 7.6.1.2. Hourly total thermal load and sky clearness factor on 22nd Jun in Birmingham, UK (52.45 ℃N, 1.73 ℃W)

7.6.2. Monthly and annual cooling and heating loads

Based on the annual weather data and detailed model settings, the results of cooling and heating load of the target building are obtained and compared in this section. Fig. 7.6.2.1 illustrates the data of monthly cooling and heating loads when the office building utilizes double glazing (DB), double glazing with dCCPC layer (dCCPC-DB) and low-E double glazing with dCCPC layer (dCCPC-lowE) as skylights. The radar chart is better to present the imperceptible differences comparing with the traditional bar chart. In general view, the locations can be categorized into three types, which are the locations where the building has cooling load only, has heating load only and has both cooling and heating loads. For the first type, the locations are Hong Kong, Miami, Bangkok and Manila. The cooling load provides obvious decreases especially in summer time when the skylights using the window with dCCPC layer. Due to the lower value of solar heat gain coefficient (SHGC), the low-E glazing with dCCPC (dCCPC-lowE) provides more reduces than the common double glazing with dCCPC (dCCPC-DB). For the locations causing heating load only, e.g. Lhasa, Kiruna, Aberdeen, Birmingham and Helsinki, it can be found that the savings on heating load are not as much as on cooling load, even the heating load after using dCCPC window is more than that of using double glazing in some months. For the locations in which

building needs cooling and heating, like Los Angeles, Rome, Beijing, Shanghai and Istanbul, similar results are obtained. The window with dCCPC can reduce cooling load in summer, and these reductions are quite much in some specific months and locations, for example, the July, August and September in Los Angeles, the July and August in Rome and Istanbul.

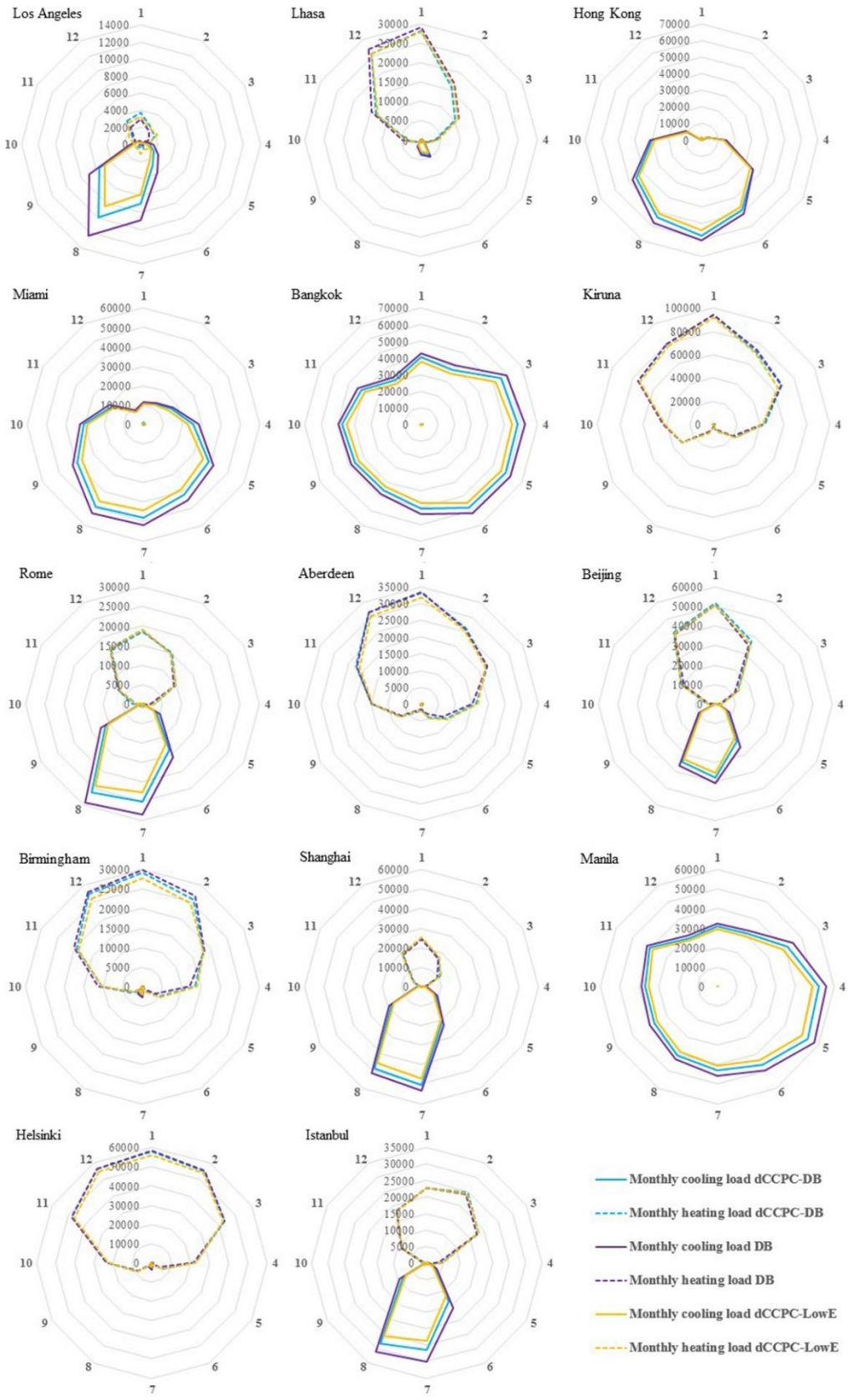


Fig. 7.6.2.1. Monthly cooling and heating loads for the office building in 14 cities with the skylights of dCCPC-DB, DB and dCCPC-lowE

The comparisons of annual cooling and heating load of using three skylights in the target building are shown in Fig. 7.6.2.2 and Fig. 7.6.2.3. The cities are arranged from low to high altitude. In terms of cooling load, except the Kiruna and Aberdeen whose the cooling load is smaller than 2000kWh that can be ignored, add a dCCPC layer can reduce the cooling load significantly, which implies that dCCPC can prevent daylight in summer time effectively. In addition, dCCPC-lowE saves more cooling load than dCCPC-DB due to the lower value of SHGC. Lhasa, Helsinki and Birmingham have quite few cooling loads so that the amount of cooling load savings are not worth to be discussed. Compared to the cooling load utilizing traditional double glazing, Los Angeles, Rome and Istanbul perform the most reducing percentages on cooling load which are more than 20%; Miami, Bangkok, Manila, Beijing and Shanghai provide less reductions ranging from 6% to 15%. For the locations in hot climates, the original cooling load is large so that the percentage of reduction is smaller although the decrease of cooling load is large quantitatively. Therefore, for the locations require both cooling and heating, the effects that dCCPC prevents solar gain are more significant.

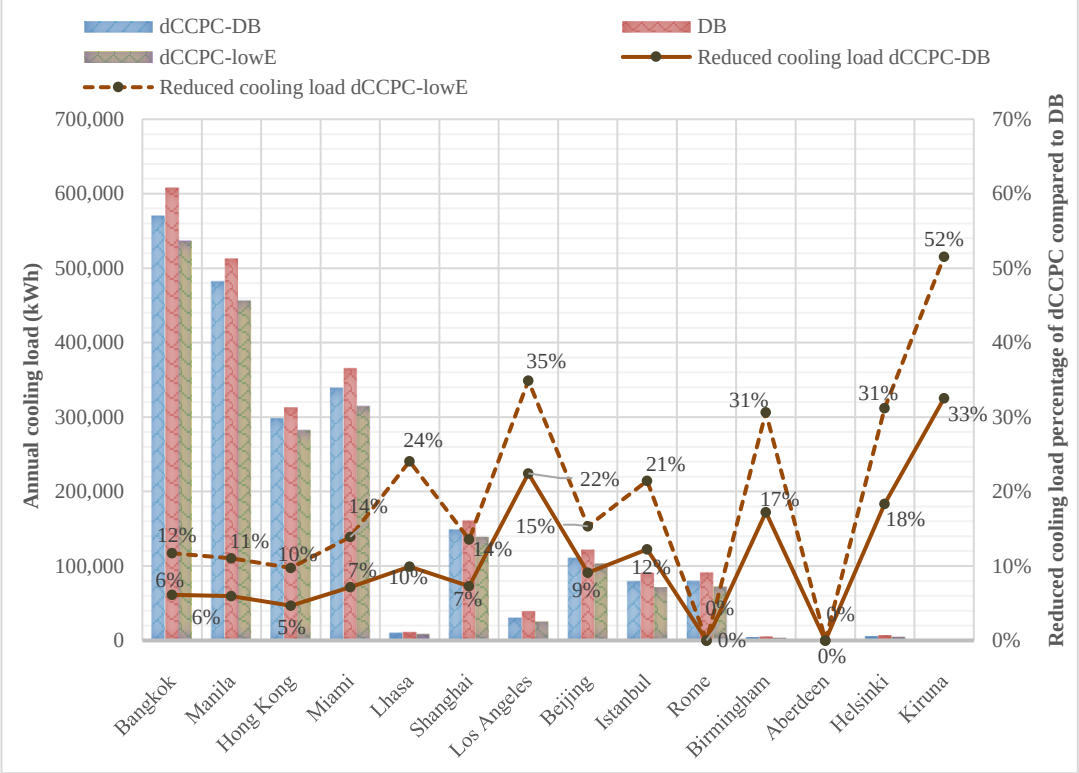


Fig. 7.6.2.2. Annual cooling load of example building with the skylights of dCCPC-DB, DB and dCCPC-lowE

Different from cooling load, dCCPC does not result in too many changes on annual heating load as shown in Fig. 7.6.2.3. For Lhasa, Birmingham and Kiruna, the low-E double glazing with dCCPC layer causes few reductions on annual heating load for the target building. Because the transmittance and SHGC of dCCPC-DB are smaller than those of standard double glazing, small increases of heating load occur for most cities when adding the dCCPC layer to skylights. Hence, dCCPC and low-e coating can reduce cooling load effectively, but the low SHGC can also lead to the increase of heating load in cold seasons. Balances should be found to save the total energy consumption on both cooling and heating for building.

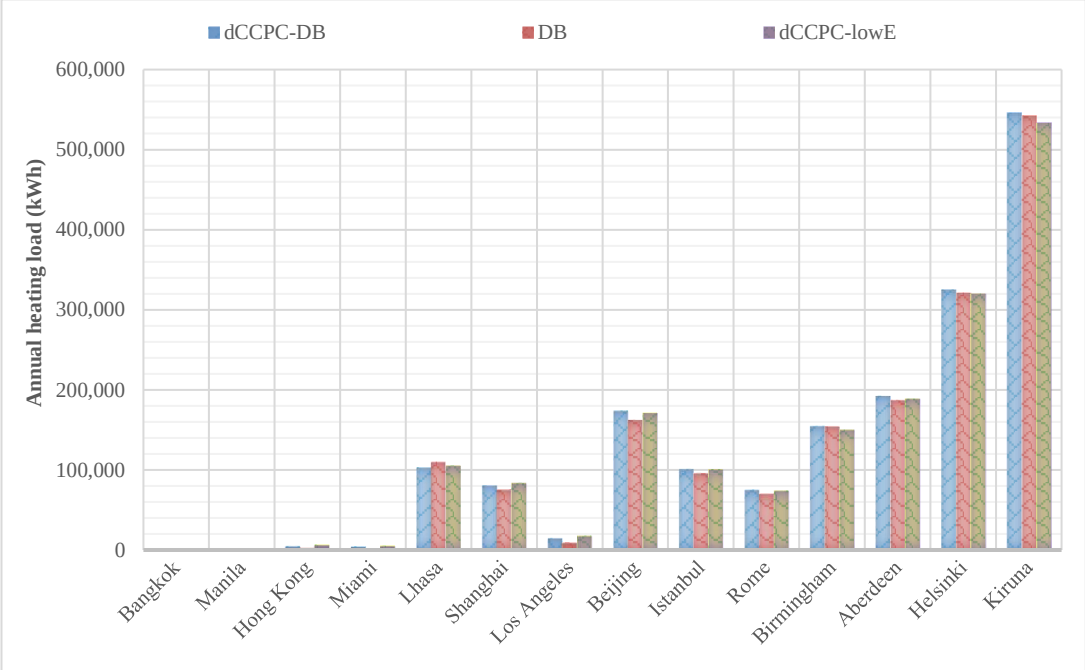


Fig. 7.6.2.3. Annual heating load of example building with the skylights of dCCPC-DB, DB and dCCPC-lowE

The annual energy consumptions on the sum of cooling and heating for the example building is summarized in Fig. 7.6.2.4, in which the effects of the skylights with dCCPC layer on the total thermal load can be found. After combining the variations on heating and cooling load, it provides different results compared to the result of either cooling or heating. It was found that the cold locations, like Helsinki, Kiruna and Aberdeen, are not suitable for using dCCPC in aspect of decreasing total thermal load. For the locations having cold winter, such as Beijing and Birmingham, heating takes more than half of the total thermal load, the energy savings on thermal load by dCCPC are quite few (< 5%). In these locations, cold seasons are long and solar gain

from window are expected to be as much as possible in winter to reduce heating load. It is important to point out that Lhasa is an exception among cold locations in which the thermal load of building is decreased after using dCCPC. Although most of the time during the whole year in Lhasa is cold, the clear sky takes about 65% of daytime during the whole year so that the annual solar radiation reaches 7.2GJ/m^2 which is extremely strong [245]. Form the annual cooling load, it can be seen that using dCCPC-DB and dCCPC-lowE reduces 10% and 24% cooling load respectively compared to using traditional double glazing. They also lead to reductions on heating load in winter time. The reason of is the dCCPC layer causes lower transmittance of skylights so that more artificial lighting is required. The thermal energy from lighting offsets some requirements on heating. For the locations having long hot seasons, the window with dCCPC provides outstanding performance of saving total thermal load: dCCPC-lowE reduces up to 23% annual thermal load compared to DB for Los Angeles, and the savings range from 10% to 14% for Hong Kong, Rome, Miami, Bangkok and Manila; the energy savings on heating and cooling by dCCPC-DB also range from 5% to 10%for these locations.

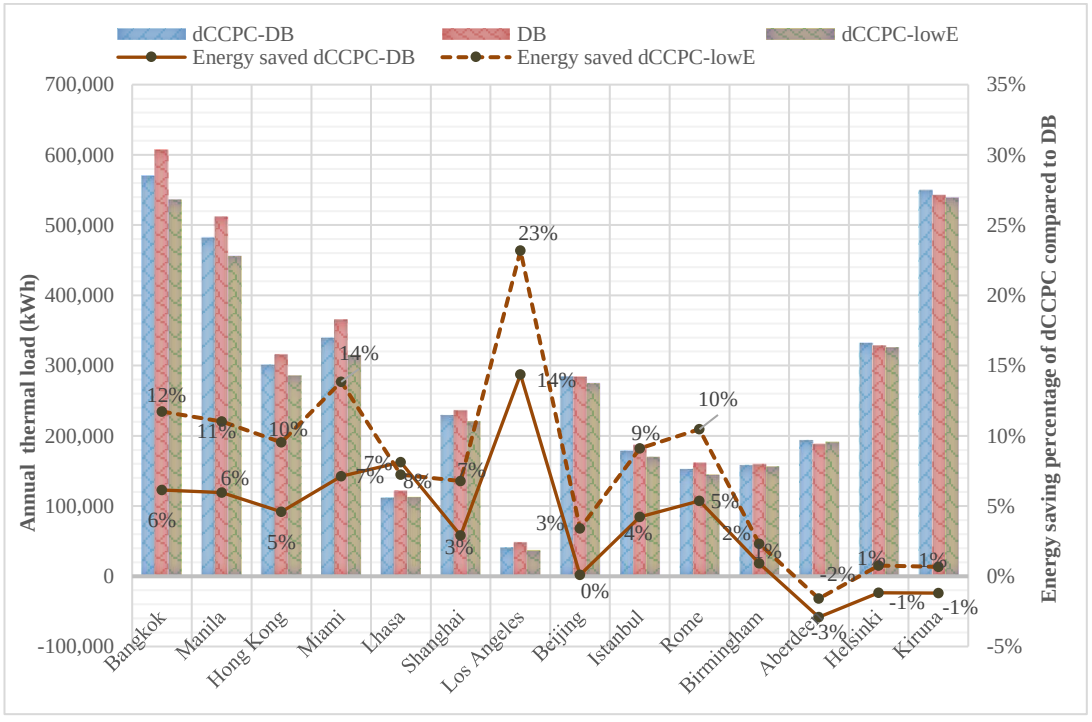


Fig. 7.6.2.4. Total annual thermal load of example building with the skylights of dCCPC-DB, DB and dCCPC-lowE

7.6.3. Energy consumption of artificial lighting

Although dCCPC provides effective daylight control, when it is integrated with standard or low-E double glazing, the total transmittance of it is smaller than that of traditional double glazing. Thus, more artificial lighting may be required to guarantee the indoor illuminance level. The annual electricity required for artificial lighting is demonstrated in Fig. 7.6.3.1. The percentage of lighting usage differences only demonstrates the comparisons between using dCCPC-DB and DB as skylights because the lighting consumptions of using dCCPC-DB and dCCPC-lowE are quite same which is less than 3%. It can be seen that the energy consumptions of lighting become more, about 6% increase, when using the skylights with dCCPC layer in general, except Beijing. It has been discussed that dCCPC has the advantage of diffusing incident light. When the sun is in lower position, traditional double glazing cannot provide a relatively large bright-area, but the dCCPC could lit larger space through diffusing. In Beijing, the sky conditions are possible to be intermediate or clear when the sun is low, and less lighting is needed during these time periods. For the locations with lower solar radiation and longer time of overcast sky, i.e. the time of overcast and overcast to intermediate sky is more than 80%, for instance, Helsinki, Birmingham, Kiruna and Aberdeen, dCCPC causes relatively large increase on the demand of artificial lighting. Results also demonstrates that Hong Kong is an exception of the cities located in low altitude. Utilizing dCCPC causes 19% increase of lighting consumption. The reason is Hong Kong has the opposite condition with Beijing: during the time when sun is low, more of the sky conditions in Hong Kong is likely to be overcast, and light is prevented by dCCPC causing much more demand on lighting. It is also important to mention another exception of Lhasa. Lhasa has strong direct sunlight and long-time clear sky conditions (about 65%). Thus, dCCPC performs low transmittance, e.g. 0.3-0.4, during these time periods so that much more lighting is needed. On the contrary, the normal double glazing can provide extreme bright indoor environment as well as the very high indoor illuminance level.

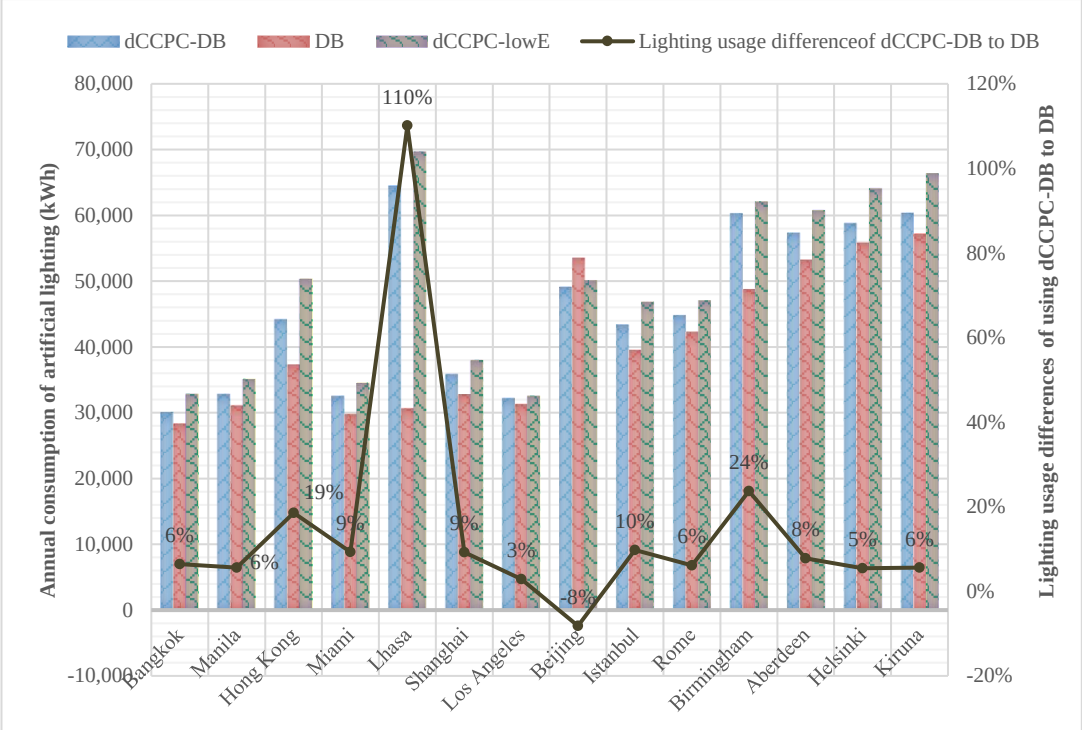


Fig. 7.6.3.1. Total Energy consumption of artificial lighting of example building with the skylights of dCCPC-DB, DB and dCCPC-lowE

The energy consumption of a building mainly consists of several parts: electricity usage of artificial lighting, electricity usage of equipment, electricity usage of fan and pump, and energy consumption of heating and cooling. As is discussed in previous sections, dCCPC can reduce total thermal load but increase lighting usage, and the variation of lighting caused by dCCPC can also lead to the change of thermal load. It is important to investigate the interactions among different energy usage sectors. In the energy simulations in this study, it is assumed that all of the systems and schedules are same. Thus the electricity usage of equipment, fan and pump are assumed to be same for different locations. The lighting and heating/cooling demands are the only two aspects that should be considered to evaluate the performance of using the window with dCCPC layer for skylights. Fig. 7.6.3.2 shows the comparisons of the sum of energy consumptions of lighting, cooling and heating when utilizing DB, dCCPC-DB and dCCPC-lowE as skylights. It can be found that for the locations with long hot seasons such as Los Angeles, Miami, Bangkok and Manila, dCCPC provides considerable reductions which is up to 13% on total energy consumptions. Small amounts (1%-5%) of energy are saved by utilizing dCCPC for the locations having temperate and continental climates, e.g. Beijing, Shanghai, Rome, Istanbul and Hong

Kong. For the locations having long cold seasons, the reduction on solar gain by dCCPC leads to more energy consumptions on heating load and artificial lighting.

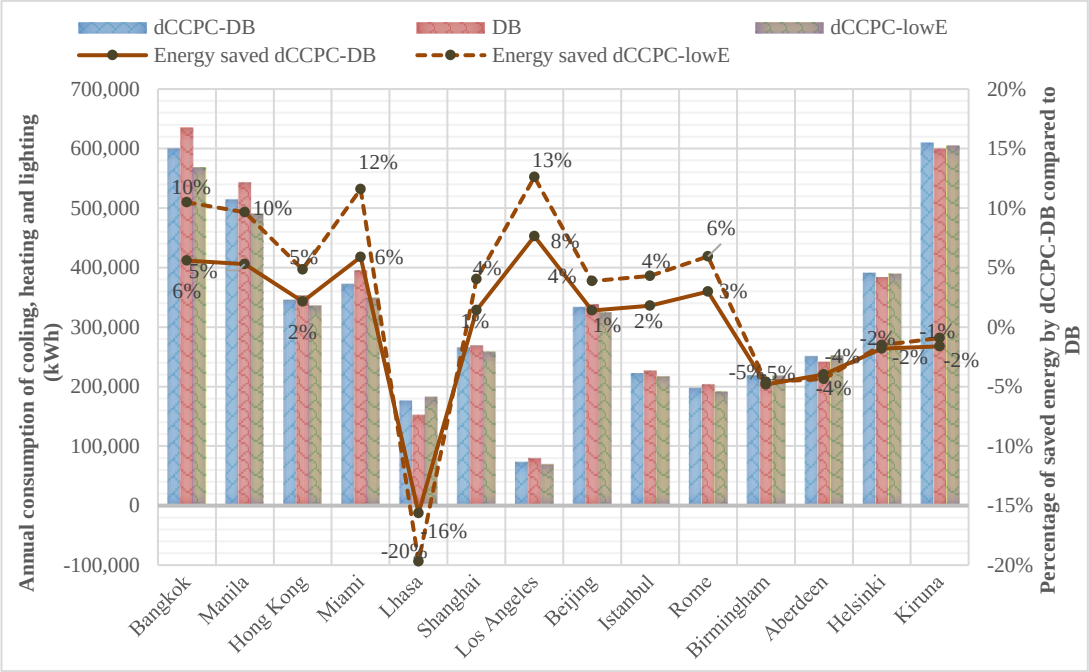


Fig. 7.6.3.2. Sum of annual cooling, heating and lighting consumptions of example building with the skylights of dCCPC-DB, DB and dCCPC-lowE

7.6.4. Visual environment and glare analysis

Except of saving energy, diffusing incident light and preventing glare are another two main advantages of dCCPC. The results of glare analysis for the respective viewpoint are shown in Fig. 7.6.4.1 in which the exposure was applied to enhance the correlations of pictures so that some other colours except white, grey and black are occurred in the HDRIs. The false colour HDRIs with luminance level are shown in Fig. 7.6.4.2. The results in both figures are for the same local times and viewpoint. It can be found that for standard double glazing and low-E double glazing, bright areas will occur under the skylights under clear and intermediate sky conditions. Under clear sky condition, the luminance of bright area is about 12,000cd/m^2 for double glazing and 9,000cd/m^2 for low-E glazing. However, it is around 4,000 cd/m^2 when using dCCPC-DB as skylight. Similar conditions also occur under intermediate sky. Hence, the dCCPC-DB can prevent the direct sunlight, that is, reduce the indoor illuminance and luminance effectively compared to the other two skylights under clear sky and intermediate sky. These three skylights provide similar indoor environment under overcast sky.

According to the light distribution in Fig. 7.6.4.2, it can be seen how the diffuse affects the indoor visual environment. For clear and intermediate sky, the HDRI of dCCPC-DB illustrates the light is distrusted on the floor more uniformly due to its diffusing effect. The luminance on the floor shows stronger contrast of double glazing and low-E glazing. Thus the visual environment provided by dCCPC should be more comfortable for occupancy. In terms of the daylight glare probability (DGP), the dCCPC-DB provides lower DGP under clear and intermediate sky compared to double glazing and low-E glazing. For clear sky, the DGP of dCCPC-DB is 0.35 which is located in the range of imperceptible glare. The DGP of low-E glazing is 0.4 which is perceptible glare and 0.43 of double glazing belonging to the disturbing glare. Under intermediate sky, the DGPs of the three skylights are all located in the range of perceptible glare but dCCPC-DB still provides the lowest value of DGP. Similar to the indoor luminance distribution, the DGP of the three skylights are almost same under overcast sky. All of the results imply that the dCCPC can controlled the incident light to a more comfortable visual environment with low daylight glare probability.

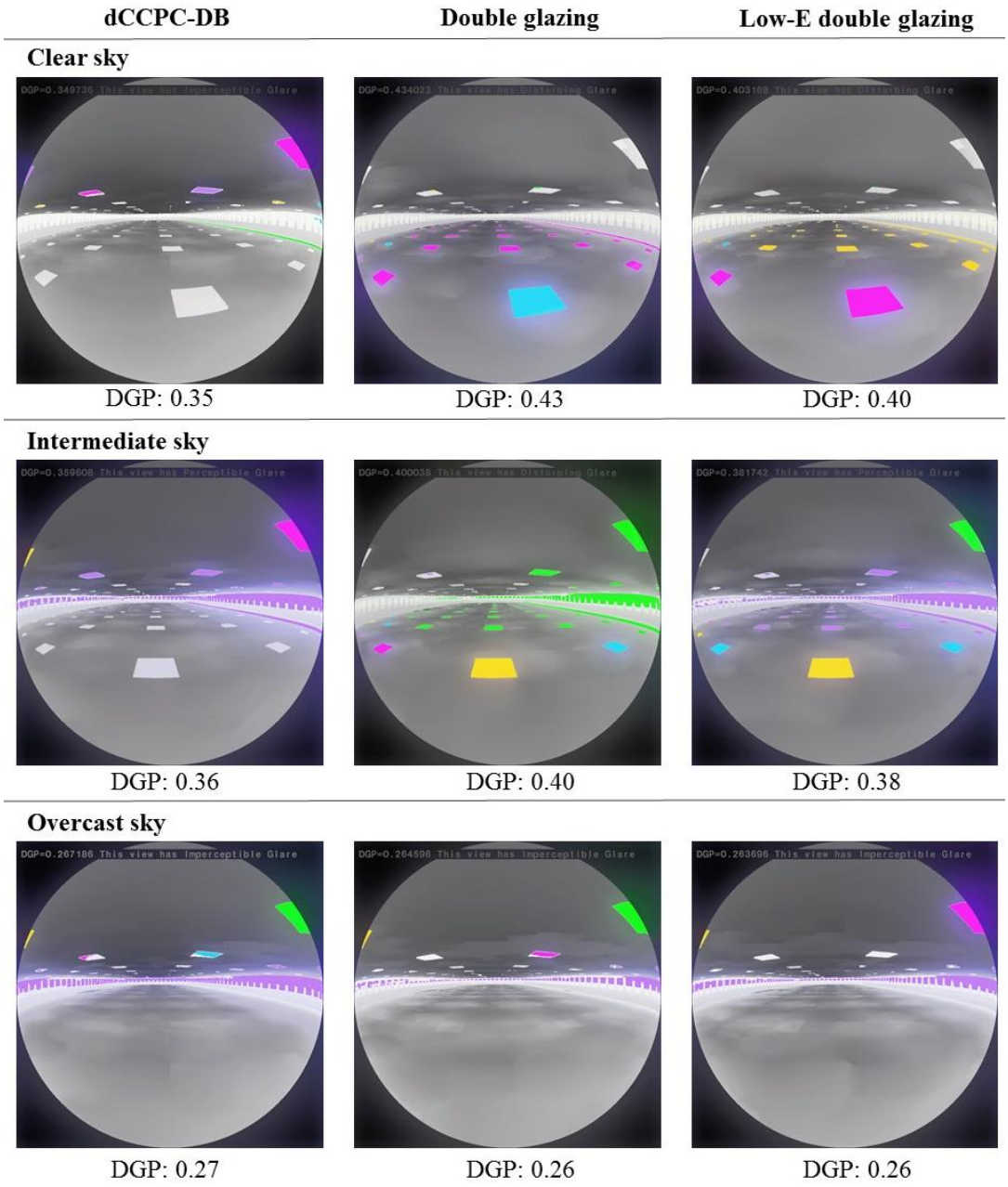


Fig. 7.6.4.1. Comparisons of HDR images of target building under different sky conditions

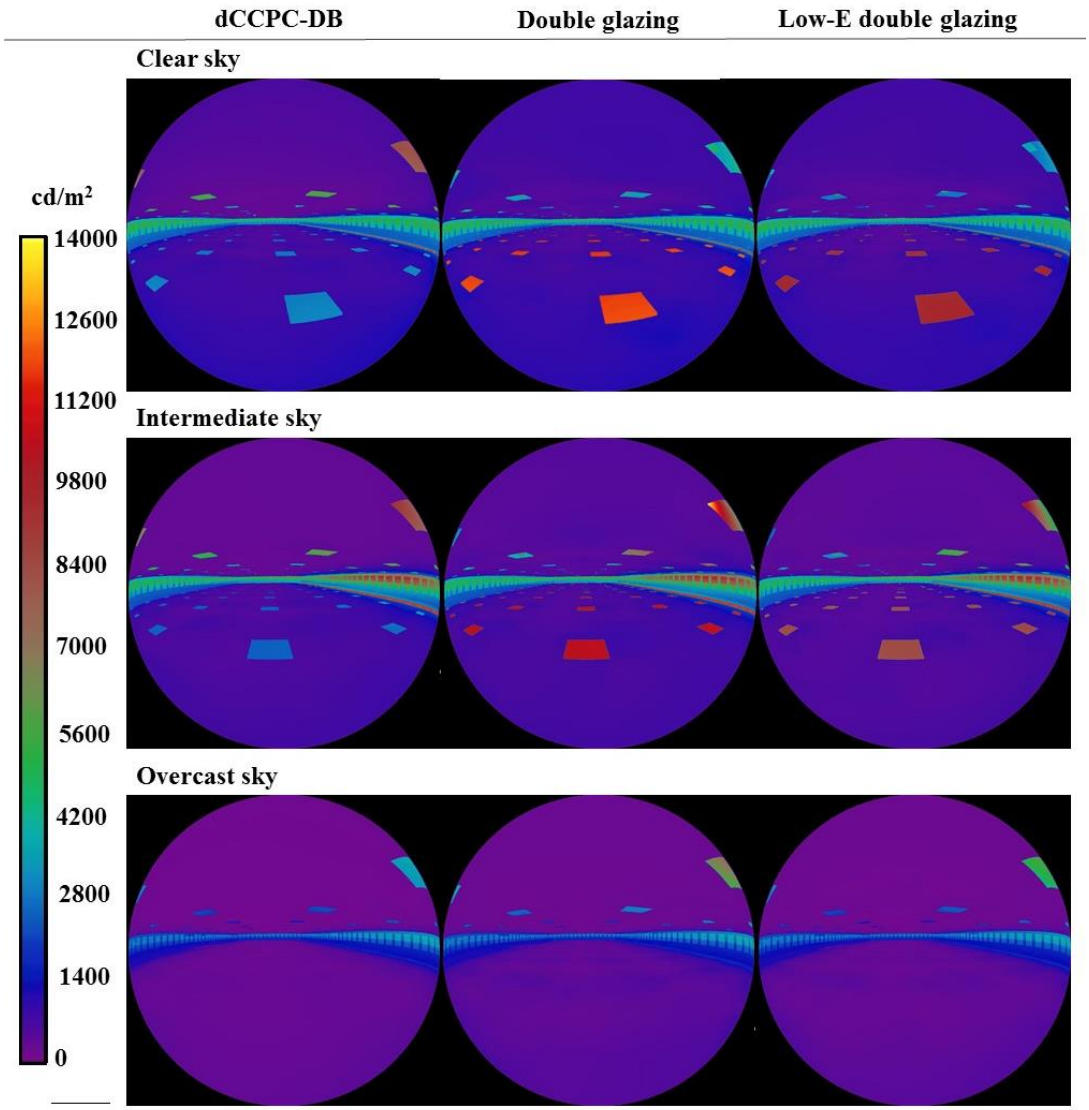


Fig. 7.6.4.2. Comparisons of indoor luminance by false colour HDR images of target building under different sky conditions

7.7. Economic analysis

7.7.1. Methodology and hypothesis

In the previous parts of this chapter, the benefits of using dCCPC as skylights were discussed from a technical point of view. Economic benefit is another important factor that affects making the decision of installing the dCCPC in practice. The payback period method is used in this section to analyse the economic benefits of dCCPC.

The payback period indicates the length of time required to recover the cost of an investment and it is usually be classified in simple payback period and discounted payback period (DPP). The second one is more popular and accurate because it takes

the time value of money into account. Thus DPP would be used in this section for economic analysis. The function of discounted payback period can be expressed by Eq. 7.7.1.1 below [246].

$$DPP = (a-1) + \frac{S_0 - {S_c}^{a-1}}{{S_t}^{a}} \quad (Eq.\,7.7.1.1)$$

where a is the year in which the cumulative present value of cash flows from investment exceed the initial cost; then $(a-1)$ is the year prior to a; S_0 is the initial cost of investment; ${S_c}^{a-1}$ is the cumulative present value of the cash flows from the investment at the end of the year $(a-1)$; ${S_t}^{a}$ is the present value of net cash flow in year a.

As introduced in the previous chapters, dCCPC panel does not require any operating and maintenance costs so that only the initial cost should be considered for it. Installing dCCPC would affects the electricity consumptions of artificial lighting and HVAC system (cooling and heating). The intangible items related to energy saving, such as carbon tax saving and the improvements of human work productivity, are not considered in this calculation. All of the analysis are based on the UK market. The inflation rate in UK is 3.1% [247]. The example office building used in previous sections are applied to do the economic benefits in this section. Table 7.7.1.1 lists the costs of installing dCCPC onto the roof of building and the money saving due to the reduction of energy consumption. The electricity price uses the average value of different period of the year. The amount of energy saving is calculated from the results of Fig. 7.6.3.2. Five typical locations from the 14 cities that are used to analyse the energy saving in previous parts are selected to calculate the payback period, which are Manila, Hong Kong, Los Angeles, Rome and Birmingham whose annual energy saving percentages are 10%, 5%, 13%, 6% and -5%.

Table 7.7.1.1. Summary of the costs and economic benefits for using dCCPC

Summary of dCCPC costs	
Manufacturing fee of dCCPC (£/m^2)	80
Installation fee of dCCPC (£/m^2)	17.5
Installation area of the example office building (m^2)	120 (5% of roof area)
Total initial cost (£)	11,700

Summary of economic benefits of dCCPC						
Location	Birmingham	Los Angeles	Hong Kong	Manila	Rome	Reference
Electricity price (p/kWh)	10.3	9.1	12.2	10.1	11.6	[248-251]
Annual total energy saving (kWh)	-9,654	10,108	17,061	52,439	12,114	N/A
Annual money saving (£)	-994	919	2,088	5,296	1,405	N/A

7.7.2. Calculation of discounted payback period

The discounted payback period is determined by Eq. 7.7.1.1 and Fig. 7.7.2.1 provides an example of calculating the discounted payback period of Hong Kong. According to the cumulated discounted cash flow, it can be found that the investment of dCCPC is paid back after the sixth years and begin to make the profit from the saved energy in the seventh year. Thus the DPP of installing dCCPC in Hong Kong is about 6.3 years. The results of all the selected locations are summarized in Fig. 7.7.2.2. Because installing dCCPC in Birmingham cannot save money, it is not included in the figure. The Manila has the shortest payback period which is 2.3 years and the Los Angeles has the longest DPP which is 16.4 years.

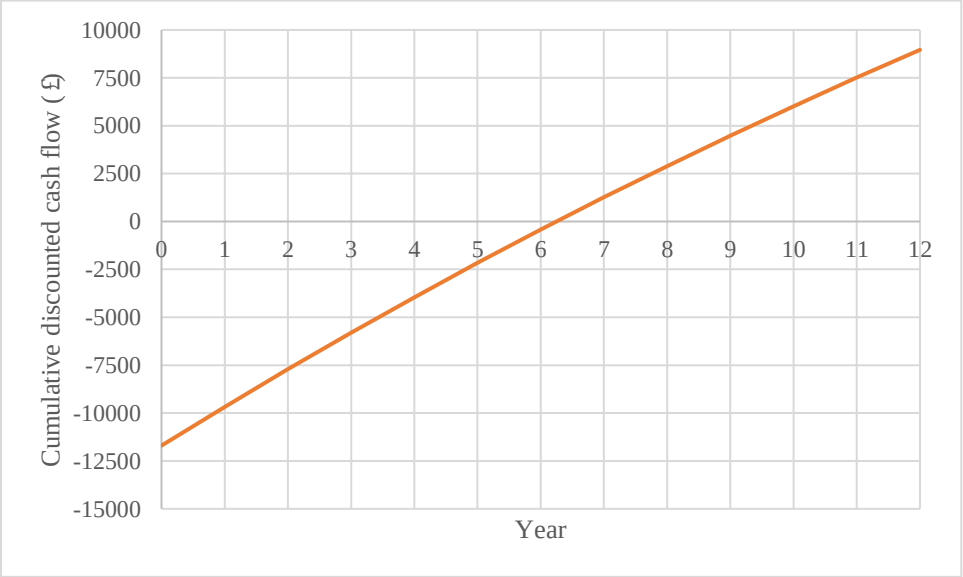


Figure 7.7.2.1. Cumulative discounted cash flow of dCCPC (Hong Kong)

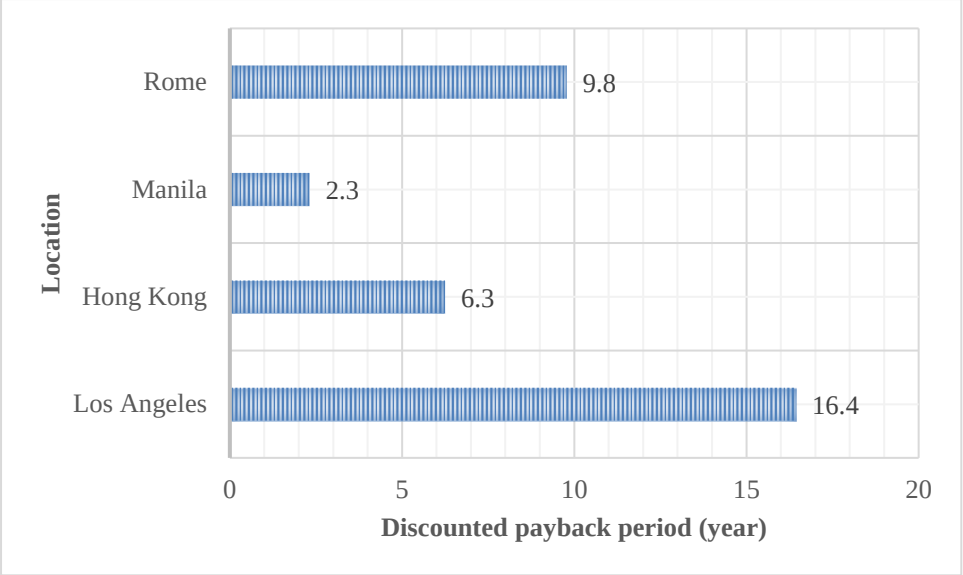


Figure 7.7.2.2. Discounted payback period for selected locations

It is interesting to find that Los Angeles has the most percentage of energy saving but its DPP is the longest. The reason should be DPP is related to the amount of saved energy rather than the percentage of energy saving compared to the building without dCCPC. In addition, because the DPP is related to various factors, e.g. capital costs, local electricity price, inflation rate, and the amount of energy saved, the change of each factors would affects the length of DPP. However, the economic analysis in this section is also worth to be presented as it provide a general ideal about the payback period of using dCCPC as skylights in practice. In addition, both technical and economic parts should be considered and all possible results should be weighed before making the decision of whether applying dCCPC in a building in practice.

7.8. Summary

This chapter investigated the energy consumption and indoor visual environment of an example office building utilizing different skylights. The economic benefits of utilizing dCCPC as skylights were analysed as well. In the part of energy consumption, 14 cities in the northern hemisphere with the altitude ranging from 13 ° to 67 ° were selected for simulations. Three types of skylights are compared, which are standard double glazing (DB), double glazing with dCCPC layer (dCCPC-DB), and double glazing with dCCPC layer and low-E coating (dCCPC-lowE). Results show that dCCPC can reduce cooling load due to effectively preventing solar gain. However, it also results in the increase demand on heating load and artificial lighting. In aspect of glare control, dCCPC provides outstanding performance comparing with standard

double glazing and standard double glazing with low-E coatings. Under overcast sky, these three skylights offers similar DGP and indoor luminance. For clear and intermediate sky, dCCPC-DB provides effective control on strong incident sunlight and the lowest values of DGP. It also make the light distributed more uniformly owing to its diffusing effect.

In view of energy saving, it is suggested that dCCPC is more suitable for the cities having long summer time, e.g. Bangkok, Manila, Miami, and Los Angeles. DCCPC is more effective under clear sky conditions. Therefore, among the cities with long-time hot seasons, the cities with long-time clear sky and more clear sky occurring at noon time like Los Angeles is the best choice. For the cities with continental climates, only the place with long-time clear sky is appropriate for using dCCPC. DCCPC is not suitable for the cities with long cold seasons. In terms of indoor visual environment, dCCPC has strong advantages in providing uniform indoor luminance and preventing glare. Hence, dCCPC is recommended for all locations for the purpose of glare control, especially for the cities with strong solar radiation.

From the economic analysis of the five selected cities, Manila provides the shortest discounted payback period which is 2.3 years only, and Los Angeles gives the longest payback period which is 16.4 years. For the cities where installing dCCPC cannot provide energy reductions, e.g. Birmingham, the payback period cannot be calculated. It was found that the discounted payback period is related to the amount of energy saved, capital cost of dCCPC and the local electricity price. The results imply that the dCCPC could cause shorter payback period for the locations with more energy saving after using dCCPC in general. However, when making the decision of whether utilizing dCCPC, all aspects including economic benefits, energy saving and visual environment should be considered to find the best solution and meet the requirements of building owner and occupants.

Chapter 8

Conclusion

8.1. Conclusion of main achievements

Compound parabolic concentrator (CPC) has been gaining ever-increasing attention from academic researchers and industrial developers owing to its stationary feature for solar energy collection with a higher efficiency. As a low concentration concentrator with a larger acceptance angle and without a tracking requirement, it is an attractive solution to improve the system performance and reduce the cost of photovoltaic (PV) system, solar thermal system, daylighting and lighting systems, etc. This thesis aims to present a comprehensive research on the dielectric crossed compound parabolic concentrator (dCCPC) focusing on its optical properties and effects on building energy and visual environment. The availability and feasibility of utilizing dCCPC as skylights on building for daylight control are investigated and proved through a series of works including literature review, simulation, experiment and case study.

The first key finding of this thesis is to verify the availability of using dCCPC in daylighting control for building, which is supported by the results of investigating the fundamental properties of dCCPC in Chapter 3, as well as the results of analysing the energy, visual performance and the economic benefits of the building with dCCPC in Chapter 7.

Considering the performance of CPC is mainly influenced by the incident angle of light, in the part of fundamental research (Chapter Three), an optical analysis software Photopia is used to simulate the daylighting control performance of different types of concentrators, and the effects by tilt angle and horizontal rotation angle on dCCPC. The performances of concentrators in Nottingham, UK (53 ° N, 1.2 ° W) are put forward as an example. The four investigated tilt angles are 29 °, 37 °, 45 °and 53 °. The tested horizontal rotation angles are from 0 °to 45 °with the 15 °interval. Results show that 3D dCPC has great advantages than 2D dCPC in control daylight, which performs higher transmittance in the morning and afternoon and lower transmittance at noon; 3D non-coated dCPC with 37 ° - 45 ° tilt angle are a better solution for controlling daylight in application with the advantages of installation, bigger tolerance in tilt angle, more stable illuminance level it provides and lower cost in manufacture. Then, the case study provided in Chapter Seven illustrates the potential of using dCCPC in daylighting control in practical aspects. In this part, the energy consumption of building, visual environment of the interior, and the economic benefits are analysed for the building installing dCCPC as skylights. In terms of building energy, 14 cities

located all over the world are selected to compare the energy variations caused by the different types of skylights which include double glazing, double glazing with dCCPC layer and double glazing with dCCPC layer and low-E coating. It was found that dCCPC can reduce cooling load from preventing solar gain effectively so that dCCPC is more suitable for the locations with long-time hot seasons. In aspect of glare control, dCCPC provides competitive advantages comparing with double glazing, low-E double glazing, prismatic diffuse panel and hemispherical diffuse panel. DCCPC could not only provide lower values of daylight glare probability (DGP), but make the light distribution become more uniformly. The economic analysis shows that for the building that dCCPC could cause more energy saving, the discounted payback period is shorter.

Another significant finding of this study is two kinds of prediction models, which are multiple nonlinear regression (MNLR) model and artificial neural network (ANN) model, are proposed to determine the optical performance of dCCPC, including optical efficiency and transmittance, in a simple, fast, and accurate way comparing with traditional ray-tracing simulation. It is illustrated in Chapter 5 and Chapter 6 of this thesis.

The most common way to accurately determine the performance of a dCCPC is through ray-tracing simulation which requires advanced optical analysis software and lots of time. Chapter Five goes back to the fundamental property of dCCPC and attempts to put forward the mathematical models of multiple nonlinear regression based on a mass of simulation results. The models can predict the transmittance of non-coated dCCPC and the both of transmittance and optical efficiency of base-coated dCCPC from several sky parameters, respectively. The agreement between predicted and simulated values is generally satisfactory. The coefficient of determination (R2) for each model is higher than 0.94 and the mean square error (MSE) is less than 0.0018. Six specific time among the whole year are selected to verify the reliability of the prediction models in practice. The limitation and significance of these models are discussed as well. The regression models provide a convenient and accurate approach to predict the optical performance of dCCPC. Following the strong correlations found of the basic MNLR prediction models, Chapter Six proposes two novel methods which are multiple nonlinear regression (MNLR) and artificial neural network (ANN) to evaluate the transmittance of dCCPC under various sky conditions including clear,

intermediate and overcast skies. For both the two prediction approaches, the coefficient of determination (R2) are higher than 0.93 and the mean square error (MSE) is less than 0.3%. The agreement between predicted and simulated results indicates the feasibility and accuracy of the two prediction methods. However, either regression or ANN model has its specific advantages and drawbacks that are compared and discussed in this study as well. Both of them are suggested with the advantages of simple, fast and accurate in determining the optical performance of dCCPC but the practical requirements should be considered as selecting the most appropriate one in application.

As dCCPC panel is designed with the purpose of practical application, this thesis also provides the research about dCCPC manufacture and test in real world in Chapter 4. In this part, four criteria, which are scale ratio, conjunction cover, truncation and gap between dCCPC components, are discussed to investigate their effects on the optical performance of dCCPC panel in consideration of the thickness, weight, manufacture requirements and accuracy of dCCPC panel. The best values of these four criteria are found for the trade-off between the optical performance and weight of dCCPC. Then the experiment are designed and untaken for testing and validating the actual optical performance of the designed dCCPC panel.

It is also important to mention that all of the works in this thesis are based on a comprehensive and up-to-date review of CPC for miscellaneous configurations, applications, performance predictions and technological advances in Chapter 2, in which numerous technically focused studies since 2000 are summarized and the outlook focusing on CPC designs and improvements is proposed. This section lays the groundwork for the whole research of this thesis.

8.2. Recommendations for further work

The study demonstrated in this thesis investigated and proved the high potential of utilizing dCCPC as skylights for daylighting control. It is recommended that the further work about dCCPC can be proceeded in three aspects. Firstly, improve the way of manufacturing dCCPC to improve the accuracy of its optical performance, and new manufacture technologies are encouraged. According to the experiment work done in this research, it is found that the accuracy of dCCPC geometry affects its optical performance significantly. New manufacture methods are recommended to focus on

the transparency and purity of dielectric material, the smoothness of polished surfaces and the accuracy of geometry. Secondly, for the MNLR and ANN prediction models, although they are accurate enough for the dCCPC in current research, more criteria are encouraged to added to widen their applicability, such as the factor relating to the geometry of dCCPC, the type of CPC, the dust deposition on surface, the type of dielectric material, the accuracy of manufacture, and so forth. Finally, with the remarkable performance of utilizing dCCPC as skylights, the asymmetric dCCPC is suggested for investigating its feasibility in daylighting control as vertical building facade, which decrease the limitations of using dCCPC for daylighting control in building.

World count: 69728

Reference

1. Alrubaih, M.S., et al., *Research and development on aspects of daylighting fundamentals.* Renewable and Sustainable Energy Reviews, 2013. **21**(Supplement C): p. 494-505.

2. Bodart, M. and A. De Herde, *Global energy savings in offices buildings by the use of daylighting.* Energy and Buildings, 2002. **34**(5): p. 421-429.

3. Palacios-Garcia, E.J., et al., *Stochastic model for lighting's electricity consumption in the residential sector. Impact of energy saving actions.* Energy and Buildings, 2015. **89**(Supplement C): p. 245-259.

4. Hölker, F., et al., *The Dark Side of Light: A Transdisciplinary Research Agenda for Light Pollution Policy*. 2010. **15**(4).

5. Liberman, J., *Light Medicine of the Future*. 1st Edition ed. 1990, New Mexico: Bear & Company.

6. Anonymous, *Ergo Biolight Report*. 1997, Ott Biolight Systems, Inc.: California.

7. Holmes, J., Guyscliffe, Holmes., *Essays on lighting*. 1975: Institute of Physics Publishing.

8. CIBSE, *Lighting Guide LG10:1999---Daylighting and window design*. 1999, CIBSE.

9. Hourani, M.M. and R.N. Hammad, *Impact of daylight quality on architectural space dynamics: Case study: City Mall – Amman, Jordan.* Renewable and Sustainable Energy Reviews, 2012. **16**(6): p. 3579-3585.

10. Sivaji, A., et al., *Lighting does Matter: Preliminary Assessment on Office Workers.* Procedia - Social and Behavioral Sciences, 2013. **97**(Supplement C): p. 638-647.

11. Schertz, W.W., et al., *Application of compound parabolic concentrators to solar photovoltaic conversion. Final report*. 1977: SciTech Connect.

12. Sarmah, N., B.S. Richards, and T.K. Mallick, *Design, development and indoor performance analysis of a low concentrating dielectric photovoltaic module.* Solar Energy, 2014. **103**(Supplement C): p. 390-401.

13. Li, G., et al., *Outdoor overall performance of a novel air-gap-lens-walled compound parabolic concentrator (ALCPC) incorporated with photovoltaic/thermal system.* Applied Energy, 2015. **144**: p. 214-223.

14. Cooper, T., et al., *Performance of compound parabolic concentrators with polygonal apertures.* Solar Energy, 2013. **95**(Supplement C): p. 308-318.

15. Yu, X., et al., *A study on use of miniature dielectric compound parabolic concentrator (dCPC) for daylighting control application.* Building and Environment, 2014. **74**: p. 75-85.

16. Nilsson, J., *Optical Design and Characterization of Solar Concentrators for Photovoltaics*. 2005, Lund University, Lund Institute of Technology: Lund.

17. Baranov, V.K., *Properties of the Parabolico-theoric focons.* Opt. Mekh. Prom., 1965. **6**: p. 1-5.

18. Baranov, V.K., *Parabolotoroidal mirrors as elements of solar energy concentrators.* Appl. Sol. Energy, 1966. **2**(1): p. 9-12.

19. Ploke, M., *Lichtführungseinrichtungen mit starker Konzentrationswirkung (English translation: A light guiding device with strong concentration action).* Optik, 1967. **25**: p. 31-43.

20. Baranov, V.K., *Device for Restricting in one plane the angular aperture of a pencil of rays from a light source (in Russian).* Russian certificate of authorship 200530, 1967.

21. Baranov, V., K., Melnikov, G. K., *Study of the illumination characteristics of hollow focons.* Sov. J. Opt. Technol., 1966. **33**: p. 408-411.

22. Hinterberger, H., Winston, R., *Efficient light coupler for threshold Čerenkov counters.* Review of Scientific Instruments, 1966. **37**: p. 1094-1095.

23. Hinterberger, H., Winston, R., *Gas Čerenkov counter with optimized light-collecting efficiency.* High Energy Phys., 1966: p. 205-206.

24. Ploke, M., *Axially Symmetrical Light Guide Arrangement*. 1969, German patent application No. 14722679.

25. Winston, R., *Principles of solar concentrators of a novel design.* Sol. Energy, 1974. **16**: p. 89-95.

26. Winston, R., Hinterberger, H. , *Principles of Cylindrical concentrators for solar energy.* Sol. Energy, 1975. **17**: p. 255-258.

27. Rabl, A., Winston, R., *Ideal concentrators for finite sorces and restricted exit angles.* Appl. Opt., 1976. **15**: p. 2880-2883.

28. Harper, D.A., Hildebrand, R. H., Pernlic, R., Platt, S. R., *Heat trap: An optimized far infrared field optics system.* Appl. Opt., 1976. **15**: p. 53-60.

29. Baylor, D.A., Fettiplace, R., *Light and photon capture in turtle receptors.* J. Physiol., 1975. **248**: p. 433-464.

30. Levi-Setti, R., Park, D. A., Winston, R., *The corneal cones of Limulus as optimized light collectors.* Nature (London), 1975. **253**: p. 115-116.

31. Winston, R., Enoch, J. M., *Retinal cone receptor as an ideal light collector.* J. Opt. Soc. Amer., 1971. **61**: p. 1120-1121.

32. Willer, U., C. Romano, and W. Schade. *Compact gas sensing system based on mid-infrared LED and resonant detection with quartz tuning fork*. in *Lasers and Electro-Optics, 2009 and 2009 Conference on Quantum electronics and Laser Science Conference. CLEO/QELS 2009. Conference on*. 2009.

33. Wang, K., et al., *High-speed duplex optical wireless communication system for indoor personal area networks.* Optics Express, 2010. **18**(24): p. 25199-25216.

34. Keränen, K., et al., *Infrared temperature sensor system for mobile devices.* Sensors and Actuators A: Physical, 2010. **158**(1): p. 161-167.

35. Gandia, L.M., G. Arzamedi, and P.M. Dieguez, *4.3.1 Redox Cycles*, in *Renewable Hydrogen Technologies - Production, Purification, Storage, Applications and Safety*. 2013, Elsevier.

36. Saitoh, T.S. and J. Takahashi. *Cooling power enhancement for 2-D and 3-D CPC sky radiators*. in *Energy Conversion Engineering Conference, 2002. IECEC '02. 2002 37th Intersociety*. 2002.

37. Nakamaru, F., Y. Matsumoto, and A. Nakazono, *Novel high-efficiency concentrator for optical fiber communication.* Photonics Technology Letters, IEEE, 2002. **14**(7): p. 953-955.

38. Liang, D. and R. Pereira, *Diode pumping of a solid-state laser rod by a two-dimensional CPC–elliptical cavity with intervening optics.* Optics Communications, 2007. **275**(1): p. 104-115.

39. Almeida, J., D. Liang, and E. Guillot, *Improvement in solar-pumped Nd:YAG laser beam brightness.* Optics & Laser Technology, 2012. **44**(7): p. 2115-2119.

40. Xing-Jie, Y., et al., *LED-Based Projection Systems.* Display Technology, Journal of, 2007. **3**(3): p. 295-303.

41. Chenhui, P., et al. *A high power light emitting diode module for projection display application*. in *Electronic Packaging Technology & High Density Packaging (ICEPT-HDP), 2010 11th International Conference on*. 2010.

42. Chenhui, P., et al. *Light collection systems for multiple LED arrays*. in *Advances in Optoelectronics and Micro/Nano-Optics (AOM), 2010 OSA-IEEE-COS*. 2010.

43. Aoki, M., et al., *Passive imaging and emissivity measurement with a 4K-cryocooled terahertz photoconductive detector.* IEICE Electronics Express, 2012. **9**(5): p. 333-338.

44. Aoki, M., et al., *Angle dependent condensing efficiency of Winston cone in terahertz region.* Infrared Physics & Technology, 2013. **56**: p. 8-11.

45. Grossman, E.N., O.D. Friedman, and A.O. Nelson, *Non-Imaging Winston Cone Concentrators for Submillimeter-Wave, Overmoded Waveguide.* Terahertz Science and Technology, IEEE Transactions on, 2014. **4**(1): p. 65-74.

46. Chemisana, D., *Building Integrated Concentrating Photovoltaics: A review.* Renewable and Sustainable Energy Reviews, 2011. **15**(1): p. 603-611.

47. Sharaf, O.Z. and M.F. Orhan, *Concentrated photovoltaic thermal (CPVT) solar collector systems: Part I – Fundamentals, design considerations and current technologies.* Renewable and Sustainable Energy Reviews, 2015. **50**: p. 1500-1565.

48. Sharaf, O.Z. and M.F. Orhan, *Concentrated photovoltaic thermal (CPVT) solar collector systems: Part II – Implemented systems, performance assessment, and future directions.* Renewable and Sustainable Energy Reviews, 2015. **50**: p. 1566-1633.

49. Norton, B., et al., *Enhancing the performance of building integrated photovoltaics.* Solar Energy, 2011. **85**(8): p. 1629-1664.

50. Grágeda, M., et al., *Review and multi-criteria assessment of solar energy projects in Chile.* Renewable and Sustainable Energy Reviews, 2016. **59**: p. 583-596.

51. Smith, E.H., *12.3.5 Atria,* in *Mechanical Engineer's Reference Book (12th Edition).* 1998, Elsevier: UK.

52. Selvakumar, N. and H.C. Barshilia, *Review of physical vapor deposited (PVD) spectrally selective coatings for mid- and high-temperature solar thermal applications.* Solar Energy Materials and Solar Cells, 2012. **98**: p. 1-23.

53. Kalogirou, S.A., *Solar thermal collectors and applications.* Progress in Energy and Combustion Science, 2004. **30**(3): p. 231-295.

54. Colangelo, G., et al., *Innovation in flat solar thermal collectors: A review of the last ten years experimental results.* Renewable and Sustainable Energy Reviews, 2016. **57**: p. 1141-1159.

55. Singh, H. and P.C. Eames, *A review of natural convective heat transfer correlations in rectangular cross-section cavities and their potential applications to compound parabolic concentrating (CPC) solar collector cavities.* Applied Thermal Engineering, 2011. **31**(14–15): p. 2186-2196.

56. Gallagher, J., *Nonimaging Optics in Solar Energy*. Nonimaging Optics in Solar Energy. 2008: Morgan & Claypool. 1-120.

57. Welford, W.T. and R. Winston, *High Collection Nonimaging Optics*. 1989: Academic Press. 1-7.

58. Winston, R. and W.T. Welford, *Design of nonimaging concentrators as second stages in tandem with image-forming first-stage concentrators.* Applied Optics, 1980. **19**(3): p. 347-351.

59. Winston, R., J.C. Miñano, and P. Benítez, *Nonimaging Optics*. 2005, Burlington: Academic Press.

60. Moore, J.H., et al., *4.3.3 Lenses and Lens Systems*, in *Building Scientific Apparatus (4th Edition)*. 2009, Cambridge University Press: USA.

61. Winston, R., *Radiant Energy Concentration*. 1976, U.S. letters patent 3923 381.

62. Winston, R., *Radiant Energy Concentration*. 1977, U.S. letters patent 4003 638.

63. Winston, R., *Cylindrical Concentrators for Solar Energy*. 1977, U.S. letters patent 4002 499.

64. Winston, R. and W. Zhang, *Pushing concentration of stationary solar concentrators to the limit.* Optics Express, 2010. **18**(S1): p. A64-A72.

65. Timinger, A., et al., *Faceted concentrators optimized for homogeneous radiation.* Applied Optics, 2000. **39**(7): p. 1152-1158.

66. van Dijk, L., et al., *3D-printed concentrator arrays for external light trapping on thin film solar cells.* Solar Energy Materials and Solar Cells, 2015. **139**: p. 19-26.

67. Cooper, T., et al., *Performance of compound parabolic concentrators with polygonal apertures.* Solar Energy, 2013. **95**: p. 308-318.

68. Bahaidarah, H., B. Tanweer, and P. Gandhidasan. *Performance analysis of a low concentrating PV-CPC system*. in *Photovoltaic Specialists Conference (PVSC), 2013 IEEE 39th*. 2013.

69. Winston, R., *Dielectric compound parabolic concentrators.* Applied Optics, 1976. **15**(2): p. 291-292.

70. Welford, W.T. and R. Winston, *The optics of nonimaging concentrators - Light and solar energy*. 1978.

71. Rabl, A., *Optical and thermal properties of Compound Parabolic Concentrators.* Solar Energy, 1976. **18**(6): p. 497-511.

72. Rabl, A., *Comparison of Solar Concentrators.* Solar energy, 1975. **18**(2): p. 93-111.

73. Rabl, A., *Solar concentrators with maximal concentration for cylindrical absorbers.* Applied Optics, 1976. **15**(7): p. 1871-1873.

74. Su, Y., et al., *Radiance/Pmap simulation of a novel lens-walled compound parabolic concentrator (lens-walled CPC).* Energy Procedia, 2012. **14**: p. 572-577.

75. Su, Y., S.B. Riffat, and G. Pei, *Comparative study on annual solar energy collection of a novel lens-walled compound parabolic concentrator (lens-walled CPC).* Sustainable Cities and Society, 2012. **4**: p. 35-40.

76. Li, G., et al., *Experiment and simulation study on the flux distribution of lens-walled compound parabolic concentrator compared with mirror compound parabolic concentrator.* Energy, 2013. **58**: p. 398-403.

77. Li, G., et al., *Design and investigation of a novel lens-walled compound parabolic concentrator with air gap.* Applied Energy, 2014. **125**: p. 21-27.

78. Li, G., et al., *Optical evaluation of a novel static incorporated compound parabolic concentrator with photovoltaic/thermal system and preliminary experiment.* Energy Conversion and Management, 2014. **85**: p. 204-211.

79. Pei, G., Li, G., Su, Y., Ji, J., *Solar inner wall lens type compound parabolic concentrator with air interlayer*. 2013, Patent Number CH203464513.

80. Sun, J. and M. Shi. *Experimental Study on A Concentrating Solar Photovoltaic/Thermal System*. in *Power and Energy Engineering Conference (APPEEC), 2010 Asia-Pacific*. 2010.

81. Bahaidarah, H.M., et al., *Experimental and numerical study on non-concentrating and symmetric unglazed compound parabolic photovoltaic concentration systems.* Applied Energy, 2014. **136**: p. 527-536.

82. Mallick, T.K., P.C. Eames, and B. Norton, *Non-concentrating and asymmetric compound parabolic concentrating building façade integrated photovoltaics: An experimental comparison.* Solar Energy, 2006. **80**(7): p. 834-849.

83. Arashi, H., et al. *Highly concentrated solar energy transmission through an optical fiber coupled with CPC*. in *Energy Conversion Engineering Conference, 1997. IECEC-97., Proceedings of the 32nd Intersociety*. 1997.

84. Mallick, T.K. and P.C. Eames, *Design and fabrication of low concentrating second generation PRIDE concentrator.* Solar Energy Materials and Solar Cells, 2007. **91**(7): p. 597-608.

85. Walze, G., et al., *Combination of microstructures and optically functional coatings for solar control glazing.* Solar Energy Materials and Solar Cells, 2005. **89**(2–3): p. 233-248.

86. Baig, H., et al., *Performance analysis of a dielectric based 3D building integrated concentrating photovoltaic system.* Solar Energy, 2014. **103**: p. 525-540.

87. Baig, H., et al., *Enhancing performance of a linear dielectric based concentrating photovoltaic system using a reflective film along the edge.* Energy, 2014. **73**: p. 177-191.

88. Arnaoutakis, G.E., et al., *Enhanced energy conversion of up-conversion solar cells by the integration of compound parabolic concentrating optics.* Solar Energy Materials and Solar Cells, 2015. **140**: p. 217-223.

89. Lampman, S., *Characterization and Failure Analysis of Plastics*. 2003, USA: ASM International.

90. Sarmah, N., B.S. Richards, and T.K. Mallick, *Design, development and indoor performance analysis of a low concentrating dielectric photovoltaic module.* Solar Energy, 2014. **103**: p. 390-401.

91. Baig, H., et al., *Numerical modelling and experimental validation of a low concentrating photovoltaic system.* Solar Energy Materials and Solar Cells, 2013. **113**: p. 201-219.

92. Baig, H., N. Sellami, and T.K. Mallick, *Trapping light escaping from the edges of the optical element in a Concentrating Photovoltaic system.* Energy Conversion and Management, 2015. **90**: p. 238-246.

93. Stine, W.B. and M.A. Geyer. *PowerFromTheSun.net*. 2001; Available from: www.powerfromthesun.net/.

94. Yu, X. and Y. Su, *A discussion of inner south projection angle for performance analysis of dielectric compound parabolic concentrator.* Solar Energy, 2015. **113**: p. 101-113.

95. Madala, S. and R.F. Boehm, *A review of nonimaging solar concentrators for stationary and passive tracking applications.* Renewable and Sustainable Energy Reviews, 2017. **71**: p. 309-322.

96. SolarPowerEurope, *Globle market outlook for solar power 2015-2019*, S. Europe, Editor. 2015, SolarPower Europe, the new EPIA (European Photovoltaic Industry Association): Belgium.

97. Meza, E., *Global CPV capacity expected to reach 1 GW by 2020*. 2014, PV magazine.

98. Jaaz, A.H., et al., *Design and development of compound parabolic concentrating for photovoltaic solar collector: Review*. Renewable and Sustainable Energy Reviews, 2017. **76**: p. 1108-1121.

99. Karathanassis, I.K., et al., *Design and experimental evaluation of a parabolic-trough concentrating photovoltaic/thermal (CPVT) system with high-efficiency cooling.* Renewable Energy, 2017. **101**: p. 467-483.

100. Grasso, G., et al., *Competitiveness of stationary planar low concentration photovoltaic modules using silicon cells: A focus on concentrating optics.* Solar Energy, 2012. **86**(6): p. 1725-1732.

101. Chen, L.L.C., *Stationary photovoltaic array module design for solar electric power generation systems*. 2003, Google Patents.

102. Chen, L.L.C., *Photovoltaic array module design for solar electric power generation systems*. 2004, Google Patents.

103. Chong, K.-K., et al., *Design and development in optics of concentrator photovoltaic system.* Renewable and Sustainable Energy Reviews, 2013. **19**: p. 598-612.

104. Li, G., et al., *Numerical and experimental study on a PV/T system with static miniature solar concentrator.* Solar Energy, 2015. **120**: p. 565-574.

105. Sellami, N. and T.K. Mallick, *Optical efficiency study of PV Crossed Compound Parabolic Concentrator.* Applied Energy, 2013. **102**: p. 868-876.

106. Sellami, N., T.K. Mallick, and D.A. McNeil, *Optical characterisation of 3-D static solar concentrator.* Energy Conversion and Management, 2012. **64**: p. 579-586.

107. Li, W., et al., *Coupled Simulation of Performance of a Crossed Compound Parabolic Concentrator with Solar Cell.* Energy Procedia, 2015. **75**: p. 325-330.

108. Gang, P., et al., *Preliminary Ray Tracing and Experimental Study on the Effect of Mirror Coating on the Optical Efficiency of a Solid Dielectric Compound Parabolic Concentrator.* Energies, 2012. **5**(9): p. 3627-3639.

109. Lamnatou, C., et al., *Life cycle energy analysis and embodied carbon of a linear dielectric-based concentrating photovoltaic appropriate for building-integrated applications.* Energy and Buildings, 2015. **107**: p. 366-375.

110. Yew, T.-K., K.-K. Chong, and B.-H. Lim, *Performance study of crossed compound parabolic concentrator as secondary optics in non-imaging dish concentrator for the application of dense-array concentrator photovoltaic system.* Solar Energy, 2015. **120**: p. 296-309.

111. Chong, K.-K., et al., *Prototype of Dense-array Concentrator Photovoltaic System Using Non-imaging Dish Concentrators and Cross Compound Parabolic Concentrator.* Energy Procedia, 2017. **105**: p. 131-136.

112. Andreev, V.M., et al. *High-efficiency (24.6% AM 0) LPE grown AlGaAs/GaAs concentrator solar cells and modules*. in *Photovoltaic Energy Conversion, 1994., Conference Record of the Twenty Fourth. IEEE Photovoltaic Specialists Conference - 1994, 1994 IEEE First World Conference on*. 1994.

113. Tsai, C.-Y., *Enhanced irradiance distribution on solar cell using optimized variable-focus-parabolic concentrator.* Optics Communications, 2013. **305**: p. 221-227.

114. Abu-Bakar, S.H., et al., *Rotationally asymmetrical compound parabolic concentrator for concentrating photovoltaic applications.* Applied Energy, 2014. **136**: p. 363-372.

115. Abu-Bakar, S.H., et al., *Performance analysis of a novel rotationally asymmetrical compound parabolic concentrator.* Applied Energy, 2015. **154**: p. 221-231.

116. Kalogirou, S.A., *Solar Energy Engineering (Second Edition)*. 2014, Boston: Academic Press. 1-49.

117. Santos-Gonz á lez, I., et al., *Numerical modeling and experimental analysis of the thermal performance of a Compound Parabolic Concentrator.* Applied Thermal Engineering, 2017. **114**: p. 1152-1160.

118. Ortiz-Rivera, E.I. and L.I. Feliciano-Cruz. *Performance evaluation and simulation of a solar thermal power plant*. in *Energy Conversion Congress and Exposition, 2009. ECCE 2009. IEEE*. 2009.

119. Al-Ghasem, A., G. Tashtoush, and M. Aladeemy. *Experimental study of tracking 2-D Compound Parabolic Concentrator (CPC) with flat plate absorber*. in *Renewable Energy Research and Applications (ICRERA), 2013 International Conference on*. 2013.

120. Mishra, R.K., V. Garg, and G.N. Tiwari, *Energy matrices of U-shaped evacuated tubular collector (ETC) integrated with compound parabolic concentrator (CPC).* Solar Energy, 2017. **153**: p. 531-539.

121. Ratismith, W., A. Inthongkhum, and J. Briggs, *Two non-tracking solar collectors: Design criteria and performance analysis.* Applied Energy, 2014. **131**: p. 201-210.

122. Canaff, M. and W. Ratismith. *High productivity non-tracking solar collectors for process heat applications*. in *Environment and Electrical Engineering (EEEIC), 2015 IEEE 15th International Conference on*. 2015.

123. Abdullahi, B., R.K. Al-dadah, and S. Mouhmud, *Optical Performance of Double Receiver Compound Parabolic Concentrator.* Energy Procedia, 2014. **61**: p. 2625-2628.

124. Abdullahi, B., et al., *Optical and thermal performance of double receiver compound parabolic concentrator.* Applied Energy, 2015. **159**: p. 1-10.

125. Gang, P., et al., *Experimental study and exergetic analysis of a CPC-type solar water heater system using higher-temperature circulation in winter.* Solar Energy, 2012. **86**(5): p. 1280-1286.

126. Xu, R.J., et al., *Experimental investigation of a solar collector integrated with a pulsating heat pipe and a compound parabolic concentrator.* Energy Conversion and Management, 2017. **148**: p. 68-77.

127. Wang, Y., et al., *Performance analysis of a novel sun-tracking CPC heat pipe evacuated tubular collector.* Applied Thermal Engineering, 2015. **87**: p. 381-388.

128. Ulavi, T., J.H. Davidson, and T. Herbrink. *Analysis of a hybrid PV/T Concept based on wavelength selective films*. in *ASME 2013 7th International Conference on Energy Sustainability*. 2013. Minneapolis, Minnesota, USA, July 14–19, 2013.

129. Yanhua, L., et al. *Thermal performance analysis of linear fresnel reflector concentrator with a compound parabolic cavity absorber*. in *Materials for Renewable Energy & Environment (ICMREE), 2011 International Conference on*. 2011.

130. Chaitanya Prasad, G.S., K.S. Reddy, and T. Sundararajan, *Optimization of solar linear Fresnel reflector system with secondary concentrator for uniform flux distribution over absorber tube.* Solar Energy, 2017. **150**: p. 1-12.

131. Baljit, S.S.S., et al., *Mathematical modelling of a dual-fluid concentrating photovoltaic-thermal (PV-T) solar collector.* Renewable Energy, 2017. **114**: p. 1258-1271.

132. Ma, X., H. Zheng, and Z. Chen, *An investigation on a compound cylindrical solar concentrator (CCSC).* Applied Thermal Engineering, 2017. **120**: p. 719-727.

133. Smyth, M., et al., *Experimental comparison of alternative convection suppression arrangements for concentrating integral collector storage solar water heaters.* Solar Energy, 2005. **78**(2): p. 223-233.

134. Antonelli, M., et al., *Electrical production of a small size Concentrated Solar Power plant with compound parabolic collectors.* Renewable Energy, 2015. **83**: p. 1110-1118.

135. Tiwari, D., et al., *Energy and exergy analysis of solar driven recuperated organic Rankine cycle using glazed reverse absorber conventional compound parabolic concentrator (GRACCPC) system.* Solar Energy, 2017. **155**: p. 1431-1442.

136. Singh, D.B. and G.N. Tiwari, *Performance analysis of basin type solar stills integrated with N identical photovoltaic thermal (PVT) compound parabolic concentrator (CPC) collectors: A comparative study.* Solar Energy, 2017. **142**: p. 144-158.

137. Singh, D.B. and G.N. Tiwari, *Exergoeconomic, enviroeconomic and productivity analyses of basin type solar stills by incorporating N identical PVT compound parabolic concentrator collectors: A comparative study.* Energy Conversion and Management, 2017. **135**: p. 129-147.

138. Nishi, Y. and T. Sema, *Estimation of exergy efficiency of compound parabolic concentrator under time-varying cloud cover condition.* Solar Energy, 2013. **98, Part C**: p. 341-348.

139. Elashmawy, M., *An experimental investigation of a parabolic concentrator solar tracking system integrated with a tubular solar still.* Desalination, 2017. **411**: p. 1-8.

140. Noyes, R., *7.15 Solar Energy*, in *Unit Operations in Environmental Engineering*. 1994, William Andrew Publishing/Noyes: USA.

141. Ulavi, T., T. Hebrink, and J.H. Davidson, *Analysis of a hybrid solar window for building integration.* Solar Energy, 2014. **105**: p. 290-302.

142. Ulavi, T., T. Hebrink, and J.H. Davidson, *Analysis of a Hybrid Solar Window for Building Integration.* Energy Procedia, 2014. **57**: p. 1941-1950.

143. Zacharopoulos, A., et al., *Linear dielectric non-imaging concentrating covers for PV integrated building facades.* Solar Energy, 2000. **68**(5): p. 439-452.

144. Mallick, T.K., et al., *The design and experimental characterisation of an asymmetric compound parabolic photovoltaic concentrator for building façade integration in the UK.* Solar Energy, 2004. **77**(3): p. 319-327.

145. Sarmah, N. and T.K. Mallick, *Design, fabrication and outdoor performance analysis of a low concentrating photovoltaic system.* Solar Energy, 2015. **112**: p. 361-372.

146. Taengchum, T., et al., *Tracing of daylight through circular light pipes with anidolic concentrators.* Solar Energy, 2014. **110**: p. 818-829.

147. Wittkopf, S., et al., *Ray tracing study for non-imaging daylight collectors.* Solar Energy, 2010. **84**(6): p. 986-996.

148. Xue, X., et al., *Study of a novel sunlight concentrating and optical fibre guiding system.* Solar Energy, 2011. **85**(7): p. 1364-1370.

149. Ullah, I. and S. Shin, *Highly concentrated optical fiber-based daylighting systems for multi-floor office buildings.* Energy and Buildings, 2014. **72**: p. 246-261.

150. Zhang, T.C., et al., *3.4.1.2 Compound Parabolic Concentrator (CPC) System*, in *Nanotechnologies for Water Environment Applications*. 2009, American Society of Civil Engineers (ASCE).

151. Tanveer, M. and G. Tezcanli Guyer, *Solar assisted photo degradation of wastewater by compound parabolic collectors: Review of design and operational parameters.* Renewable and Sustainable Energy Reviews, 2013. **24**: p. 534-543.

152. MathWorks, T. *Matlab*. n.d. [cited 2016 2/13]; Available from: http://uk.mathworks.com/index.html?s_tid=gn_logo.

153. Synopsys. *LightTools Illumination Design Software*. 2015 [cited 2016 2/13]; Available from: https://optics.synopsys.com/lighttools/lighttools-product-literature.html.

154. ZEMAX. *Zemax*. [cited 2016 2/13]; Available from: http://www.zemax.com/products/opticstudio/about.

155. BreaultResearchOrganization. *APEX*. [cited 2016 2/13]; Available from: http://www.breault.com/software/apex-features.

156. LAMBDA. *TracePro*. 2016 [cited 2016 6/22]; Available from: http://www.lambdares.com/tracepro.

157. COMSOL. *Introduction to COMSOL Multiphysics*. n.d. [cited 2016 2/15]; Available from: https://www.comsol.com/comsol-multiphysics#overview.

158. CADMicrosolutions. *OPTISWORKS*. [cited 2016 2/15]; Available from: http://www.cadmicro.com/products/optisworks/#toggle-id-1.

159. BerkeleyLab. *Radiance*. [cited 2016 2/15]; Available from: http://radsite.lbl.gov/radiance/framew.html.

160. Ward, G.J. *The RADIANCE Lighting Simulation and Rendering System*. Available from: http://radsite.lbl.gov/radiance/papers/sg94.1/Siggraph1994a.pdf.

161. Schregle, R., *The RADIANCE Photon Map Extension User Manual*. 2015, Luceme University of Applied Sciences and Arts.

162. Photopia. *Photopia User's Guide.* n.d. [cited 2017 5th April]; Available from: http://www.ltioptics.com/en/photopia-standalone-base.html.

163. Wittkopf, S.K., *Daylight performance of anidolic ceiling under different sky conditions.* Solar Energy, 2007. **81**(2): p. 151-161.

164. ANSYS. *Fluid Dynamics*. [cited 2016 2/17]; Available from: http://resource.ansys.com/staticassets/ANSYS/staticassets/resourcelibrary/brochure/fluid-dynamics-brochure.pdf.

165. F-ChartSoftware. *EES Engineering Equation Solver*. [cited 2016 2/17]; Available from: http://www.fchart.com/ees/.

166. SIMENS. *LMS Imagine.Lab Amesim.* [cited 2016 6/22]; Available from: https://www.plm.automation.siemens.com/en_us/products/lms/imagine-lab/amesim/.

167. Ahmed, O.K. and Z.A. Mohammed, *Dust effect on the performance of the hybrid PV/Thermal collector.* Thermal Science and Engineering Progress, 2017. **3**: p. 114-122.

168. Said, S.A.M., et al., *The effect of environmental factors and dust accumulation on photovoltaic modules and dust-accumulation mitigation strategies.* Renewable and Sustainable Energy Reviews, 2018. **82**: p. 743-760.

169. Xu, R., et al., *Analysis of the optimum tilt angle for a soiled PV panel.* Energy Conversion and Management, 2017. **148**: p. 100-109.

170. Gholami, A., et al., *Experimental investigation of dust deposition effects on photo-voltaic output performance.* Solar Energy, 2018. **159**: p. 346-352.

171. Sayyah, A., M.N. Horenstein, and M.K. Mazumder, *Energy yield loss caused by dust deposition on photovoltaic panels.* Solar Energy, 2014. **107**: p. 576-604.

172. Anonymous, *Engineering Design Handbook-Environmental Series Part Five-Glossary of Environmental Terms: (AMCP 706-119)*. 2011: U.S. Army material command. Electronic.

173. Tina, G.M., et al., *Optical and thermal behavior of submerged photovoltaic solar panel: SP2.* Energy, 2012. **39**(1): p. 17-26.

174. NewportCorporation. *Oriel Sol3A Class AAA solar simulator*. 2012 [cited 2017 13th Oct]; Available from: http://assets.newport.com/webDocuments-EN/images/29355.pdf.

175. Tektronix. *Keithley 2400 SourceMeter® SMU Instruments*. 2016 [cited 2016 6/16]; Available from: http://www.tek.com/keithley-source-measure-units/keithley-smu-2400-series-sourcemeter.

176. Esen, V., Ş. Sağlam, and B. Oral, *Light sources of solar simulators for photovoltaic devices: A review.* Renewable and Sustainable Energy Reviews, 2017. **77**: p. 1240-1250.

177. VISHAY, *Ambient Light Sensors-Circuit and Window Design*. 2012, VISHAY Semiconductors.

178. PVEducation. *Spectral Response*. n.d. [cited 2018 4th Feb]; Available from: http://www.pveducation.org/pvcdrom/solar-cell-operation/spectral-response.

179. Luque, A., G. Sala, and J.C. Arboiro, *Electric and thermal model for non-uniformly illuminated concentration cells.* Solar Energy Materials and Solar Cells, 1998. **51**(3-4): p. 269-290.

180. Stacey, R.W. and P.G. McCormick, *Effect of concentration on the performance of flat plate photovoltaic modules.* Solar Energy, 1984. **33**(6): p. 565-569.

181. Luque, A., G. Sala, and J.C. Arboiro, *Electric and thermal model for non-uniformly illuminated concentration cells.* Solar Energy Materials and Solar Cells, 1998. **51**(3): p. 269-290.

182. Tian, M. and Y. Su, *A study on use of three-dimensional miniature dielectric compound parabolic concentrator (3D dCPC) for daylighting control application*, in *14th International Conference on Sustainable Energy Technologies -SET 2015*. 2015: Nottingham, UK.

183. Tian, M. and Y. Su, *three dimensional dielectric compound parabolic concentrator (3D dCPC) for daylighting control in roofing*, in *11th Conference on Advanced Building Skins*. 2016: Bern, Switzerland.

184. Perez, R., et al., *Modeling daylight availability and irradiance components from direct and global irradiance.* Solar Energy, 1990. **44**(5): p. 271-289.

185. EnergyPlus, *EnergyPlus Version 8.7 Documentation - Engineering Reference*. 2016, U.S. Department of Energy.

186. Kleindienst, S., M. Bodart, and M. Andersen, *Graphical Representation of Climate-Based Daylight Performance to Support Architectural Design.* LEUKOS: The Journal of the Illuminating Engineering Society of North America, 2008. **5**(1): p. 39-61.

187. Piderit, M., C. Cauwerts, and M. Diaz, *Definition of the CIE standard skies and application of high dynamic range imaging technique to characterize the spatial distribution of daylight in Chile.* Journal of Construction, 2014. **13**(2): p. 22-30.

188. SARL, A., *XLSTAT Help Documentation*. 2016: Paris, FRANCE.

189. Nau, R. *Statistical forecasting: notes on regression and time series analysis*. Linear regression models n.d. [cited 2017 19th Oct]; Available from: https://people.duke.edu/~rnau/compare.htm.

190. Lewis, C.D., *Industrial and business forecasting methods: a practical guide to exponential smoothing and curve fitting*. 1982, London: Butterworth scientific.

191. Rabl, A., J. O'Gallagher, and R. Winston, *Design and test of non-evacuated solar collectors with compound parabolic concentrators.* Solar Energy, 1980. **25**(4): p. 335-351.

192. EnergyPlus. *EnergyPlus Weather Data*. n.d. [cited 2017 5/21]; Available from: https://energyplus.net/weather.

193. Michigan, U.o. *Multiple Linear Regression*. n.d. [cited 2017 5th April]; Available from: http://dept.stat.lsa.umich.edu/~kshedden/Courses/Stat401/Notes/401-multreg.pdf.

194. IESNA, I.E.S.o.N.A., *Calculation of Daylight Availability (IES RP-21)*. 1984, IES: New York.

195. B.S.I., B.S.I., *Spatial distribution of daylight - CIE standard general sky. BS ISO 15469:2004*. 2004.

196. Reinhart, C. and A. Fitz, *Findings from a survey on the current use of daylight simulations in building design.* Energy and Buildings, 2006. **38**(7): p. 824-835.

197. Tian, M. and Y. Su, *Multiple nonlinear regression model for predicting the optical performances of dielectric Crossed Compound Parabolic Concentrator (dCCPC).* Sol. Energy, 2018. **159**: p. 212-225.

198. Mellit, A., et al., *Artificial intelligence techniques for sizing photovoltaic systems: A review.* Renewable and Sustainable Energy Reviews, 2009. **13**(2): p. 406-419.

199. Mohanraj, M., S. Jayaraj, and C. Muraleedharan, *Applications of artificial neural networks for thermal analysis of heat exchangers – A review.* International Journal of Thermal Sciences, 2015. **90**: p. 150-172.

200. Mohanraj, M., S. Jayaraj, and C. Muraleedharan, *Applications of artificial neural networks for refrigeration, air-conditioning and heat pump systems—A review.* Renewable and Sustainable Energy Reviews, 2012. **16**(2): p. 1340-1358.

201. Azlan Hussain, M., *Review of the applications of neural networks in chemical process control — simulation and online implementation.* Artificial Intelligence in Engineering, 1999. **13**(1): p. 55-68.

202. Janjai, S. and P. Plaon, *Estimation of sky luminance in the tropics using artificial neural networks: Modeling and performance comparison with the CIE model.* Applied Energy, 2011. **88**(3): p. 840-847.

203. Wong, S.L., K.K.W. Wan, and T.N.T. Lam, *Artificial neural networks for energy analysis of office buildings with daylighting.* Applied Energy, 2010. **87**(2): p. 551-557.

204. Fonseca, R.W.d., E.L. Didoné, and F.O.R. Pereira, *Using artificial neural networks to predict the impact of daylighting on building final electric energy requirements.* Energy and Buildings, 2013. **61**: p. 31-38.

205. Kim, W., Y. Jeon, and Y. Kim, *Simulation-based optimization of an integrated daylighting and HVAC system using the design of experiments method.* Applied Energy, 2016. **162**: p. 666-674.

206. Kalogirou, S.A. and M. Bojic, *Artificial neural networks for the prediction of the energy consumption of a passive solar building.* Energy, 2000. **25**(5): p. 479-491.

207. Navada, S.G., C.S. Adiga, and S.G. Kimi, *Prediction of Daylight Availability for visual comfort.* International Journal of Applied Engineering Research, 2016. **11**(7): p. 4711-4717.

208. Kazanasmaz, T., M. Günaydin, and S. Binol, *Artificial neural networks to predict daylight illuminance in office buildings.* Building and Environment, 2009. **44**(8): p. 1751-1757.

209. Hu, J. and S. Olbina, *Illuminance-based slat angle selection model for automated control of split blinds.* Building and Environment, 2011. **46**(3): p. 786-796.

210. Lou, I. and Y. Zhao, *Sludge bulking prediction using principle component regression and artificial neural network.* Mathematical Problems in Engineering, 2012. **2012**: p. 17.

211. Adamowski, J., et al., *Comparison of multiple linear and nonlinear regression, autoregressive integrated moving average, artificial neural network, and wavelet artificial neural network methods for urban water demand forecasting in Montreal, Canada.* Water Resources Research, 2012. **48**(1): p. n/a-n/a.

212. Yu, H. and B. Wilamowski, *Chapter 12 Levenberg-Marquardt Training*, in *Intelligent Systems*. 2011, CRC Press. p. 1-16.

213. Pramanik, N. and R.K. Panda, *Application of neural network and adaptive neuro-fuzzy inference systems for river flow prediction.* Hydrological Sciences Journal, 2009. **54**(2): p. 247-260.

214. Adamowski, J. and C. Karapataki, *Comparison of Multivariate Regression and Artificial Neural Networks for Peak Urban Water-Demand Forecasting: Evaluation of Different ANN Learning Algorithms.* Journal of Hydrologic Engineering, 2010. **15**(10): p. 729-743.

215. Daliakopoulos, I.N., P. Coulibaly, and I.K. Tsanis, *Groundwater level forecasting using artificial neural networks.* Journal of Hydrology, 2005. **309**(1): p. 229-240.

216. Adamowski, J. and H.F. Chan, *A wavelet neural network conjunction model for groundwater level forecasting.* Journal of Hydrology, 2011. **407**(1): p. 28-40.

217. MathWorks. *Neural Network Toolbox (R2017a)*. 2017 [cited 2017 6th July]; Available from: https://cn.mathworks.com/help/nnet/index.html.

218. Haykin, S., *Neural Networks: A Comprehensive Foundation*. 1998: Prentice Hall PTR. 842.

219. López, G. and C.A. Gueymard, *Clear-sky solar luminous efficacy determination using artificial neural networks.* Solar Energy, 2007. **81**(7): p. 929-939.

220. Pattanasethanon, S., et al., *An accuracy assessment of an empirical sine model, a novel sine model and an artificial neural network model for forecasting illuminance/irradiance on horizontal plane of all sky types at Mahasarakham, Thailand.* Energy Conversion and Management, 2008. **49**(8): p. 1999-2005.

221. Lowry, G., *Energy saving claims for lighting controls in commercial buildings.* Energy and Buildings, 2016. **133**(Supplement C): p. 489-497.

222. Attia, S., M. Hamdy, and S. Ezzeldin, *Twenty-year tracking of lighting savings and power density in the residential sector*. Energy and Buildings, 2017. **154**(Supplement C): p. 113-126.

223. Dubois, M.-C. and Å. Blomsterberg, *Energy saving potential and strategies for electric lighting in future North European, low energy office buildings: A literature review.* Energy and Buildings, 2011. **43**(10): p. 2572-2582.

224. Ahadi, A.A., M.R. Saghafi, and M. Tahbaz, *The study of effective factors in daylight performance of light-wells with dynamic daylight metrics in residential buildings.* Solar Energy, 2017. **155**(Supplement C): p. 679-697.

225. Hraska, J., *Chronobiological aspects of green buildings daylighting.* Renewable Energy, 2015. **73**(Supplement C): p. 109-114.

226. Wong, I.L., *A review of daylighting design and implementation in buildings.* Renewable and Sustainable Energy Reviews, 2017. **74**(Supplement C): p. 959-968.

227. S. R. Kellert, J. Heerwagen, and M. Mador, *Biophilic Design: The Theory Science and Practice of Bringing Buildings to Life*. 2008: John Wiley & Sons.

228. CIBSE, *Enviornmental design-CIBSE Guide A*, in *2.7.5 Illuminance data*. 2012, The Chartered Institution of Building Services Engineers: London. p. 2-35.

229. LightingResearchCenter. *Reflectance*. n.d. [cited 2017 21st Sep]; Available from: http://www.lrc.rpi.edu/education/learning/terminology/reflectance.asp.

230. BritishStandardInstitution(BSI), *BS EN 12464-1:2011 Light and lighting - Lighting of work places. Indoor work places.* 2011, BSI.

231. CIBSE, *Environmental design-CIBSE Guide A*, in *1.8.3 Lighting for performance*. 2012, The Chartered Instituion of Building Services Engineers: London. p. 1-22.

232. Meek, C. and K. Wymelenberg, *Daylighting and integrated lighting design*. 2015, New York: Routledge.

233. Rhinoceros. *Rhino 5 Features*. n.d. [cited 2017 5th Oct]; Available from: https://www.rhino3d.com/eu/.

234. Grasshopper. *Grasshopper - algorithmic modeling for rhino*. n.d. [cited 2017 5th Oct]; Available from: http://www.grasshopper3d.com/.

235. Anonymous, *The RADIANCE 4.2 synthetic imaging system*. 2014, Lawrence Berkeley Laboratory: Berkeley.

236. J., A., Jakubiec and F. C., Reinhart. *Overview and inroduction to DAYSIM and current research developments*. 2012 [cited 2017 8th Oct]; Available from: https://www.radiance-online.org//community/workshops/2012-

copenhagen/Day1/Jakubiec/jakubiec,reinhart_radiance-workshop-presentation_daysim.pdf.

237. EnergyPlus, *Energyplus version 8.8.0 documentation-engineering reference*. 2017, U.S. Department of Energy.

238. Mead, D. *'Trans' materials - modelling and specifying a next generation*. 2010 [cited 2017 29/9]; Available from: https://radiance-online.org//community/workshops/2010-freiburg/PDF/DavidMead.pdf.

239. CIBSE, *Energy consumption guide 19: energy use in offices*. 2000.

240. Goia, F., M. Haase, and M. Perino, *Optimizing the configuration of a fa ̧ade module for office buildings by means of integrated thermal and lighting simulations in a total energy perspective.* Applied Energy, 2013. **108**(Supplement C): p. 515-527.

241. Goia, F., *Search for the optimal window-to-wall ratio in office buildings in different European climates and the implications on total energy saving potential.* Solar Energy, 2016. **132**(Supplement C): p. 467-492.

242. Anonymous. *Windows for high-performance commercial buildings*. n.d. [cited 2017 12th Oct]; Available from: http://www.commercialwindows.org/shgc.php.

243. Wienold, J. and J. Christoffersen, *Evaluation methods and development of a new glare prediction model for daylight environments with the use of CCD cameras.* Energy and Buildings, 2006. **38**(7): p. 743-757.

244. McNeil, A. and G. Burrell, *Applicability of DGP and DGI for evaluating glare in a brightly daylit space*, in *ASHRAE and IBPSA-USA SimBuild 2016: Building Performance Modeling Conference*. 2016, ASHRAE: Salt Lake City, UT.

245. Wu, M., X. Liu, and H. Tang, *Simulation Analysis on the Solar Heating System Combined with Tabs in Lhasa, China of Annex 59.* Energy Procedia, 2015. **78**(Supplement C): p. 2439-2444.

246. Anonymous. *Discounted Payback Period*. n.d. [cited 2018 5th Feb]; Available from: http://accounting-simplified.com/management/investment-appraisal/discounted-payback-period.html.

247. Anonymous. *UK inflation rate at near six-year high*. 2017 [cited 2018 5th Feb]; Available from: http://www.bbc.co.uk/news/business-42320052.

248. Anonymous. *Quarterly: Industrial electricity prices in the EU for small, medium, large and extra large consumers (QEP 5.4.1, 5.4.2, 5.4.3 AND 5.4.4)*. 2017 [cited 2018 5th Feb]; Available from: https://www.gov.uk/government/statistical-data-sets/international-industrial-energy-prices.

249. Anonymous. *Commercial electricity rates in Los Angeles*. n.d. [cited 2018 5th Feb]; Available from: https://www.electricitylocal.com/states/california/los-angeles/.

250. Rivera, D. *Philippine electricity rates still highest in Southeast Asia*. 2017 [cited 2018 5th Feb]; Available from: http://www.philstar.com/business/2017/08/25/1732332/philippine-electricity-rates-still-highest-southeast-asia.

251. Kao, E. *Electricity bills in Hong Kong to see 1 per cent cut, but lawmakers want more*. 2015 [cited 2018 5th Feb]; Available from: http://www.scmp.com/news/hong-kong/economy/article/1891723/electricity-bills-hong-kong-see-1-cent-cut-lawmakers-want.

Appendix A. MNLR model for predicting the optical efficiency of base-coated dCCPC under all sky conditions

The multiple nonlinear regression (MNLR) model for calculating the optical efficiency of base-coated dCCPC under clear, intermediate and overcast sky conditions is as shown in Eq. A-1. The architecture of network for the corresponding ANN model is the same as that of non-coated dCCPC which was introduced in Chapter 6. The parameter values of Eq. A-1 was presented in Table A-1. Fig. A-1 and A-2 demonstrate the comparison between simulated and predicted results of MNLR and ANN models, respectively. The goodness of each model is summarized in Table. A-2. The ANN model provides higher accuracy with the higher R^2 of 0.99 and lower MSE of 0.06%. In addition, the deviations of most results are within ±10%. For MNLR model, it provides less accuracy but still acceptable. Most of the deviations are located within ±20%. The R^2 is still relatively high which is 0.981 and the MSE is 0.17%.

$$\eta_{opt}(\theta_h, \gamma, \varepsilon) = \begin{cases} a_1 \cos(b_1\theta_h + b_2)\cos(b_3\gamma + b_4)(c_1 + c_2\varepsilon + c_3\gamma + c_4\theta_h \\ +c_5\theta_h\gamma + c_6\varepsilon\gamma + c_7\theta_h\varepsilon + c_8\varepsilon^2\theta_h\gamma + c_9\theta_h^2\varepsilon\gamma + c_{10}\gamma^2\varepsilon\theta_h, & \varepsilon > 1.2 \\ +c_{11}\varepsilon^2\theta_h^2\gamma^2 + c_{12}\varepsilon^2 + c_{13}\theta_h^2 + c_{14}\gamma^2) + a_2 \\ \eta_{opt,0}, & 1 \le \varepsilon \le 1.2 \end{cases}$$

(Eq. A-1)

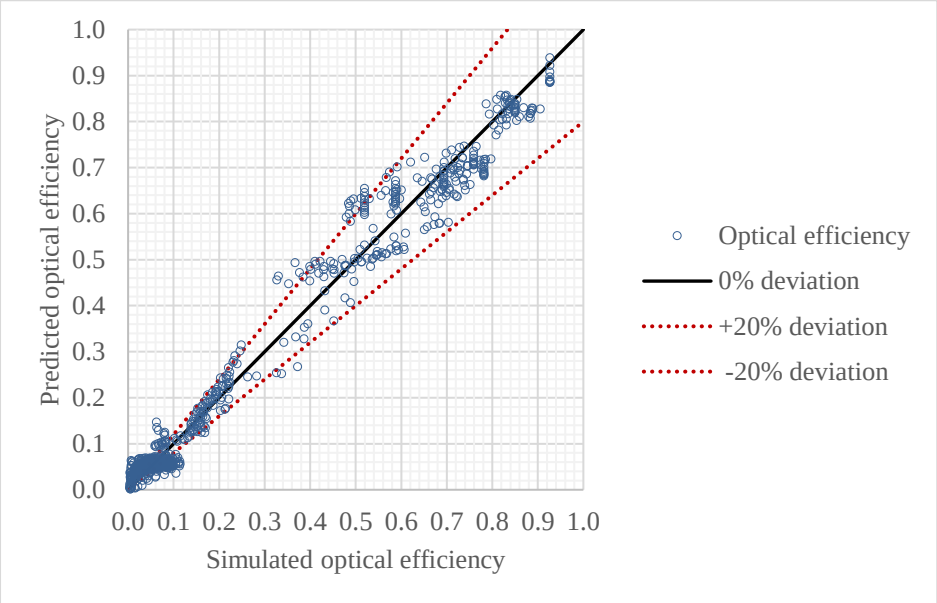


Figure A.1 Comparison between simulated and predicted optical efficiency of non-coated dCCPC under clear and intermediate skies (MNLR)

Table A-1. Table 5.3.2.1. Parameter values of Eq. A-1 for predicting the optical efficiency of base-coated dCCPC

Parameter values of Eq. 5.3.1.1-12 ($\theta_h \geq 70°$)					
a_1	5.565879	c_2	-0.065458	c_9	-0.016424
a_2	0.326730	c_3	0.737212	c_{10}	0.001858
b_1	1.037010	c_4	-0.871353	c_{11}	0.000237
b_2	2.936690	c_5	0.598688	c_{12}	0.000461
b_3	0.940567	c_6	0.028425	c_{13}	-0.051842
b_4	3.657444	c_7	-0.000377	c_{14}	-0.188613
c_1	-0.805497	c_8	-0.000034	$\eta_{opt,0}$	0.19151
Parameter values of Eq. 5.3.1.1-12 ($\theta_h < 70°$)					
a_1	34.649120	c_2	-0.044706	c_9	-0.022813
a_2	0.078639	c_3	1.976457	c_{10}	-0.009434
b_1	0.014816	c_4	0.661873	c_{11}	0.000027
b_2	1.575254	c_5	-0.322520	c_{12}	0.000635
b_3	3.852602	c_6	0.018975	c_{13}	-0.432110
b_4	1.188881	c_7	0.032122	c_{14}	-1.803695
c_1	-0.654670	c_8	-0.000356	$\eta_{opt,0}$	0.19151

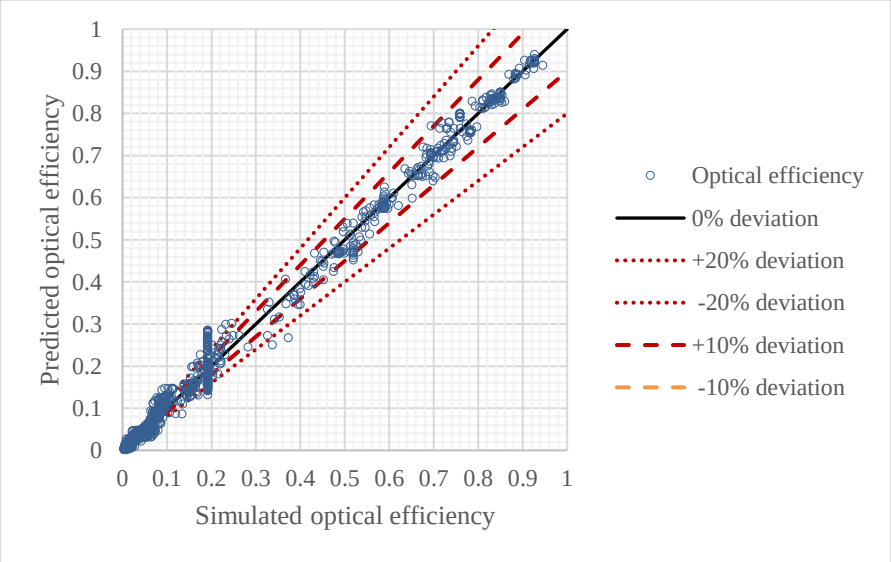


Figure A.2. Comparison between simulated and predicted optical efficiency of non-coated dCCPC (ANN)

Table A-2. Comparison between the correlations of regression formula and ANN model

CPC type	Independent variables	Dependent variables	Regression		ANN	
			R^2	MSE	R^2	MSE
Base-coated	$\theta_h, \gamma, \varepsilon$	η_{opt}	0.981	0.0017	0.993	0.0006

Appendix B. Supplementary figures and tables

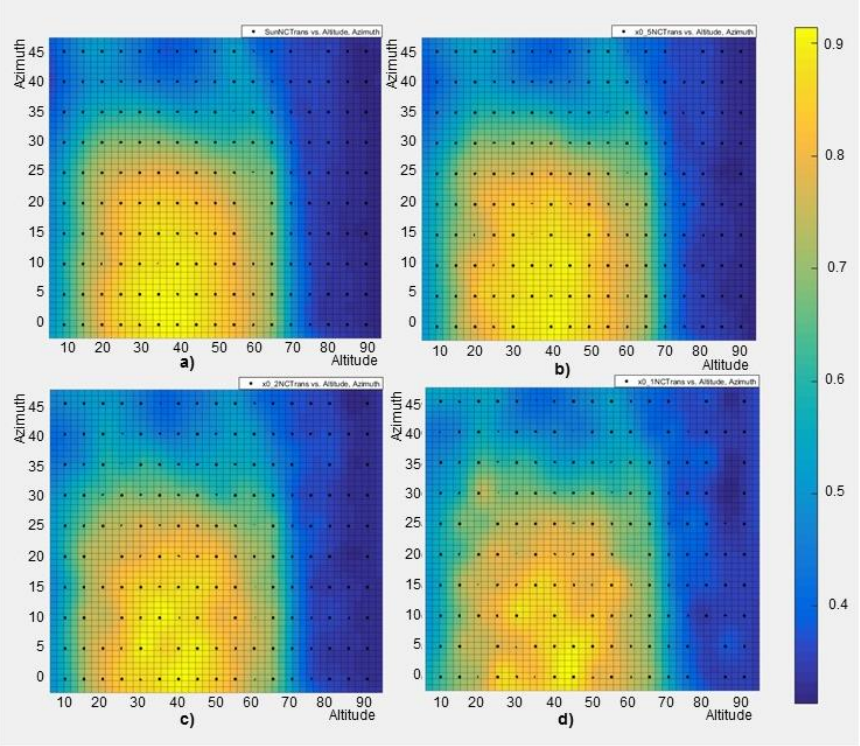


Figure B-1. 2D contour plots of transmittance versus solar altitude and azimuth under clear sky with different sunlight lumen ratios in sky model (φ_{lumen}): a) only direct sunlight; b) $\varphi_{lumen} = 1{:}1$ ($\varepsilon \geq 6.6$) ; c) $\varphi_{lumen} = 1{:}4$ ($\varepsilon \approx 3.6{\sim}6.6$) ; d) $\varphi_{lumen} = 1{:}9$ ($\varepsilon \approx 3{\sim}3.6$)

Table B-1. Parameter values of Eq. 5.3.1.1-1 - Eq. 5.3.1.1-11 for simulated non-coated dCCPC

Eq. 5.3.1.1-1	a_1	-0.232908	a_2	-0.315859	a_3	-0.000689	a_4	0.920885
Eq. 5.3.1.1-2	a_1	0.356634	a_2	0.843854	a_3	-0.000514	a_4	-0.372863
Eq. 5.3.1.1-3	a_1	5.013431	a_2	0.211949	a_3	-0.000492	a_4	-4.399681
	b_1	0.245632	b_2	2.183480				
Eq. 5.3.1.1-4	a_1	0.203053	a_2	0.830325	a_3	-0.000601	a_4	-0.204193
	b_1	3.043950	b_2	-1.946651	b_3	1.031683	b_4	-0.019142
Eq. 5.3.1.1-5	a_1	-0.148874	a_2	-0.401887	a_3	-0.000016	a_4	0.817815
Eq. 5.3.1.1-6	a_1	0.405930	a_2	0.546335	a_3	-0.000017	a_4	-0.127103
	b_1	1.515476	b_2	-0.970654	b_3	-1.006522	b_4	0.059443
Eq. 5.3.1.1-7	a_1	-0.008679	a_2	0.626795				
Eq. 5.3.1.1-8	a_1	0.014342	a_2	0.555678	b_1	-2.644212	b_2	1.610049
	b_3	2.469599	b_4	-0.235906				
Eq. 5.3.1.1-9	a_1	0.473580	a_2	0.397204	b_1	2.100950	b_2	-1.357810
	b_3	2.066359	b_4	-0.146640				
Eq. 5.3.1.1-10	a_1	-1.671734	a_2	0.385077	b_1	2.197839	b_2	1.568689
	b_3	0.261123	b_4	1.778506	c_1	-1.769722	c_2	-0.014123
	c_3	1.931195	c_4	0.587510	c_5	-0.536572	c_6	0.027779
	c_7	0.011019	c_8	-0.021769				
Eq. 5.3.1.1-11	a_1	-0.261408	a_2	0.408440	b_1	2.311628	b_2	1.511448
	b_3	1.923447	b_4	2.341663	c_1	-3.150923	c_2	-0.017137
	c_3	3.226629	c_4	1.155791	c_5	-1.119102	c_6	0.021083
	c_7	0.006956	c_8	0.000254	c_9	-0.012680	c_{10}	0.037775
	c_{11}	-0.000919						

Appendix C. Calculation of inner perpendicular projection angle

Based on the optical path analysis in Chapter 7.2 and Figure 7.2.1, the outer and inner projection angle of dCCPC are added to the coordinate system as shown in Fig. C-1 for further calculation. The outer projection angle θ_n is the equivalent solar altitude θ_h', and the inner perpendicular projection angle θ_n' is the projection angle of the refracted ray (the projection plane is either the vertical north-south plane or east-west plane), which was proposed by Yu and Su [94] initially and was used to calculate the transmittance variation of 2D dCPC. In this example of calculation, the vertical north-south plane is used as the projection plane as an example for calculation. The outer and inner projection angle of incident ray $\overrightarrow{SO}$ are in south-north direction. $\Delta\theta_i$ is the difference between the angles of incidence and refraction. The line OS_1' is the extension of the line of S_1O so that the angle between $\overrightarrow{S_1'O}$ and $\overrightarrow{NO}$ is equal to the refracted angle θ_i' which is the angle between $\overrightarrow{OS_1}$ and $\overrightarrow{ON_1}$.

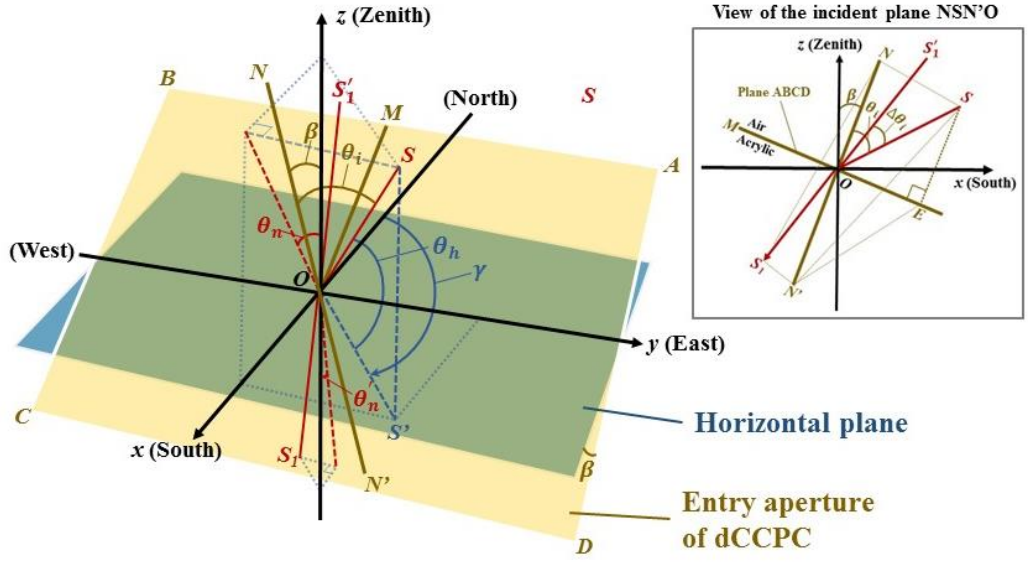


Fig. C-1. Coordinate system of an optical path through a south-facing tilted dCCPC. S: sun position; $\overrightarrow{SO}$: incident ray; $\overrightarrow{OS_1}$: refracted ray; ABCD: top surface of tilted dCCPC; β: tilt angle; NON': normal of the plane ABCD; E: projection of point S onto the plane ABCD; S': projection of point S onto the horizontal plane; $\overrightarrow{OM}$: equivalent north direction of the plane ABCD; OS_1' is the extension of the line S_1O; θ_h: solar altitude; γ: solar azimuth angle; $\Delta\theta_i$: difference between incident angle and refraction angle.

The normal vector of the incidence plane NSN'O can be calculated by:

$$\vec{n} = \overrightarrow{OS} \times \overrightarrow{ON} = \begin{vmatrix} \boldsymbol{i} & \boldsymbol{j} & \boldsymbol{k} \\ -\cos\theta_h \cos\gamma & \cos\theta_h \sin\gamma & \sin\theta_h \\ \sin\beta & 0 & \cos\beta \end{vmatrix}$$

$$= (\cos\theta_h \sin\gamma \cos\beta)\boldsymbol{i} + (\cos\theta_h \cos\gamma \cos\beta + \sin\theta_h \sin\beta)\boldsymbol{j} - (\cos\theta_h \cos\gamma \sin\beta)\boldsymbol{k}$$

Hence the equation for the surface NSN'O is

$$(\cos\theta_h \sin\gamma \cos\beta)x + (\cos\theta_h \cos\gamma \cos\beta + \sin\theta_h \sin\beta)y - (\cos\theta_h \cos\gamma \sin\beta)z = 0$$

(Eq. C-1)

If the length of the vector $\overrightarrow{OS_1'} = (x_0, y_0, z_0)$ is assumed to be 1,

$$\cos\theta_i' = \frac{\overrightarrow{OS_1'} \times \overrightarrow{ON}}{\left|\overrightarrow{OS_1'}\right| \cdot |\overrightarrow{ON}|} = x_0 \sin\beta + z_0 \cos\beta \quad \text{(Eq. A-2)}$$

According to the Snell's law, the relationship between incident angle and refracted angle is

$$n = \frac{\sin\theta_i}{\sin\theta_i'}$$

The angle between $\overrightarrow{OS_1'}$ and $\overrightarrow{OS}$ is $\Delta\theta_i$, which can be expressed by

$$\cos\Delta\theta_i = \cos(\theta_i - \theta_i') = \frac{\overrightarrow{OS_1'} \times \overrightarrow{OS}}{\left|\overrightarrow{OS_1'}\right| \cdot \left|\overrightarrow{OS}\right|} = -x_0 \cos\theta_h \sin\gamma + y_0 \cos\theta_h \sin\gamma + z_0 \sin\theta_h$$

(Eq. C-3)

In addition, (x_0, y_0, z_0) should also satisfy the surface equation Eq. C-1 because the point S_1' lies in the plane NSN'O. Therefore, the value of x_0, y_0, z_0 can be solved based on Eq. C-1, C-2 and C-3.

$$x_0 = -\frac{(\cos\theta_h \cos\gamma \cos\beta + \sin\theta_h \sin\beta)(\cos\Delta\theta_i \cos\beta - \cos\theta_i' \sin\theta_h) - \cos^2\theta_h \sin^2\gamma \sin\beta \cos\theta_i'}{(\cos\theta_h \cos\gamma \cos\beta + \sin\theta_h \sin\beta)^2 + \cos^2\theta_h \sin^2\gamma}$$

$$y_0 = \frac{\cos\theta_h \sin\gamma\,(\cos\theta_h \cos\gamma \cos\beta + \sin\theta_h \sin\beta)[\cos\Delta\theta_i\,(\sin^2\beta + \cos^2\beta) + \cos\theta_i'\,(\cos\theta_h \cos\gamma \sin\beta - \sin\theta_h \cos\beta)]}{(\cos\theta_h \cos\gamma \cos\beta + \sin\theta_h \sin\beta)[\cos^2\theta_h \sin^2\gamma + (\sin\theta_h \sin\beta + \cos\theta_h \cos\gamma \cos\beta)^2]}$$

$$z_0 = \frac{(\cos\theta_h \cos\gamma \cos\beta + \sin\theta_h \sin\beta)(\cos\Delta\theta_i \sin\beta + \cos\theta_i' \cos\theta_h \cos\gamma) + \cos^2\theta_h \sin^2\gamma \sin\beta \cos\theta_i'}{(\cos\theta_h \cos\gamma \cos\beta + \sin\theta_h \sin\beta)^2 + \cos^2\theta_h \sin^2\gamma}$$

The inner projection angle in south-north direction can be calculated by

$$\tan\theta_n' = \frac{z_0}{x_0}$$

$$= \frac{(cos\,\theta_h\,cos\,\gamma\,cos\,\beta + sin\,\theta_h\,sin\,\beta)(cos\,\Delta\theta_i\,sin\,\beta + cos\,\theta_i'\,cos\,\theta_h\,cos\,\gamma) + cos^2\,\theta_h\,sin^2\,\gamma\,sin\,\beta\,cos\,\theta_i'}{cos^2\,\theta_h\,sin^2\,\gamma\,sin\,\beta\,cos\,\theta_i' - (cos\,\theta_h\,cos\,\gamma\,cos\,\beta + sin\,\theta_h\,sin\,\beta)\big(cos\,\Delta\theta_i\,cos\,\beta - cos\,\theta_i'\,sin\,\theta_h\big)}$$

Appendix D. Predictions of the optical efficiency by inner perpendicular projection angle for dCCPC

D.1. Inner perpendicular projection angle and optical efficiency

For 2D base-coated dielectric CPC, it was found that the optical efficiency has strong correlation with inner south projection angle as shown in Fig. D.1-1, which indicates the optical efficiency is determined by inner south projection angle only [94]. Due to the similar working principle and structure, 3D dielectric CPC is possible to perform this property as well. The inner perpendicular projection angle for 3D dCCPC is equivalent to the inner south projection angle for 2D dCPC, which is defined and calculated in Appendix C. Fig. D.1-2 shows how it impacts the optical efficiency under various azimuth angles for the only-sun condition. Because sun illuminance proportion does not affects the curve tendency, the simulation results of 2D dCCPC under sun without sky dome are used to figure out their relationships. Although the tendency of each curve is not as consistent as they are of 2D dCPC for different azimuth angles, they still overlap each other approximately. When the azimuth angles of incident light are 40 °and 45 °, the optical efficiency curves perform small deviations with others. There is no parabolic surface facing this incident direction perpendicularly so that the light path of the incident light whose azimuth angle is close to 45 °is more complex and unpredictable, and it does not completely conform the internal reflection light path in CPC. However, the results still indicate that there is strong correlation between inner perpendicular projection angle and optical efficiency of base-coated 3D dCCPC.

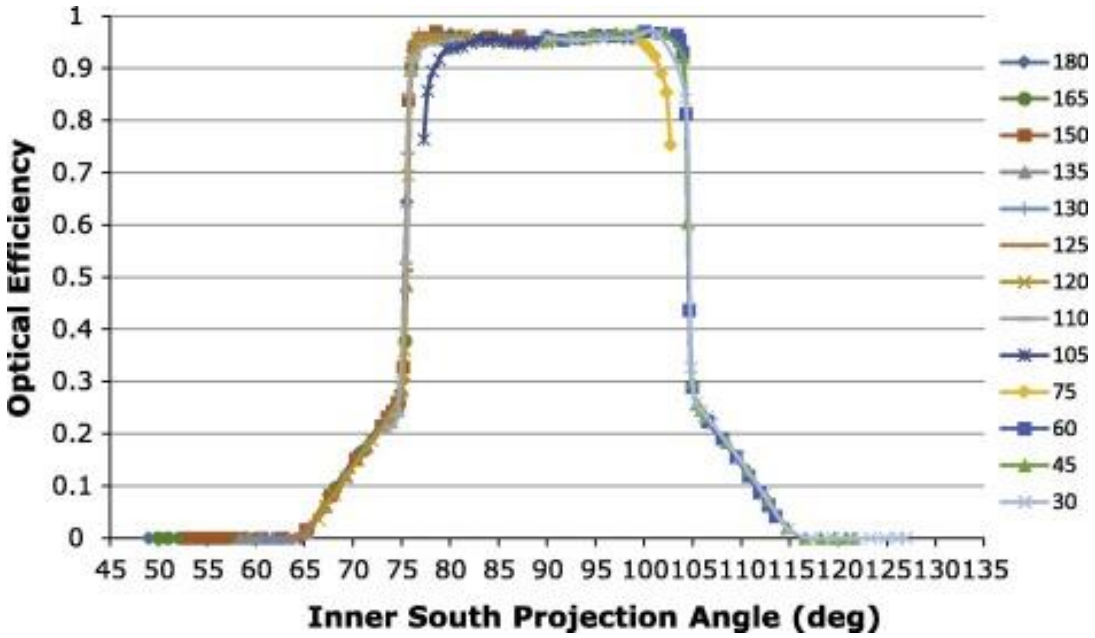


Figure D.1-1. The correlation between inner south projection angle and optical efficiency for various solar azimuths of base-coated 2D dCPC [94]

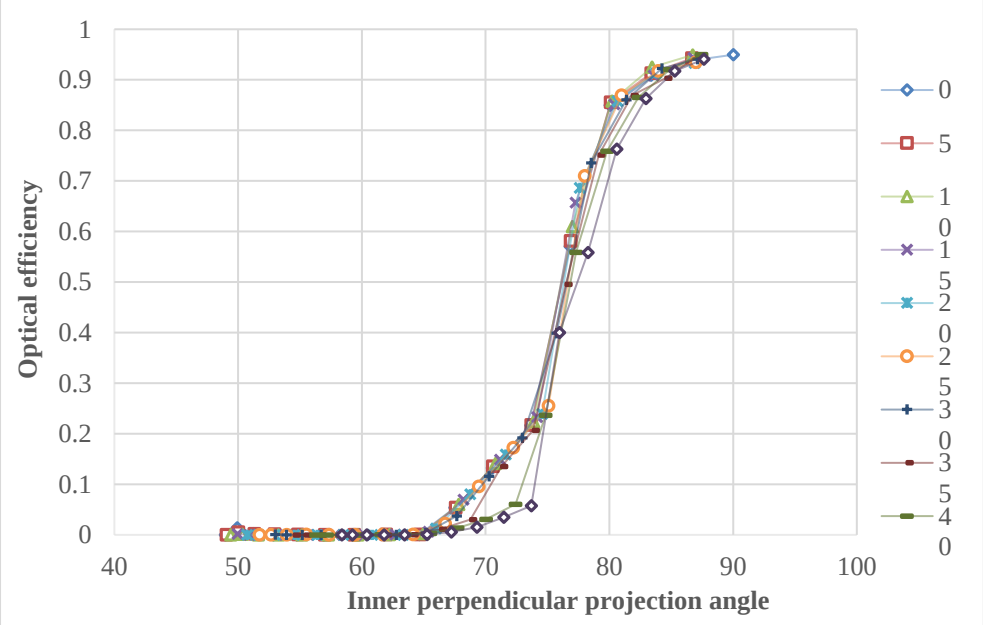


Figure D.1-2. The correlation between inner perpendicular projection angle (projected plane: north-south plane) and optical efficiency for various solar azimuths of base-coated dCCPC (direct sunlight only)

Based on the strong correlation discovered in Fig. D.1-1, it is found that the correlation fits the two-term Gaussian function (Eq. D.1-1) very well. By the regression in MATLAB using Trust-Region algorithm without robust, the goodness of fit gives the sum of squared errors of prediction (SSE) of 0.1392 and the coefficient of

determination (R^2) of 0.9946 which indicate the fitting is quite good. The parameters obtained for this regression are: a_1 =0.9638, b_1 =1.543, c_1 =0.1967, a_2 =0.2863, b_2=1.385 and c_2=0.06824.

$$\eta_{opt}(direct\ sunlight\ only) = a_1 e^{-\left(\frac{\theta_n' - b_1}{c_1}\right)^2} + a_2 e^{-\left(\frac{\theta_n' - b_2}{c_2}\right)^2} \qquad (\text{Eq. D. } 1-1)$$

Where θ_n' is the inner perpendicular projection angle; a_n, b_n, c_n are regression coefficients and $c_n \neq 0$.

In order to make Eq. D.1-1 fit different clear sky conditions with various sky clearness factor, a polynomial term and a constant was added to the original equation as expressed by Eq. D.1-2. Based on the simulation data of different sky clearness factor, the goodness of fit of Eq. D.1-2 has the SSE of 0.9976 and the R^2 of 0.988. Table 4.1.1 illustrates the values of parameters for Eq. D.1-2 for simulated dCCPC. Once the equation and parameter values are determined, it can be used to predict the optical efficiency of 3D dCCPC for any specific sun position and clear sky condition. In addition, the strong correlations among the inner perpendicular projection angle, optical efficiency and sky clearness factor was also be validated by ANN prediction model as well and provides the high value of R^2 which is 0.995.

$$\eta_{opt} = \left[a_1 e^{-\left(\frac{\theta_n' - b_1}{c_1}\right)^2} + a_2 e^{-\left(\frac{\theta_n' - b_2}{c_2}\right)^2}\right] \cdot (a_3\theta_n' + a_4\varepsilon + a_5\theta_n'\varepsilon + a_6) + a_7 \qquad (Eq. D. 1-2)$$

D.2. Inner perpendicular projection angle and transmittance

Except for optical efficiency, it was proved that the sum of transmittance and surface reflection has strong correlation with inner south projection angle for 2D base-coated dCPC as shown in Fig. D.2-1 [94]. It can be found that the sum of transmittance and surface reflectance is mainly affected by inner south projection angle rather than azimuth angle. Thus the relationships between these two variables for 3D base-coated dCCPC are plotted in Fig. D.2-2. They do have correlation when the inner perpendicular projection angle ranges from 75 °-90 °. However, when the inner perpendicular projection angle is smaller than 75 °, the sun of transmittance and surface reflection also affected by azimuth angle, especially when the azimuth is within 20 °-45 °. In addition, because the tendencies of transmittance of non-coated CCPC is similar to those of base-coated CCPC, no strong correlation between inner

perpendicular projection angle and transmittance was found for non-coated CCPC either.

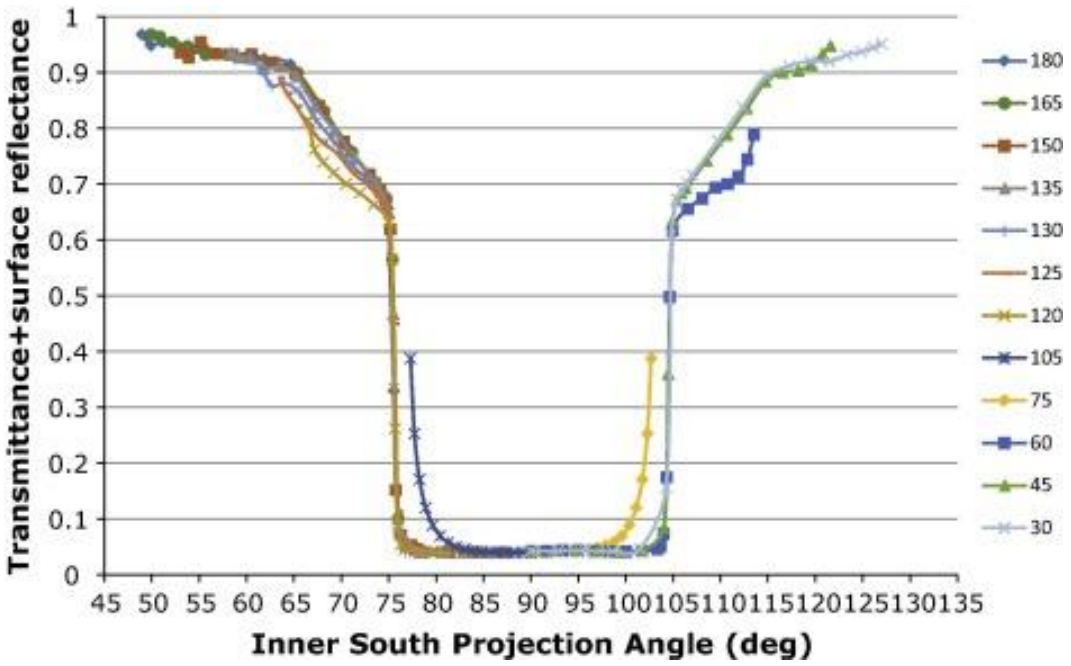


Figure D.2-1. The correlation between inner south projection angle and the sum of transmittance and surface reflection for various solar azimuth of base-coated 2D CPC [94]

Figures D.2-1 and D.2-2 also explain the difference of 2D and 3D dCPC in controlling incident light. 2D dCPC has only two parabolic surfaces. Considering a light ray is a vector, the component of the light ray in the direction along the axis without curved surface would not be reflected several times and it will be transmitted throughout 2D CPC or absorbed by the base. For 2D base-coated dCPC, the final destination of incident light rays can be mainly divided into two parts, one goes onto base calculated as optical efficiency, the other goes throughout CPC that is regarded as transmittance. The lights absorbed and reflected out by CPC are quite few that can be ignored. Different from 2D dCPC, the four parabolic surfaces of 3D dCCPC result in more complicated light path in it. Apart from the lights absorbed by base and transmitted out, a part of incident light are reflected out of 3D dCCPC again from its entry aperture after a series of total internal reflections. In addition, the edges of curved surfaces that connecting with each other also cause the light passing through CPC directly which is also called edge effects. The influences affected by the factors listed above become more obvious as the azimuth angle of incident light is closer to 45 °.

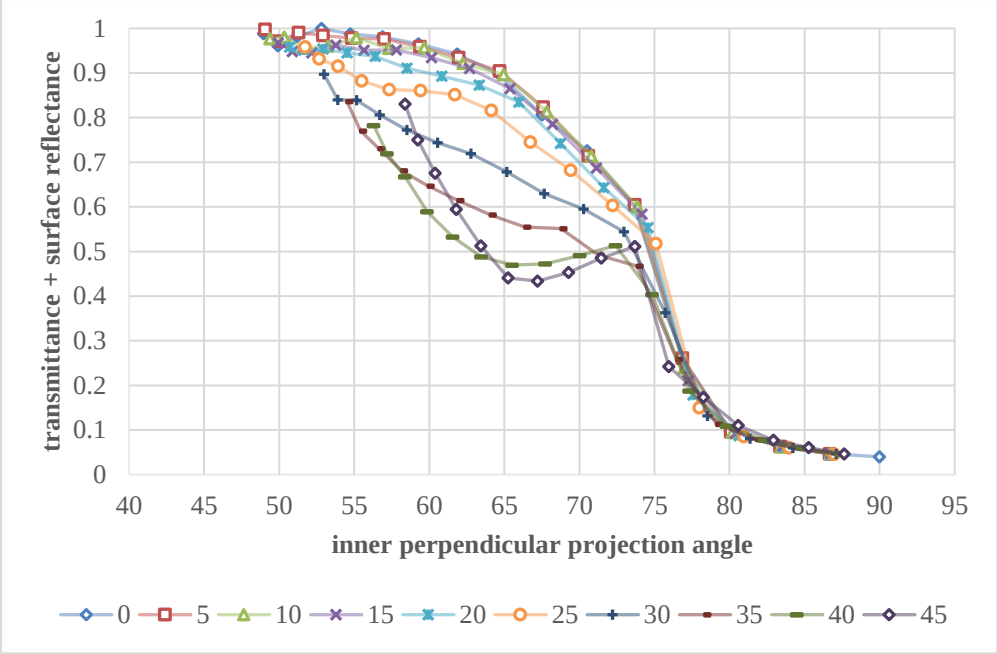


Figure D.2-2. The correlation between inner perpendicular projection angle and the sum of transmittance and surface reflection for various solar azimuth of base-coated CCPC (direct sunlight only)

D.3. Investigations of the correlations among inner perpendicular projection angle, sky clearness factor and other dependent variables

In Appendix D.2, it was found that there is no strong correlations between inner perpendicular projection angle and transmittance, or between inner perpendicular projection angle and the sum of transmittance and surface reflection for dCCPC. This is also indicated by the Artificial Neural Network (ANN) method. Due to the high accuracy of ANN prediction, other dependent variables were attempted to find out the new correlations related to inner perpendicular projection angle. Table D.3-1 shows the correlation coefficients of the best ANN models obtained in trial and error procedure when the inner perpendicular projection angle and sky clearness factor are applied as independent variables. Fig. D.3-1 presents the comparison between predicted and simulated results for the four ANN models. It can be found that the correlation coefficients (R) of the models for non-coated dCCPC are much less than that for base-coated dCCPC. However, the deviations between predicted and simulated values are still big although the values of correlation coefficients (R) are close to 1 for the models of base-coated dCCPC, which means the models are not

available to describe the correlations between the independent and dependent variables successfully.

Table D.3-1. Correlation coefficients of trained ANN models 2 (Independent variables: θ_n', ε; dependent variables: T or $T + R_{ref}$)

CPC type	Independent variables	Dependent variables	Correlation coefficient (R)				MSE (for all data)
			Training (70%)	Validation (15%)	Test (15%)	All (100%)	
Non-coated	θ_n', ε	$T + R_{ref}$	0.7990	0.8394	0.7427	0.7963	0.0117
Non-coated	θ_n', ε	T	0.8015	0.7312	0.8234	0.7952	0.0116
Base-coated	θ_n', ε	$T + R_{ref}$	0.9727	0.9663	0.9472	0.9683	0.0071
Base-coated	θ_n', ε	T	0.9330	0.9289	0.8988	0.9277	0.0112

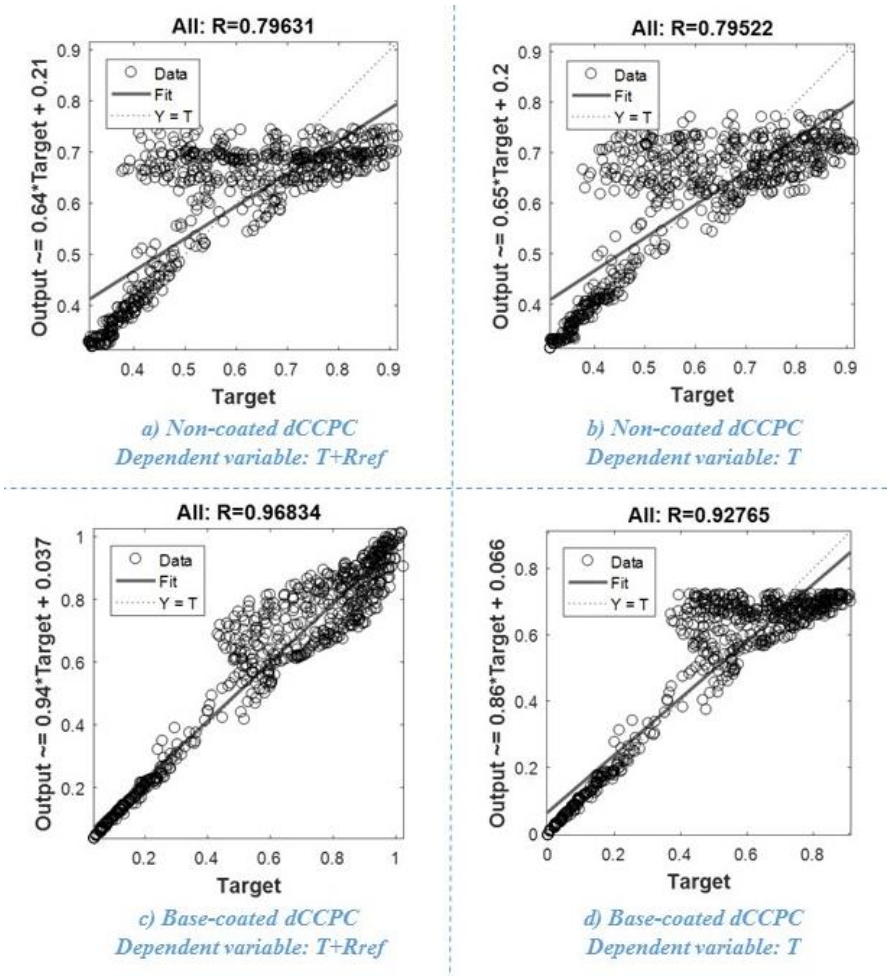


Figure D.3-1. Comparison between predicted and simulation results for ANN models when the independent variables are θ_n' and ε